FACULTY OF ENGINEERING AND ARCHITECTURE

Offshore Green Hydrogen Production via PEM Electrolysers

Siavash Asiaban

Doctoral dissertation submitted to obtain the academic degree of
Doctor of Electromechanical Engineering

Supervisors

Prof. Lieven Vandevelde, PhD - Dimitar Bozalakov, PhD

Department of Electromechanical, Systems and Metal Engineering
Faculty of Engineering and Architecture, Ghent University

December 2025

GHENT UNIVERSITY

FACULTY OF ENGINEERING AND ARCHITECTURE

Offshore Green Hydrogen Production via PEM Electrolysers

Siavash Asiaban

Doctoral dissertation submitted to obtain the academic degree of
Doctor of Electromechanical Engineering

Supervisors

Prof. Lieven Vandevelde, PhD - Dimitar Bozalakov, PhD

Department of Electromechanical, Systems and Metal Engineering
Faculty of Engineering and Architecture, Ghent University

December 2025

GHENT UNIVERSITY

ISBN 978-94-93464-89-6
NUR 959
Wettelijk depot: D/2025/10.500/149

Members of the Examination Board

Chair

Prof. Em. Luc Taerwe, PhD, Ghent University

Other members entitled to vote

Prof. Bashir Bakhshideh Zad, PhD, Université de Mons
Prof. Frederik De Belie, PhD, Ghent University
Prof. Jeroen De Kooning, PhD, Ghent University
Louis Sileghem, PhD, ArcelorMittal

Supervisors

Prof. Lieven Vandevelde, PhD, Ghent University
Dimitar Bozalakov, PhD, Ghent University

Acknowledgements

Looking back at the past years, I feel lucky to have been surrounded by people who supported me throughout this PhD. I would like to thank all of them here.

My deepest appreciation goes to my supervisors, Prof. Lieven Vandevelde and Dr. Dimitar Bozalakov. Lieven, thank you for giving me the opportunity to pursue my PhD in your team and for always answering my questions with patience and enthusiasm. Mitko, I never saw you as a boss, but rather as a friend. Thank you for all your help (and for all the drinks we shared) throughout these past years.

I would also like to sincerely thank the defence committee, Prof. Bashir Bakhshideh Zad, Prof. Frederik De Belie, Prof. Jeroen De Kooning, Dr. Louis Sileghem and the chairman, Prof. Luc Taerwe, for taking the time to review my thesis and for offering insightful recommendations.

I am also grateful to the administrative and technical personnel, Ingrid, Marilyn, Kathleen, Katrien, Nic, Tony and Vincent.

I would also like to thank my colleagues from the EnSy Lab, who made the past years (and the receptions) much more enjoyable: Nezmin, Arash, Mohammad, Shima, Faezeh, Akbar, Nienke, Lisa, Sander, Daan, Cedric and Benjamin. I am especially grateful to Nezmin and Arash, who have been far more than colleagues and have been true friends to me from the very first day I arrived in Belgium.

My heartfelt thanks go to my dad, my mom and my brother, who never asked why, where or how whenever I needed their help. You three have always been my main motivation in life, and I am fully aware of the many times you sacrificed yourselves to support me. Dad, may you rest in peace, and thank you for everything you did for us.

Last, but absolutely not least, I keep in my thoughts the young generation in my homeland, especially Iranian girls, who are bravely shining on the front line of the peaceful “Woman, Life, Freedom” movement.

Contents

Summary

Due to the depletion of fossil fuel reserves, the growing demand for electricity, rising energy security concerns, and the urgent need to enhance environmental sustainability, renewable energy sources (RESs) have emerged at the forefront of the global energy transition. Despite their advantages, the variability of RESs presents substantial challenges to grid stability and reliable operation. To address these issues, numerous strategies have been explored in the literature to accommodate their intermittency and facilitate the large-scale integration of renewables into power systems.

The conversion of renewable electricity into green molecules has been proposed in the literature as a means of accommodating their inherent fluctuations. This thesis focuses on green hydrogen production through electrolysis, which offers system operators a means of stabilising the grid when mismatches occur between mechanical driving generation and net electrical consumption. Electrolysers are the primary devices for sustainable hydrogen production, using water and electricity to split water molecules into hydrogen and oxygen.

Regarding the water demand for electrolysers, reliance on clean water causes challenges for green hydrogen production, particularly given the increasing global water scarcity. In addition, freshwater resources are unevenly distributed worldwide. To address these limitations, researchers have investigated the substitution of freshwater with alternative sources, including groundwater, brackish water, and seawater.

With respect to the power requirements of electrolysers, offshore wind energy has emerged as one of the most promising renewable sources, particularly for countries with access to the sea. Employing offshore wind to power electrolysers also allows their direct deployment at sea, where seawater can be used as an alternative to freshwater. Furthermore, producing hydrogen at sea is especially valuable for regions with limited onshore areas, while also creating opportunities to integrate other marine renewables such as wave and tidal power. Moreover, it aligns with the emerging concept of energy islands, where energy conversion, storage facilities, and associated infrastructure are co-located offshore in proximity to wind farms. Accordingly, the main focus of this thesis is on offshore hydrogen production.

Nevertheless, utilising electrolysers offshore presents operational and maintenance challenges and results in higher costs, which need to be considered. In addition, seawater contains impurities, particularly high concentrations of sodium and chlorine, making its direct use more complex than clean water, as these impurities accelerate degradation, reduce efficiency, and impose stricter requirements on the materials used in electrolysers and their auxiliary systems.

Generally, two main pathways exist for producing hydrogen from seawater: direct seawater electrolysis (DSWE) and seawater electrolysis with upfront water treatment. DSWE demands a fundamental redesign of commercial electrolysers and the development of advanced electrocatalysts for both alkaline (AE) and proton exchange membrane (PEM) electrolysers. As stated, this stems from the high concentrations of corrosive chloride ions in seawater, which negatively affect the performance of the electrolysers. In contrast, applying upfront water treatment potentially adds extra components and system complexity, which can increase costs. Yet, studies indicate that the additional energy requirements, capital costs, operating costs and final hydrogen price resulting from the integration of upfront water treatment systems remain marginal, since these contributions are negligible compared with the substantially higher requirements of the electrolysis process itself. Therefore, this thesis focuses on offshore hydrogen production coupled with upfront water treatment systems.

As for the selection of desalination technology, membrane-based seawater desalination is widely regarded as one of the most practical solutions. Within this category, reverse osmosis (RO) and forward osmosis (FO) are the leading candidates. RO is a pressure-driven process in which hydraulic pressure is applied to overcome the osmotic gradient, whereas FO relies solely on the natural osmotic pressure difference across the membrane, eliminating the need for hydraulic pressure. Although this makes RO more energy-intensive than FO, it remains the preferred option due to its high reliability and excellent salt rejection. Moreover, continuous advances in membrane design, low-friction materials, and variable-frequency drives have lowered RO's energy consumption from roughly 20 kWh/m^3_{water} in the 1970s to just 2–3 kWh/m^3_{water} today. Consequently, RO has become the dominant technology in commercial seawater desalination, while FO has not yet reached large-scale deployment.

Among the two most advanced electrolyser technologies, PEM electrolysers demonstrate several advantages over their alkaline counterparts. Capable of operating at current densities above 2 A/cm^2, PEM units achieve the same hydrogen output with only about one-fifth of the footprint of AEs. Their solid electrolyte also enables rapid response, in contrast to the slower dynamics of AEs, whose liquid electrolyte increases inertia, leading to a slower ion transport. The fast start-up and ramping capability make PEM electrolysers particularly suitable for integration with intermittent RESs, where operation under fast dynamics is required, while AEs remain better suited to fixed-power

applications. In addition, PEM electrolysers benefit from low gas crossover rates, enabling operation across a wide range of power densities, and generally achieve higher efficiency than alkaline systems. However, their behaviour under dynamic conditions requires thorough assessment. Therefore, this research investigates offshore hydrogen production using PEM electrolysers coupled with seawater reverse osmosis (SWRO) systems for water desalination.

In the context of offshore hydrogen production using a PEM electrolyser integrated with an SWRO unit, the first essential step is the development of a dynamic model of the PEM electrolyser. This stems from the fluctuating output of RESs, which results in variable power input to electrolysers. Although PEM electrolysers exhibit rapid response characteristics, their operation is not instantaneous. Capturing this dynamic behaviour is critical in flexibility studies where electrolysers are integrated with RESs. Neglecting capacitive effects and dynamic response can lead to substantial errors in estimating both electricity consumption and hydrogen output, with the scale of miscalculation depending on the operating conditions and system parameters. Over a 20-year lifetime, such inaccuracies may significantly affect techno-economic analyses, given the cost difference between electricity input and hydrogen output.

In this thesis, the dynamic PEM electrolyser model is formulated through mathematical equations that describe the electrochemical interactions of the anode, cathode, membrane, voltage, and thermal modules. This approach overcomes the limitations of circuit-based models, whose parameters are only valid under fixed operating conditions. As a result, circuit-based models often fail in flexibility studies, where frequent changes in operating states, particularly power input, must be considered.

Following the development of the dynamic PEM electrolyser model, integration with an SWRO system is required. While many studies recognise the strong potential of coupling reverse osmosis systems with PEM electrolysers for offshore hydrogen production, only a limited number address their integrated operation. Because the energy demand and costs of water treatment are minor compared with the overall hydrogen production process, this step is often overlooked, even though it represents an essential part of the system. Therefore, a coupled SWRO-PEM model, combining the two most promising technologies for seawater-based offshore hydrogen production, is required for comprehensive analysis. While it is true that the additional energy use, cost, and footprint of a reverse osmosis unit are negligible relative to the electrolyser, hydrogen production with upfront water treatment is only acceptable and competitive with DSWE if the treated water consistently meets the minimum requirements in terms of quantity and quality. This aspect is examined in detail in this thesis.

As electricity consumption represents the dominant cost in electrolysis, and electrolysers are inherently power-intensive, an optimised operational strategy

is essential to ensure profitable operation. Furthermore, the fast response capability of PEM electrolysers makes their potential for providing ancillary services, such as frequency containment reserve (FCR), a key area for further research, which is also explored in this study.

The main contributions of this research include the development of a dynamic mathematical model, validated against experimental data, that accurately replicates the behaviour of a PEM electrolyser while remaining computationally efficient for large-scale power system simulations. In addition, an SWRO model is presented, which is also validated against experimental data, and integrated with the PEM electrolyser model, thereby enabling offshore hydrogen production assessment using a coupled SWRO-PEM framework. Moreover, the investigation of several operational modes of PEM electrolysers under different electricity price trajectories provides valuable insights for plant operators, allowing them to identify optimal strategies that minimise hydrogen production costs, maximise revenues, and ensure competitiveness with hydrogen produced through alternative technologies.

Samenvatting

Door de uitputting van fossiele brandstofreserves, de groeiende vraag naar elektriciteit, toenemende bezorgdheid over energiezekerheid en de dringende noodzaak om de ecologische duurzaamheid te verbeteren, zijn hernieuwbare energiebronnen (renewable energy sources - RESs) op de voorgrond getreden in de wereldwijde energietransitie. Ondanks hun voordelen vormt de variabiliteit van RESs een aanzienlijke uitdaging voor de stabiliteit en betrouwbare werking van het elektriciteitsnet. Om deze problemen aan te pakken, zijn in de literatuur tal van strategieën onderzocht om hun intermitterende karakter op te vangen en de grootschalige integratie van hernieuwbare energiebronnen in elektriciteitssystemen te vergemakkelijken.

In de literatuur is de omzetting van hernieuwbare elektriciteit naar groene moleculen voorgesteld als een manier om hun inherente schommelingen op te vangen. Deze thesis richt zich op de productie van groene waterstof door middel van elektrolyse, waarmee systeembeheerders het elektriciteitsnet kunnen stabiliseren wanneer de hoeveelheid opgewekte energie niet overeenstemt met het elektriciteitsverbruik. Elektrolyse, waarbij elektriciteit wordt gebruikt om watermoleculen te splitsen in waterstof en zuurstof, is momenteel de voornaamste methode voor duurzame waterstofproductie.

De afhankelijkheid van schoon water voor de productie van groene waterstof vormt een belangrijke uitdaging, gezien de toenemende waterschaarste. Bovendien zijn zoetwaterbronnen ongelijk verdeeld over de wereld. Onderzoek naar de vervanging van zoet water voor elektrolyse wijst in de richting van alternatieve bronnen, zoals grondwater, brak water of zeewater.

Wat betreft de stroombehoefte van elektrolyse is offshore windenergie een van de meest veelbelovende hernieuwbare bronnen gebleken, in het bijzonder voor landen met toegang tot de zee. Door offshore windenergie te gebruiken voor elektrolyse-installaties kunnen deze ook direct op zee worden ingezet, met gebruik van zeewater als alternatief voor zoet water. De productie van waterstof op zee is vooral waardevol voor regio's met beperkte landoppervlakte, en biedt tegelijk ook de mogelijkheid om andere hernieuwbare energiebronnen uit de zee, zoals golf- en getijdenenergie, te integreren. Bovendien sluit dit aan bij het opkomende concept van energie-eilanden, waar energieomzetting,

opslagfaciliteiten en alle bij horende infrastructuur samen offshore in de buurt van windparken worden ondergebracht.

Het offshore gebruik van elektrolyse-installaties brengt echter operationele en onderhoudsmatige uitdagingen met zich mee en resulteert in hogere kosten, waarmee rekening moet worden gehouden. Bovendien bevat zeewater onzuiverheden, met name hoge concentraties natrium en chloor, waardoor het directe gebruik ervan complexer is dan bij schoon water, aangezien deze onzuiverheden de afbraak versnellen, de efficiëntie verminderen en strengere eisen stellen aan de materialen die in elektrolyse-installaties en hun hulpsystemen worden gebruikt.

We onderscheiden twee belangrijke manieren om waterstof uit zeewater te produceren: directe zeewaterelektrolyse (direct seawater electrolysis - DSWE) en zeewaterelektrolyse met voorafgaande waterbehandeling. DSWE vereist een fundamenteel herontwerp van commerciële elektrolyseapparaten en de ontwikkeling van geavanceerde elektrokatalysatoren voor zowel alkalische elektrolyse (alkaline electrolyser - AE) als protonuitwisselingsmembraan (proton exchange membrane - PEM) elektrolyse, omwille van de hoge concentraties corrosieve chloride-ionen die de prestaties van de elektrolyseapparaten negatief beïnvloeden. Daarentegen kan het toepassen van voorafgaande waterbehandeling extra componenten en systeemcomplexiteit met zich meebrengen, wat de kosten kan verhogen. Studies tonen echter aan dat de extra energiebehoefte, kapitaalkosten, exploitatiekosten en uiteindelijke waterstofprijs als gevolg van de integratie van voorafgaande waterbehandelingssystemen marginaal blijven, aangezien deze bijdragen verwaarloosbaar zijn in vergelijking met de aanzienlijk hogere eisen van het elektrolyseproces zelf. Dit proefschrift focust daarom op offshore waterstofproductie in combinatie met voorafgaande waterbehandelingssystemen.

Onder de beschikbare technologieën, ontziltingstechnologie wordt ontzilting van zeewater met behulp van membranen algemeen beschouwd als een van de meest praktische oplossingen. Binnen deze categorie zijn omgekeerde osmose (reverse osmosis - RO) en voorwaartse osmose (forward osmosis - FO) de belangrijkste kandidaten. RO is een drukgestuurd proces waarbij hydraulische druk wordt toegepast om de osmotische gradiënt te overwinnen, terwijl FO uitsluitend vertrouwt op het natuurlijke osmotische drukverschil over het membraan, waardoor hydraulische druk overbodig is. Hoewel RO hierdoor energie-intensiever is dan FO, blijft het de voorkeursoptie vanwege de hoge betrouwbaarheid en uitstekende zoutverwijdering. Bovendien hebben voortdurende verbeteringen in het ontwerp van membranen, wrijvingsarme materialen en frequentieregelaars het energieverbruik van RO teruggebracht van ongeveer 20 $\mathrm{kWh/m^3_{water}}$ in de jaren 1970s tot slechts 2–3 $\mathrm{kWh/m^3_{water}}$ vandaag de dag. Daardoor is RO de dominante technologie geworden in commerciële zeewaterontzilting, terwijl FO momenteel niet op grote schaal wordt toegepast.

Van de twee meest geavanceerde elektrolyseertechnologieën biedt PEM-elektrolyse verschillende voordelen ten opzichte van haar alkalische tegenhanger. PEM-units kunnen werken bij stroomdichtheden van meer dan 2 A/cm^2 en bereiken dezelfde waterstofproductie met slechts een vijfde van de voetafdruk van AE-toestellen. Hun vaste elektrolyt maakt ook een snelle respons mogelijk, in tegenstelling tot de tragere dynamiek in AE, waar de vloeibare elektrolyt de inertie vergroot, wat leidt tot een trager ionentransport. Door de snelle opstart- en opvoermogelijkheden is PEM-elektrolyse bijzonder geschikt voor integratie met intermitterende RESs, waar een snelle dynamiek vereist is, terwijl AE beter geschikt is voor toepassingen met een vast vermogen. Dankzij lage gascrossover-snelheden, kunnen PEM toestellen over een breed scala aan vermogensdichtheden werken en over het algemeen een hoger rendement behalen dan alkalische systemen. Hun gedrag onder dynamische omstandigheden moet echter grondig worden beoordeeld. In dit proefschrift wordt het onderzoek naar PEM-elektrolyse in combinatie met zeewateromgekeerde osmose (seawater reverse osmosis - SWRO)-systemen voor waterontzilting voor gebruik in offshore waterstofproductie beschreven.

Een eerste essentiële stap is de ontwikkeling van een dynamisch model van de PEM-elektrolyseinstallatie, aangezien de-fluctuerende output van RESs resulteert in een variabele stroomtoevoer naar elektrolyse-installaties. Hoewel PEM-elektrolyse-installaties een snelle respons vertonen, is hun werking niet onmiddellijk. Het vastleggen van dit dynamische gedrag is van cruciaal belang in flexibiliteitsstudies waarbij elektrolyse-installaties worden geïntegreerd met RESs. Het negeren van capacitieve effecten en dynamische respons kan leiden tot aanzienlijke fouten bij het schatten van zowel het elektriciteitsverbruik als de waterstofproductie, waarbij de omvang van de misrekening afhankelijk is van de operationele omstandigheden en systeemparameters. Over een levensduur van 20 jaar kunnen dergelijke onnauwkeurigheden een aanzienlijke invloed hebben op techno-economische analyses, gezien het kostenverschil tussen elektriciteitsinput en waterstofoutput.

In dit proefschrift wordt het dynamische PEM-elektrolysemodel geformuleerd aan de hand van wiskundige vergelijkingen die de elektrochemische interacties van de anode, kathode, membraan, spanning en thermische modules beschrijven. Deze benadering overwint de beperkingen van modellen gebaseerd op circuits, waarvan de parameters alleen geldig zijn onder vaste bedrijfsomstandigheden. Als gevolg daarvan schieten modellen gebaseerd op circuits vaak tekort in flexibiliteitsstudies, waarbij rekening moet worden gehouden met frequente veranderingen in de bedrijfsomstandigheden, met name het opgenomen vermogen.

Na de ontwikkeling van het dynamische PEM-elektrolysemodel is integratie met een SWRO-systeem vereist. Hoewel veel studies het grote potentieel erkennen van het koppelen van omgekeerde osmose-systemen aan

PEM-elektrolyseinstallaties voor offshore waterstofproductie, gaat slechts een beperkt aantal in op de geïntegreerde werking ervan. Omdat de energiebehoefte en kosten van waterbehandeling gering zijn in vergelijking met het totale waterstofproductieproces, wordt deze stap vaak over het hoofd gezien, ook al vormt deze een essentieel onderdeel van het systeem. Daarom is voor een uitgebreide analyse een gekoppeld SWRO-PEM-model nodig, waarin de twee meest veelbelovende technologieën voor offshore waterstofproductie op basis van zeewater worden gecombineerd. Hoewel het extra energieverbruik, de kosten en de voetafdruk van een omgekeerde osmose-eenheid verwaarloosbaar zijn in vergelijking met de elektrolyse-eenheid, is waterstofproductie met voorafgaande waterbehandeling alleen acceptabel en concurrerend met DSWE als het behandelde water consequent voldoet aan de minimumvereisten in termen van kwantiteit en kwaliteit. Dit aspect wordt in deze thesis uitvoerig onderzocht.

Aangezien het elektriciteitsverbruik de belangrijkste kostenpost vormt bij elektrolyse en elektrolyse-installaties inherent energie-intensief zijn, is een geoptimaliseerde operationele strategie essentieel om een rendabele werking te garanderen. Bovendien maakt het snelle reactievermogen van PEM-elektrolyse-installaties hun potentieel voor het leveren van ondersteunende diensten, zoals frequentiebegrenzingsreserve (frequency containment reserve - FCR), tot een belangrijk gebied voor verder onderzoek, dat ook in de huidige studie wordt meegenomen.

De belangrijkste bijdragen van dit onderzoek zijn onder meer de ontwikkeling van een dynamisch wiskundig model, gevalideerd aan de hand van experimentele gegevens, dat het gedrag van een PEM-elektrolyse-installatie nauwkeurig nabootst en tegelijkertijd computationeel efficiënt blijft voor grootschalige simulaties van energiesystemen. Daarnaast wordt een SWRO model gepresenteerd, dat eveneens is gevalideerd aan de hand van experimentele gegevens en geïntegreerd is met het PEM-elektrolyseapparaatmodel, waardoor offshore waterstofproductie kan worden beoordeeld met behulp van een gekoppeld SWRO-PEM-raamwerk. Bovendien levert het onderzoek naar verschillende operationele modi van PEM-elektrolyseapparaten onder verschillende elektriciteitsprijstrajecten waardevolle inzichten op voor exploitanten van installaties, waardoor zij optimale strategiën kunnen identificeren die de waterstofproductiekosten minimaliseren, de inkomsten maximaliseren en het concurrentievermogen ten opzichte van waterstof geproduceerd met alternatieve technologieën waarborgen.

List of Abbreviations

AC	Alternating Current
AE	Alkaline Electrolyser
AEM	Anion Exchange Membrane
AFC	Alkaline Fuel Cell
aFRR	Automatic Frequency Restoration Reserve
BESS	Battery Energy Storage System
BoP	Balance of Plant
BRP	Balance Responsible Party
CAES	Compressed Air Energy Storage
CapEx	Capital Expenditure
CCS	Carbon Capture and Storage
CCUS	Carbon Capture, Utilisation and Storage
CESS	Chemical Energy Storage System
CSP	Concentrated Solar Power
DAC	Direct Air Capture
DC	Direct Current
DHI	Diffuse Horizontal Irradiance
DMFC	Direct Methanol Fuel Cell
DNI	Direct Normal Irradiance
DRFC	Discrete Regenerative Fuel Cell
DSM	Demand-Side Management
DSO	Distribution System Operator
DSWE	Direct Seawater Electrolysis
EENS	Expected Energy Not Served
EESS	Electrical Energy Storage System
EF	Environmental Footprint
ESS	Energy Storage System
EU	European Union
FC	Fuel Cell
FCO	Full Capacity Operation
FCR	Frequency Containment Reserve
FO	Forward Osmosis
FR	Fresnel Reflector

FSP	Flexibility Service Provider
GHG	Greenhouse Gas
GHI	Global Horizontal Irradiance
GWP	Global Warming Potential
HFC	Hydrogen Fuel Cell
HVDC	High Voltage Direct Current
IPCC	Intergovernmental Panel on Climate Change
IRENA	International Renewable Energy Agency
ISO	Independent System Operator
LCA	Life Cycle Assessment
LCOE	Levelised Cost of Electricity
LCOH	Levelised Cost of Hydrogen
LCOW	Levelised Cost of Water
LNG	Liquefied Natural Gas
LOHC	Liquid Organic Hydrogen Carriers
LOLE	Loss of Load Event
LOLP	Loss of Load Probability
MCA	Market Clearing Algorithm
MCP	Market Clearing Price
MCV	Market Clearing Volume
MEA	Membrane Electrolyte Assembly
mFRR	Manual Frequency Restoration Reserve
MPPT	Maximum Power Point Tracking
NDC	Nationally Determined Contribution
NDP	Net Driving Pressure
NPV	Net Present Value
O&M	Operation and Maintenance
OpEx	Operating Expenditure
P2G2P	Power-to-Gas-to-Power
PAO	Price-adaptive Operation
PEM	Proton Exchange Membrane
PEMFC	Proton Exchange Membrane Fuel Cell
PFAS	Per- and Polyfluoroalkyl substances
PFSA	Perfluoro-Sulfonic Acid
PHES	Pumped Hydroelectric Storage
PHT	Photothermal
PO	Partial Oxidation
PPA	Power Purchase Agreement
PSO	Power System Operator
PT	Parabolic Trough
PV	Photovoltaic

RED	Renewable Energy Directive
RES	Renewable Energy Source
RFB	Redox Flow Battery
RO	Reverse Osmosis
RoCoF	Rate of Change of Frequency
SD	Solar Dish
SMES	Superconducting Magnetic Energy Storage
SMR	Steam Methane Reforming
SO	Solid Oxide
SOFC	Solid Oxide Fuel Cell
SSM	Supply-Side Management
ST	Solar Tower
SWRO	Seawater Reverse Osmosis
TDS	Total Dissolved Solids
TESS	Thermal Energy Storage System
TSO	Transmission System Operator
UC	Ultra-Capacitors
URFC	Unitised Regenerative Fuel Cell

List of Notations and Symbols

A	Area, m^2
C	Concentration, mol/m^3
C_b	Brine concentration, ppm
C_e^t	Variable electricity price, €/MWh
C_{FCR}^t	FCR provision price, €/MWh
C_f	Feed concentration, ppm
C_H	Upper percentile threshold
C_L	Lower percentile threshold
C_l	Lumped thermal capacitance, J/K
C_p	Permeate concentration, ppm
CF	Cash flow, €
c_p	Specific heat capacity, J/kg.K
c'_p	Specific heat capacity, J/mol.K
D	Binary diffusion coefficient, m^2/s
D_e	Load damping factor, W/Hz
D_f	Diffusivity, m^2/s
D_w	Diffusion coefficient, m^2/s
d_h	Hydraulic diameter, m
E	Equivalent weight, kg
E_0	Standard cell reversible voltage, V
E_{act}	Activation energy, J/mol
e	Error
F	Faraday constant, A.s/mol
f	Frequency, Hz
H	Enthalpy, J/mol
$H_{2,be}$	Hydrogen break-even price, €/kg
$H_{2,gen}^t$	Generated hydrogen, kg
H_e	Grid inertia constant, s
h	Heat transfer coefficient, $W/m^2.K$
h_c	Channel height, m
h_l	Head loss, bar
I	Current, A

i	Discount rate
i_{p}	Number of ions produced during solute dissociation
J_{s}	Solute flux, $\mathrm{kg/m^2.h}$
J_{w}	Water flux, $\mathrm{L/m^2.h}$
j	Current density, $\mathrm{A/m^2}$
j_0	Exchange current density, $\mathrm{A/m^2}$
k	Price sensitivity coefficient, $\mathrm{MW^2.h/€}$
k_{m}	Mass transfer coefficient, m/s
k_{s}	Solute permeability, m/h
k_{st}	Temperature coefficient for solute, K
k_{w}	Water permeability, $\mathrm{L/m^2.h.bar}$
k_{wt}	Temperature coefficient for water, K
l	Length, m
M	Molar mass, kg/mol
M_{s}	Salt transfer rate through membrane, kg/s
$\dot{M}$	Flow rate, kg/s
m	Mass, kg
N	Number of moles
n	Number of cells
n_{d}	Electro-osmotic drag coefficient
n_{t}	Number of turbines
$\dot{N}$	Flow rate, mol/s
$\dot{n}$	Molar flux, $\mathrm{mol/m^2.s}$
P	Pressure, Pa
P_{e}	Power, W
P_{el}	Operating power of the electrolyser, MW
P^t_{FCR}	Power adjusted by the electrolyser for FCR provision, MW
P_{min}	Minimum power of the electrolyser, MW
P_{rated}	Rated power of the electrolyser, MW
P^t_{res}	Reserved capacity of the electrolyser for FCR provision, MW
p	Partial pressure, Pa
Q	Heat flow, W
Q_{b}	Brine flow rate, $\mathrm{m^3/day}$
Q_{e}	Electric charge, C
Q_{f}	Feed flow rate, $\mathrm{m^3/day}$
Q_{p}	Permeate flow rate, $\mathrm{m^3/day}$
R	Resistance, $\Omega.\mathrm{m^2}$
R_{r}	Recovery rate
R_{u}	Universal gas constant, J/K.mol
Re	Reynolds number
r	Mean pore radius, m
S_{r}	Salt rejection

Sc	Schmidt number
Sh	Sherwood number
T	Temperature, K
t	Time, s
V	Voltage, V
v	Volume, m^3
v_c	Cross-flow velocity, m/s
v_e	Valence, C/mol
w	Channel width, m
X	Molar fraction
y	year
Z_{exp}	Number of experiments

Greeks

α	Charge transfer coefficient
α_{el}	Reserved capacity coefficient of the electrolyser
β_x	Concentration polarisation factor
γ_{el}	Baseload coefficient of the electrolyser
δ	Thickness, m
δ_{hl}	Head loss coefficient
ϵ	Porosity
ε/k	Lennard-Jones potential, K
Θ	Mean molecular radii, Å
Λ	Coolant to water mole ratio
μ	Viscosity, kg/m.s
Ω	Diffusion collision integral
λ	Water content of membrane
ξ	Tortuosity
π	Osmotic pressure, bar
ρ	Density, kg/m^3
σ	Conductivity, S/m
τ	Dimensionless temperature
Φ	Osmotic coefficient
Ω	Diffusion collision integral

List of Figures

List of Tables

Chapter 1

Introduction

This chapter introduces the general idea and broad context of the research presented in this thesis, including the motivations and objectives. Additionally, it provides an overview of the conducted work, and describes the thesis structure.

1.1 Context of the Research

Due to several factors, such as fossil fuel depletion, climate change, and energy security, the integration of renewable energy sources (RESs) into the power grid has become inevitable [1]. However, despite their environmental and economic benefits, the intermittent nature of RESs poses several challenges to the power system, including reduced stability, reliability, and flexibility [2].

Among various strategies to address RESs intermittency, the production of green molecules, such as hydrogen, has gained considerable attention [3]. For instance, instead of curtailing renewable generation during periods of surplus, the excess electricity can be converted into hydrogen via electrolysis, which has the potential to be combusted to produce electricity or converted back to electricity using fuel cells. In addition to grid balancing, green hydrogen can replace conventional hydrogen, currently produced mainly through fossil fuel-based methods such as steam methane reforming, thereby reducing carbon dioxide emissions across multiple sectors [4].

Electrolysers, which require only water and electricity, are considered the most viable option for green hydrogen production to date [5]. To address the issue of freshwater consumption, recent studies have explored the use of alternative water sources, such as seawater, particularly in countries with coastal access [6]. This approach also supports the energy island concept, allowing electrolysers to be installed offshore and thereby reducing land use, lowering electrical energy transmission costs, and enabling direct integration with offshore RESs [7]. This is especially advantageous for the integration of

offshore wind energy, a promising renewable energy source for countries with access to the sea [8].

For the types of electrolysers, alkaline and proton exchange membrane (PEM) electrolysers are the two mature technologies [9, 10]. Owing to its solid membrane (typically Nafion), the PEM electrolyser offers a faster response to fluctuating renewable power input than the alkaline electrolyser, which employs a liquid electrolyte (typically KOH) [11, 12]. Therefore, PEM electrolysers demonstrate greater suitability for renewable energy applications. Nonetheless, given the high costs associated with green hydrogen production via electrolysers and the intermittent nature of RESs, determining the optimal operational strategy that maximises revenue while providing optimal support to the power grid remains a crucial area of investigation.

This research addresses key aspects of offshore hydrogen production using an integrated PEM electrolyser and seawater reverse osmosis (SWRO) system. The main contributions of the study include the development of a dynamic mathematical model for the PEM electrolyser, which is essential for flexibility studies. This model is further integrated with a developed SWRO model to evaluate the operation of both units at the single-system level. Finally, the optimal operational strategy for the electrolyser is determined under various scenarios, based on historical electricity data in Belgium and the national targets set by the federal government.

This study differentiates itself from prior research, such as [13] and [14], by primarily focusing on hydrogen production, irrespective of its specific application. This approach makes the study versatile and suitable for cases in which the production of hydrogen derivatives, such as methane or methanol, is intended. For example, in offshore applications, hydrogen can be produced and combined with seawater-derived CO_2 to form methane or methanol.

In addition, this study is based on an accurate PEM electrolyser model which, unlike circuit-based models, enables reliable estimation of the system behaviour in hydrogen production applications. The main drawback of circuit-based models, as elaborated in Chapter 4, arises from the fixed values assigned to resistors and capacitors across the entire operating range of the electrolyser. This results in the PEM electrolyser exhibiting a constant time response irrespective of the operating conditions, which does not reflect practical behaviour. To improve the accuracy of such models, adaptive algorithms have been proposed in which circuit parameters are recalculated for different electrical input currents. Although this enhances performance to some extent, it remains difficult for these approaches to capture the influence of other operating conditions, such as temperature and pressure, which play a significant role in real electrochemical dynamics.

It is worth mentioning that although the Belgian power system is used as the reference case in this study, the developed models and methods for seawater

electrolysis are applicable to other power systems as well. Hence, Belgium serves as a representative test case for this research.

1.2 Overview

The rest of this thesis is organised as follows:

Chapter 2 provides an overview of the challenges associated with the intermittency and integration of RESs into the power grid, as their variability is among the primary drivers behind the use of hydrogen production from RESs. The chapter focuses on the two most widely used RESs worldwide, namely wind and solar energy. The global status, historical evolution, and main technological advancements related to these two sources are also presented. Subsequently, various approaches to address the intermittency of these sources are discussed.

Chapter 3 explores the different pathways for hydrogen production. This includes a review of hydrogen generation methods based on both fossil fuels and RESs. The chapter then focuses on water electrolysis technologies, including alkaline, PEM, and solid oxide electrolysers. The structure of the power system and the potential of hydrogen production to provide grid flexibility are then explored. Lastly, Belgian government policies and national targets for hydrogen production are reviewed to provide a foundation for the upcoming chapters.

Chapter 4 presents the development of a dynamic mathematical model for the PEM electrolyser. Following a literature review, all relevant modules of the PEM electrolyser, including the anode, cathode, membrane, voltage, and thermal modules, are described in detail, along with their interactions and corresponding mathematical equations. The model is then validated using experimental data under both steady-state and dynamic operating conditions.

Chapter 5 focuses on the modelling of a reverse osmosis (RO) desalination system for seawater. After a review of relevant literature, a model based on the solution-diffusion method is developed. Thereafter, the model is validated using two sets of experimental data: one with low salinity and another with high salinity levels comparable to seawater. The chapter concludes with the integration of the upscaled RO model and the PEM electrolyser model from Chapter 4 to form a coupled seawater electrolysis system.

Chapter 6 offers a comprehensive techno-economic analysis of PEM electrolyser operation modes in the context of projected electricity prices and

potential evolutions of the Belgian energy system. Following a review of the literature, the scenarios for the investigation of electrolyser operation modes are defined. These include operating the electrolyser at full capacity, operating it based on day-ahead market electricity prices, and operating it based on grid frequency to provide ancillary services. The methodology for estimating future electricity prices in the Belgian power system is then described, and hourly electricity prices are predicted for three potential energy system configurations. Subsequently, the hydrogen break-even price is calculated for the defined scenarios, and the results are compared. This chapter also provides a cost breakdown of green hydrogen production and applies a sensitivity analysis to identify the key parameters influencing the hydrogen break-even price.

Chapter 7 discusses a life cycle assessment (LCA) of hydrogen production using a desalination system and PEM electrolyser, coupled with offshore wind energy and hydrogen storage. After a literature review, the LCA methodology is developed in accordance with ISO 14040 and 14044 standards. First, the goals and scope, functional unit, and system boundary of the study are defined. Afterwards, a life cycle inventory is compiled, including the materials required for each subsystem based on the chosen functional unit. Emissions associated with each material are then quantified using the Environmental Footprint v3.0 impact assessment method. Finally, the results are analysed to determine the contribution of each subsystem, namely the wind turbine, desalination system, PEM electrolyser, and storage system, to the overall environmental load across various impact categories.

Chapter 8 summarises the main conclusions drawn from this thesis and presents potential directions for further research.

1.3 Author Bibliography

This section provides an overview of the author's publications and their connection to the chapters of this thesis. The material presented in the subsequent chapters is reflected in the following works. Publications 1 and 2 correspond to the content of Chapter 2, whereas Publications 3 and 4 are associated with Chapter 3. Publication 5 relates directly to the material developed in Chapter 4, and Publication 6 covers the main elements discussed in Chapter 5. The work presented in Chapter 6 has been submitted for publication and is under review at the time of writing this thesis.

1. **S. Asiaban**, N. Kayedpour, A. E. Samani, D. Bozalakov, J. D. M. De Kooning, G. Crevecoeur, and L. Vandevelde, "Wind and solar intermittency and the associated integration challenges: A comprehensive review

including the status in the Belgian power system." *Energies*, vol. 14, no. 9, p. 2630, 2021.

2. N. Kayedpour, A. E. Samani, **S. Asiaban**, N. Singh, J. D. M. De Kooning, L. Vandevelde, and G. Crevecoeur. "Wind turbine anomaly detection using surrogate models." In *18th EAWE PhD Seminar on Wind Energy*. 2022. http://hdl.handle.net/1854/LU-01GNHSB2TAD2TKM30JJ02J37NP

3. **S. Asiaban**, N. Kayedpour, D. Bozalakov, and L. Vandevelde. "Production of green molecules at sea using the concept of energy island." In *European PhD Hydrogen Conference (EPHyC)* pp. 537-539. 2024. http://hdl.handle.net/1854/LU-01HW5M67W6EXXND5HRZDBT7TN

4. N. Kayedpour, **S. Asiaban**, A. E. Samani, J. D. M. De Kooning, L. Vandevelde, and G. Crevecoeur. "Navigating towards a sustainable energy future: overbuilding renewables and hydrogen integration strategies." In *European PhD Hydrogen Conference (EPHyC)*, 2024. http://hdl.handle.net/1854/LU-01HYFQVX25TVKF5A493NNS4FZA

5. **S. Asiaban**, D. Bozalakov, and L. Vandevelde. "Development of a dynamic mathematical model of PEM electrolyser for integration into large-scale power systems." *Energy Conversion and Management: X*, vol. 23, p. 100610, 2024.

6. **S. Asiaban**, D. Bozalakov, E. Cornelissen, and L. Vandevelde. "Offshore Hydrogen Production via the PEM Electrolyser Coupled with the Reverse Osmosis System." *IEEE Access*, vol. 13, pp. 161685-161708, 2025.

Bibliography

[1] M. Cakir, I. Cankaya, I. Garip, and I. Colak, "Advantages of using renewable energy sources in smart grids," in *2022 10th International Conference on Smart Grid (icSmartGrid)*, pp. 436–439, IEEE, 2022.

[2] S. Asiaban, N. Kayedpour, A. E. Samani, D. Bozalakov, J. D. M. De Kooning, G. Crevecoeur, and L. Vandevelde, "Wind and solar intermittency and the associated integration challenges: A comprehensive review including the status in the Belgian power system," *Energies*, vol. 14, no. 9, p. 2630, 2021.

[3] M. Awad, A. Said, M. H. Saad, A. Farouk, M. M. Mahmoud, M. S. Alshammari, M. L. Alghaythi, S. H. A. Aleem, A. Y. Abdelaziz, and A. I. Omar, "A review of water electrolysis for green hydrogen generation considering pv/wind/hybrid/hydropower/geothermal/tidal and wave/biogas energy systems, economic analysis, and its application," *Alexandria Engineering Journal*, vol. 87, pp. 213–239, 2024.

[4] F. Moreno-Brieva, J. Guimón, and J. C. Salazar-Elena, "From grey to green and from west to east: The geography and innovation trajectories of hydrogen fuel technologies," *Energy Research & Social Science*, vol. 101, p. 103146, 2023.

[5] M. Tofighi-Milani, S. Fattaheian-Dehkordi, and M. Lehtonen, "Electrolysers: A review on trends, electrical modeling, and their dynamic responses," *IEEE Access*, 2025.

[6] Y. Zhang, Y. Zhang, Z. Li, E. Yu, H. Ye, Z. Li, X. Guo, D. Zhou, C. Wang, Q. Sha, *et al.*, "A review of hydrogen production via seawater electrolysis: current status and challenges," *Catalysts*, vol. 14, no. 10, p. 691, 2024.

[7] M. A. Useche, O. Gomis-Bellmunt, V. Albernaz, M. Cheah-Mane, B. Castro, and P. Gebraad, "Energy islands: Opportunities, challenges and topologies," *Challenges and Topologies*, 2024.

[8] A. Lüth, Y. Werner, R. Egging-Bratseth, and J. Kazempour, "Electrolysis as a flexibility resource on energy islands: The case of the North Sea," *Energy Policy*, vol. 185, p. 113921, 2024.

[9] S. Sebbahi, N. Nabil, A. Alaoui-Belghiti, S. Laasri, S. Rachidi, and A. Hajjaji, "Assessment of the three most developed water electrolysis technologies: Alkaline water electrolysis, proton exchange membrane and solid-oxide electrolysis," *Materials Today: Proceedings*, vol. 66, pp. 140–145, 2022.

[10] I. Vincent and D. Bessarabov, "Low cost hydrogen production by anion exchange membrane electrolysis: A review," *Renewable and Sustainable Energy Reviews*, vol. 81, pp. 1690–1704, 2018.

[11] Z. Abdin, C. Webb, and E. M. Gray, "Modelling and simulation of a proton exchange membrane (PEM) electrolyser cell," *International Journal of Hydrogen Energy*, vol. 40, no. 39, pp. 13243–13257, 2015.

[12] Y. Zeng, M. Luo, C. Qin, C. Liu, and B. Chen, "Investigation on the performance of proton exchange membrane water electrolyzer coupled with a catalyst layer pore network model," *Energy Conversion and Management: X*, vol. 21, p. 100523, 2024.

[13] A. Ebneali Samani, *Flexible integration of energy-intensive CCU based processes and wind energy in the electrical power system*. PhD thesis, Ghent University, 2022.

[14] A. Dadkhah, *Flexible operation of power-to-hydrogen and electrical loads to provide grid support*. PhD thesis, Ghent University, 2022.

Chapter 2

Intermittency of Renewable Energy Sources

Renewable energy sources (RESs) have drawn significant attention in recent years as a means to facilitate the transition towards a low-carbon energy system. Although they deliver more environmentally friendly energy compared to fossil fuels, the inherently intermittent nature of RESs results in fluctuating power generation, which hinders their large-scale penetration into the power system. This chapter provides an overview of the most widely used RESs globally, namely wind and solar energy, and the challenges associated with their integration into the power system.

The rest of this chapter is organised as follows: Section 2.1 provides an overview of the motivations for shifting towards RESs, along with their main advantages and limitations. In Section 2.2, the impact of the volatile nature of RESs, particularly wind and solar energy, on the power system operation are assessed. Section 2.3 and Section 2.4 review wind and solar energy, respectively, including their historical development, technological milestones, and global deployment statistics. These sections also present a brief assessment of the impact of the COVID-19 pandemic on the progress of RESs deployment, in order to evaluate the resiliency of these renewable sources. Additionally, the variations of wind speed and solar irradiance are appraised. Section 2.5 discusses the technologies to combat the volatile nature of wind and solar energy by assessing the existing approaches for accommodating or mitigating their intermittency. Finally, in Section 2.6, the key conclusions of the chapter are presented, including a comparison of the dominant RES technologies.

2.1 Introduction

Due to the depletion of fossil fuels, growing awareness of energy security, increasing electricity demands, and ever-rising concerns about environmental issues, renewable energy sources are attracting greater attention over time. For example, oil and gas reserves in the UK's North Sea are in decline, as the peak of extraction has already occurred in 2003 [1]. Based on the International Energy Agency (IEA) projections, the global peak in crude oil extraction is expected to occur shortly after 2028, most likely in 2029 or 2030 [2, 3]. For natural gas, the authors in [4] estimate that the global production peak will occur between 2034 and 2046.

Regarding the environmental matters, when fossil fuels are combusted, their carbon combines with oxygen during the burning process, and carbon dioxide (CO_2) is released [5]. In [6] and [7], it is demonstrated that climate change is directly linked to CO_2 in the atmosphere, as it traps radiated heat from the surface of the Earth and raises global temperature. According to [8], the average global surface temperature has increased by approximately 1 °C since the late 19th century. Meanwhile, the Paris Agreement defines 1.5 °C as the threshold for global temperature rise, and the Intergovernmental Panel on Climate Change (IPCC) has already warned about the consequences of exceeding this limit [9, 10]. Moreover, among the three major reservoirs in which CO_2 is stored, namely the atmosphere, biosphere, and oceans, approximately 93% of CO_2 can be found in ocean water. This gas can move freely between these reservoirs [11]. As ambient temperature rises, ocean temperatures also increase accordingly, which reduces their ability to hold CO_2 and leads to its release back into the atmosphere. This process reinforces itself, as the additional CO_2 in the atmosphere traps more heat, resulting in more atmosphere temperature rise, and, in turn, leading to further warming and a continued rise in ocean temperatures [7].

Given the aforementioned considerations, transitioning to alternative energy sources is crucial. RESs offer a clean and eco-friendly form of energy, and their abundant resource availability makes them a promising alternative to fossil fuels. Energy security is also of paramount global importance. With a considerable portion of proven oil reserves of the world situated in the Middle East, the tendency towards switching to reliable alternatives is increasing in other countries [12]. Another attractive advantage is that RESs provide a substantial number of job opportunities. According to the International Renewable Energy Agency (IRENA), RESs supported 16.2 million jobs in 2023, with over 18% growth compared to 2022 [13]. By 2050, IRENA projects that RESs could provide as many as 42 million jobs globally [14]. Being offered in various formats, RESs can be utilised to some extent in nearly all countries, with the specific type primarily depending on the geographical and climate

conditions.

To date, different renewable energy sources have been introduced, among which solar energy, wind energy, tidal energy, hydro energy, geothermal energy, and bioenergy are the most popular ones. The term 'renewable energy' refers to sources that are sustainable and endless in nature. However, despite their renewable nature, these sources depend on specific environmental conditions. For example, wind energy requires sufficient wind speeds to rotate turbine blades. Similarly, solar panels require clear skies to capture the necessary radiation components for electricity generation. This introduces a major drawback of RESs, which is intermittency [15–17]. It is worth mentioning that the intermittency levels of RESs differ. For instance, geothermal energy is not intermittent and is not dependent on weather, time of day, or seasonal fluctuations, and it provides a continuous and stable output with high capacity factors. However, extensive efforts have been made to address the intermittency issue of volatile RESs and, where possible, to accommodate or even mitigate the variability of their power output. Additionally, from the perspective of electrical grids, integrating some RESs into the power system presents technical challenges. This stems from the volatile nature of their output, which can adversely affect voltage, frequency and power quality of the electrical systems. Nevertheless, it is important to note that RESs can also support grid stability by providing ancillary services [18]. Although renewable energy sources may offer financial benefits to consumers, particularly when supported by government incentives, the technologies involved are typically more expensive upfront compared to conventional energy systems. To combat the fluctuating nature of RESs, energy storage systems have been introduced [19,20]. Yet, these systems could be expensive, especially for large-scale capacities.

Overall, the advantages of RESs significantly outweigh their limitations. That is why studies demonstrate that public attitudes towards RESs are satisfactorily acceptable, with an increasing trend of favourable perception across most countries [21–23]. However, efforts to raise public awareness remain necessary [24].

This chapter presents a comprehensive review of solar and wind energy, followed by a particular emphasis on the context of Belgium. It is worth noting that hydro-power is also used in Belgium. Regardless, due to its relatively small contribution compared to wind and solar, and the limited potential for further development in Belgium, mainly because of the quite flat topography of the country, it is not addressed in this study. Additionally, although the tendency towards utilising bioenergy is increasing in Belgium, it is excluded from this study. This is primarily because bioenergy is far more predictable than solar and wind energy, and the focus of this chapter is on intermittent RESs.

2.2 Intermittency and Power System

The primary goal of a system operator is to reliably match the electric generation and demand at all times, and at the lowest possible cost. The intermittency of wind and solar energy adversely affects the power system, with the extent of these impacts depending on the characteristics of the power system, its inherent flexibility, and the penetration level of volatile RESs in the grid [25]. The effects of fluctuating power output of wind and solar on the grid can be classified into two main groups: short-term impacts, which include maintaining system balance on an operational timescale (minutes to hours), and long-term impacts, which involve ensuring sufficient power supply during peak load conditions [25].

The first short-term impact of integrating renewable energy sources into the power system is the negative effect of wind speed and solar irradiance uncertainty on system reserves. As mentioned, a constant balance between supply and demand must be maintained. To account for unexpected generation losses and sudden changes in demand, utilities maintain operating reserves within the power system. When determining the required reserve capacity, all potential fluctuations in demand or generation must be taken into account. Inevitably, due to the variable nature of wind and solar energy, the scheduled operating reserve must be increased to ensure reliable system regulation, which consequently raises integration cost [26]. In Fig. 2.1, the resulting change in the power system reserves is shown [27]. As shown, with the growing share of intermittent RESs, wind energy in this case, the reserve capacity must be increased to compensate for the uncertainty in their output.

Several studies have investigated the aforementioned impact and potential

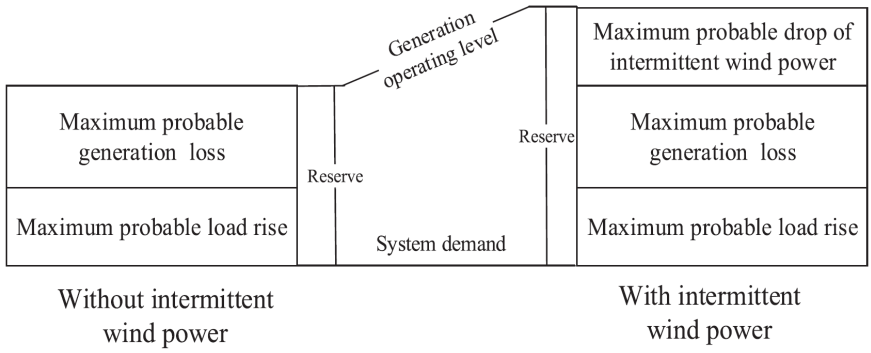

Figure 2.1: Impact of RESs intermittency on power system reserve requirements [27], modified in [28]

strategies to prevent an undesirable increase in reserve capacity. The authors in [29] modelled this effect and examined the increase in power system reserves as a function of wind and solar photovoltaic (PV) penetration levels. Overall, they concluded that for wind penetration levels up to 30%, the primary reserve capacity increases by 0.3–1.0% of the installed generation capacity, whereas at a 40% penetration level, reserve requirements can exceed 1%. The observed discrepancies across studies for identical penetration levels are attributed to dissimilar reserve sizing methodologies applied in the studies. Moreover, the authors concluded that as a result of the lower predictability of PV, the reserve requirements for a given level of PV penetration are higher than for wind. In [30], the reserve requirement associated with wind intermittency, referred to as wind power reserve, is quantified. In their case study involving a 100 MW load, 10% wind power uncertainty, and a load uncertainty interval of [-2,2], it is deduced that the wind power reserve increases linearly with respect to the wind penetration rate. Quantitatively, as the wind penetration rate, defined as the ratio of wind power output to total load, increased from no wind penetration to 50%, the wind power reserve, defined as the share of system reserve dedicated to compensating for wind uncertainty, rose from no reserve requirement to 10%. Despite this additional reserve requirement, higher wind penetration reduces reliance on conventional generation, leading to a reduction of up to over 25% in the operating cost of the power system at penetration levels of up to 50%.

The second short-term impact of wind and solar intermittency concerns the expected reduction in CO_2 emissions. For instance, while it is theoretically anticipated that replacing a conventional power plant with a wind power plant of equivalent generation capacity would eliminate the associated CO_2 emissions, this is not always the case in real-world applications. The extent of CO_2 emission reduction relies on the type of generation or fuel source being substituted. Moreover, conventional power plants are typically designed to operate at specific output levels at which their performance is optimised. Nevertheless, due to the growing share of intermittent RESs in the power system, online generators must either increase their ramping rate – defined as the ability of a generator to change its output – or undergo increased start-up and shut-down cycles to accommodate both load variations and RESs output fluctuations. For example, instances may occur where demand rises while RESs output drops, or vice versa. In both situations, an apparent increased rate of change in the system load happens, leading to non-optimal performance of conventional power plants [26, 31]. Therefore, the efficiency of power plants decreases, and their CO_2 emissions increase, as illustrated in Fig. 2.2 [28].

The authors in [28] and [29] compared several studies and showed that at intermittent RESs penetration levels (as a percentage of annual load) of 11% (wind), 23% (wind-solar), and 33% (wind-solar), the average increase in spe-

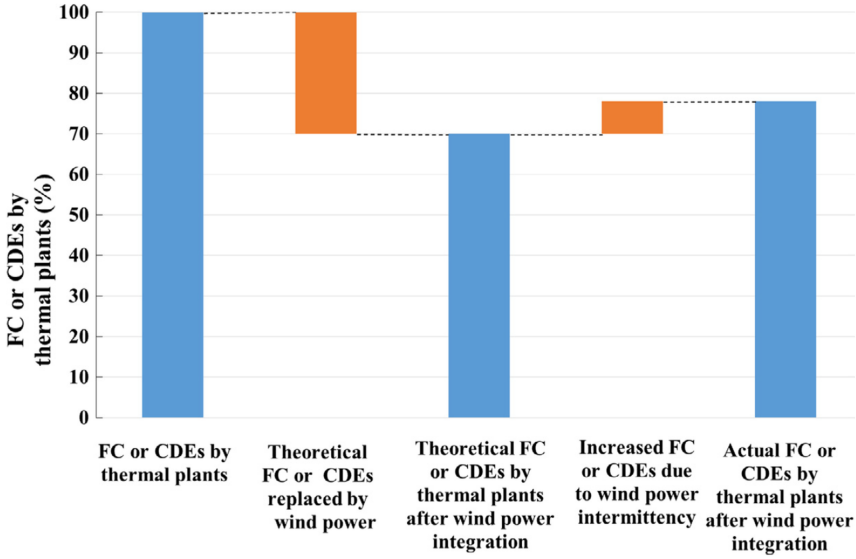

Figure 2.2: Schematic illustration of the expected and actual reductions in fuel consumption (FC) or CO_2 emissions (CDEs) associated with the penetration of intermittent RESs [28]

cific CO_2 emissions of thermal plants are 7%, 2.3%, and <1%, respectively. However, as confirmed by [28], despite the reduced effectiveness in CO_2 reduction, integrating RESs into the power system still has a significant positive impact on lowering CO_2 emissions.

The decrease in the expected increase of specific CO_2 emissions at higher RESs penetration levels can be explained by several system-level effects. At low penetration levels, only a small share of thermal generation is displaced, and the existing set of thermal units is required to cycle more frequently and operate for longer periods at part load, which increases their specific CO_2 emissions. At higher penetration levels, however, the least efficient and least flexible thermal units are displaced first, leaving only the most efficient and flexible units in operation. These remaining units increasingly operate in a peaking-only mode, which reduces the number of inefficient part-load hours and therefore lowers the marginal increase in specific CO_2 emissions. The studies investigated in [28] and [29] also concern different locations, namely East Germany (11% wind), the Western United States (23% wind–solar), and the United States Western Interconnection (33% wind–solar), and the types of thermal units displaced in these systems differ, which influences how specific CO_2 emissions evolve with higher shares of renewable energy. Finally, the composition of the renewable mix also plays a role, since aggregated wind–solar portfolios exhibit lower net variability, which reduces the required ramping of thermal plants

and consequently mitigates the increase in specific CO_2 emissions at higher penetration levels.

The third short-term effect is that intermittent RESs can influence transmission and distribution losses, thereby increasing costs. Depending on the location of wind farms and solar plants, particularly in relation to the voltage level of the integration point and the distance to the load, this impact can be either positive or negative. According to [25], in the UK, where wind power production is concentrated in the north, the estimated additional transmission costs are projected to increase, reaching 2 €/MWh and 3 €/MWh at penetration levels of 20% and 30%, respectively. In [32], based on eighteen months of experience and daily monitoring of forecasted transmission losses, an increase in losses was observed during periods of high wind speed, whereas a decrease occurred around noon when PV generation reached its peak. However, their analysis excluded days with adverse weather conditions, such as rain or snow, due to additional corona losses in transmission lines. The impacts of the intermittent output of wind and PV generation over a one-day period are shown in Fig. 2.3(a) and Fig. 2.3(b), respectively [32].

The fourth short-term impact of the intermittent nature of wind and solar power arises when their output power exceeds the level that can be safely absorbed and utilised by the grid. This typically happens during periods of high wind speeds and clear days. To maintain frequency, voltage, and overall grid stability, a certain number of conventional power plants must remain online at all times. Inevitably, when the output power from solar and wind generation units exceeds a specific threshold, curtailment becomes necessary. According to [25], a wind energy penetration level of approximately 10% is the point at which curtailment may become necessary. However, this is a rough estimate and depends strongly on factors such as transmission line capacity, grid infrastructure, demand levels, and interconnection capacity with neighbouring countries. The authors in [33] noted that high curtailment levels are primarily due to inadequate transmission capacity. Specifically, curtailment levels vary significantly by region. In areas where transmission capacity and infrastructure are limited, curtailment can be substantially reduced by upgrading grid infrastructure, expanding transmission capacity, and integrating additional technologies and interconnections that enhance power system flexibility.

The fifth short-term impact of RESs on the power system concerns their influence on grid characteristics. As previously discussed in this chapter, the primary challenge in transitioning to RESs lies in their intermittent and unpredictable nature, as well as their non-dispatchable characteristics, which result in mismatches between electricity generation and consumption. Furthermore, the liberalisation of the electricity market and the increased volume of transactions have led to significant fluctuations in electricity prices and have complicated the management of power system security and reliability [34]. RESs can

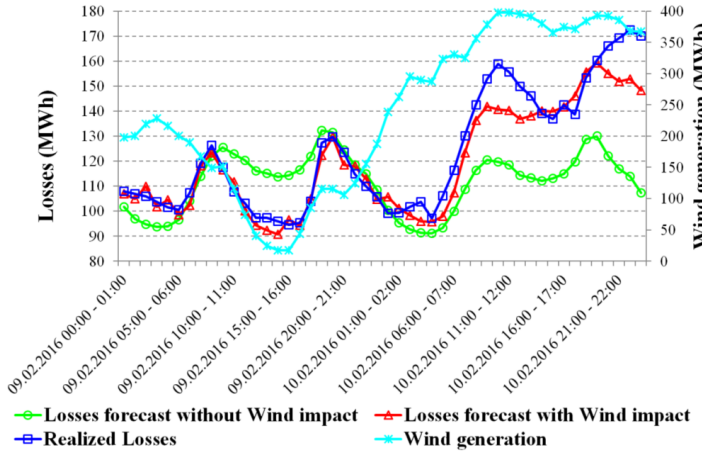

(a) Wind generation impact

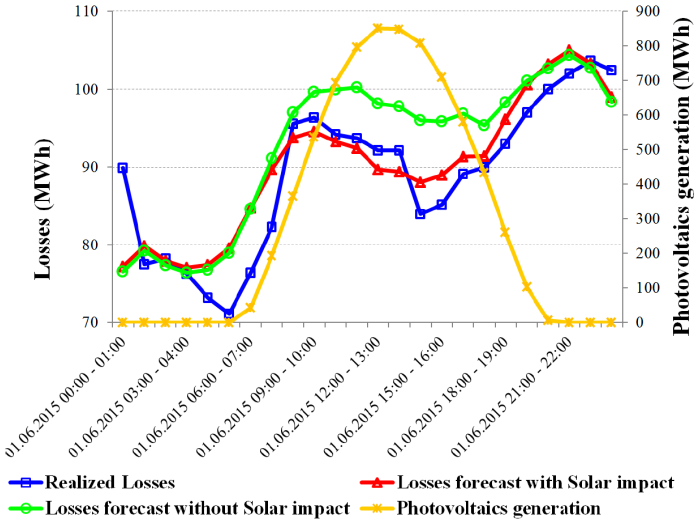

(b) PV generation impact

Figure 2.3: Forecasted transmission losses over a 24-hour period with and without wind and PV generation [32]

contribute to power system stability by providing ancillary services. These services are necessary to dynamically address the aforementioned issues and to maintain power system quality and safety. Ancillary services are generally categorised into several groups, including frequency control, voltage control, and emergency control services [18].

Wind and solar energy sources have become increasingly attractive par-

ticipants in electricity markets. In [35], the authors examined the potential for wind power integration in Denmark, focusing on its ability to provide a full range of relevant frequency and voltage control services. In the US, the provision of ancillary services by wind generation resources was investigated in [36], where the potential for inertia emulation and primary frequency support, along with the influence of different control architectures, is summarised. The economic viability of wind technology as a participant in the Spanish secondary regulation market is analysed in [37]. In [38], a wind power trading model incorporating a regulation strategy was proposed for the California day-ahead electricity market. The authors in [39] explored the grid code requirements and wind turbine control methods necessary for frequency control participation in Ireland and the UK. In addition to wind-based ancillary services, control strategies for PV generators to adjust their active power output for frequency regulation have been proposed in [40] and [41]. Moreover, a state-space dynamic model for PV systems capable of providing full ancillary services support is developed in [42]. The authors in [43] suggested a reactive power regulation method, using three-phase control strategies, to enable PV inverters to deliver ancillary service.

The long-term impact of RESs is on power system adequacy. In general, the reliability of a power system can be evaluated using three terms: reliability, security, and adequacy [44]. Reliability refers to all measures that ensure the delivery of the required amount of electrical energy to all points of utilisation within the power system. Security is the ability of the system to withstand unforeseen events, such as the loss of network elements or faults like short circuits in parts of the grid. Adequacy is defined as the ability of the power system to supply electrical energy to consumers and meet load demand within specified voltage and frequency limits, while taking operating constraints into account.

Capacity credit is an index used to quantify the amount of load that can be supplied by a generation unit in the power system without increasing the loss of load probability (LOLP), a widely recognised reliability metric. LOLP represents the probability of a loss of load event (LOLE) occurring within the power system. The capacity credit of a generating unit indicates its contribution to system adequacy and its ability to enhance overall reliability [45]. Capacity credit is typically expressed as a percentage of the installed capacity of the generation unit. It is evident that a reduction in capacity credit results in a greater amount of additional capacity being required to maintain system adequacy [28]. According to [46], based on several studies, at low penetration levels below 5%, the capacity credit of wind energy is approximately equal to the average wind power output. At higher penetration levels, such as above 40% of total generation, the capacity credit tends towards a fixed percentage. This percentage is determined by the LOLP in the absence of wind energy and

the probability of wind producing zero output. Furthermore, in a power system dominated by a few large power plants, the capacity credit of wind energy tends to be higher than in a system composed of many smaller generation units. Distributing a wind farm over a larger geographical area can also increase the capacity credit by approximately 20% compared to that of a single-site installation. Similarly, a strong correlation between wind power output and electricity demand – although not always present – can also raise the capacity credit by around 20%. The authors in [47] investigated the capacity credit of PV and wind energy in the Moroccan power system at penetration levels of 16%, 20%, and 27%. In all three cases, the mix consisted of 21.8% PV and 78.2% wind. The corresponding capacity credits were calculated as 30.0%, 26.6%, and 23.7%, respectively. The study concluded that as the penetration level increases, the capacity credit decreases and eventually reaches a saturation point.

2.3 Wind Energy

In this section, the most notable milestones in the field of wind energy are reviewed, and various approaches to wind harvesting are compared both qualitatively and quantitatively. Subsequently, wind speed variations and their impact on power output fluctuations are examined.

2.3.1 History and Improvements

The exploitation of wind energy began with the use of windmills. While some sources suggest that the earliest use of wind energy involved a wind-powered device in Egypt, dating to either the 1st century A.D. or B.C. [48], other scholars question its functionality, structure, and even existence [49, 50]. The next recorded use of windmills dates to the 9th century A.D., in the Persian region of Seistan (now part of Iran) [51], followed by the appearance of windmills in England during the 12th century [52]. However, due to limitations such as their non-transportable and non-dispatchable nature, windmills were eventually replaced by coal-powered technologies during the Industrial Revolution. In the late 19th century, with the development of electrical generators, windmills were once again employed to drive these generators. In the subsequent years, the authors in [53] proposed the use of three-blade wind turbines – similar to modern designs – instead of two-blade variants, as they were superior to two-blade ones in that they could result in far less vibration. The next breakthrough occurred at the end of the 20th century, driven by remarkable advancements in supporting technologies such as aerodynamics, materials science, power electronics, control engineering, and computer science, among others [54].

In general, wind energy harvesting can be categorised into onshore and offshore wind energy, with the former deployed on land and the latter in bodies of water, such as oceans. The first commercial wind turbine was onshore, constructed in the late 1800s. Nearly a century later, the first offshore wind farm, consisting of 11 turbines, was established in Denmark in 1991 [55, 56]. Although onshore wind turbines have reached maturity due to their earlier development and currently account for the majority of existing wind farms, offshore wind harvesting has also gained increasing attention in recent years due to its advantageous features. Wind speeds at sea are not only higher but also more predictable and consistent, which reduces turbine fatigue and contributes to longer infrastructure lifetimes. Additionally, offshore turbines do not occupy land, resulting in lower noise emissions and minimal visual impact on the landscape. On the other hand, due to their remote location, the technological costs associated with offshore turbines are higher than those of onshore turbines. Furthermore, offshore turbines require more extensive maintenance, which is typically more difficult and time-consuming than for their onshore counterparts [56, 57].

The cumulative onshore and offshore wind energy installations in Europe and globally over the past ten years are illustrated in Fig. 2.4(a) and Fig. 2.4(b), respectively [58]. By the end of 2024, the leading countries in the onshore market were China with 482.6 GW, the US with 152.9 GW, Germany with 63.6 GW, India with 48.1 GW, and Spain with 31.8 GW. In contrast, with regard to cumulative offshore installations by the end of the same year, China led with 39.0 GW, followed by the UK with 14.7 GW, Germany with 9.21 GW, the Netherlands with 4.7 GW, and Chinese Taipei with 2.9 GW [59].

Another noteworthy point is the response of the wind energy sector during the unprecedented circumstances of the COVID-19 pandemic, as examined in [61] and [62]. While the fossil fuel industry experienced significant market fluctuations, the wind energy sector demonstrated comparatively stable performance. Prior to the pandemic, projections for 2020 anticipated the installation of 75.5 GW of new wind power capacity. Although a reduction of approximately 20% was initially expected due to the crisis, revised forecasts – taking into account installations completed during the first half of 2020 – predicted only a 6% decline. This demonstrates the strong resilience of the wind energy industry.

2.3.2 Wind Speed Variations

Wind speed exhibits variability across both space and time. Spatially variations are classified into three groups in [25]: global, regional, and local. Globally, variations in altitude and solar insolation result in the formation of diverse climate zones across the planet. At the regional scale, geographical features

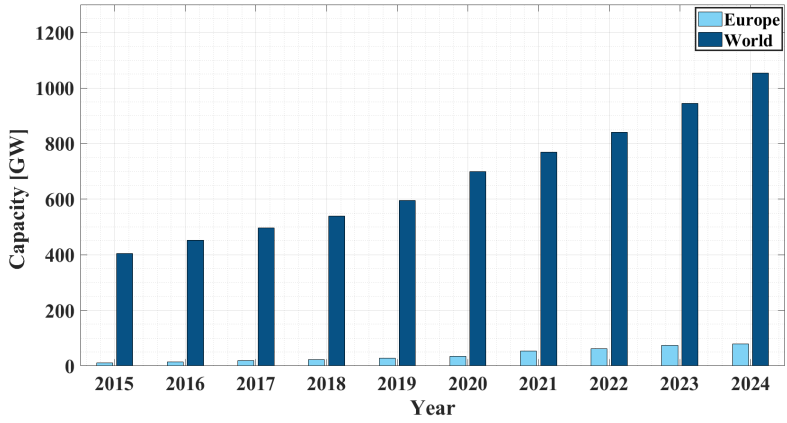

(a) Onshore capacity

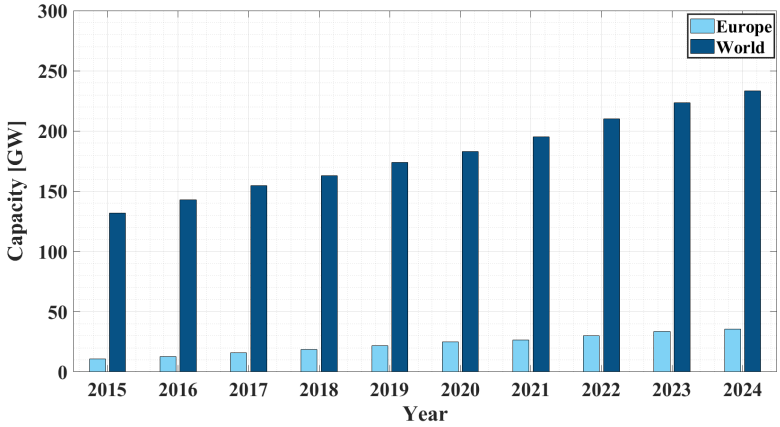

(b) Offshore capacity

Figure 2.4: Cumulative installed wind power capacity in Europe and globally over the past ten years [60]

such as plains, mountains, or a combination of both influence wind patterns. Additionally, the size of a landmass and its proximity to the sea are key regional factors affecting wind flow. On the local scale, the type of vegetation and the shape and features of the land surface, collectively referred to as topography, play a major role in wind speed variability. However, numerous studies, including [63] and further supported by [25, 64], have shown that the standard deviation of mean wind power output over successive 20-year periods is typically 10% or less. This suggests that the spatial variability of wind as a resource has relatively low long-term uncertainty.

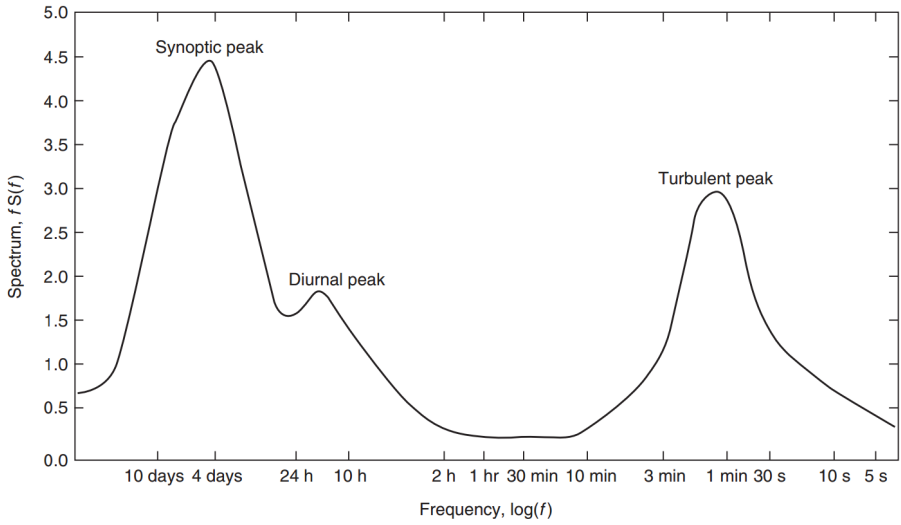

Figure 2.5: Peaks of turbulence, diurnal, and synoptic temporal variations recorded at Brookhaven National Laboratory, US [67], modified in [68]

From a temporal perspective, it is necessary to divide time into intervals to apply appropriate methods for wind speed prediction. In other words, while some techniques are suited to long-term forecasting, others are only applicable to short-term predictions. As a result, depending on the chosen forecasting approach, time intervals are defined, ranging from seconds to years [25,65,66]. Since wind speed varies across all time scales (seconds, minutes, hours, days, months, and years), the duration of time intervals is selected accordingly and can generally be categorised into four main groups: very short-term (a few seconds to a few minutes), short-term (a few minutes to a few hours), medium-term (a few hours to one month ahead), and long-term (more than one month ahead). According to [25] and [64], temporal wind variations can be further classified into:

- Turbulence, representing fluctuations on the order of seconds to minutes;
- Diurnal variations, linked to the time of day;
- Synoptic variations, associated with the passage of weather systems;
- Seasonal and annual patterns, reflecting longer-term climatic changes.

In Fig. 2.5, peaks corresponding to turbulence, diurnal, and synoptic variations in a wind spectrum recorded in the US are shown [67,68].

Unlike turbulence, which is inherently unpredictable, diurnal and seasonal wind variations can be forecasted with a reasonable degree of accuracy. Annual fluctuations, although generally less predictable than seasonal changes, tend to exhibit relatively minor variability. Synoptic variations are also predictable, though typically only a few days in advance. Furthermore, each type of wind variation impacts the power system differently. While these impacts fall outside the scope of this research, they are thoroughly analysed in [25].

It is important to note that temporal fluctuations in wind power can be mitigated through the aggregation of outputs from multiple wind turbines. This aggregation contributes positively to both power system operation and overall power quality.

According to [25], the aggregation of wind power production mitigates temporal variability through two primary mechanisms: increasing the number of turbines within a wind farm and geographically dispersing wind farms over a wider area. Firstly, a greater number of wind turbines in a single wind farm helps smooth out the effects of turbulence, as wind gusts do not strike all turbines simultaneously. This results in a reduction of the turbulence peak observed in Fig. 2.5 [67, 68]. As reported in [64], the variability in output power decreases proportionally to $n_t^{-0.5}$, where n_t is the number of turbines. The study concluded that a relatively modest number of turbines is sufficient to achieve significant smoothing. Secondly, the spatial distribution of wind farms over a broader geographical area lessens the influence of diurnal and synoptic variations, since weather systems do not affect all locations simultaneously. Expanding the geographical spread of wind turbines increases the area over which weather patterns must travel, thereby reducing simultaneous fluctuations across turbines [25]. Consequently, aggregated output from dispersed wind farms exhibits significantly lower ramp rates compared to a single large wind farm [25]. The extent of this smoothing effect is highly dependent on local meteorological conditions and the total area covered by the aggregated wind farms [25]. For instance, based on 10-minute and 1-hour interval data, the authors in [69] estimated that aggregating the outputs of 17 geographically dispersed wind farms can reduce variability by approximately 60–70% compared to a single wind farm.

In Table 2.1, the characteristics and predictability of various types of temporal wind variations are summarised [64].

2.4 Solar Energy

This section provides a detailed overview of solar energy, beginning with key historical breakthroughs, followed by an assessment of its applications in electricity generation. Finally, it discusses the variability associated with solar

Table 2.1: Summary of temporal wind variations and their predictability [64]

Classification	Predictability	Aggregation effect
Annual	Not predictable but small	NA
Seasonal	Predictable	Limited
Synoptic	Predictable few days ahead	Through wider geographical dispersion
Diurnal	Predictable	NA
Turbulences	Not predictable	Ideally $n_t^{-0.5}$ rule

irradiance.

2.4.1 History and Improvements

The first practical utilisation of solar energy is believed to have occurred between 287–212 B.C. [70]. However, from the perspective of electricity generation, a major milestone was reached in 1839 when it was discovered that light could enhance electricity production between two metal electrodes immersed in an acidic solution. This phenomenon was later defined as the photovoltaic effect [71]. In 1873, selenium was identified as a photoconductor, which led to further advancements. Later, in 1876, it was observed that selenium generates electricity when exposed to sunlight [72]. Building upon this discovery, the first solar cell made from selenium was developed in 1883, although its efficiency was less than 1% [71]. A significant breakthrough occurred in 1954 when silicon replaced selenium, leading to the creation of the first silicon photovoltaic cell. This cell, with an efficiency of 6%, was capable of powering an electrical device for several hours [73].

Solar energy can be harnessed in various ways. In addition to several applications of solar energy, such as in building heating [74], water heating [75], ventilation [74, 76], and transportation, including solar-powered cars [77] and bicycles [78], which are beyond the scope of this study, solar electricity has attracted significant attention in the past years. It can be divided into two main categories of PV solar systems and concentrated solar power (CSP).

Being the primary technology for solar energy harvesting, PV systems generate electricity by directly converting sunlight into electrical energy. In these systems, semiconducting materials absorb solar irradiance, causing the release of electrons, which then flow through the semiconductor material to generate an electric current. The resulting direct current (DC) is subsequently converted into alternating current (AC) through inverters. A typical PV system comprises the following components [79]:

- PV arrays, which convert solar irradiance into electrical energy;
- An optional battery storage system, used to store energy when needed;

- DC/DC converters, employed to increase voltage levels if necessary, or to perform maximum power point tracking (MPPT), commonly using algorithms such as Perturb and Observe, also known as the Hill Climber method; and
- DC/AC inverters, which convert the generated DC electricity into AC electricity for consumption by AC loads.

Generally, PV cells are categorised into various generations according to the materials and manufacturing techniques employed. The first generation, based on crystalline silicon, dominated the market for many years. The second generation consists of thin-film cells, utilising materials such as amorphous silicon, cadmium telluride, and copper indium gallium selenide (CIGS). Third-generation cells, which are still under development, incorporate materials such as organic semiconductors, dye-sensitised solar cells (DSSC), and perovskite solar cells. Research into fourth-generation cells aims to enhance the efficiency and durability of previous generations through advanced technologies, including tandem solar cells, hot-carrier solar cells, and quantum dot solar cells [80].

In CSP plants, mirrors are used to concentrate solar irradiance onto a central point or along a line, where a heat-transfer fluid absorbs the energy to produce steam and generate electricity through a conventional thermodynamic cycle [81]. Depending on the type of apparatus used for concentrating sunlight, CSP technologies are typically classified into four main types: parabolic trough (PT), solar tower (ST), Fresnel reflector (FR), and solar dish (SD).

PT, the most mature CSP technology, employs parabolic mirrors with a curved cross-section extended linearly in the third dimension. These mirrors focus solar irradiance onto heat-collecting receivers mounted along the focal line. Both the mirrors and receivers track the movement of the sun from east (sunrise) to west (sunset) [81, 82]. In ST systems, numerous computer-controlled mirrors, called heliostats, focus sunlight onto a single receiver located at the top of a central tower. Each heliostat is capable of dual-axis tracking to follow the position of the sun individually [81]. Although FR systems are similar to their PT counterparts, they use flat or slightly curved mirrors instead of parabolic ones. These mirrors reflect solar irradiance onto a fixed linear receiver and are arranged at various angles. FR systems may use single-axis or dual-axis tracking to follow the sun [81, 83]. Resembling a satellite dish in shape, the SD system consists of a parabolic reflector that focuses sunlight onto a receiver located at the focal point. Both the dish and receiver track the sun simultaneously [81, 83]. A schematic of the four CSP plant types, i.e., PT, ST, FR, and SD, is depicted in Fig. 2.6 [84, 85].

Initially, PT was the most widely adopted CSP technology, accounting for over 90% of the total installed CSP capacity. However, since 2010, ST systems

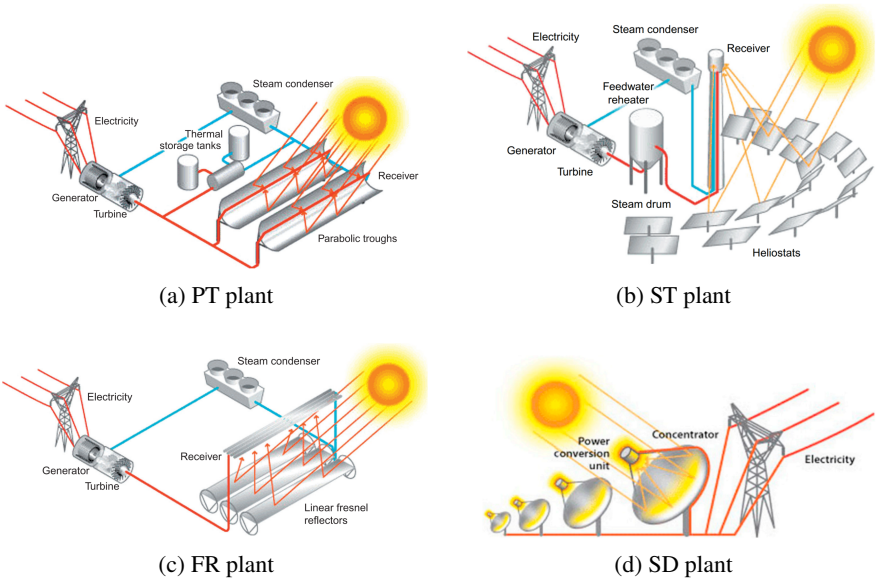

(a) PT plant (b) ST plant

(c) FR plant (d) SD plant

Figure 2.6: Schematic diagram of CSP technologies [84, 85]

have gained preference due to their ability to achieve higher operating temperatures, which results in greater efficiency and improved cost-effectiveness compared to SD systems [86]. Unlike PT and FR plants, which focus sunlight along a linear focal line and typically reach operating temperatures between 300-550 °C, both ST and SD systems concentrate sunlight onto a single focal point, enabling them to attain significantly higher temperatures in the range of 800-1000 °C. FR is the most recent CSP technology. The capacity factor of CSP plants can be enhanced by incorporating thermal energy storage systems. Notably, higher operating temperatures generally require more expensive storage solutions. Despite its relative simplicity, and although the manufacturing and installation costs of FR plants are lower than those of PT systems, it remains unclear whether FR-generated electricity is more cost-effective. SD systems are superior to other CSP technologies since they do not require cooling systems for waste heat dissipation, making them particularly suitable for deployment in water-scarce regions. Finally, high-temperature ST systems are considered to hold the greatest potential among CSP technologies in terms of capacity factor, thermal efficiency, storage integration, and overall cost. If complemented by further technological advances and commercial deployment, ST systems could deliver electricity at lower costs [81]. A summary of the main characteristics of different CSP technologies is presented in Table 2.2 [81, 83].

When comparing PV solar systems and CSP technologies, the most striking difference lies in their deployment scale. According to [58], by the end of 2024,

Table 2.2: Comparison of leading CSP technologies [81, 83]

Technology	Relative cost	Land occupancy	Thermo-dynamic efficiency	Operating temperature range (°C)	Solar concentration ratio	Require cooling system
PT	Low	Large	Low	20-400	15-45	Yes
ST	High	Medium	High	300-565	150-1500	Yes
FR	Very low	Medium	Low	50-300	10-40	Yes
SD	Very high	Small	High	120-1500	100-1000	No

the cumulative installed capacity of solar PV had reached 1858.62 GW, whereas CSP remained in its early stages with only 6.86 GW deployed globally. Several facts can justify this. First, it is important to consider how solar irradiance is modified as it passes through the atmosphere. Aside from the portion absorbed by suspended particles, solar irradiance reaching the Earth's surface is categorised into three components:

- Direct component or direct normal irradiance (DNI), which travels through the atmosphere without scattering;
- Indirect or diffuse horizontal irradiance (DHI), which results from scattering by atmospheric particles and the Earth's surface; and
- Reflected irradiance, which is typically negligible.

These components are illustrated in Fig. 2.7 [87]. The total amount of solar irradiance received on a horizontal surface, known as Global Horizontal Irradiance (GHI), is the sum of these three components..

Unlike solar PV systems, which can utilise all three components of sunlight, CSP systems rely exclusively on the direct component. Although DNI can account for up to 90% of total irradiance on clear, sunny days, it becomes negligible under cloudy conditions. Consequently, CSP plants are only cost-effective in regions with high DNI values, typically exceeding 2000 kWh/m^2/year, such as those found in Sun Belt regions. However, high DNI levels can also be achieved at high altitudes, where atmospheric scattering is minimal. In optimal areas with DNI levels greater than 2800 kWh/m^2/year, CSP systems can deliver a generation potential of 100-130 GWhe/km^2/year which is approximately equivalent to the annual output of a 20 MW coal-fired power plant operating at a 75% capacity factor [81].

A notable advantage of CSP technology is its compatibility with thermal energy storage. Since CSP converts solar energy into heat, excess thermal energy can be stored and later used to generate electricity during cloudy periods or at night. This feature allows CSP to mitigate the intermittency commonly associated with variable renewable energy sources such as solar PV and wind. In contrast, because solar PV systems convert sunlight directly into electricity,

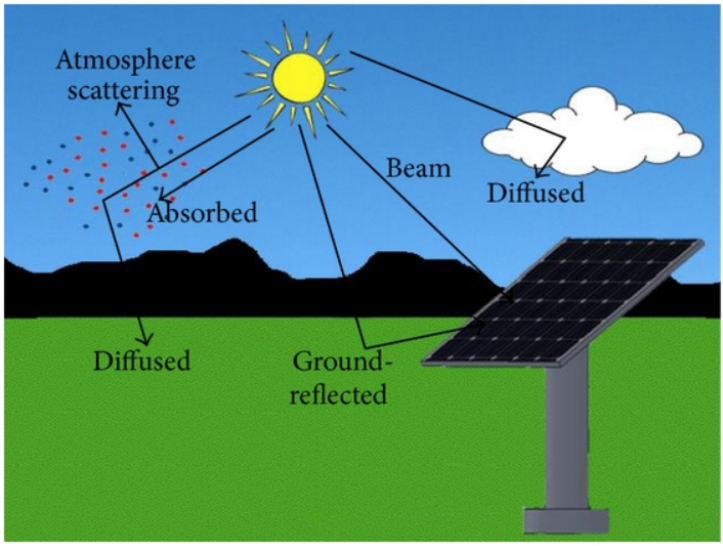

Figure 2.7: Interaction of incoming solar irradiance with atmospheric components [87]

they cannot benefit from thermal storage, and large-scale electricity storage remains a significant technical and economic challenge.

The cumulative installed capacities of solar PV and CSP technologies worldwide and in Europe over the past ten years are presented in Fig. 2.8(a) and Fig. 2.8(b), consecutively [58].

Globally, by the end of 2024, China led in cumulative installed solar PV capacity with 887.3 GW, followed by the US with 175.9 GW, India with 97.0 GW, Japan with 91.6 GW, and Germany with 89.9 GW. Regarding cumulative solar thermal installations, the leading countries were Spain with 2.3 GW, the US with 1.5 GW, the UAE with 600.0 MW, China with 570.0 MW, and Morocco with 540.0 MW [59].

From a resiliency perspective during the COVID-19 pandemic, global solar energy was initially projected to see 107 GW of additional installations in 2020. However, according to [88], new installations amounted to 19.0 GW in the first quarter and 21.1 GW in the second quarter of 2020, representing a decrease of approximately 25% and 9%, respectively, compared to the same periods in 2019. Yet, it is important to note that the more severe lockdown measures implemented in the early months of 2020 were gradually eased in the latter half of the year. As a result, a substantial decline in annual installations was not observed, thereby demonstrating the strong resilience of the solar energy sector in the face of global disruptions.

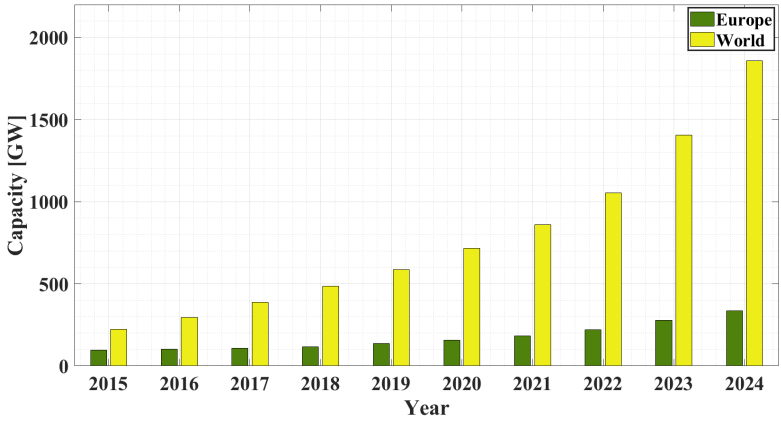

(a) PV capacity

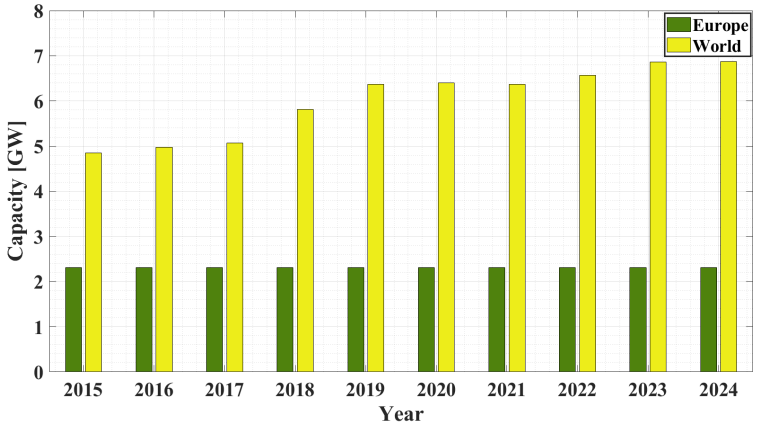

(b) CSP capacity

Figure 2.8: Global cumulative installed solar power capacity over the past ten years in Europe and worldwide [58]

2.4.2 Solar Irradiance Variations

Similar to wind speed, solar irradiance exhibits both spatial and temporal variability. However, the variability of solar irradiance reaching the Earth's surface is primarily analysed by examining its constituent components, i.e., DNI, DHI, and reflected irradiance, the latter of which is generally negligible.

From a spatial perspective, solar irradiance varies with distance, and changes in the position of the sun influence the output of solar energy systems. In [89], the authors analysed one-year daily and monthly averages of

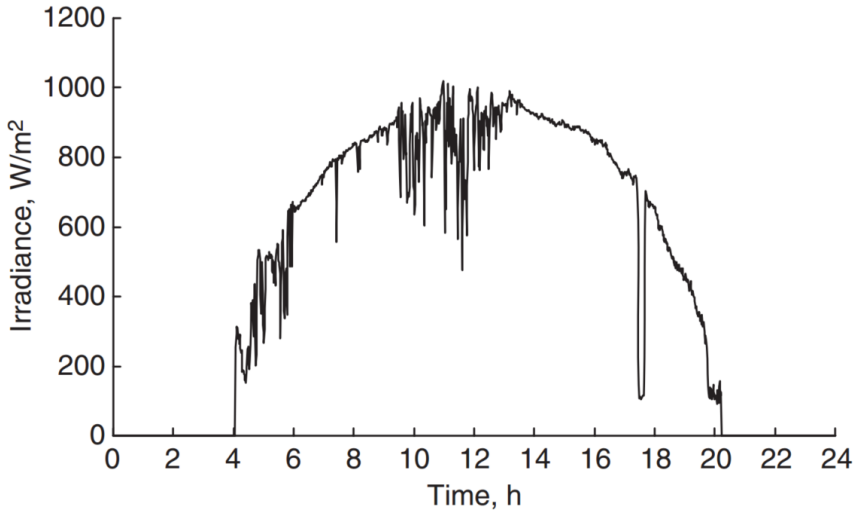

Figure 2.9: Impact of a moving cloud on the irradiance time series [1]

GHI using satellite imagery for three sites in Germany. A reference site was compared with two others located approximately 55 km and 633 km away. While the GHI values at the closer site were not identical to those at the reference, they exhibited strong correlation. Regardless, at the more distant site, significant discrepancies in GHI patterns were observed, and the differences became more pronounced with increasing distance. Furthermore, substantial daily fluctuations around the monthly average were noted at all three locations.

Importantly, PV output variability caused by the position of the sun is relatively uniform and predictable. In contrast, fluctuations in PV output due to cloud movement are irregular and can vary considerably. On consistently clear or overcast days, variations in PV output are typically minimal. Nevertheless, under partly cloudy conditions, where GHI exhibits rapid and irregular changes, the impact on PV power generation becomes significant [90]. In [1], this effect is illustrated, as shown in Fig. 2.9, where a marked drop in irradiance is visible before 18:00 on a summer day in the UK, due to a passing cloud. Such cloud events can cause PV output to decrease by more than 60% within seconds, driven by a sudden reduction in solar insolation. The time required for a cloud to shade an entire PV installation depends on several factors, including the size of the PV system, cloud speed, cloud height, and other atmospheric conditions. For example, in the case of a 100 MW PV system, a passing cloud may take several minutes to fully cover the array [90].

In addition to cloud cover, several other atmospheric conditions also influ-

ence solar irradiance and, consequently, solar power generation. These include dust storms, the concentration of water vapour or ice particles, the types of water droplets or ice crystals, and both the type and concentration of aerosols present in the atmosphere [91].

When comparing PV and CSP technologies, it is important to highlight that CSP plants exhibit lower output variability due to the presence of a thermal mass, such as oil or water. This thermal mass effectively buffers short-term fluctuations in solar irradiance, smoothing the output of the plant. Acting similarly to a storage medium, it enables CSP systems to better withstand transient atmospheric conditions even in the absence of a large-scale energy storage system (ESS).

As with wind farms, solar power fluctuations can be mitigated through the aggregation of multiple solar plants. By geographically distributing installations, the impact of passing clouds is reduced: a single cloud may not affect all plants simultaneously, and some parts of the system may remain unaffected altogether. This spatial diversity helps smoothen the overall power output and enhances grid stability.

2.5 Accommodating or Mitigating Intermittency

Finding technological solutions to mitigate the adverse effects of intermittent RESs is a widely discussed topic in the literature. Intermittent RESs not only exhibit variable generation patterns on a daily basis, but also undergo rapid short-term fluctuations. As a result, balancing these variations over both long and short time scales is essential. Although several strategies exist to address intermittency, ESSs continue to attract significant interest. Thus, in this study, mitigation and accommodation solutions are categorised into two main groups: solutions not associated with ESSs and solutions associated with ESSs. The former can be further subdivided into supply-side management (SSM) and demand-side management (DSM).

By controlling the output of generation units, including RESs, it is possible to reduce the adverse impacts of intermittency on the power system. This approach is referred to as SSM. The first method mentioned for accommodating the variable output of wind and solar power, as described in Sections 2.3.2 and 2.4.2, involves the aggregation of wind farms or solar plants, which helps reduce their output variability to some extent. In Fig. 2.10(a) and Fig. 2.10(b), the impacts of aggregating wind turbines and solar PV plants are illustrated, respectively [92, 93].

For PV plants, assuming time-series data are collected while the systems operate at rated capacity, aggregating 5 and 23 sites reduces the maximum 1-minute change in output to 40% and 20%, respectively, significantly lower

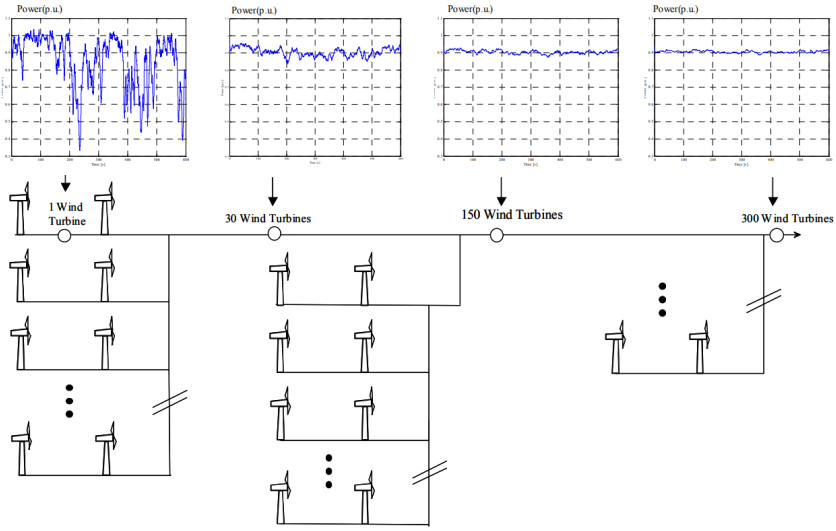

(a) Impact of wind turbine aggregation on output power [92]

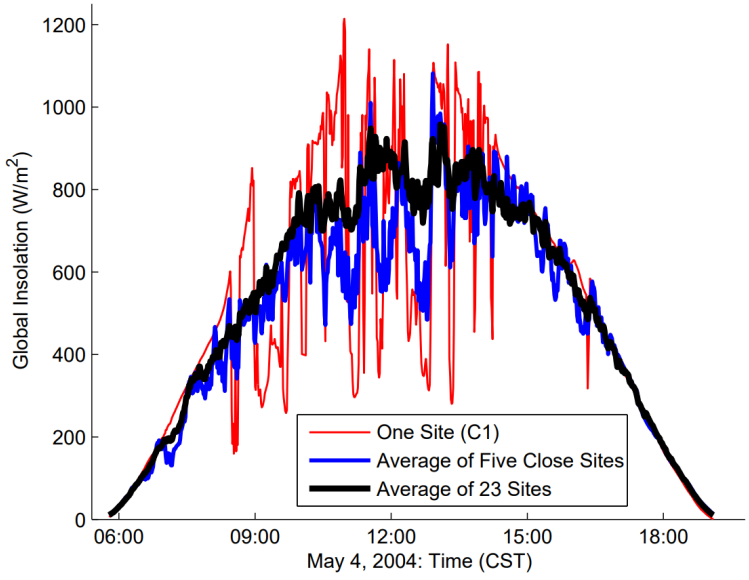

(b) Impact of aggregating 5 and 23 PV power plants on GHI variations during a partly cloudy day [93]

Figure 2.10: Effect of aggregating intermittent RESs plants

than the 80% fluctuation observed at a single site [93].

Furthermore, wind speed and solar irradiance forecasting methods, which are outside the scope of this thesis, can mitigate the effects of intermittency by providing system operators with an approximate insight into the near-future generation of wind and solar energy. Besides, the authors in [94] examined the seasonal and annual patterns of wind and solar output and found that these sources can complement each other during certain periods. For this reason, numerous studies have focused on combining these two intermittent sources, addressing issues such as system reliability and grid integration challenges [95], hybrid system cost assessment [95, 96], load-following capability [97], CO_2 emissions [98], and system sizing [97], among others.

The optimal allocation of generation technologies largely depends on the geographical region in which the hybrid system is implemented. In general, any generation unit or technological component that can offer a complementary generation pattern to wind or solar may be combined with them to reduce output variability. For example, coupling intermittent RESs with flexible generation sources such as gas turbines, integrating plug-in electric vehicles, provided that a moderate share of vehicle owners are incentivised to participate [99], or using diesel generators alongside more stable RESs can help smooth power fluctuations [100].

To address the added reserve requirements imposed by wind power, the authors in [101] proposed a multi-objective stochastic optimisation model to determine the optimal set-point for wind farms. The study aims to maximise the set-point while simultaneously increasing the probability of achieving it in real-time operation, thereby reducing the uncertainty of output power.

Power curtailment, i.e., intentionally reducing the output of RES plants, is another generation-side strategy for managing intermittency. Additionally, as elaborated in Section 2.2, RESs plants can contribute to power system stability by providing ancillary services. Lastly, dispatchable power plants with high availability and fast ramp rates can be used to compensate for RESs fluctuations. Among these, gas turbine generators are particularly well-suited due to their reliability and rapid response capabilities [102].

In terms of DSM, which is also referred to as demand-side response in the literature, flexibility can be provided to the grid to a certain extent, both at the residential and industrial levels. According to [103], DSM can be categorised into two main types: energy reduction programmes, which aim to decrease overall energy consumption by promoting more efficient processes or equipment, and load management programmes, which seek to reshape the load profile by encouraging consumers to reduce demand during peak periods, typically through incentive-based measures. The authors in [104] examined the potential contribution of industry to grid flexibility by co-optimising the operation of a chlor-alkali electrolysis process. Their findings showed that the

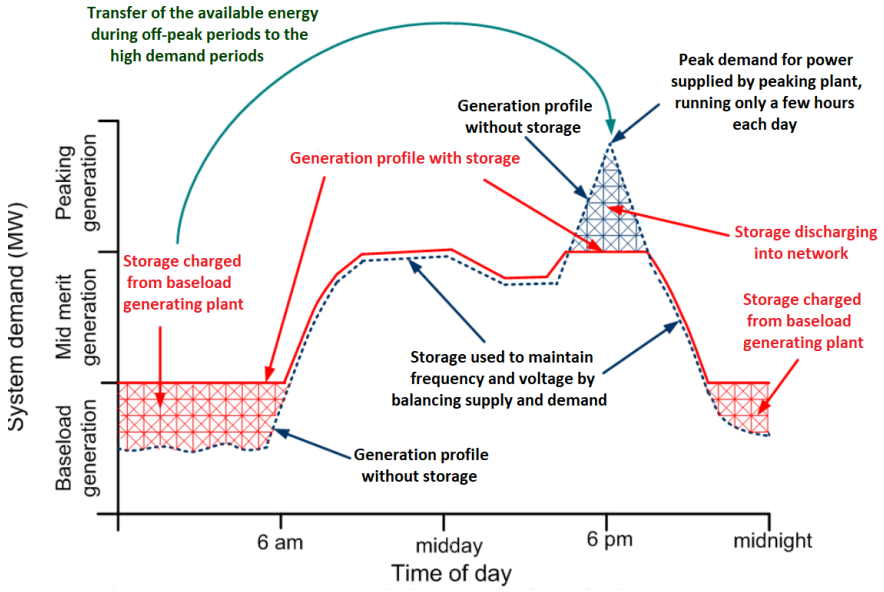

Figure 2.11: Function of ESSs for power smoothing [105]

flexible operation of the electrolyser can have a positive impact on the power system, offering valuable support for balancing electricity demand and supply.

ESSs can ease the large-scale integration of intermittent RESs. As previously discussed, synchronising electricity demand with production is inherently challenging, particularly in the presence of RESs. At certain times, RESs output may be insufficient during peak demand periods, while at other times, surplus energy may be generated when demand is low. By storing excess energy produced during low-demand periods and releasing it during peak hours, ESSs offer an effective solution for mitigating the intermittency of RESs, as illustrated in Fig. 2.11 [105]. In addition to this balancing function, ESSs can also provide ancillary services to the power grid, such as frequency regulation and voltage support, making them a versatile and valuable technology when combined with RESs [106, 107].

Generally, ESSs can be classified into five main categories based on the form of energy in which electricity is stored: mechanical, electrochemical, chemical, electromagnetic, and thermal. Each category can be further subdivided depending on the materials used, the manufacturing process, and the form of stored energy, as shown in Fig. 2.12 [108].

There are three commonly used technologies in the category of mechanical ESSs: flywheel, pumped hydroelectric storage (PHES), and compressed air energy storage (CAES). As the name implies, these systems store and release electricity using mechanical energy. The flywheel system stores energy in

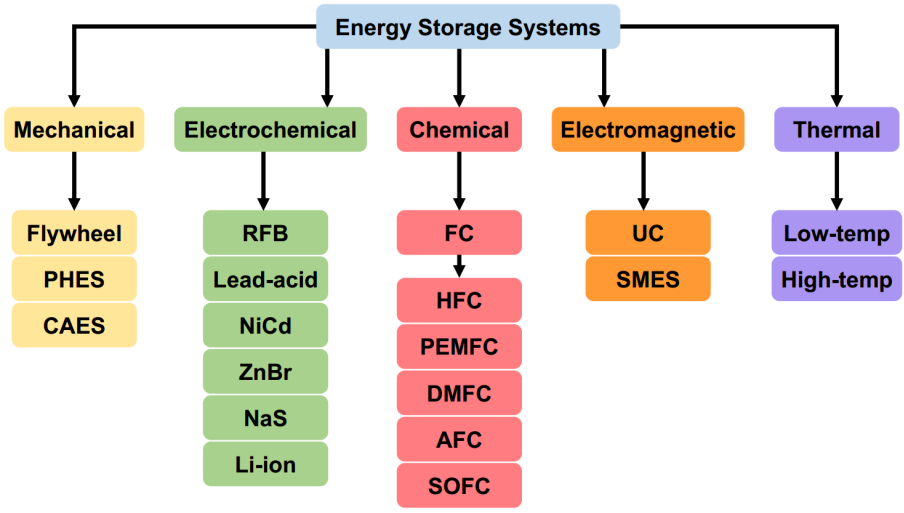

Figure 2.12: Classification of different types of ESSs [108]

kinetic form through a high-speed rotating rotor, typically operating at 20000 to 50000 rpm. PHES, the most mature and widely deployed ESS technology, stores energy in the form of gravitational potential energy by moving water between two reservoirs located at different elevations. Finally, CAES stores energy by using off-peak electricity or surplus renewable energy to compress air, which is then stored in underground or above-ground structures and later expanded to generate electricity when needed.

Electrochemical energy storage systems operate based on reversible chemical reactions, storing energy in the form of chemical energy. One such technology is the redox flow battery (RFB), also known as a flow battery, which is an electrochemical cell that generates energy through two chemical components dissolved in liquids and stored in external tanks. Among electrochemical storage technologies, battery energy storage systems (BESSs) are among the most widely adopted. BESSs consist of numerous individual battery cells connected in series, parallel, or a combination of both. A typical battery cell includes a negative electrode (anode), a positive electrode (cathode), and an electrolyte serving as the ionic conductor. Depending on the materials used for these components, various types of BESSs have been developed. The most common types of BESSs include the lead-acid battery, nickel-cadmium (NiCd) battery, zinc-bromide (ZnBr) battery, sodium-sulphur (NaS) battery, and lithium-ion (Li-ion) battery. Among these, the Li-ion battery is currently the most prominent. Based on the materials used for the electrodes, Li-ion batteries can be further categorised. Common cathode materials include nickel manganese cobalt (NMC), nickel cobalt aluminium oxide (NCA), and lithium

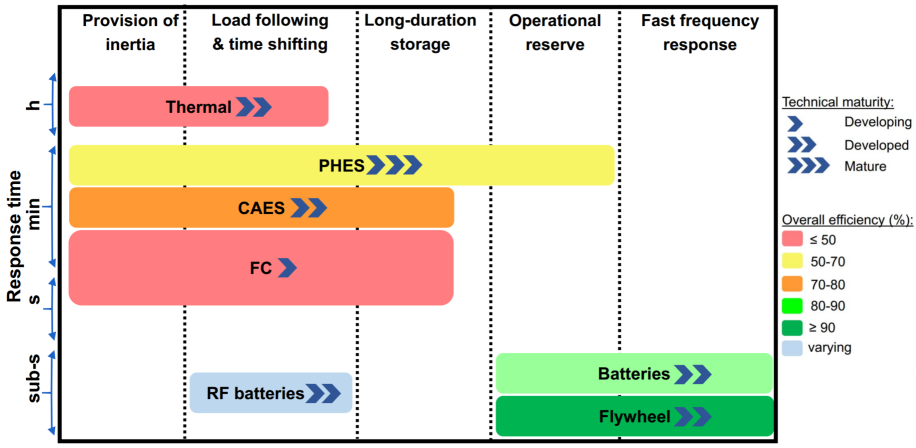

Figure 2.13: Comparison of various ESSs [20, 108, 113–115]

iron phosphate (LFP), while graphite and carbon black are widely used for the anode [109].

Chemical energy storage systems (CESSs) store and release energy through chemical reactions. The most well-known technology in this category is the fuel cell (FC), which generates electricity from the chemical energy of a fuel. A wide range of fuels has been studied in the literature and proposed for use in fuel cells [110]. Due to its high energy density and other favourable properties, the hydrogen fuel cell (HFC) has received significant attention in recent years [111, 112]. Among the existing fuel cell types, proton exchange membrane fuel cell (PEMFC), direct methanol fuel cell (DMFC), alkaline fuel cell (AFC), and solid oxide fuel cell (SOFC) are the most well-known [108]. Although the power-to-hydrogen-to-power cycle has a relatively low round-trip efficiency, hydrogen production itself has the potential to address the intermittency of renewable energy sources. Hydrogen can be generated from RESs through electrolysers, devices that require only water and electricity to split water molecules into hydrogen and oxygen. Electrolysers can address the intermittency of RESs by generating hydrogen when electricity supply surpasses demand and decreasing their consumption when supply falls below demand. Since this thesis focuses on hydrogen production from RESs, hydrogen production and the associated technologies are examined in detail in the subsequent chapters.

Unlike other types of ESSs, electrical energy storage systems (EESSs) do not involve any form of energy conversion. Instead, they store energy directly in an electromagnetic field, typically using ultra-capacitors (UCs) or superconducting magnetic energy storage (SMES) systems, which rely on superconducting electromagnets.

The final category, thermal energy storage systems (TESSs), stores energy

Table 2.3: Strengths and challenges facing Belgium on the path to decarbonisation [116]

Strengths	Challenges
- In line with its strategy, Belgium has established and maintained a robust and interconnected electricity and gas infrastructure as well as a leading position in market design and integration	- Stemming from small area of Belgium, only a limited part of the country's demand could be provided by domestic renewable generation, making Belgium unable to rely upon domestic capacity on the way of decarbonisation
- Surrounded by large countries such as Germany, France and the UK with different strategies in terms of energy, giving Belgium the freedom to opt for their best choices	- In the current market design, with the presence of higher amounts of renewables in the system, the profitability of conventional units are of concerns
- Situated at the centre of Europe, crossroads of important renewable generation hubs and close to the main load centres	- Meeting load demand becomes growingly burdensome as in less than a decade from now nuclear plants are supposed to phase-out in Belgium

in the form of heat. Depending on the operating temperature, TESSs can be classified as either low-temperature or high-temperature systems. High-temperature TESSs are further divided into three sub-categories: sensible heat, latent heat, and thermo-chemical (sorption) energy storage [108].

Among the various types of energy storage systems, BESSs and Flywheels exhibit the highest efficiencies, ranging between 95–98% and 90–95%, respectively. In contrast, HFCs have the lowest efficiency, typically ranging from 20–50%. When it comes to lifetime (measured in cycles), flywheels outperform other technologies, offering approximately 100k-1M cycles. On the other hand, RFB and lead-acid batteries have comparatively shorter lifespans, with cycle ranges of approximately 0.3-1.4k and 0.25-2.5k, respectively. Concerning response time, most of the ESSs technologies discussed provide a rapid response in the order of milliseconds. However, PHESs and CAESs exhibit slower response times in the order of minutes, while TESSs typically respond in the order of hours [108]. In Fig. 2.13, the characteristics of the most common ESSs are summarised.

2.6 Discussion and Conclusions

To address fossil fuel depletion, mitigate air pollution, and comply with commitments under the Paris Agreement, many countries are committed to transitioning to alternative forms of energy. RESs have emerged as leading candidates to replace fossil fuels due to their abundance and environmental benefits. Nevertheless, while the adoption of RESs offers numerous advantages, they also pose significant challenges for TSOs, particularly with regard to maintaining power system reliability and preserving frequency response. Therefore, the

integration of RESs must be conducted in a structured and carefully planned manner to effectively manage their associated impacts.

Among the various RESs, wind and solar energy are widely recognised. However, both are inherently volatile, resulting in erratic and difficult-to-predict power output. In the case of wind energy, electricity is generated using either onshore or offshore turbines. Onshore wind technology is more mature, having undergone nearly a century of earlier development compared to offshore systems. Nevertheless, offshore wind harvesting is increasingly gaining acceptance, particularly in countries with access to seas or oceans, owing to its advantageous characteristics. Notably, wind speeds over water bodies are typically higher and more stable than those on land, resulting in greater and more predictable power output. Consequently, offshore wind can partially reduce the intermittency associated with wind energy. Additionally, offshore turbines are subject to lower structural fatigue, thereby increasing the lifespan of the supporting infrastructure. From an environmental perspective, offshore turbines do not require land use, as they are installed in marine environments. However, this advantage comes at the cost of more complex technology requirements and higher maintenance expenses.

Concerning solar energy, PV and CSP are the two dominant technologies for generating electricity globally. However, as CSP is highly dependent on geographical location and is economically viable primarily in regions with DNIs>2000 kWh/m^2/year, to make it cost-justifiable, PV systems are more widely adopted worldwide. While PV systems convert solar irradiance directly into electricity, CSP plants concentrate solar energy onto a point or line to first generate thermal energy (heat and steam), which is subsequently converted into electricity. Depending on the optical configuration used to concentrate sunlight, CSP plants are further categorised into PT, ST, FR, and SD systems. Among these, PT plants are the most mature and widely deployed. Nonetheless, ST systems have gained increasing attention in recent years due to their favourable balance between cost and efficiency.

When comparing solar and wind energy, solar irradiance exhibits more predictable variability than wind speed. In other words, the diurnal cycle of solar irradiance provides a more foreseeable pattern for the output power of solar systems. Additionally, the higher correlation between solar power generation and electricity demand facilitates the integration of solar energy into the power grid. Table 2.4 summarises the most significant characteristics of wind and solar energy, including their respective sub-technologies.

Considering the Belgian power system, and in line with the planned decommissioning of nuclear plants, and commitments under the Paris Agreement, Elia, in collaboration with the relevant authorities, is working to establish a clear and feasible roadmap towards national decarbonisation targets. In Belgium, solar PV and wind energy constitute the dominant share among the various

renewable energy sources. Owing to its access to the North Sea, Belgium is also investing significantly in offshore wind farms, positioning itself as one of the leading countries in this domain.

In the following chapter, a review of hydrogen production methods, both fossil fuel-based and renewable energy-based, is conducted. Additionally, the chapter discusses how hydrogen production can contribute to addressing the intermittency of RESs.

Table 2.4: Comparison of solar, wind and their related technologies

RES type	Advantage	Disadvantage	Technology	Advantage
Wind	- A proven renewable source - Able to provide inertia for the grid - Could be available 24/7 - Occupies a small are	- Intermittent - Eyesore on the nature - Noise pollution	Onshore	- A proven technology - Easier and quicker to install - Shorter distance to load - Cheaper compared to onshore turbines
			Offshore	- Higher wind speed - More foreseeable and consistent wind - Less mechanical stress of turbine - Less importance of noise
Solar	- A proven renewable source - More predictable compared to wind - Higher correlation with the demand	- Decreases inertia of the grid - Not available after daylight - Intermittent	PV	- Collects all three components of the sunlight - A proven technology - Declining cost of equipment - Easier to manufacture - Low operating and maintenance cost - Locally available
			CSP	- Able to use thermal storage systems - Higher efficiency compared to PV - Low operating cost

Table 2.5: Comparison of solar, wind and their related technologies (cont.)

Disadvantage	Maturity	Recently developing	Cumulative installed capacity (2024) World / Belgium
- Noise pollution - Occupies land - Eyesore on the land	High	NA	1053.40 / 3.33 GW (Onshore)
- More maintenance costs - Harder to build - Eyesore on the sea - Negative impact on marine life	Medium	Yes	79.43 / 2.26 GW (Offshore)
- Needs additional equipment such as inverters - Low efficiency - Dependent on the location, such as for residential purposes or whether panels are covered by tall buildings - Requires large area for land-mounted plants	High	NA	1858.62 / 9.75 GW (PV)
- Only use DNI component of the sunlight - Strongly dependant on the geographical location - Hard and expensive to manufacture - Requires large area	PT: High ST: Medium FR: Low SD: Low	PT: NA ST: Yes FR: No SD: No	6.86 / - GW (CSP)

Bibliography

[1] D. Infield and L. Freris, *Renewable Energy in Power Systems*. John Wiley & Sons, 2020.

[2] Enerdata, "Crude oil production." https://yearbook.enerdata.net/crude-oil/world-production-statistics.html. Accessed: December 8, 2025.

[3] J. Timperley, "Is the decline of oil in sight?." https://www.bbc.com/future/article/20230726-an-experts-guide-to-peak-oil-and-what-it-really-means. Accessed: December 8, 2025.

[4] D. Sen, K. I. Hamurcuoglu, M. Z. Ersoy, K. M. Tunç, and M. E. Günay, "Forecasting long-term world annual natural gas production by machine learning," *Resources Policy*, vol. 80, p. 103224, 2023.

[5] C. J. Cleveland and C. G. Morris, *Handbook of energy: chronologies, top ten lists, and word clouds*. Elsevier, 2013.

[6] P. N. Pearson, G. L. Foster, and B. S. Wade, "Atmospheric carbon dioxide through the Eocene–Oligocene climate transition," *Nature*, vol. 461, no. 7267, pp. 1110–1113, 2009.

[7] T. Muneer, M. Kolhe, and A. Doyle, *Electric vehicles: prospects and challenges*. Elsevier, 2017.

[8] NASA, "Earth is warming at an unprecedented rate." https://science.nasa.gov/climate-change/evidence. Accessed: December 8, 2025.

[9] "The Paris Agreement." https://unfccc.int/process-and-meetings/the-paris-agreement/the-paris-agreement. Accessed: December 8, 2025.

[10] O. Hoegh-Guldberg, D. Jacob, M. Bindi, S. Brown, I. Camilloni, A. Diedhiou, R. Djalante, K. Ebi, F. Engelbrecht, J. Guiot, *et al.*, "Impacts of 1.5 °C global warming on natural and human systems," *Global warming of 1.5 °C. An IPCC Special Report*, 2018.

[11] C. L. Sabine, "Carbon dioxide in the ocean and atmosphere." https://www.waterencyclopedia.com/Bi-Ca/Carbon-Dioxide-in-the-Ocean-and-Atmosphere.html. Accessed: December 8, 2025.

[12] J. Desjardins, "Map: The countries with the most oil reserves." https://www.visualcapitalist.com/map-countries-most-oil-reserves/, 2019. Accessed: December 8, 2025.

[13] IRENA and ILO, "Renewable energy and jobs – annual review 2024." https://www.irena.org/Publications, International Renewable Energy Agency, Abu Dhabi, and International Labour Organization, Geneva, 2024.

[14] R. Ferroukhi, X. Casals, and B. Parajuli, "Measuring the socio-economics of transition: Focus on jobs." https://www.irena.org/Technical-Papers, 2020.

[15] P. Heptonstall, R. Gross, and F. Steiner, "The costs and impacts of intermittency – 2016 update: A systematic review of the evidence on the costs and impacts of intermittent electricity generation technologies." https://ukerc.ac.uk/publications, 2017.

[16] G. Notton, M.-L. Nivet, C. Voyant, C. Paoli, C. Darras, F. Motte, and A. Fouilloy, "Intermittent and stochastic character of renewable energy sources: Consequences, cost of intermittence and benefit of forecasting," *Renewable and Sustainable Energy Reviews*, vol. 87, pp. 96–105, 2018.

[17] D. Suchet, A. Jeantet, T. Elghozi, and Z. Jehl, "Defining and quantifying intermittency in the power sector," *Energies*, vol. 13, no. 13, p. 3366, 2020.

[18] A. Banshwar, N. K. Sharma, Y. R. Sood, and R. Shrivastava, "Renewable energy sources as a new participant in ancillary service markets," *Energy Strategy Reviews*, vol. 18, pp. 106–120, 2017.

[19] Y. Yang, S. Bremner, C. Menictas, and M. Kay, "Battery energy storage system size determination in renewable energy systems: A review," *Renewable and Sustainable Energy Reviews*, vol. 91, pp. 109–125, 2018.

[20] H. Zhao, Q. Wu, S. Hu, H. Xu, and C. N. Rasmussen, "Review of energy storage system for wind power integration support," *Applied Energy*, vol. 137, pp. 545–553, 2015.

[21] S. O. Hazboun and H. S. Boudet, "Public preferences in a shifting energy future: Comparing public views of eight energy sources in North America's pacific Northwest," *Energies*, vol. 13, no. 8, 2020.

[22] F. Ribeiro, P. Ferreira, M. Araújo, and A. C. Braga, "Public opinion on renewable energy technologies in Portugal," *Energy*, vol. 69, pp. 39–50, 2014.

[23] S. Ntanos, G. Kyriakopoulos, M. Chalikias, G. Arabatzis, and M. Skordoulis, "Public perceptions and willingness to pay for renewable energy: A case study from Greece," *Sustainability*, vol. 10, no. 3, 2018.

[24] A. Qazi, F. Hussain, N. A. Rahim, G. Hardaker, D. Alghazzawi, K. Shaban, and K. Haruna, "Towards sustainable energy: A systematic review of renewable energy sources, technologies, and public opinions," *IEEE Access*, vol. 7, pp. 63837–63851, 2019.

[25] T. Ackermann *et al.*, *Wind power in power systems*, vol. 140. Wiley Online Library, 2005.

[26] Y.-h. Wan and B. K. Parsons, "Factors relevant to utility integration of intermittent renewable technologies," tech. rep., National Renewable Energy Lab., Golden, CO (United States), 1993.

[27] T. Reddoch, P. Barnes, J. Lawler, and J. Skroski, "Strategies for minimizing operational impacts of large wind turbine arrays on automatic generation control systems," *ASME. J. Sol. Energy Eng.*, 1982.

[28] G. Ren, J. Liu, J. Wan, Y. Guo, and D. Yu, "Overview of wind power intermittency: Impacts, measurements, and mitigation solutions," *Applied Energy*, vol. 204, pp. 47–65, 2017.

[29] A. S. Brouwer, M. Van Den Broek, A. Seebregts, and A. Faaij, "Impacts of large-scale intermittent renewable energy sources on electricity systems, and how these can be modeled," *Renewable and Sustainable Energy Reviews*, vol. 33, pp. 443–466, 2014.

[30] H. Huang, M. Zhou, and G. Li, "An endogenous approach to quantifying the wind power reserve," *IEEE Transactions on Power Systems*, vol. 35, no. 3, pp. 2431–2442, 2019.

[31] F. Gutiérrez-Martín, R. Da Silva-Álvarez, and P. Montoro-Pintado, "Effects of wind intermittency on reduction of CO_2 emissions: The case of the Spanish power system," *Energy*, vol. 61, pp. 108–117, 2013.

[32] S. I. Sulakov, "Forced renewables penetration impact on ohmic transmission losses," in *2016 19th International Symposium on Electrical Apparatus and Technologies (SIELA)*, Bourgas, Bulgaria, 2016.

[33] S. Pfenninger and J. Keirstead, "Renewables, nuclear, or fossil fuels? Scenarios for Great Britain's power system considering costs, emissions and energy security," *Applied Energy*, vol. 152, pp. 83–93, 2015.

[34] L. Šćekić, S. Mujović, and V. Radulović, "Pumped hydroelectric energy storage as a facilitator of renewable energy in liberalized electricity market," *Energies*, vol. 13, no. 22, p. 6076, 2020.

[35] P. A. Østergaard, "Ancillary services and the integration of substantial quantities of wind power," *Applied Energy*, vol. 83, no. 5, pp. 451–463, 2006.

[36] V. Y. Singarao and V. S. Rao, "Frequency responsive services by wind generation resources in United States," *Renewable and Sustainable Energy Reviews*, vol. 55, pp. 1097–1108, 2016.

[37] E. Saiz-Marin, J. García-González, J. Barquin, and E. Lobato, "Economic assessment of the participation of wind generation in the secondary regulation market," *IEEE Transactions on Power systems*, vol. 27, no. 2, pp. 866–874, 2012.

[38] Z.-S. Zhang, Y.-Z. Sun, and L. Cheng, "Potential of trading wind power as regulation services in the California short-term electricity market," *Energy policy*, vol. 59, pp. 885–897, 2013.

[39] F. Díaz-González, M. Hau, A. Sumper, and O. Gomis-Bellmunt, "Participation of wind power plants in system frequency control: Review of grid code requirements and control methods," *Renewable and Sustainable Energy Reviews*, vol. 34, pp. 551–564, 2014.

[40] R. Rajan and F. M. Fernandez, "Power control strategy of photovoltaic plants for frequency regulation in a hybrid power system," *International Journal of Electrical Power & Energy Systems*, vol. 110, pp. 171–183, 2019.

[41] P. Zarina, S. Mishra, and P. Sekhar, "Exploring frequency control capability of a PV system in a hybrid PV-rotating machine-without storage system," *International Journal of Electrical Power & Energy Systems*, vol. 60, pp. 258–267, 2014.

[42] E. I. Batzelis, G. Anagnostou, I. R. Cole, T. R. Betts, and B. C. Pal, "A state-space dynamic model for photovoltaic systems with full ancillary services support," *IEEE Transactions on Sustainable Energy*, vol. 10, no. 3, pp. 1399–1409, 2018.

[43] L. S. Xavier, A. F. Cupertino, and H. A. Pereira, "Ancillary services provided by photovoltaic inverters: Single and three phase control strategies," *Computers & Electrical Engineering*, vol. 70, pp. 102–121, 2018.

[44] A. Mercados, "E-bridge REF-E identification of appropriate generation and system adequacy standards for the internal electricity market," *Final report prepared for the European Commission*, 2016.

[45] M. Amelin, "Comparison of capacity credit calculation methods for conventional power plants and wind power," *IEEE Transactions on Power Systems*, vol. 24, no. 2, pp. 685–691, 2009.

[46] M. Diesendorf *et al.*, "The economic value of wind power in electricity grids," *Proceedings of the International Colloquium on Wind Energy, BHRA Fluid Engineering, Cranfield, Bedford, England*, 1981.

[47] A. Bouramdane, A. Tantet, and P. Drobinski, "Adequacy of renewable energy mixes with concentrated solar power and photovoltaic in Morocco: Impact of thermal storage and cost," *Energies*, vol. 13, no. 19, p. 5087, 2020.

[48] B. Woodcroft *et al.*, *The Pneumatics of Hero of Alexandria: From the Original Greek*. Charles Whittingham, 1851.

[49] D. G. Shepherd, "Historical development of the windmill," tech. rep., Cornell Univ., Ithaca, NY (USA). Dept. of Mechanical and Aerospace Engineering, 1990.

[50] A. G. Drachmann, "Heron's windmill," in *Renewable Energy*, Routledge, 2018.

[51] H. P. Vowles, "Early evolution of power engineering," *Isis*, vol. 17, no. 2, pp. 412–420, 1932.

[52] H. P. Vowles, "An inquiry into origins of the windmill," *Transactions of the Newcomen Society*, vol. 11, no. 1, pp. 1–14, 1930.

[53] M. L. Jacobs, "Experience with Jacobs wind-driven electric generating plant, 1931-1957," *Wind Energy Conversion Systems*, pp. 155–8, 1973.

[54] J. F. Manwell, J. G. McGowan, and A. L. Rogers, *Wind energy explained: theory, design and application*. John Wiley & Sons, 2010.

[55] "The world's first offshore wind farm is retiring." https://orsted.com/en/media/newsroom/news/2017/03/the-worlds-first-offshore-wind-farm-is-retiring, 2017. Accessed: December 8, 2025.

[56] "Onshore vs Offshore Wind: What are the differences and facts?." https://greencoast.org/onshore-vs-offshore-wind/, 2019. Accessed: December 8, 2025.

[57] M. D. Esteban, J. J. Diez, J. S. López, and V. Negro, "Why offshore wind energy?," *Renewable Energy*, vol. 36, no. 2, pp. 444–450, 2011.

[58] IRENA, *Renewable Capacity Statistics 2025*. International Renewable Energy Agency, Abu Dhabi, 2025.

[59] IRENA: International Renewable Energy Agency , "Country rankings." https://www.irena.org/Statistics/View-Data-by-Topic/Capacity-and-Generation/Country-Rankings. Accessed: December 8, 2025.

[60] IRENA, *Renewabl Energy Statistics 2020*. International Renewable Energy Agency, Abu Dhabi, 2020.

[61] "Colossal six months for offshore wind support renewable energy investment in first half of 2020." https://about.bnef.com/blog, 2020. Accessed: December 8, 2025.

[62] "GWEC: Wind power industry to install 71.3 GW in 2020, showing resilience during COVID-19 crisis." https://gwec.net, 2020. Accessed: December 8, 2025.

[63] E. L. Petersen, N. G. Mortensen, L. Landberg, J. Højstrup, and H. P. Frank, "Wind power meteorology. Part II: siting and models," *Wind Energy: An International Journal for Progress and Applications in Wind Power Conversion Technology*, vol. 1, no. 2, pp. 55–72, 1998.

[64] M. Albadi and E. El-Saadany, "Overview of wind power intermittency impacts on power systems," *Electric Power Systems Research*, vol. 80, no. 6, pp. 627–632, 2010.

[65] M. Santhosh, C. Venkaiah, and D. Vinod Kumar, "Current advances and approaches in wind speed and wind power forecasting for improved renewable energy integration: A review," *Engineering Reports*, p. e12178.

[66] M. S. Nazir, F. Alturise, S. Alshmrany, H. Nazir, M. Bilal, A. N. Abdalla, P. Sanjeevikumar, Z. M Ali, *et al.*, "Wind generation forecasting methods and proliferation of artificial neural network: A review of five years research trend," *Sustainability*, vol. 12, no. 9, p. 3778, 2020.

[67] I. Van der Hoven, "Power spectrum of horizontal wind speed in the frequency range from 0.0007 to 900 cycles per hour," *Journal of Meteorology*, vol. 14, no. 2, pp. 160–164, 1957.

[68] T. Burton, D. Sharpe, N. Jenkins, and E. Bossanyi, *Wind energy handbook*, vol. 2. Wiley Online Library, 2001.

[69] TrueWind, "An analysis of the impacts of large-scale wind generation on the Ontario electricity system," *Report prepared for the Canadian Independent Electricity System Operator*, 2005.

[70] V. Belessiotis and E. Papanicolaou, "3.03 - history of solar energy," in *Comprehensive Renewable Energy* (A. Sayigh, ed.), pp. 85 – 102, Oxford: Elsevier, 2012.

[71] L. Szabó, "The history of using solar energy," in *2017 International Conference on Modern Power Systems (MPS)*, pp. 1–8, 2017.

[72] L. Richardson, "History of solar energy: Timeline and invention of solar panels: Energysage." https://news.energysage.com, 2018. Accessed: December 8, 2025.

[73] J. Perlin, *Let it shine: the 6,000-year story of solar energy*. New World Library, 2013.

[74] H.-M. Henning and J. Döll, "Solar systems for heating and cooling of buildings," *Energy Procedia*, vol. 30, pp. 633–653, 2012.

[75] A. Jamar, Z. Majid, W. Azmi, M. Norhafana, and A. Razak, "A review of water heating system for solar energy applications," *International Communications in Heat and Mass Transfer*, vol. 76, pp. 178–187, 2016.

[76] "Solar Attic Fans: Residential Ventilation Products: Solatube By Perk Inc." https://www.solatulsa.com/attic-fans/. Accessed: December 8, 2025.

[77] F. A. Tiano, G. Rizzo, G. De Feo, and S. Landolfi, "Converting a conventional car into a hybrid solar vehicle: a LCA approach," *IFAC-PapersOnLine*, vol. 51, no. 31, pp. 188–194, 2018.

[78] T. Suresh, T. Subha, C. S. Kumar, and T. Subash, "A study of novel technique-solar powered bicycle," *Materials Today: Proceedings*, 2020.

[79] I. Yahyaoui, *Advances in Renewable Energies and Power Technologies: Volume 1: Solar and Wind Energies*. Elsevier, 2018.

[80] A. C. Lazaroiu, M. Gmal Osman, C.-V. Strejoiu, and G. Lazaroiu, "A comprehensive overview of photovoltaic technologies and their efficiency for climate neutrality," *Sustainability*, vol. 15, no. 23, p. 16297, 2023.

[81] G. Simbolotti, "Concentrating solar power: technology brief," *IEA-ETSAP and IRENA*, 2013.

[82] H. M. Steinhagen and F. Trieb, "Concentrating solar power, a review of the technology," *Ingenia*, vol. 18, pp. 43–50, 2004.

[83] H. Zhang, J. Baeyens, J. Degrève, and G. Cacères, "Concentrated solar power plants: Review and design methodology," *Renewable and Sustainable Energy Reviews*, vol. 22, pp. 466–481, 2013.

[84] P. Breeze, *Solar power generation*. Academic Press, 2016.

[85] S. Qazi, *Standalone Photovoltaic (PV) Systems for Disaster Relief and Remote Areas*. Elsevier, 2016.

[86] HelioCSP, "Concentrated solar power had a global total installed capacity of 6,451 MW in 2019." http://helioscsp.com, 2020. Accessed: October 18, 2021.

[87] J. F. Lee, N. A. Rahim, and Y. A. Al-Turki, "Performance of dual-axis solar tracker versus static solar system by segmented clearness index in Malaysia," *International Journal of Photoenergy*, vol. 2013, 2013.

[88] IEA: International Energy Agency , "COVID-19 and the resilience of renewables – Renewables 2020, IEA, Paris ." https://www.iea.org/reports/renewables-2020. Accessed: June 26, 2023.

[89] A. Hammer, H. Beyer, C. Richter, D. Lincot, and A. Guermard, "Solar radiation, spatial and temporal variability," *Encyclopedia of Sustainability Science and Technology, edited by: Meyers, RA, Springer, New York*, vol. 9744, p. 9758, 2012.

[90] A. Mills, "Understanding variability and uncertainty of photovoltaics for integration with the electric power system," *The Electricity Journal*, 2009.

[91] Y. V. Makarov, P. V. Etingov, and J. Ma, "Incorporating forecast uncertainty in utility control center," in *Renewable Energy Integration*, pp. 145–157, Elsevier, 2017.

[92] P. Rosas, "Dynamic influences of wind power on the power system," *PhD Thesis, Technical University of Denmark. Denmark*, 2004.

[93] A. Mills, "Implications of wide-area geographic diversity for short-term variability of solar power," 2010.

[94] E. Takle and R. Shaw, "Complimentary nature of wind and solar energy at a continental mid-latitude station," *International Journal of Energy Research*, vol. 3, no. 2, pp. 103–112, 1979.

[95] F. Giraud and Z. M. Salameh, "Steady-state performance of a grid-connected rooftop hybrid wind-photovoltaic power system with battery

storage," *IEEE Transactions on Energy Conversion*, vol. 16, no. 1, pp. 1–7, 2001.

[96] J. L. Bernal-Agustín, R. Dufo-López, and D. M. Rivas-Ascaso, "Design of isolated hybrid systems minimizing costs and pollutant emissions," *Renewable Energy*, vol. 31, no. 14, pp. 2227–2244, 2006.

[97] A. González, J.-R. Riba, A. Rius, and R. Puig, "Optimal sizing of a hybrid grid-connected photovoltaic and wind power system," *Applied Energy*, vol. 154, pp. 752–762, 2015.

[98] B. O. Bilal, V. Sambou, P. Ndiaye, C. Kébé, and M. Ndongo, "Study of the influence of load profile variation on the optimal sizing of a standalone hybrid PV/wind/battery/diesel system," *Energy Procedia*, vol. 36, pp. 1265–1275, 2013.

[99] Y. Zhao, M. Noori, and O. Tatari, "Boosting the adoption and the reliability of renewable energy sources: Mitigating the large-scale wind power intermittency through vehicle to grid technology," *Energy*, vol. 120, pp. 608–618, 2017.

[100] E. Rahimi, A. Rabiee, J. Aghaei, K. M. Muttaqi, and A. E. Nezhad, "On the management of wind power intermittency," *Renewable and Sustainable Energy Reviews*, vol. 28, pp. 643–653, 2013.

[101] V.-H. Bui, A. Hussain, T.-T. Nguyen, and H.-M. Kim, "Multi-objective stochastic optimization for determining set-point of wind farm system," *Sustainability*, vol. 13, no. 2, 2021.

[102] L. Balling, "Fast cycling and rapid start-up: new generation of plants achieves impressive results," *Modern power systems. San Francisco CA*, vol. 31, no. 1, pp. 35–41, 2011.

[103] K. Karunanithi, S. Saravanan, B. Prabakar, S. Kannan, and C. Thangaraj, "Integration of demand and supply side management strategies in generation expansion planning," *Renewable and Sustainable Energy Reviews*, vol. 73, pp. 966–982, 2017.

[104] J. Baetens, J. D. De Kooning, G. Van Eetvelde, and L. Vandevelde, "A two-stage stochastic optimisation methodology for the operation of a Chlor-Alkali electrolyser under variable DAM and FCR market prices," *Energies*, vol. 13, no. 21, p. 5675, 2020.

[105] H. Ibrahim and A. Ilinca, "Techno-economic analysis of different energy storage technologies," in *Energy Storage-Technologies and Applications*, IntechOpen, 2013.

[106] A. Dadkhah, D. Bozalakov, J. D. De Kooning, and L. Vandevelde, "On the optimal planning of a hydrogen refuelling station participating in the electricity and balancing markets," *International Journal of Hydrogen Energy*, vol. 46, no. 2, pp. 1488–1500, 2021.

[107] A. E. Samani, A. D'Amicis, J. D. De Kooning, D. Bozalakov, P. Silva, and L. Vandevelde, "Grid balancing with a large-scale electrolyser providing primary reserve," *IET Renewable Power Generation*, vol. 14, no. 16, pp. 3070–3078, 2020.

[108] J. Liu, C. Hu, A. Kimber, and Z. Wang, "Uses, cost-benefit analysis, and markets of energy storage systems for electric grid applications," *Journal of Energy Storage*, vol. 32, 2020.

[109] H. C. Hesse, M. Schimpe, D. Kucevic, and A. Jossen, "Lithium-ion battery storage for the grid—a review of stationary battery storage system design tailored for applications in modern power grids," *Energies*, vol. 10, no. 12, p. 2107, 2017.

[110] D. Shekhawat, J. J. Spivey, and D. A. Berry, *Fuel cells: technologies for fuel processing*. Elsevier, 2011.

[111] M. Momirlan and T. N. Veziroglu, "The properties of hydrogen as fuel tomorrow in sustainable energy system for a cleaner planet," *International Journal of Hydrogen Energy*, vol. 30, no. 7, pp. 795–802, 2005.

[112] P. P. Edwards, V. L. Kuznetsov, W. I. David, and N. P. Brandon, "Hydrogen and fuel cells: towards a sustainable energy future," *Energy policy*, vol. 36, no. 12, pp. 4356–4362, 2008.

[113] D. Enescu, G. Chicco, R. Porumb, and G. Seritan, "Thermal energy storage for grid applications: Current status and emerging trends," *Energies*, vol. 13, no. 2, 2020.

[114] IRENA, *Electricity Storage Valuation Framework: Assessing system value and ensuring project viability*. International Renewable Energy Agency, Abu Dhabi, 2020.

[115] S. Kharel and B. Shabani, "Hydrogen as a long-term large-scale energy storage solution to support renewables," *Energies*, vol. 11, no. 10, 2018.

[116] Elia group, *Elia's view on Belgium's Energy Vision for 2050*. Elia, Brussels, Belgium, 2017.

Chapter 3

Hydrogen Production and the Power System

As stated in Chapter 2, among the strategies proposed in the literature to manage renewable energy sources (RESs) variability, hydrogen production using renewable electricity stands out as a promising approach due to its advantages. To address the intermittency of RESs, electrolysers can adjust their power consumption to help system operators balance supply and demand. Additionally, hydrogen production offers the potential for long-term energy storage. Although seasonal storage, for instance, producing hydrogen in summer using excess solar energy and utilising it in winter, requires substantial storage volumes, the required storage capacity can be considerably reduced when hydrogen is stored at very high pressure, for example, around 700 bar as liquid hydrogen. Regardless of the required storage size, hydrogen remains well-suited for long-term energy storage because the stored energy does not degrade over time, and once hydrogen is compressed or liquefied, it can be stored for months with negligible losses [1]. In contrast, batteries experience self-discharge and gradually lose stored energy even when not in use. The self-discharge rate depends on the battery chemistry, typically a few percent per month for lithium-ion systems and considerably higher for technologies such as lead-acid [2]. Consequently, batteries are more appropriate for short-term storage and fast-cycling applications, while hydrogen provides a more effective solution for long-duration storage where preserving the stored energy over extended periods is essential.

In this chapter, a review of the literature on hydrogen production pathways, as an approach to accommodate the RESs intermittency, is presented. Additionally, in the context of fossil fuel-based hydrogen generation, the most favourable feedstocks and their primary production processes are outlined. Factors influencing electrolysis are also discussed. As the primary focus of this research is on green hydrogen production, particular attention is paid to technologies

associated with generating hydrogen from RESs. This chapter also includes a review of the electricity market and its mechanism, which has an influence on operation mode of electrolysers when it comes to the flexibility provision with them.

The remainder of this chapter is structured as follows: Section 3.1 provides an introduction, including a discussion of common terminology used to refer to hydrogen produced through different pathways. In Section 3.2, hydrogen production technologies, based on both fossil fuels and RESs, are examined. Section 3.3 reviews various types of electrolysers used for green hydrogen production and compares different green hydrogen generation methods. Section 3.4 discusses the structure of the electricity market and grid balancing mechanisms, including an overview of the ancillary services market within the Belgian electricity system. Section 3.5 focuses on offshore hydrogen production, reviewing potential pathways for generating hydrogen from seawater. This section further discusses Belgian government policies related to hydrogen development. Finally, in Section 3.6, conclusions are drawn, and based on the literature reviews conducted in the previous chapter and the current one, the overall framework for the subsequent chapters is defined.

3.1 Introduction

Hydrogen is a simple and highly abundant element on Earth, with the ability to store and deliver energy. It is an odourless, colourless, tasteless, and non-toxic gas, and its release is not known to pollute air or water. Under standard conditions, its solubility in water is extremely low. However, hydrogen rarely exists in its elemental form and must be extracted from compounds such as water, coal, natural gas, or biomass. Fossil fuels and RESs are the two primary energy sources for hydrogen production, with the former emitting carbon dioxide (CO_2) as a by-product. Therefore, to enable sustainable hydrogen production from fossil fuels, CO_2 must be captured and stored.

The IEA report presents the global trend in hydrogen production, comparing fossil fuel-based hydrogen with hydrogen produced from renewable energy sources, as illustrated in Fig. 3.1(a). While global hydrogen production from renewables declined between 2019 and 2024, Fig. 3.1(b) shows that global hydrogen consumption increased by approximately 2–3% per year over the same period. This clearly indicates that hydrogen production from renewable sources still requires significant improvement in order to compete with fossil fuel-based hydrogen [3]. A key reason for the decline in hydrogen production from renewable sources during this period is the widespread delay or cancellation of RES-based hydrogen projects. Among the 190 projects announced globally for 2023 over the preceding three years, only 0.3 GW of the initially planned 4.3 GW

of electrolysis capacity became operational, corresponding to approximately 7% [4]. These disruptions were partly driven by the disruptions associated with the COVID-19 pandemic, which affected supply chains, investment decisions and construction schedules. In addition, several renewable energy projects that were expected to supply electricity for these hydrogen facilities also experienced delays, further constraining RES-based hydrogen output. As a result, the shortfall in renewable hydrogen production contributed to a relative increase in blue hydrogen deployment, primarily through steam methane reforming coupled with carbon capture and storage.

In general, various colours are assigned to hydrogen based on the primary energy source used and whether the production process includes a carbon capture, utilisation, and storage (CCUS) system. Fossil fuel-based hydrogen is classified as black (or brown), grey, blue, and turquoise, with coal, natural gas without CCUS, natural gas with CCUS, and natural gas via pyrolysis serving as the respective sources. Electricity-based hydrogen is categorised as yellow, pink, and green, depending on whether it is produced using grid electricity of mixed origin, nuclear power, and RESs, respectively. The different hydrogen colours, along with their corresponding primary energy sources and greenhouse gas (GHG) emission levels, are illustrated in Fig. 3.2. At present, grey hydrogen remains the dominant type, accounting for 95% of total production [5].

3.2 Hydrogen Production Pathways

This section discusses the pathways for hydrogen production from both fossil fuels and renewable energy sources.

3.2.1 Hydrogen Production from Natural Gas

The most well-known method for producing hydrogen from natural gas is steam methane reforming (SMR), which accounts for approximately 95% of current global hydrogen production [7]. In this endothermic conversion, shown in (3.1), methane reacts with high-temperature water vapour at a pressure of 3 to 25 bar and temperatures between 700 and 1000 °C, resulting in hydrogen and carbon monoxide (CO) through the water-gas shift reaction. Subsequently, the CO, comprising approximately 12% of the product gas, can be further reacted with steam to generate additional hydrogen along with CO_2, as illustrated in (3.2). Finally, in a process known as pressure swing adsorption, CO_2 and other impurities are removed to yield nearly pure hydrogen. Alternative hydrocarbons such as ethanol, propane, and gasoline can also be used in the steam reforming process [7, 8].

$$CH_4 + H_2O + \text{heat} \rightarrow CO + 3H_2 \tag{3.1}$$

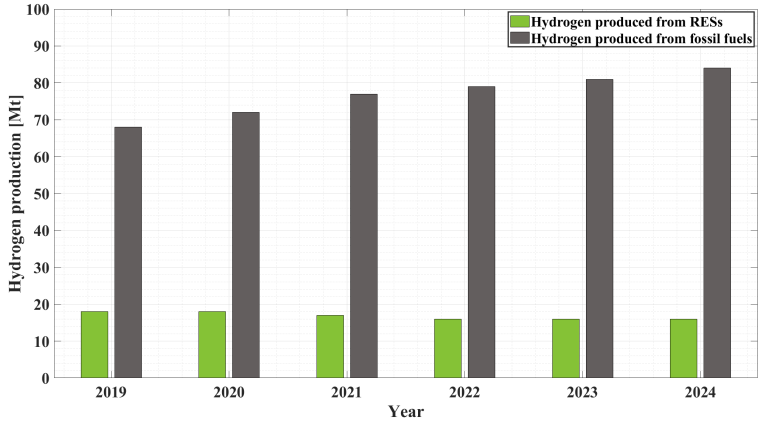

(a) Global hydrogen production from fossil fuels and RESs

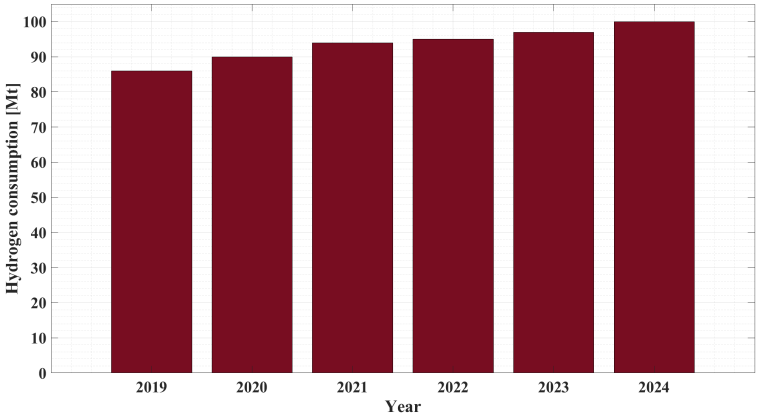

(b) Global hydrogen consumption

Figure 3.1: Global hydrogen production and consumption from 2019 to 2024

$$CO + H_2O \rightarrow CO_2 + H_2 + \text{heat} \tag{3.2}$$

3.2.2 Hydrogen Production from Oil

Through partial oxidation (PO), heavy hydrocarbons that are not suitable for steam reforming are mixed with a limited amount of oxygen. The restricted oxygen supply prevents the complete oxidation of the hydrocarbons, resulting in the formation of CO and hydrogen, rather than CO and water. Unlike SMR, partial oxidation is an exothermic reaction. The general form of a PO reaction

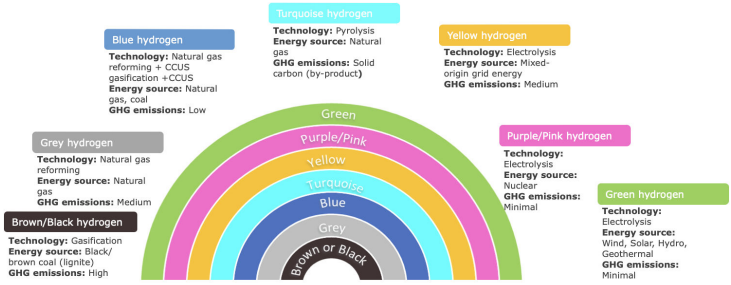

Figure 3.2: Hydrogen colour classifications and their corresponding primary energy sources [6]

and the idealised PO reaction of heating oil are shown in (3.3) and (3.4), respectively.

$$C_nH_m + \frac{n}{2}O_2 \rightarrow nCO + \frac{m}{2}H_2 + \text{heat} \tag{3.3}$$

$$C_{12}H_{24} + 6O_2 \rightarrow 12CO + 12H_2 + \text{heat} \tag{3.4}$$

It is worth noting that hydrogen can also be produced from methane via PO. In (3.5) and (3.6), the PO and water-gas shift reactions of methane are illustrated, respectively. By comparing (3.1) and (3.5), it can be observed that PO yields less hydrogen per unit of input fuel than SMR [7].

$$CH_4 + \frac{1}{2}O_2 \rightarrow CO + 2H_2 + \text{heat} \tag{3.5}$$

$$CO + H_2O \rightarrow CO + \frac{1}{2}O_2 \rightarrow CO2 + H_2 \tag{3.6}$$

3.2.3 Hydrogen Production from Coal

There are several methods for producing hydrogen from coal through gasification processes, which are discussed in detail in [9]. Gasification generally refers to the conversion of any carbon-based raw material into synthesis gas (syngas) using air, steam, and oxygen. An example of a typical gasification reaction is provided in (3.7).

$$C(s) + H_2O + \text{heat} \rightarrow CO + H_2 \tag{3.7}$$

Although hydrogen production from coal is more complex than from natural gas, the abundance of coal makes it an attractive and commercially viable option.

3.2.4 Hydrogen Production via Electrolysis

Electrolysis, which is the focus of this thesis, involves splitting water molecules into hydrogen and oxygen using electricity. This process is the reverse of that occurring in a fuel cell, as discussed in Section 2.5. In this method, hydrogen is produced in an electrolyser unit consisting of two electrodes immersed in an electrolyte. By applying a direct current (DC) between the electrodes, water molecules are split, forming hydrogen at the cathode and oxygen at the anode. According to Faraday's laws of electrolysis, two parameters influence the magnitude of electrolytic effects. The first law states that the mass of an element deposited at an electrode (m) is directly proportional to the amount of electric charge (Q_e). The second law states that for the same amount of charge, the mass of different elements altered at an electrode is directly proportional to their equivalent weights (E), defined as the molar mass (M) divided by valence (v_e). Faraday's laws of electrolysis are presented in (3.8).

$$\begin{aligned} m &\sim Q_e \\ m &\sim E \\ E &= \frac{M}{v_e} \end{aligned} \tag{3.8}$$

The overall reaction for water electrolysis is presented as follows:

$$2H_2O + 2\Delta G^\circ \rightarrow 2H_2 + O_2 \tag{3.9}$$

where ΔG° is the Gibbs free energy, which is equal to 237 kJ/mol under standard conditions. However, the specific approach used to achieve this reaction varies across different types of electrolysers.

Given that the primary focus of this work is hydrogen production via electrolysis, the following section is dedicated to reviewing the various types of electrolysers.

3.3 Water Electrolysis Technologies

There are several types of electrolysers capable of splitting water into hydrogen and oxygen. Based on the method of hydrogen production, the three main types are the alkaline electrolyser (AE), proton exchange membrane (PEM) electrolyser, and solid oxide (SO) electrolyser. These technologies are examined in more detail in this section.

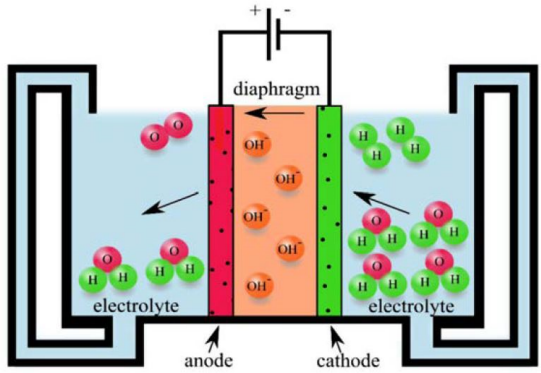

Figure 3.3: Schematic diagram of an alkaline electrolyser [8]

3.3.1 Alkaline Electrolyser

As the most mature and developed type of electrolyser, the alkaline electrolyser is the leading technology for water electrolysis worldwide. In this system, water is introduced at the cathode, where a reduction reaction occurs, producing hydrogen. The resulting hydroxide ions (OH^-) then migrate through the diaphragm to the anode, where they undergo oxidation. The reduction, oxidation, and overall reaction kinetics of the AE are presented in (3.10), (3.11), and (3.12), respectively. The purity of the hydrogen and oxygen produced by an alkaline electrolyser can reach approximately 99.9% and 99.5%, respectively. A schematic of an AE is illustrated in Fig. 3.3.

$$2H_2O + 2e^- \rightarrow H_2 + 2OH^- \tag{3.10}$$

$$2OH^- \rightarrow \frac{1}{2}O_2 + H_2O + 2e^- \tag{3.11}$$

$$2H_2O \rightarrow 2H_2 + O_2 \tag{3.12}$$

In an AE, as the name suggests, an alkaline electrolyte, typically an aqueous solution of potassium hydroxide (KOH) or sodium hydroxide (NaOH), is used. The electrolyte, added to water at a concentration of 20–40 wt%[1], facilitates ion transport between the cathode and anode. Generally, KOH is preferred over NaOH due to its higher conductivity and the reduced energy loss associated with the oxygen evolution reaction. At present, commercial and mature AEs are considered low-temperature (50–80 °C) and low-pressure (up to 30 bar)

[1] wt%: weight per cent, also known as w/w. It is calculated by dividing the weight of the solute by the total weight of the solution and multiplying by 100.

technologies [8, 10]. Nonetheless, to enhance the performance of hydrogen production systems, ongoing research continues to explore elevated operating temperatures and pressures for AEs.

The authors in [11] compared the efficiency of an alkaline electrolyser under three different operating pressure and temperature conditions: 70–80 °C at 30 bar, 80–90 °C at above 60 bar, and above 90 °C at above 100 bar. The results indicated an improvement in voltage efficiency, defined as the ratio of the minimum thermodynamic voltage required for water splitting to the actual cell operating voltage, from 64–78% to 70–82%, and subsequently to 74–87% under the respective operating conditions.

For the efficient storage and transport of hydrogen, compression of the outlet hydrogen (typically around 30 bar before compression) is required. This process relies on mechanical compressors, which not only increase the cost and complexity of the system but are also prone to failure. However, by raising the operating pressure within the electrolyser itself, the need for external mechanical hydrogen compression systems can be eliminated. In this regard, PEM electrolysers are preferred over alkaline electrolysers, as the former utilise a solid electrolyte that permits large pressure gradients across the cell. In contrast, alkaline electrolysers employ porous separators that only support balanced-pressure operation [12].

3.3.2 PEM Electrolyser

Unlike AE, in PEM electrolysers, water is fed into the anode and decomposed into hydrogen protons (H^+), electrons, and oxygen through an oxidation reaction driven by the applied DC current. The generated electrons migrate through the external electric circuit to the cathode, while the hydrogen protons travel through the membrane to the cathode. At the cathode, the reduction reaction occurs, resulting in the production of hydrogen. The reactions at the anode, cathode, and the overall redox reaction in the PEM electrolyser are shown in (3.13), (3.14), and (3.15), respectively.

$$2H_2O \rightarrow 4H^+ + 4e^- + O_2 \tag{3.13}$$

$$4H^+ + 4e^- \rightarrow 2H_2 \tag{3.14}$$

$$H_2O \rightarrow H_2 + \frac{1}{2}O_2 \tag{3.15}$$

Using the PEM electrolyser, gas purities of approximately 99.99% can be achieved. The operating principle of the PEM electrolyser is illustrated in Fig. 3.4.

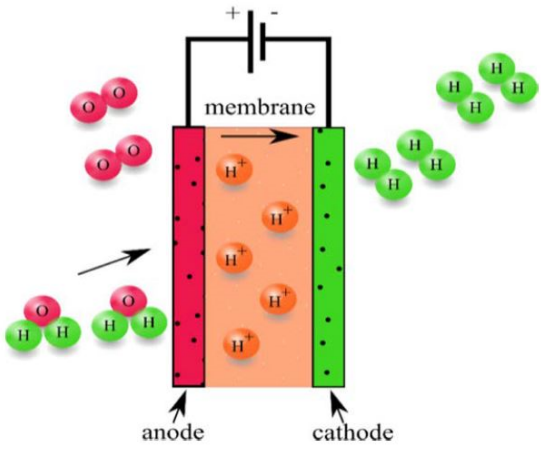

Figure 3.4: Schematic diagram of a PEM electrolyser [8]

In the PEM electrolyser, a solid ion-conducting membrane, rather than a liquid electrolyte as used in AE, is employed to separate the two electrodes. The most commonly used membrane for this purpose is Nafion. The PEM electrolyser is classified as a low-temperature and low-pressure electrolyser, with operating conditions similar to those of AE, typically at temperatures of 50–80 °C and pressures up to 30 bar. Similar to AE, efforts have been made to enhance PEM performance by increasing its operating temperature and pressure.

The authors in [13] assessed a high-pressure PEM electrolyser operating at 80, 200, 350, and 700 bar, and compared the results with a PEM operating at the conventional 30 bar in combination with a mechanical compressor. The selected pressure values correspond to industrial applications such as e-fuel production (30–120 bar), hydrogen injection into natural gas pipelines (70 bar), hydrogen storage ($\geq$ 200 bar), and ammonia production (200–300 bar). The findings indicate that the energy consumption of the system is higher when using direct electrochemical compression compared to a combination of electrochemical and mechanical compression. The discrepancy in energy use was measured as 0.22, 2.33, 5.57, and 15.48 kWh/kg_{H_2} at 80, 200, 350, and 700 bar, respectively. This is attributed to the greater energy losses in the compression stage of self-pressurised electrolysers relative to mechanical compression. Additionally, the study concludes that high-pressure electrolysis at 80, 200, and 350 bar could be economically feasible if electricity prices fall below 0.4, 0.16, and 0.09 €/kWh, respectively, assuming a PEM electrolyser system cost of 900 €/kW and a compressor cost of 3800 €/kW.

Increasing the operating temperature of an electrolyser can enhance its efficiency. However, this requires the development of more durable materials.

In [14], the impact of increasing the stack temperature on cell performance and overall system efficiency, including the hydrogen compression system, is explored. The findings suggest that there is an optimal stack temperature for each operating point, which solely depends on the electrode pressure and cell voltage, and can be calculated analytically. Moreover, optimising the temperature leads to a noticeable reduction in hydrogen permeation at low current densities. The authors further conclude that research and development efforts do not need to focus on creating long-lasting materials for 90 °C operation, as the optimal stack temperature is lower within the relevant current density range constrained by efficiency requirements. Conversely, the optimal temperature approaches ambient levels at low current densities and increases with current density, reaching 80 °C at approximately 1.6 V. This enhances the overall system efficiency and mitigates safety concerns related to hydrogen permeation through the membrane, which could generate explosive gases on the oxygen side. A lower stack temperature of 80 °C, instead of 90 °C, also improves stack durability.

3.3.3 Solid Oxide Electrolyser

The solid oxide electrolyser is the least developed among the three common types of electrolysers, namely AE and PEM. Existing systems remain at the pilot-scale to early commercial project level. Since hydrogen production in SO electrolysers is achieved at high temperatures, the development of more resilient materials is required to ensure reliable and durable operation. Similar to AE, water content, albeit in the form of steam, is introduced at the cathode, where it is decomposed into hydrogen and oxide ions. These ions then travel through the solid ceramic electrolyte to the anode, while the electrons migrate through the external circuit to the same location, where oxygen molecules are formed. The reactions taking place in an SO electrolyser are shown in (3.16)–(3.18).

$$H_2O + 2e^- \rightarrow H_2 + O^{2-} \tag{3.16}$$

$$O^{2-} \rightarrow \frac{1}{2}O_2 + 2e^- \tag{3.17}$$

$$H_2O \rightarrow H_2 + \frac{1}{2}O_2 \tag{3.18}$$

In SO electrolysers, a ceramic material that conducts oxide ions, with a thickness of approximately 30–150 µm is utilised, such as zirconium dioxide (ZrO_2) ceramic stabilised with yttrium or scandium oxides. As mentioned, electrolysis in an SO electrolyser is performed at high temperatures ranging

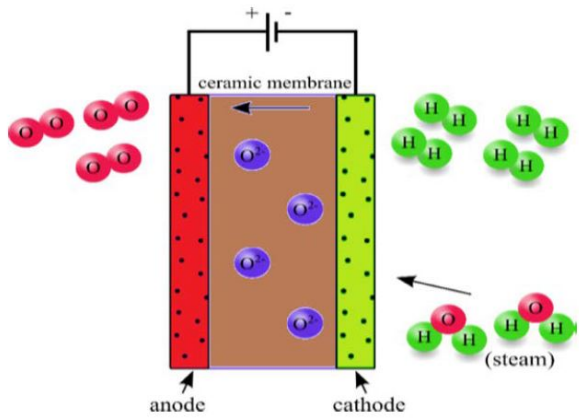

Figure 3.5: Schematic diagram of an SO electrolyser [8]

from 700 to 1000 °C. Although these conditions yield exceptionally high efficiencies, degradation of cell components due to the elevated temperatures remains the primary obstacle to the further development of SO electrolysers. The achievable purity of hydrogen and oxygen in SO electrolysers is approximately 99.99% and over 95%, respectively. A schematic representation of an SO electrolyser is shown in Fig. 3.5. Similar to alkaline and PEM electrolysers, the typical maximum operating pressure is around 30 bar. A recent study indicated that a limited operational period, possibly a few hundred hours, may be enough to predict the long-term performance of an SO electrolyser [15].

3.4 Power Grid Stability and Balancing

In line with the global ambition of carbon reduction and neutrality, conventional large-scale fossil fuel power plants are being phased out and replaced by renewable-based units. Although increasing the share of RESs in the electric power network offers substantial benefits, it also introduces several technical challenges for system operators, as discussed in Chapter 2, which may compromise the stability of the power system.

Power system stability can be categorised into angular (rotor angle) stability and voltage stability. The former refers to the ability of the electric grid to maintain the synchronism of its rotating synchronous machines. When a positive or negative imbalance occurs between the mechanical driving generation and the net electrical consumption, generators accelerate or decelerate relative to their synchronous rotational speed and may oscillate around that speed. If the generators fail to maintain synchronism, their protection systems disconnect them from the power system. This can trigger a runaway situation, potentially

resulting in cascading power plant shutdowns and widespread blackouts. Voltage stability, by contrast, concerns the power system's capability to maintain acceptable voltage levels at all nodes following a disturbance. Traditionally, to ensure angular (transient) stability and to support voltage stability, generators are equipped with speed and voltage control systems.

The aforementioned considerations necessitate maintaining a close balance between generation and load at all times. Moreover, due to the unique nature of electricity, it must be consumed almost immediately after it is produced. Although various commercialised storage technologies exist, such as batteries and pumped hydro storage, storing electricity on a large scale remains economically unfeasible. Consequently, ensuring power system stability requires accurate generation planning and reliable load forecasting. This complex task is managed within the electricity market, the functioning of which is discussed in the following section.

3.4.1 Electricity Markets

With the increasing share of intermittent RESs generation and the inherently unpredictable nature of power demand, aligning generation with load profiles has become a challenging task. Historically, the electricity market operated under a monopolistic structure, characterised by vertical integration in which a single company was responsible for electricity generation, transmission, and distribution, all at a fixed, imposed price. This structure, illustrated in Fig. 3.6, remained dominant until the 1980s. Prior to that, consumers had no alternative suppliers, as each utility held exclusive control over a specific region.

Although the monopolistic structure offered certain advantages, such as reduced complexity in market configuration, it was not cost-effective. Consequently, to lower electricity prices and limit government involvement in public utilities, the electricity market was liberalised. This transition introduced competition in electricity production and added a new participant to the market: the retailer. The liberalised structure of the electricity market is illustrated in Fig. 3.7 [16]. Generally, several entities are involved in the current structure of the electricity market, including generators, transmission system operators (TSOs), distribution system operators (DSOs), independent system operators (ISOs), market regulators, market operators, retailers, and consumers. Generators produce electricity and sell it in the wholesale market to either retailers or large consumers. TSOs and DSOs are responsible for operating the transmission and distribution networks, respectively, while ISOs oversee the overall security of the power system. The market regulator establishes the rules governing the market and monitors for potential abuses. Lastly, as the name implies, the market operator is responsible for matching supply and demand and handling market settlements.

Due to the complexity of the liberalised market and the requirement to maintain a near-continuous balance between electricity generation and consumption, a new electricity trading scheme was developed to prevent power imbalances. To distribute responsibilities across different sectors and simplify operations, the wholesale market is divided into three sub-markets: the futures/forward market, the spot market, and the balancing market, as illustrated in Fig. 3.8.

The first phase of electricity trading takes place in the futures/forward market, where long-term bilateral agreements are established between producers, retailers, and, in some cases, consumers. These agreements are made from several years to a few days in advance. This market provides a secure platform for electricity trading by ensuring price stability and mitigating the risk of short-term price volatility through price hedging. While forward contracts are typically customised, specifying quantities, delivery dates, payment terms, prices, and penalties for non-compliance, standardised contracts are used in the futures market. However, a key drawback of futures/forward contracts is that they introduce greater uncertainty in balancing generation and consumption, as they are concluded well in advance of delivery [16].

To compensate for the uncertainty associated with the futures/forward market, the spot market is introduced, which is further divided into the day-ahead and intraday markets. As the name implies, the day-ahead market is conducted

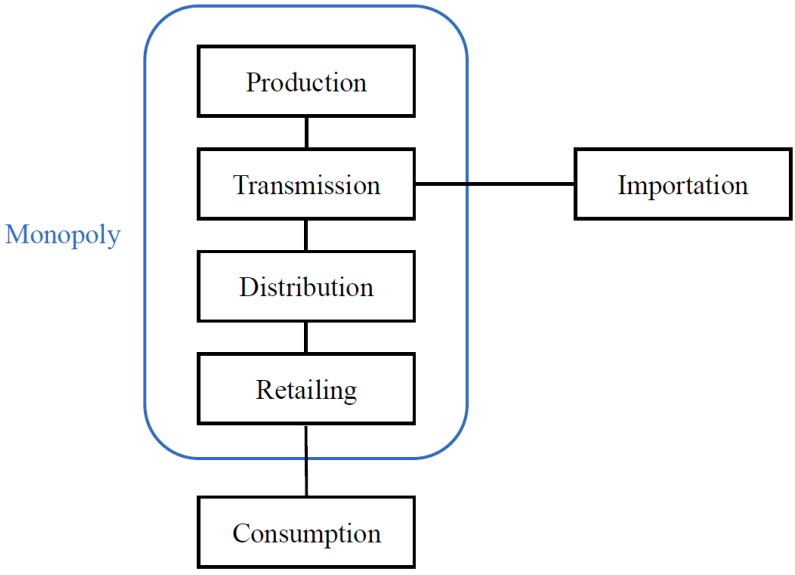

Figure 3.6: Structure of a monopolistic electricity market [16]

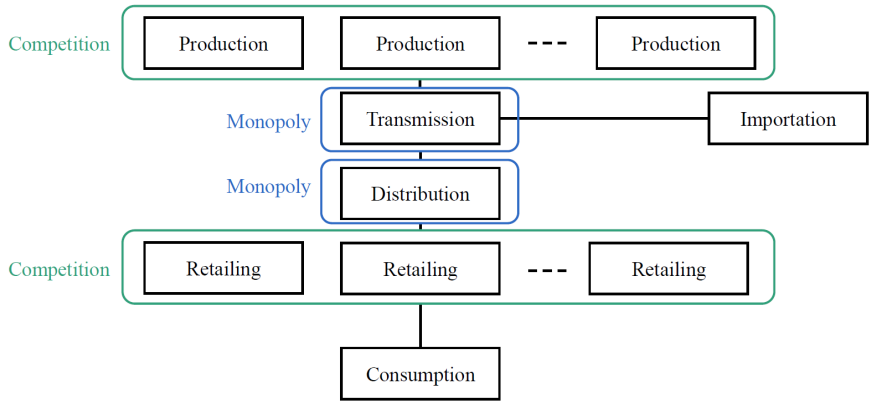

Figure 3.7: Structure of a liberalised electricity market [16]

one day before delivery and is typically organised as a pool. In this setup, market participants submit their bids and offers for each hour of the following day to the market operator, who aggregates the supply and demand into two separate curves and identifies their intersection, where supply and demand are balanced. This procedure is known as the market clearing algorithm (MCA), which determines both the market clearing price (MCP) and the market clearing volume (MCV), as illustrated in Fig. 3.9. All supply and demand offers at or below the MCP are accepted, and the respective parties are scheduled for generation or consumption on the following day. The MCA aims to maximise social welfare.

However, a key disadvantage of the day-ahead market is that it still takes place a relatively long time before the actual delivery, typically between 12 and 36 hours in advance, as shown in Fig. 3.8. Consequently, deviations between projected and actual generation or consumption are likely, for example, due to inaccuracies in weather forecasts. These discrepancies may lead to errors in the predicted levels of electricity generation and demand. In the event of an undesired positive or negative imbalance, the responsible market participants must adopt one of the following three strategies to restore balance to the grid [16].

The first strategy involves compensation using other generation or consumption assets within the portfolio of the market participant responsible for the imbalance.

If no capacity is available, market participants still have the opportunity to adjust their positions through the intraday market. Since trading in this market occurs closer to real-time, it enables participants to modify their positions before delivery. In general, transactions in the intraday market can take place

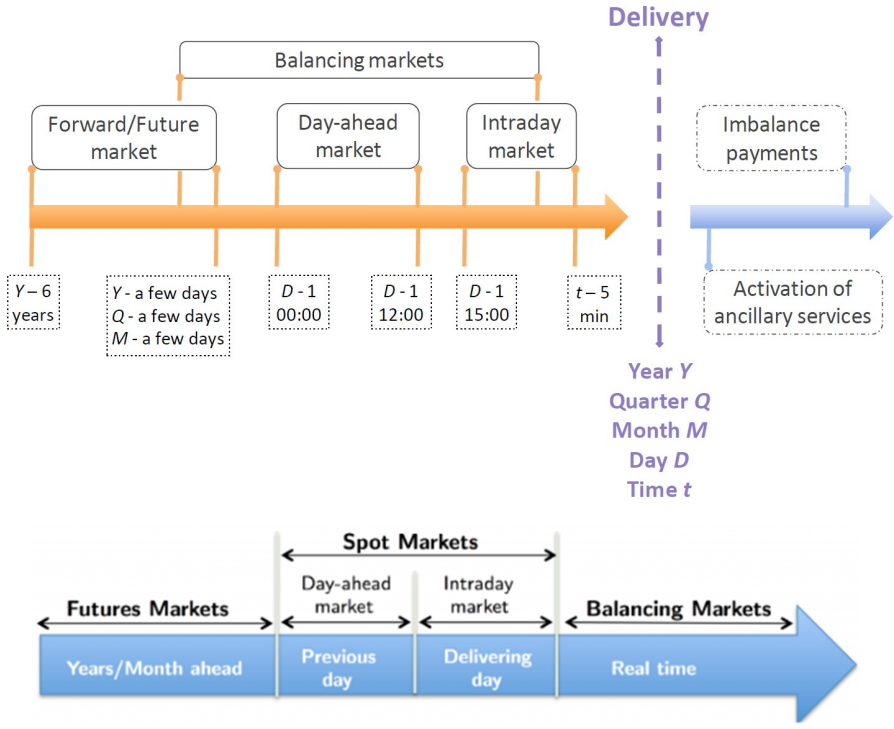

Figure 3.8: Overview of the electricity market [16]

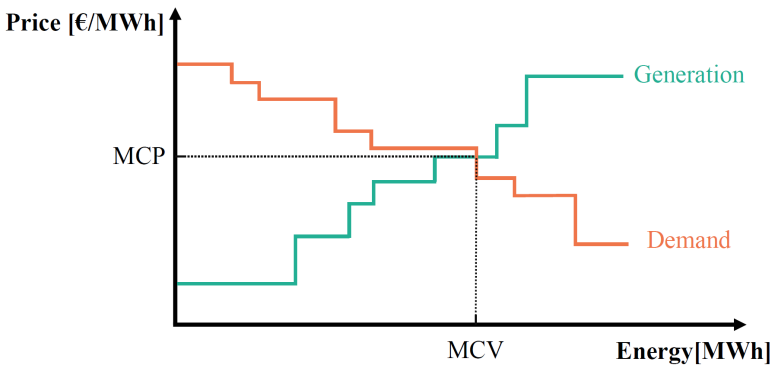

Figure 3.9: Day-ahead market clearing process

from the day before up to a few minutes prior to delivery. In some cases, the structure of the intraday market is similar to that of the day-ahead market. However, in certain countries, such as Belgium, market participants submit bids specifying the required amount of energy and the corresponding time interval.

Once a supply and a demand offer are matched, the transaction is confirmed, and the associated market participants are obligated to generate or consume accordingly.

Even though the intraday market operates closer to real time, discrepancies between demand and supply may still occur. Therefore, as a final measure, if neither of the previously mentioned strategies is feasible, the market participant resorts to the third category of the electricity market: the balancing market. Similar to the intraday market, this stage also takes place near real time, but it occurs after delivery. The market operator monitors generation and consumption by observing the grid frequency, enabling real-time balancing of the market. When the frequency deviates from its nominal value, typically 50 Hz in most countries, and exceeds a specific threshold, the operator acquires ancillary services at a cost referred to as the imbalance price, in order to restore supply-demand equilibrium. The cost of activating ancillary services is recovered by penalising the market participants responsible for the imbalance. In other words, the imbalance price reflects the cost of acquiring and activating these services. Units that assist the operator by absorbing or supplying the imbalance can generate revenue by offering ancillary services. Accurate forecasting of the imbalance price may encourage participants to refrain from trading in earlier markets if it appears more profitable to operate within the balancing market. Nevertheless, to discourage deliberate speculation on either the generation or consumption side, given that the imbalance price is generally higher than the MCP, a two-price imbalance settlement mechanism is enforced by the operator. Under this system, participants responsible for causing the imbalance are charged the imbalance price, while those who unintentionally support the system by providing additional generation or consumption capacity are compensated only at the MCP determined in the day-ahead market, without receiving any additional reward.

Ancillary services include various types, such as frequency control (primary, secondary, and tertiary reserves), voltage control (primary, secondary, and tertiary control), and system restart (black start capability).

Frequency control involves three types of reserves: the primary reserve, or frequency containment reserve (FCR); the secondary reserve, or automatic frequency restoration reserve (aFRR); and the tertiary reserve, or manual frequency restoration reserve (mFRR). FCR is intended to stabilise the frequency within ±0.4% of the nominal value of 50 Hz. To achieve this, it must respond very quickly, within 30 seconds, to compensate for any potential frequency deviations. aFRR serves two purposes: to regulate the frequency back to 50 Hz, thereby relieving the burden on FCR, and to ensure that the actual physical import/export levels remain aligned with the contractually agreed values within a control area. In Belgium, the set-point signal, calculated every 10 seconds by the Belgian TSO (Elia), is based on real-time measurements of the discrepancy

between actual and contractual import/export balances and is sent to all power plants providing aFRR services. mFRR relieves the burden on aFRR and is manually controlled by TSO dispatchers, with a response time ranging from a few minutes up to a maximum of 15 minutes. It is typically activated when the aFRR reserve is saturated or at risk of saturation, for instance, following the sudden loss of a major generation unit. The tertiary reserve can be supplied by different sources, including running generation units, non-operational units with fast start-up capabilities, or even consumers connected to the distribution or transmission network [17].

In Fig. 3.10, the activation process of Elia's reserve types is illustrated. It is noteworthy that the blue shaded area in Fig. 3.10 represents the grid inertia, and both shaded blue regions have an equal area in the figure. In power systems, inertia refers to the kinetic energy stored in large rotating machines, which plays a critical role in maintaining stability during disturbances such as generation outages or abrupt load variations.

One major concern in a power system with high penetration of RESs is the reduction or loss of grid inertia. Traditionally, this inertia has been inherently provided by synchronous generators in conventional fossil-fuelled power plants. By contrast, renewable energy sources are interfaced through power electronic converters. Consequently, power systems undergoing a low-carbon transition are evolving into low-inertia grids, thereby weakening the grid's natural ability to withstand and recover from disturbances.

Grid inertia determines the rate of frequency deviation following a disturbance. A reduction in inertia therefore accelerates frequency dynamics [18]. For example, as illustrated in Fig. 3.10, when the mechanical driving power becomes insufficient to meet the electrical load in a low-inertia system, the frequency nadir, defined as the minimum frequency reached during the transient response, may drop below 49 Hz. This condition triggers under-frequency load shedding, a protective mechanism designed to prevent a complete power system collapse [19]. The most recent incident at the time this research was conducted occurred on 28 April 2025, when the grid frequency in the Iberian Peninsula dropped to 48 Hz, activating automatic load shedding and causing power cuts across Spain, Portugal, and parts of southern France [20].

Generally, when net electrical consumption exceeds mechanical generation, the grid frequency decreases, whereas when it falls below mechanical generation, the frequency increases above its nominal value. The rate of change of frequency (RoCoF) following such an incident depends on both the system inertia and the size of the power system, as expressed in (3.19):

$$\frac{df}{dt} = \frac{\Delta P_{\mathrm{e}}}{2H_{\mathrm{e}}} . f_0 + \frac{D_{\mathrm{e}}}{2H_{\mathrm{e}}} . \Delta f \tag{3.19}$$

where f_0 is the frequency at the start of the disturbance ($t = 0$), ΔP_{e} is

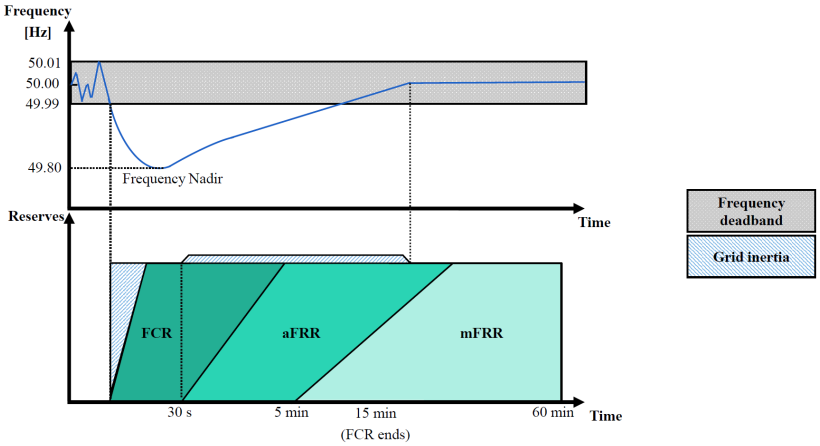

Figure 3.10: Process of reserve capacity activation by Elia [17]

the difference between the mechanical driving power and the electrical load, H_e is the system inertia, and D_e is the load damping factor of the power system. In traditional power systems, H_e originates from the rotating masses of synchronous machines directly connected to the grid. In power systems with a high penetration of RESs, which are connected to the grid via converters, the total system inertia consists of both the inertia provided by synchronous machines and the so-called synthetic inertia [21]. The first term on the right-hand side of (3.19) reflects the generation-side contribution to RoCoF, while the second term represents the load-side contribution. Since the latter is generally much smaller during the initial transient, it is commonly neglected in RoCoF analysis.

To control frequency deviations following a disturbance, the inertial response is the immediate mechanism that counteracts the imbalance and limits the initial frequency drop, as illustrated in Fig. 3.10. However, owing to their intermittent nature, a high penetration of RESs exacerbates frequency deviations and, by their nature, does not contribute to inertia unless additional control strategies are implemented. Consequently, beyond the inertial response, stabilising the grid frequency requires the activation of ancillary frequency control services, such as FCR, aFRR, and mFRR. The potential of electrolysers to provide FCR, and the implications of such operation on the cost of hydrogen production, are examined in Chapter 6.

In summary, the market operator is responsible for procuring a set of services from voluntary producers and consumers that can adjust their generation or consumption to maintain the real-time balance between electricity supply and demand, thereby stabilising the system. The following section explores the role of hydrogen in this context and how it can support the system operator.

3.4.2 Power System Downward Regulation

In the case of a positive mismatch, where mechanical driving generation exceeds net electrical consumption, chemical energy storage, such as in the form of hydrogen or its derivatives like methane and methanol, enables the system operator to avoid power curtailment. That is, the surplus electricity can be converted into hydrogen using an electrolyser and later utilised for various purposes, including industry, transportation, electricity generation, heating, or conversion into other molecules. Regarding ancillary service provision, a 25 MW PEM electrolyser integrated into the Belgian transmission system was investigated in [22] for its potential to provide FCR, with the results indicating that the optimal economic strategy was to operate the electrolyser at 55% baseload capacity and allocate the remainder for ancillary services. In [23], an optimisation model was developed to assess the techno-economic feasibility of a hydrogen refuelling station serving the mobility sector while also providing ancillary services. The findings demonstrate that participation in the ancillary services market, when combined with optimal component sizing and dispatch, can result in up to a 16% increase in revenue and a 6.4% reduction in the hydrogen break-even price by 2030.

Therefore, regardless of the application, the electricity consumption profile of an electrolyser can be submitted to the day-ahead market to help manage RESs variability and provide flexibility for the system operator. Additionally, electrolysers can further support the power system by delivering ancillary services, primarily FCR and aFRR, in the event of a positive imbalance. In a low-inertia grid, where there is insufficient natural response to frequency deviations, electrolysers can play a crucial role in stabilisation. However, to achieve this, accurate dynamic scheduling and a fast, robust, and efficient control system are essential to promptly respond to frequency fluctuations, maximise revenue, and justify the investment costs associated with electrolysers.

3.4.3 Power System Upward Regulation

As previously discussed, hydrogen can serve as a medium for storing electricity and subsequently converting it back into electrical energy, a process referred to as power-to-gas-to-power (P2G2P). When electricity demand exceeds generation, the stored hydrogen can be employed for the upward regulation of the grid through various means. In the literature, three commonly explored methods for electricity generation in conjunction with electrolysers include: using hydrogen as the primary fuel in gas-fired power plants, feeding hydrogen into fuel cells, and integrating battery systems with electrolysers. The flexible operation of electrolysers also relies on the performance of the associated integrated systems. This section examines electricity generation methods using

hydrogen that can support the power system during frequency drops. It is worth noting that, in addition to the following approaches, the same ancillary service products, such as FCR and aFRR, can also be provided for upward regulation, as electrolysers are able to reduce their power consumption when electricity demand exceeds supply.

Hydrogen-fired Plants

In the first method, electricity is sustainably generated by burning either green or blue hydrogen to produce steam, which subsequently drives a turbine. The round-trip efficiency of this approach depends strongly on the type of plant used. For instance, when green hydrogen is produced using an electrolyser with an efficiency of 70% and then burned in an open-cycle gas turbine with an efficiency of about 40%, the resulting round-trip efficiency is below 40%. This can be increased to approximately 60% when the heat generated during combustion is utilised, for example, when hydrogen is burned in a combined heat and power plant with an efficiency of around 90% [24]. In addition, if hydrogen is burned in a combined-cycle gas turbine with an efficiency of about 60%, the resulting round-trip efficiency is approximately 42% when considering a 70% electrolyser efficiency. A fundamental question in this context is whether it is justifiable to convert renewable electricity into hydrogen and subsequently reconvert it into electricity, given the relatively low round-trip efficiency, rather than using the renewable electricity directly. Additionally, it is worth considering whether CCS systems should be integrated directly into existing gas-fired power plants, as opposed to employing CCS in the production of blue hydrogen from fossil fuels prior to electricity generation. This consideration is supported by the fact that capturing carbon at the pre-combustion stage during blue hydrogen production is both technically easier and economically more feasible than post-combustion capture in gas-fired power plants. In the post-combustion stage, the CO_2 concentration and pressure are relatively low, whereas blue hydrogen production involves higher CO_2 pressures, allowing for the capture of approximately 97–98% of the produced CO_2, in contrast to significantly lower rates in conventional gas-fired plants. Moreover, the relatively low capacity factor of conventional gas-fired plants, typically below 50%, further reduces the cost-effectiveness of CO_2 capture [24]. By the end of this decade, a 1.8 GW blue hydrogen-fired power plant is planned for construction in Keadby, northeast England. The plant is intended to provide backup capacity for variable renewable energy sources, with a particular focus on offshore wind [24].

With some modifications, existing gas-fired power plants can be adapted to operate using hydrogen. Although the conversion costs are relatively low, the economic viability of burning hydrogen for electricity generation remains

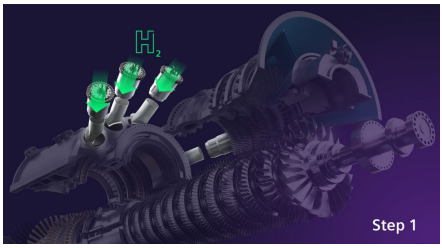

(a) Upgrade of the gas burner

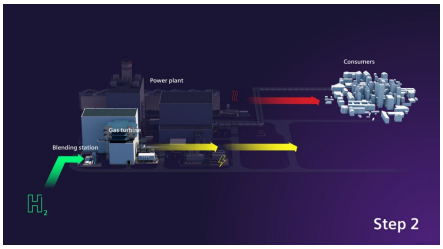

(b) Adjusting of BoP equipment

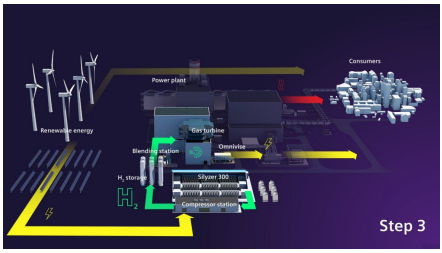

(c) RESs integration

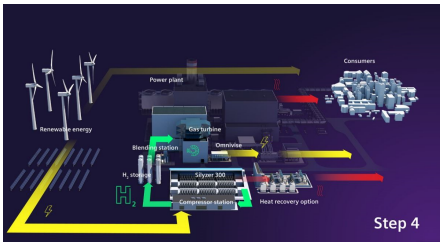

(d) Installation of heat pumps and thermal energy storage systems

Figure 3.11: Conversion of a conventional gas-fired power plant to operate on green hydrogen [25]

questionable. This is primarily due to the significantly lower cost of natural gas compared to green, blue, or even grey hydrogen. However, with anticipated reductions in electrolyser capital costs and an increasing share of renewable energy in the power mix, the cost of green hydrogen is expected to decline considerably. It is important to note that the electricity price is the primary driver of green hydrogen production costs, followed by capital expenditure (CapEx), water, and operating expenditure (OpEx). From a financial perspective, given the current cost differential between hydrogen and fossil fuels, it is more economically rational to prioritise hydrogen use in sectors such as transportation and industry rather than electricity generation. Nevertheless, as the cost of green hydrogen continues to decline, hydrogen-fuelled electricity generation may become a viable and competitive option in the future.

The conversion process of an existing gas-fired power plant to a hydrogen-fired configuration is illustrated in Fig. 3.11 [25].

The first step involves upgrading the gas turbine burner, as hydrogen exhibits higher reactivity and flame velocity compared to natural gas. This causes the flame to propagate closer to the burner, thereby increasing the risk of damage to the gas turbine. Consequently, a modified burner design is required. It is

worth noting that even before a full transition to 100% hydrogen combustion, the gas turbine can operate on hydrogen–natural gas blends. According to [26], operating a gas turbine with a 30% hydrogen and 70% natural gas mixture results in approximately 10% lower CO_2 emissions compared to using natural gas alone.

The second step requires adjustments to the balance of plant (BoP) equipment. For example, since hydrogen combustion in nitrogen-rich air leads to the formation of nitrogen oxides (NO_x), a selective catalytic reduction (SCR) system must be incorporated to reduce these emissions.

Third, the integration of RESs, electrolysers, and hydrogen storage systems into the plant configuration enables the use of sustainable electricity for hydrogen production and storage. On-site hydrogen generation and storage are also feasible, which further reduces costs by eliminating the need for hydrogen transportation.

Finally, the installation of heat pumps and thermal storage units allows for the cogeneration of electricity and heat, thereby improving the overall system efficiency. The recovered heat can be used to generate steam and drive a secondary turbine [24, 25].

Fuel Cell

In the second technique, hydrogen can be converted back into electricity using a fuel cell (FC) when required. An electrolyser and a fuel cell can also be integrated into a single system, forming what is known as a discrete regenerative fuel cell (DRFC), as illustrated in Fig. 3.12(a). If an oxygen storage system is added to the DRFC, a fully closed-loop DRFC unit is obtained. Furthermore, to reduce CapEx, achieve a more compact design, and enhance specific energy, a bifunctional electrochemical cell has been proposed that can operate in both FC and electrolyser modes [27]. This configuration is known as a unitised regenerative fuel cell (URFC), shown in Fig. 3.12(b). Regenerative fuel cells present an appealing solution for addressing negative imbalances in the grid, as they function as a form of energy storage, complementing other commercialised energy storage technologies such as secondary batteries and pumped-storage systems.

Both utility-scale batteries and pumped-storage systems exhibit a round-trip efficiency of approximately 80%. Nevertheless, despite this high efficiency, several limitations hinder their deployment on a large scale. For batteries, the primary concern is insufficient durability under deep cycling conditions. Furthermore, the inherent coupling of energy storage capacity and rated power, along with limited specific energy due to weight, acts as a constraint on scalability. To overcome this coupling, the redox flow batteries (RFBs), as discussed in Section 2.5, have been proposed. Unlike conventional batteries that store

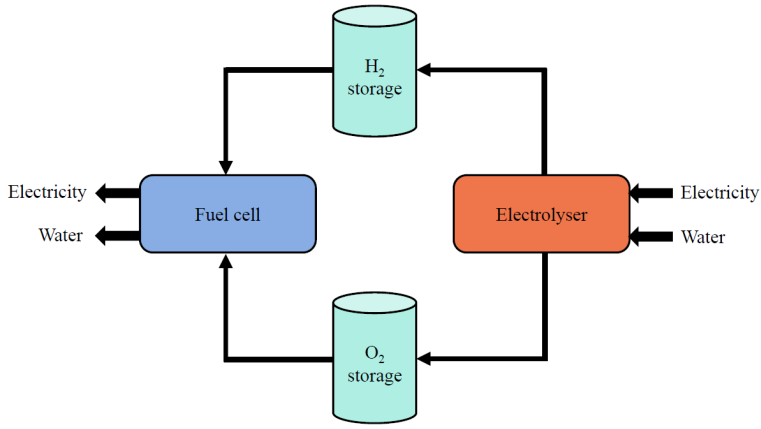

(a) DRFC

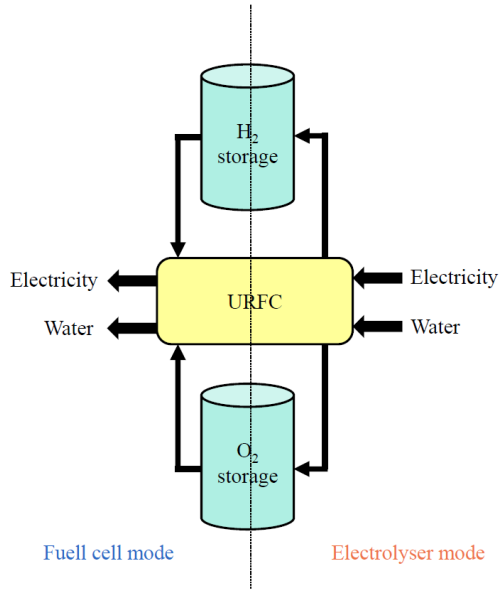

(b) URFC

Figure 3.12: Configurations of regenerative fuel cells [27]

reactants within the cell, RFBs store them in external tanks, thus allowing the decoupling of energy storage capacity and rated power [28]. While increasing the tank size enhances the storage capacity, the rated power can be improved by either stacking additional cells or enlarging the electrode area. However, it should be noted that due to the bulk nature of the electrolyte solution, the

specific energy of RFBs remains relatively low. Sharing the concept of external reactant storage, URFC systems store H_2 and O_2 in separate external tanks, which also results in decoupled storage capacity and rated power. Yet, owing to the absence of a liquid electrolyte, URFCs offer significantly higher specific energy than RFBs, typically ranging from 0.4 kWh/kg to 1.2 kWh/kg, including the mass of hydrogen and oxygen. In addition, compared to conventional batteries, URFCs can undergo charge-discharge cycles with minimal impact on durability. Due to these advantages, URFCs have gained considerable attention in recent years for their potential in both upward and downward grid regulation. Similar to electrolysers, URFCs are generally categorised into three main types: alkaline-URFC, PEM-URFC, and SO-URFC, with efficiency ranges of approximately 30–40%, 40–50%, and 60–80%, respectively [27]. As a result, various studies have aimed to enhance URFC performance, particularly in terms of efficiency, through multiple strategies [29–31].

In general, regenerative fuel cells exhibit lower round-trip efficiency than batteries and pumped-storage systems, primarily due to the sluggish kinetics of oxygen-related reactions. Moreover, their high costs and the technical challenges associated with hydrogen storage have hindered their commercial deployment and kept them at the developmental stage.

Considering hydrogen-fired power plants, although NO_x emissions are generated from hydrogen combustion, these plants remain a competitive option compared to FCs. This is primarily due to the higher efficiency of combined cycle power plants operating on hydrogen, which reaches approximately 63–64%, with potential for further improvement through increased combustion temperatures. In contrast, the efficiency of a typical fuel cell is limited to around 60%. Additionally, constructing a combined cycle power plant is significantly less expensive than building a fuel cell system of equivalent capacity. As a result, the levelised cost of electricity (LCOE) for combined cycle power plants is considerably lower than that of fuel cells. Furthermore, as previously mentioned, existing gas-fired power plants can be retrofitted to operate on hydrogen, thereby reducing the capital investment required for hydrogen-fired power generation.

Therefore, for large-scale electricity production using hydrogen, hydrogen-fired power plants are expected to become the dominant solution in the future, whereas fuel cells are likely to play a leading role in decarbonising the mobility sector. It is anticipated that the transition to fully hydrogen-powered plants will commence between 2025 and 2030. However, the precise timeline will largely depend on other factors such as government subsidies, carbon pricing, and CO_2 taxation policies.

Battolyser Systems

As the third approach, secondary batteries are integrated into electrolyser systems to complement them by providing upward regulation for grid balancing purposes. A combined battery and electrolyser system, known as a battolyser, is capable of mitigating short-term grid fluctuations via the battery component, while addressing longer-term variations through electrolysis. The battolyser operates as a battery until it is fully charged, at which point it transitions into electrolysis mode, producing hydrogen. Furthermore, the battery can supply the required electricity for the electrolysis process itself, thereby increasing the capacity factor of the electrolyser. This configuration is employed in [32] to enhance the performance of wind-to-hydrogen systems. In this study, a 765 kWh battery was added to a system comprising an 836.5 kW wind farm and a 276 kW electrolyser. The authors reported that the battery supported the electrolyser for 770 hours over one year, delivering 122 MWh of electricity and increasing the electrolyser's capacity factor from 8.5% (without battery support) to 20.5%. The resulting hydrogen can be subsequently used in hydrogen-fired power plants or as industrial feedstock.

In [33], the performance of a nickel-iron battery integrated with an alkaline electrolyser was investigated. The authors examined the impact of the battery's physical configuration and determined the optimal dimensions of the nickel and iron electrodes. The optimisation resulted in an efficiency increase from 80% in the base case to 86%. Similarly, in [34], a techno-economic analysis evaluated the integration of a battolyser, battery, or electrolyser into a wind farm. The findings indicated that, based on the LCOE, incorporating a battolyser or battery into a wind energy system to utilise curtailed wind results in a lower LCOE compared with using an electrolyser alone.

3.5 Molecules at Sea

As discussed in Section 3.4, multiple operational strategies are available for electrolysers to support the integration of intermittent renewable energy sources into the power system. However, electrolysers are still relatively expensive technologies, and their optimal operation is essential for maximising revenue. The main objective of this thesis is to investigate the behaviour of PEM electrolysers and to identify optimal pathways for hydrogen production using them, with the Belgian power system as a case study.

Considering Belgium's access to the North Sea and the ongoing development of an energy island by Elia, this study specifically investigates green hydrogen production at sea. The produced hydrogen can subsequently be combined with CO_2 to synthesise other molecules such as methane or methanol. In addition to the option of direct air capture (DAC) for CO_2, offshore hydrogen

production provides the opportunity to integrate the process with CO_2 extraction from seawater, where the concentration of CO_2 is significantly higher than in air [35, 36].

Producing hydrogen and other renewable molecules at sea via electrolysis is a relatively recent concept that has not yet been commercialised on a large scale. This approach addresses the issue of freshwater consumption for electrolysis by proposing the use of seawater instead. Moreover, in regions with limited onshore space, offshore production of renewable molecules appears to be a promising alternative. There may also be opportunities to integrate other marine renewable energy sources, such as wave and tidal energy. However, deploying electrolysers at sea presents challenges related to operation and maintenance (O&M), as well as increased costs. These factors must be carefully considered, particularly for electrolyser types that require more intensive O&M. When producing green hydrogen or other green molecules such as methanol offshore, several differences arise compared to onshore electrolysis, which significantly affect the design and configuration of the hydrogen production system.

To begin with, using seawater for the electrolysis process can help address the issue of water scarcity, which affects approximately 1.2 billion people worldwide. However, due to the presence of impurities in seawater compared to freshwater sources on land, feeding electrolysers directly with seawater can adversely affect their lifetime and performance. Therefore, in certain types of electrolysers, such as alkaline or PEM, desalination is required, which introduces additional components, increases system complexity, and raises the overall cost of the wind-hydrogen system. In Fig. 3.13, the two most likely approaches for hydrogen production from seawater are depicted. The first method, shown in Fig. 3.13(a), involves direct seawater electrolysis, while the second, illustrated in Fig. 3.13(b), incorporates upfront seawater treatment and purification prior to electrolysis.

Despite the absence of conclusive evidence favouring one method over the other, it is well known that direct seawater electrolysis requires significant re-engineering of currently available electrolysers, as well as the development of new electrocatalysts for both alkaline and PEM technologies. This need arises from the high concentration of corrosive chloride ions in seawater.

Regarding electrolyser technologies, alkaline electrolysers use a diaphragm rather than an ion-selective membrane, the latter being highly susceptible to performance and durability degradation in the presence of trace ionic impurities. However, a recent study on seawater electrolysis technologies for offshore hydrogen production suggests that the differences between alkaline and PEM electrolysers are relatively minor [38]. The study assessed AE, PEM, SO electrolysers, and direct seawater electrolysis based on economic, environmental, and social criteria using five different decision-making methodologies. It con-

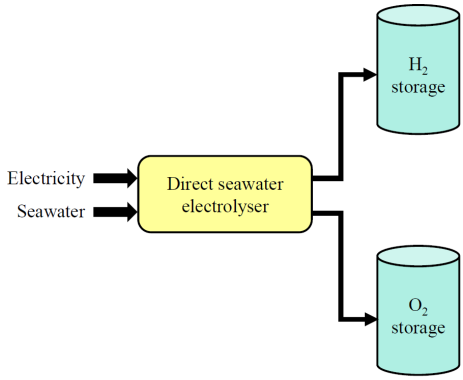

(a) Direct seawater electrolysis

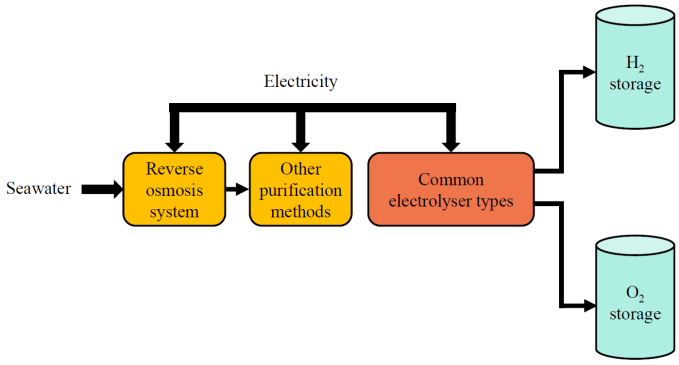

(b) Seawater electrolysis with upfront water treatment and purification

Figure 3.13: Common approaches to seawater electrolysis [37]

cluded that both alkaline and PEM electrolysers are likely to play a significant role in offshore hydrogen production, with PEM currently offering the most promising short-term applicability. Nevertheless, the study notes that if AE technology advances sufficiently to become less vulnerable at sea, it could emerge as the more favourable option. This is primarily due to AE's lower cost compared to PEM and its longer service life in marine environments, as it does not suffer from irreversible damage caused by feedwater impurities.

In addition, the authors of [39] identify the combination of seawater reverse osmosis (SWRO) with a PEM electrolyser as the most viable near-term solution for hydrogen production at sea. This configuration is seen as a more practical

alternative to investing in the development of novel catalysts and systems for direct seawater electrolysis. The study concludes that, within the SWRO-PEM system, the energy demand for electrolysis remains the dominant contributor, rendering the capital and operating costs of the SWRO unit negligible in comparison. Numerically, the inclusion of the SWRO system increases the levelised cost of hydrogen by less than 0.1 €/kg and CO_2 emissions by less than 0.1%. In Fig. 3.14, the breakdown of the energy requirements, CapEx, OpEx, and levelised cost for the SWRO-PEM configuration is illustrated.

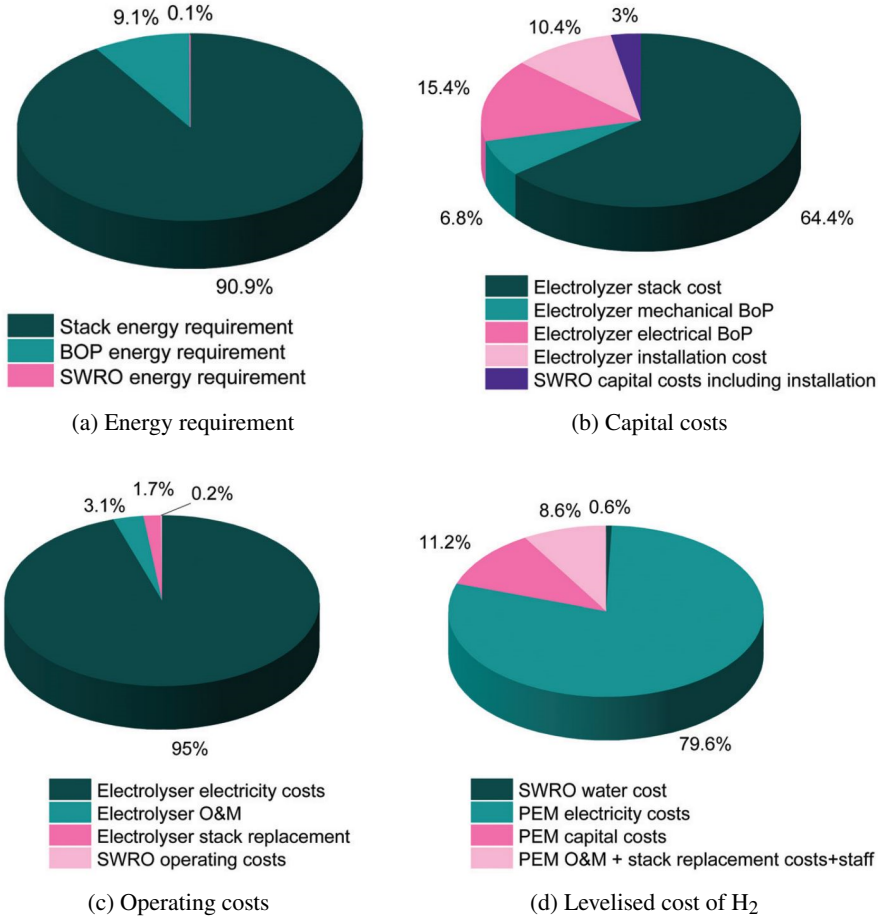

(a) Energy requirement

(b) Capital costs

(c) Operating costs

(d) Levelised cost of H_2

Figure 3.14: Cost breakdown of an SWRO-PEM electrolysis system [39]

Among the three electrolyser types discussed, alkaline, PEM, and SO, the latter still requires extensive research to demonstrate its technical and economic viability and is therefore excluded from this study. Alkaline electrolysis rep-

resents the most mature technology for water electrolysis. In addition to its longer lifespan compared to PEM, it also benefits from lower CapEx due to the use of non-noble metal catalysts. However, it presents several drawbacks, including limited dynamic operational capability, lower gas purity, reduced current densities, and lower operating pressures. Furthermore, the physical footprint of a PEM electrolyser is approximately five times smaller than that of an equivalent alkaline system.

From the perspective of the electrical grid, AE systems exhibit slower response times under dynamic operation. The difference in the dynamical behaviour originates from the type of ion transported and the medium through which it moves. In alkaline electrolysers, charge is carried by OH^- ions that migrate through a liquid KOH electrolyte. This liquid phase has a high viscosity, and OH^- ions exhibit lower ionic mobility compared with protons. Consequently, when the electrical load changes, the ionic flux adjusts more slowly, resulting in a slower transient response. In contrast, PEM electrolysers use a solid polymer electrolyte (Nafion) in which H^+ protons are the charge carriers. Protons possess significantly higher mobility, and their transport through the polymer occurs much more rapidly than OH^- transport in liquid alkaline solutions. As a result, PEM electrolysers can re-establish ionic conduction paths more quickly following load changes, leading to a faster dynamic response. This characteristic becomes particularly critical when electrolysers are coupled with intermittent renewable energy sources such as wind or solar, where rapid load-following capabilities are essential. Due to their slower response, AE systems are generally unsuitable for providing FCR and are instead limited to participating in aFRR. Consequently, AE is typically operated in fixed-load mode. In contrast, PEM electrolysers can start up within several minutes and ramp from idle to full capacity within seconds, qualifying them as fast-response electrolysers suitable for grid-support applications [40, 41].

Considering the aforementioned characteristics of both alkaline and PEM electrolysers in offshore and onshore applications, the PEM electrolyser is selected for integration into the offshore hydrogen production system in this thesis, with the subsequent analyses based on this type of electrolyser.

3.5.1 Belgian Government Policy towards Hydrogen

In order to evaluate scenarios as realistically as possible, it is essential to examine national policies concerning hydrogen and its derivatives. This is because a country's policy influences the configuration of the electrolysis system by determining the available financial resources and supporting infrastructure.

In October 2021, the Belgian federal government published its vision and strategy for hydrogen and its derivatives up to 2050 as part of the national energy transition plan. The strategy is built on four pillars: positioning Belgium as

an import and transit hub for renewable molecules in Europe, strengthening Belgian leadership in hydrogen technologies, establishing a robust hydrogen market, and promoting cooperation as a key success factor [42].

Given Belgium's central location in Western Europe and its major ports along the North Sea, the federal government aims, under the first pillar, to position the country as an import and transit hub for green molecules in the region. Moreover, the government has projected that to meet national demand, Belgium will need to import 20 TWh of renewable hydrogen and its derivatives by 2030, rising to between 200 TWh and 350 TWh by 2050. These imports are expected to come from other European countries and, predominantly, from third countries via the North Sea, southern corridors, and maritime routes. The government considers importing these molecules to be more cost-effective than domestic production. In parallel, Elia forecasts that Belgium's energy demand will exceed the capacity of its local renewable energy production. According to their estimates, local renewable generation will be able to meet, at most, the country's electricity demand by 2050. As a result, Belgium will continue to depend on energy imports.

According to the second pillar, the Belgian federal government seeks to reinforce the leadership of Belgian companies and research institutions engaged in hydrogen and related technologies, such as electrolysers. To this end, the government has allocated substantial funding to support further research, innovation, and pilot projects focused on hydrogen technologies. The government also aims to develop an electrolysis capacity of at least 150 MW by 2026. This relatively modest and less ambitious target, especially when compared to countries such as Germany and the Netherlands, which have announced multi-gigawatt-scale projects, is primarily due to Belgium's limited land availability, dense population, and constrained offshore space, all of which hinder the feasibility of large-scale green hydrogen production. Given these limitations and Elia's projections, it becomes evident that local renewable energy production remains essential to decarbonise key sectors such as electricity generation and transportation. Moreover, Belgium has relatively limited potential for underground hydrogen storage, which presents an additional challenge to ensuring security of supply.

Under the third pillar, the Belgian government aims to establish a robust market for hydrogen, and potentially its derivatives, to enable the optimal and secure transport of these molecules between import hubs, industrial clusters, and neighbouring countries. The strategy involves not only leveraging the existing pipeline infrastructure but also expanding it. In the first phase, the government plans to commission at least 100 to 160 km of new hydrogen pipelines by 2026. Additionally, by 2028, Belgium intends to interconnect its hydrogen transport network with those of Germany, France, and the Netherlands, thereby supporting the country's objective outlined in the first pillar.

The Belgian government considers efficient and extensive collaboration essential at all stages to realise the objectives of the first three pillars. Accordingly, under the fourth pillar, the government intends to strengthen cooperation with regional governments, hydrogen stakeholders, such as companies, research institutions, and universities active in hydrogen technologies, and other relevant actors, including European and international partners.

Currently, the annual hydrogen demand in Belgium is estimated at approximately 15 TWh, primarily for industrial applications [43]. The government projects that demand for hydrogen and its derivatives will increase by a factor of 7 to 10, reaching between 125 and 200 TWh/year by 2050, compared to 15–20 TWh/year in 2020 and 20–30 TWh/year in 2030 [44]. Within the electricity grid, hydrogen is expected to serve as a complementary solution to batteries, storing surplus renewable electricity and discharging it during periods of scarcity. In this way, hydrogen will contribute to both downward and upward regulation of the power system, helping to address the intermittency of renewable energy sources. The electricity and hydrogen markets will ultimately determine the optimal balance between battery and hydrogen storage systems.

3.6 Discussion and Conclusions

This chapter reviewed the challenges faced by the electric power network as large-scale fossil fuel power plants are phased out and replaced by renewable-based units. In such a low-inertia power grid, maintaining system stability by balancing generation and demand becomes increasingly complex.

Within the electricity market, energy is traded among various key stakeholders, including generators, TSOs, DSOs, ISOs, market regulators, market operators, retailers, and consumers. These entities cooperate to ensure the efficient operation of the market and to satisfy energy demand. When deviations occur between scheduled and actual generation or consumption, ancillary services can be activated to restore balance. In the context of frequency control, three main reserve types are utilised: FCR, aFRR, and mFRR.

In terms of electrolysers, the most well-known types are alkaline, PEM, and SO electrolyser. While the SO electrolyser is still in the R&D stage, the alkaline electrolyser is the most mature technology, followed by the PEM type. To commercialise an electrolyser, there are several deciding factors which affect its widespread use. From a business perspective, the associated costs must be considered, including CapEx, OpEx, maintenance, and, where applicable, replacement expenditures. Another decisive factor is revenue, which can be maximised by improving the performance of the electrolyser, such as efficiency, dynamic response, and electricity consumption. Moreover, depend-

Table 3.1: Qualitative comparison of alkaline, PEM and SO electrolysers [8,41,45,46]

	Alkaline	PEM	Solid oxide
Maturity	Mature	Developed	Developing
Commercialised	Yes	Yes	No
Lifetime	Long	Medium	Short
Efficiency	Medium	Medium	High
Operating temperature	Low	Low	High
Operating pressure	Low	Low	High
Cost	Medium	High	High
Current density	Low	High	Medium
Partial load range	Low	High	High
Dynamic	Slow	Fast	Fast
Cold start time	Medium	Low	High
Overload capability	Medium	High	-
Catalyst	Non-noble	Noble	Non-noble
Output gas purity	Medium	High	High

Table 3.2: Quantitative comparison of Alkaline, PEM and SO electrolysers [47–50]

	Alkaline	PEM	Solid oxide
Current density [A/cm^2]	0.2–0.4	0.6–2.0	0.3–1.0
Operating pressure [bar]	≤ 30	≤ 30	≤ 30
Operating temperature [°C]	50–80	50–80	700–1000
Overload [% nominal load]	< 150	< 200	Not available yet
Stack lifetime [h]	< 90000	< 20000	< 40000
System lifetime [year]	20–30	10–20	Not available yet
Efficiency [%]	62–82	67–81	close to perfect
Cell voltage [V]	1.8–2.4	1.8–2.2	0.95–1.3
Partial load range [%]	20–40	0–10	Not available yet
Purity of hydrogen [%]	> 99.8	~ 99.999	~ 99.999
Electrolyte	KOH	Polymer Nafion	Yttria stabilised Zirconium
Charge carrier	OH	H	O
Cost [€/kW]	800–1500	1000–2100	> 2000
Cold start time [min]	15	< 15	> 60

ing on the application and operating environment, durability also affects the commercialisation potential.

A comparison of the qualitative and quantitative characteristics of the three electrolysers discussed above is presented in Table 3.1 and Table 3.2.

Electrolysers can support grid stability by participating in the ancillary services market. During periods of power surplus, electrolysers can absorb excess electricity, thereby reducing the risk of curtailment. However, to realise this potential, precise dynamic scheduling and fast, reliable control systems are essential. In periods of power deficit, electrolysers can reduce their power

consumption to help the power system.

As discussed in Chapter 2, the offshore framework is selected mainly due to the chosen case study for this thesis, i.e., Belgium, which has significant potential for integrating offshore wind energy into its power system, owing to its access to the North Sea.

In the following chapter, the PEM electrolyser technology, which is the chosen electrolyser type for this thesis, is explored in detail, and the corresponding model is developed.

Bibliography

[1] M. Ghaedi and R. Gholami, "Characterization and assessment of hydrogen leakage mechanisms in salt caverns," *Scientific reports*, vol. 15, no. 1, p. 185, 2025.

[2] B. Babu, "Self-discharge in rechargeable electrochemical energy storage devices," *Energy Storage Materials*, vol. 67, p. 103261, 2024.

[3] M. M. H. Bhuiyan and Z. Siddique, "Hydrogen as an alternative fuel: A comprehensive review of challenges and opportunities in production, storage, and transportation," *International Journal of Hydrogen Energy*, vol. 102, pp. 1026–1044, 2025.

[4] A. Odenweller and F. Ueckerdt, "The green hydrogen ambition and implementation gap," *Nature Energy*, vol. 10, no. 1, pp. 110–123, 2025.

[5] N. Huet, "Europe's energy crisis is boosting green hydrogen: Is it the future?." https://www.euronews.com/next/2022/11/24/europe-energy-crisis-is-boosting-green-hydrogen. Accessed: December 8, 2025.

[6] M. Rodríguez, "Hydrogen present and future. part 2." https://www.tecnicasreunidas.es/articulo/hydrogen-present-and-future-part-2/. Accessed: December 8, 2025.

[7] U.S. Department of Enegry, "Hydrogen production: Natural gas reforming." https://www.energy.gov/eere/fuelcells/hydrogen-production-natural-gas-reforming. Accessed: December 8, 2025.

[8] M. B. Syed, "Technologies for renewable hydrogen production," in *Bioenergy Resources and Technologies*, pp. 157–198, Elsevier, 2021.

[9] A. Midilli, H. Kucuk, M. E. Topal, U. Akbulut, and I. Dincer, "A comprehensive review on hydrogen production from coal gasification: Challenges and opportunities," *International Journal of Hydrogen Energy*, vol. 46, no. 50, pp. 25385–25412, 2021.

[10] J. Brauns and T. Turek, "Alkaline water electrolysis powered by renewable energy: A review," *Processes*, vol. 8, no. 2, p. 248, 2020.

[11] C. Ziems, D. Tannert, and H. J. Krautz, "Project presentation: Design and installation of advanced high pressure alkaline electrolyzer-prototypes," *Energy Procedia*, vol. 29, pp. 744–753, 2012.

[12] M. Schalenbach, G. Tjarks, M. Carmo, W. Lueke, M. Mueller, and D. Stolten, "Acidic or alkaline? towards a new perspective on the efficiency of water electrolysis," *Journal of The Electrochemical Society*, vol. 163, no. 11, p. F3197, 2016.

[13] R. Hancke, T. Holm, and Ø. Ulleberg, "The case for high-pressure PEM water electrolysis," *Energy Conversion and Management*, vol. 261, p. 115642, 2022.

[14] F. Scheepers, M. Stähler, A. Stähler, E. Rauls, M. Müller, M. Carmo, and W. Lehnert, "Temperature optimization for improving polymer electrolyte membrane-water electrolysis system efficiency," *Applied Energy*, vol. 283, p. 116270, 2021.

[15] B. Königshofer, M. Höber, G. Nusev, P. Boškoski, C. Hochenauer, and V. Subotić, "Accelerated degradation for solid oxide electrolysers: Analysis and prediction of performance for varying operating environments," *Journal of Power Sources*, vol. 523, p. 230982, 2022.

[16] D. Ernst, "Electricity market." https://damien-ernst.be/. Accessed: 11 December 2022.

[17] Elia group, *Adequacy and flexibility study for Belgium 2020-2030*. Elia, Brussels, Belgium, 2019.

[18] L. Mehigan, D. Al Kez, S. Collins, A. Foley, B. Ó'Gallachóir, and P. Deane, "Renewables in the European power system and the impact on system rotational inertia," *Energy*, vol. 203, p. 117776, 2020.

[19] U. Rudez and R. Mihalic, "Analysis of underfrequency load shedding using a frequency gradient," *IEEE Transactions on Power Delivery*, vol. 26, no. 2, pp. 565–575, 2009.

[20] ENTSO-E , "ENTSO-E expert panel initiates the investigation into the causes of Iberian blackout - 2025." https://www.entsoe.eu/news/2025/05/09/entso-e-expert-panel-initiates-the-investigation-into-the-causes-of-iberian-blackout/. Accessed: December 8, 2025.

[21] J. Van de Vyver, J. D. De Kooning, B. Meersman, L. Vandevelde, and T. L. Vandoorn, "Droop control as an alternative inertial response strategy for the synthetic inertia on wind turbines," *IEEE Transactions on Power Systems*, vol. 31, no. 2, pp. 1129–1138, 2015.

[22] A. E. Samani, A. D'Amicis, J. D. De Kooning, D. Bozalakov, P. Silva, and L. Vandevelde, "Grid balancing with a large-scale electrolyser providing primary reserve," *IET Renewable Power Generation*, vol. 14, no. 16, pp. 3070–3078, 2020.

[23] A. Dadkhah, D. Bozalakov, J. D. De Kooning, and L. Vandevelde, "On the optimal planning of a hydrogen refuelling station participating in the electricity and balancing markets," *International Journal of Hydrogen Energy*, vol. 46, no. 2, pp. 1488–1500, 2021.

[24] L. Collins, "Why hydrogen-fired power plants will play a major role in the energy transition." https://www.rechargenews.com/energy-transition/why-hydrogen-fired-power-plants-will-play-a-major-role-in-the-energy-transition/2-1-1045768, Jul 2021.

[25] Siemens Energy, "Hydrogen power plants." https://www.siemens-energy.com/global/en/home/products-services/product/hydrogen-power-plants.html. Accessed: 18 March 2023.

[26] N. Z. Shilling, "Emissions and performance implications of hydrogen fuel in heavy duty gas turbines," *Clean Air Task Force*, 2023.

[27] Y. Wang, D. Y. Leung, J. Xuan, and H. Wang, "A review on unitized regenerative fuel cell technologies, part A: Unitized regenerative proton exchange membrane fuel cells," *Renewable and Sustainable Energy Reviews*, vol. 65, pp. 961–977, 2016.

[28] A. Z. Weber, M. M. Mench, J. P. Meyers, P. N. Ross, J. T. Gostick, and Q. Liu, "Redox flow batteries: a review," *Journal of Applied Electrochemistry*, vol. 41, no. 10, pp. 1137–1164, 2011.

[29] A. Lim, J. S. Lee, S. Lee, S. Y. Lee, H.-j. Kim, S. J. Yoo, J. H. Jang, Y.-E. Sung, and H. S. Park, "Polymer electrolyte membrane unitized regenerative fuel cells: Operational considerations for achieving high round trip efficiency at low catalyst loading," *Applied Catalysis B: Environmental*, vol. 297, p. 120458, 2021.

[30] J. N. Qiao, H. Guo, H. Chen, and F. Ye, "Improving round-trip energy efficiency of a unitized regenerative fuel cell by adopting staircase flow channel and counter flow configuration," *Energy Conversion and Management*, vol. 271, p. 116345, 2022.

[31] D. Qiu, L. Peng, X. Lai, *et al.*, "kW-grade unitized regenerative fuel cell stack design for high round-trip efficiencies," *Energy Conversion and Management*, vol. 270, p. 116277, 2022.

[32] H. Tebibel, "Battery energy storage system for enhancing the electrolyzer capacity factor in small-scale WindtH_2 system with a smoothing control strategy: Constrained multi-objective Pareto optimization and case study in Algeria," *Journal of Energy Storage*, vol. 52, p. 105017, 2022.

[33] A. M. Raventos, G. Kluivers, J. Haverkort, W. De Jong, F. M. Mulder, and R. Kortlever, "Modeling the performance of an integrated battery and electrolyzer system," *Industrial & Engineering Chemistry Research*, vol. 60, no. 30, pp. 10988–10996, 2021.

[34] B. Jenkins, D. Squires, J. Barton, D. Strickland, K. Wijayantha, J. Carroll, J. Wilson, M. Brenton, and M. Thomson, "Techno-economic analysis of low carbon hydrogen production from offshore wind using battolyser technology," *Energies*, vol. 15, no. 16, p. 5796, 2022.

[35] A. Sodiq, Y. Abdullatif, B. Aissa, A. Ostovar, N. Nassar, M. El-Naas, and A. Amhamed, "A review on progress made in direct air capture of CO_2," *Environmental Technology & Innovation*, vol. 29, p. 102991, 2023.

[36] H. D. Willauer, F. DiMascio, D. R. Hardy, and F. W. Williams, "Feasibility of CO_2 extraction from seawater and simultaneous hydrogen gas generation using a novel and robust electrolytic cation exchange module based on continuous electrodeionization technology," *Industrial & Engineering Chemistry Research*, vol. 53, no. 31, pp. 12192–12200, 2014.

[37] S. Dresp, F. Dionigi, M. Klingenhof, and P. Strasser, "Direct electrolytic splitting of seawater: opportunities and challenges," *ACS Energy Letters*, vol. 4, no. 4, pp. 933–942, 2019.

[38] R. d'Amore Domenech, O. Santiago, and T. J. Leo, "Multicriteria analysis of seawater electrolysis technologies for green hydrogen production at sea," *Renewable and Sustainable Energy Reviews*, vol. 133, p. 110166, 2020.

[39] M. Khan, T. Al-Attas, S. Roy, M. M. Rahman, N. Ghaffour, V. Thangadurai, S. Larter, J. Hu, P. M. Ajayan, and M. G. Kibria, "Seawater electrolysis for hydrogen production: a solution looking for a problem?," *Energy & Environmental Science*, vol. 14, no. 9, pp. 4831–4839, 2021.

[40] B. Yodwong, D. Guilbert, M. Phattanasak, W. Kaewmanee, M. Hinaje, and G. Vitale, "Proton exchange membrane electrolyzer modeling for power electronics control: a short review," *Journal of Carbon Research*, vol. 6, no. 2, p. 29, 2020.

[41] S. S. Kumar and V. Himabindu, "Hydrogen production by PEM water electrolysis–a review," *Materials Science for Energy Technologies*, vol. 2, no. 3, pp. 442–454, 2019.

[42] Belgian federal Hydrogen Strategy — FPS Economy, "Belgian federal hydrogen strategy." https://economie.fgov.be/en/themes/energy/sources-and-carriers-energy/hydrogen/belgian-federal-hydrogen. Accessed: 12 December 2022.

[43] Deloitte, "The role of clean gas in a climate neutral Belgium." https://www2.deloitte.com/be/en/pages/energy-and-resources/articles/. Accessed: 12 December 2022.

[44] T. Brijs, A. Leuridan, J. Geerinck, and C. Brognaux, "A five-step plan towards growing the role of hydrogen in Belgium's economy." https://www.bcg.com/publications/2022/five-step-plan-towards-growing-role-of-hydrogen-in-belgiums-economy. Accessed: 15 December 2022.

[45] M. El-Shafie, S. Kambara, and Y. Hayakawa, "Hydrogen production technologies overview," *Hydrogen Knowledge Centre*, 2019.

[46] K. Kamlungsua, P. Su, and S. Chan, "Hydrogen generation using solid oxide electrolysis cells," *Fuel cells*, vol. 20, no. 6, pp. 644–649, 2020.

[47] Chemical Industry Digest, "Way forward to carbon-free electricity for e-mobility." https://chemindigest.com/way-forward-to-carbon-free-electricity-for-e-mobility/. Accessed: December 8, 2025.

[48] R. Bhandari, C. A. Trudewind, and P. Zapp, "Life cycle assessment of hydrogen production via electrolysis–a review," *Journal of Cleaner Production*, vol. 85, pp. 151–163, 2014.

[49] P. Frink, "Hydrogen energy storage study (technical report)," 2018.

[50] M. David, C. Ocampo-Martínez, and R. Sánchez-Peña, "Advances in alkaline water electrolyzers: A review," *Journal of Energy Storage*, vol. 23, pp. 392–403, 2019.

Chapter 4

Development of a Dynamic Mathematical Model for PEM Electrolyser

In this chapter, the model associated with the chosen electrolyser in this thesis, namely, the proton exchange membrane (PEM) electrolyser, is developed, and the corresponding modules, along with their governing equations, are presented. Additionally, to verify the model, it is validated against both static and dynamic experimental data.

4.1 Introduction

PEM electrolyser stands as a promising candidate for sustainable hydrogen production from renewable energy sources (RESs). Given the fluctuating nature of RESs, accurate modelling of the PEM electrolyser is crucial. Nonetheless, complex models of the PEM electrolyser demand substantial time and resource investments when integrating them into a large-scale power system. The majority of introduced models in the literature are either overly intricate or fail to effectively reproduce the dynamic behaviour of the PEM electrolyser. To this end, this chapter aims to develop a model that not only captures the dynamic response of the PEM electrolyser, crucial for conducting flexibility studies in the power system, but also avoids complexity for seamless integration into large-scale simulations without compromising accuracy.

The rest of this chapter is organised as follows: In Section 4.2, based on the literature, a comparison is made between the two mature electrolyser types (alkaline electrolyser and PEM electrolyser), and the relevant literature related to the chosen electrolyser model (PEM electrolyser) is reviewed. Section 4.3 is dedicated to a thorough modelling methodology of each simulated module.

This includes the anode, cathode, membrane, voltage, and thermal components. Section 4.4 presents the results obtained from the model under various operating conditions. Additionally, the results undergo validation against experimental data to ensure the accuracy of the model. To achieve this, a comparison is made between the static results of the model and those of the experimental data, followed by a similar comparison for the dynamic results. Finally, in Section 4.5, the obtained results are discussed, conclusions are drawn, and the overall direction of the subsequent chapter is defined.

4.2 Literature Review

As discussed in Chapter 3, the PEM electrolyser was selected for integration into the offshore hydrogen production system in this research.

In this context, there are ongoing endeavours in the literature to model the performance of the PEM electrolyser. These models can be divided into two major categories: circuit-based models, which are built upon electrical elements, and mathematical models, which are grounded in electrochemical principles. Concerning the first group, the authors in [1] have modelled a static-dynamic model of the PEM electrolyser using circuit elements. In this approach, two parallel RC branches are employed to represent the behaviour of the anode and cathode. The capacitors are used to mimic the capacitance behaviour of the cell, accounting for the specific time needed by the charges to travel inside the anode and cathode. While the resistor of the cathode solely models the heat loss, the resistor of the anode represents both the Gibbs energy and heat loss in the anode. Moreover, the model incorporates a constant voltage source and a series resistor to simulate the reversible voltage and membrane loss, respectively. Finally, using experimental tests and system identification techniques, the values of the circuit elements are determined. Nevertheless, the main drawback of the model is its limited applicability. That is, the adapted values for the circuit elements are only valid for the specific operation conditions, including input current, temperature and pressure, making the model less reliable when used under different operating conditions.

In order to improve the accuracy of the aforementioned model, the authors in [2] have proposed an adaptive algorithm in which the parameters of the circuit are calculated based on different electrical input currents. However, even with utilising the adaptive approach, it remains challenging to model the effects of other operating conditions, such as temperature and pressure.

As far as the second group is concerned, in [3], a mathematical model of the PEM electrolyser consisting of four compartments, namely the anode, cathode, membrane and voltage, was introduced and simulated in Matlab/Simulink. The model is created based on the conservation of the mole balance of associated

substances at the anode and cathode. Regarding the membrane, electro-osmosis and diffusion are taken into account as the driving forces for water mass transfer through the membrane. This approach enables the calculation of the partial pressure of all substances at the anode and cathode, which is later used for computing the reversible cell voltage.

The same concept of modelling was followed in [4] and [5]. However, as opposed to what is claimed in the mentioned articles, the models replicate the static response of the PEM electrolyser and do not account for its dynamic behaviour. This is confirmed by [6] and does stem from the fact that the capacitance behaviour of the PEM electrolyser is not modelled in any of the compartments. Thus, the close relationship between transport and electricity flow via Faraday's law yields a static response.

Following these articles, the authors in [7] have incorporated balance of plants (BoP) components, namely water pump, cooling fan, storage tank, water tank, power supply, control units and sensors to the same electrolyser model. Similar to its predecessors, this model solely simulates the static response of the PEM electrolyser.

A detailed static model has been presented and validated in [6]. In this article, mechanisms and phenomena that are generally neglected in other articles have been taken into account. In the membrane, in addition to the electro-osmosis and diffusion mechanisms, the water flow from the cathode to the anode due to the pressure gradient is considered. Within the voltage ancillary, the concentration overvoltage is addressed. Meanwhile, in the ohmic overvoltage sub-module, the model goes beyond the commonly considered membrane resistance, taking into account the resistances of the bipolar plates and electrodes in a detailed manner. Nevertheless, the values of the mentioned parameters are generally insignificant when contrasted with other associated factors, and do not have a notable impact on the accuracy of the model [7, 8].

Although not validated against the experimental data, the study conducted in [9] explored the dynamic behaviour of a high-pressure PEM electrolyser. The investigation involved considering the non-ideal behaviour of hydrogen and incorporating the unsteady state mass balance equation of substances at the anode and cathode. Additionally, the energy balance equations of the anode, cathode and membrane electrolyte assembly (MEA) are included. In this article, a one-dimensional dynamic model of the PEM electrolyser is presented where physio-electrochemical phenomena such as water flow through the membrane via electro-osmotic drag, diffusion and permeation are considered. Furthermore, the gas permeation through the membrane, e.g. hydrogen, gas volume variations in the anode and cathode channels, gas compressibility, and water vaporisation are taken into account. The model allows for characterising gas purity at the cell/stack output. Yet, as admitted by the authors, assumptions such as similar oxygen and hydrogen concentrations on the membrane surface

reduce the accuracy of the model.

None of the previously mentioned models has considered the thermal characteristics of the PEM electrolyser, which is of paramount importance when it comes to assessing its dynamic response. However, several models in the literature have taken this into consideration.

The authors in [10] modelled a PEM electrolyser consisting of a steady-state voltage module as well as a linear dynamic thermal model. In this article, using an identification approach, the electrical and thermal parameters of the model are determined. The main purpose of the article is to develop monitoring algorithms. The authors in [8] have modelled the voltage ancillary beside a thermal module which is based on the lumped thermal capacitance.

In [11], a thermal module consisting of the heat exchange between the PEM electrolyser and the surrounding area, the sum of entropic flows of both heat sources and sinks, water tank thermal energy accumulation, and heat loss via conduction is introduced. Thereafter, the model is validated experimentally.

However, none of these models have taken into account the accurate models of the anode, cathode or membrane compartments, which are of use as the partial pressure of the substances at the anode and cathode are used in the voltage calculations. Moreover, this prevents the monitoring of partial pressures at the anode and cathode, the water flow through the membrane, which affects the performance of the electrolyser and restricts simulating the electrolyser behaviour at the non-similar anode and cathode pressures.

Generally, the literature faces a scarcity of a fast and precise model of the PEM electrolyser, which can effectively replicate the static response of the electrolyser as well as its dynamic behaviour. In this chapter, a newly developed model of the PEM electrolyser is presented. This model distinguishes itself from prior literature models by incorporating detailed mathematical modules not only for the anode, cathode, membrane and voltage but also for the thermal compartment. The deliberate simplification, excluding non-essential mechanisms in each module, ensures smooth integration of the model into large-scale simulations. This is of significant importance for electrical engineers engaged in flexibility studies, as complex elements like generators and transformers are already part of power system models. Notably, unlike some of the referenced articles such as [3–5, 7], the model accurately replicates the genuine dynamic response of the PEM electrolyser, rather than solely its static behaviour. Moreover, the precision of the model is validated against experimental data in both static and dynamic operation modes. By following the outlined steps in this chapter, researchers can simply simulate a fast and reliable model of the PEM electrolyser. Lastly, with minor adjustments, this model can simulate the dynamic and static response of the alkaline electrolyser as well.

As mentioned earlier, the anode, cathode, membrane, and voltage modules are important because they enable the simulation of the electrolyser's behaviour

under various operating pressures. This further helps to calculate the partial pressures of the substances at the electrodes, impacting the deviation of the reversible cell voltage from its standard value, thereby the calculations of efficiency and cooling requirements of the electrolyser. The significance of the thermal module lies in enabling the model to mimic the dynamic behaviour of the PEM electrolyser which becomes of substantial importance when coupled with the RESs. Consequently, the derived results from the model align more closely with the actual power consumption and produced hydrogen quantity by the electrolyser. This is intriguing when it comes to conducting flexibility studies on the PEM electrolyser as the evaluation of ancillary services like FCR or automatic frequency restoration reserve (aFRR) provision can be assessed more precisely [12–14].

Besides, as the feed water is an input to the model, it is capable of accounting for the dynamic changes in the feed water system, an influential factor when considering the employment of non-pure water like seawater. By coupling the electrolyser with the seawater desalination system, e.g. seawater reverse osmosis desalination system, the dynamic behaviour of the entire system can be explored. Furthermore, the model is able to effectively capture the dynamic changes in the produced hydrogen. This facilitates the assessment of producing other green molecules, such as methanol, while investigating the impact of the electrolyser on the subsequent systems. Finally, while retaining a high level of accuracy, it has been tried to ensure the model remains simple so that it can be easily integrated into the power system simulations smoothly and limit simulation time. This simplicity is particularly appealing for large-scale and long-term simulations. In Table 4.1, the main characteristics of the developed model and existing models in the literature are highlighted.

It should be noted that MATLAB already includes an electrolyser block that represents the electrolyser as an electrical load. Nonetheless, the electrolyser model provided by MATLAB/Simulink is primarily designed as a general-purpose component for system-level studies. Most of the underlying electrochemical equations in these Simscape blocks are not directly accessible, which limits the ability to examine the governing relations. As a result, although the MATLAB implementation is indeed highly practical for preliminary design studies, microgrid simulations or controller development, it remains a generic representation of a PEM electrolyser rather than a fully physics-based formulation.

In contrast, the PEM electrolyser model developed in this thesis is explicitly equation-based and fully transparent. All voltage contributions, such as the Nernst voltage, activation overvoltage and ohmic overvoltage, which will be elaborated in detail in the subsequent sections, are modelled separately. This enables direct interpretation of their physical behaviour and allows analysis of how each mechanism responds during electrolyser operation. Fur-

thermore, although concentration overvoltage, for instance, is neglected in this work because it is known to be negligible within the typical operating range of PEM electrolysers, it can be incorporated straightforwardly into the model when relevant. The same applies to other physical mechanisms. For example, hydraulic-pressure-driven water transport through the membrane or heat transfer between the electrolyser and the surrounding environment can be included when their effects are known to be significant. In this thesis, these terms are omitted because their influence is negligible under the operating conditions studied, but the modular structure of the model allows such phenomena to be added without requiring any redesign of the mathematical framework.

In a nutshell, this chapter pursues three main goals: 1) Developing a static-dynamic model that behaves nearly similar to a real-life PEM electrolyser, enabling flexibility studies, integrating it as an asset in microgrids providing flexibility, power systems, etc.; 2) Keeping the model as simple as possible to facilitate its utilisation in extensive and long-term studies; 3) Achieving a trade-off between accuracy and simplicity in the model.

Table 4.1: Comparison between the existing literature and the proposed model
(L: Low, BA: Below Average, A: Average, AA: Above Average, H: High, NA: Not Applicable)

Reference	Developed model	[6]	[1]	[2]	[3]	[4]	[5]	[7]	[8]	[9]	[10]	[11]
Anode/cathode module	✓	✓	✗	✗	✓	✓	✓	✓	✗	✓	✗	✗
Membrane module	✓	✓	✗	✗	✓	✓	✓	✓	✗	✓	✗	✓
Thermal module	✓	✗	✗	✗	✗	✗	✗	✗	✓	✓	✓	✓
Voltage module	✓	✓	✓	✓	✓	✓	✓	✓	✓	✓	✓	✓
Dynamic	✓	✗	✓	✓	✗	✗	✗	✗	✓	✓	✓	✓
Accuracy in operation range	H	AA	L	BA	A	A	A	A	AA	H	H	A
Complexity	A	AA	L	BA	A	BA	A	A	A	H	AA	A
Static validation (Polarisation curve)	✓	✓	✗	✗	✗	✓	✓	✓	✗	✗	✓	✓
Dynamic validation	✓	NA	✓	✓	NA	NA	NA	NA	✓	✗	✓	✓

4.3 Model Development

As mentioned in Chapter 3, in the PEM electrolyser, water is fed into the anode, and due to the applied current in the oxidation reaction, decomposes to hydrogen protons, electrons and oxygen, as shown in (4.1). Later, while the electrons migrate through the electric circuit towards the cathode, the produced positive ions travel through the proton-conductive membrane and reach the cathode as well to participate in the reduction reaction, expressed in (4.2). As a result of this reaction, hydrogen is produced at the cathode. The overall reaction, known as redox, is shown in (4.3).

$$2H_2O \rightarrow 4H^+ + 4e^- + O_2 \tag{4.1}$$

$$4H^+ + 4e^- \rightarrow 2H_2 \tag{4.2}$$

$$H_2O \rightarrow H_2 + \frac{1}{2}O_2 \tag{4.3}$$

The developed model is composed of five various compartments, namely the anode, cathode, membrane, voltage and thermal. The anode and cathode modules are modelled based on the molar balance of relevant substances, specifically water and oxygen for the anode, in addition to water and hydrogen for the cathode. In the membrane compartment, the mechanisms via which the water traverses the membrane are modelled, i.e., electro-osmotic drag and diffusion. The voltage ancillary incorporates the reversible voltage calculations along with the ohmic overvoltage of the membrane and activation overvoltages of the anode and cathode subsystems. Lastly, within the thermal module, the heat sources and sinks, as well as the injected water into the electrolyser for cooling purposes, are simulated.

A general overview of the interactions between the modules, simulated in MATLAB/Simulink, is shown in Fig. 4.1. In the forthcoming subsections, an exhaustive elaboration of each module is presented.

4.3.1 Anode Module

Based on (4.1), the molar balances of oxygen and water are considered in the anode module. The oxygen and water molar flow rate equations at the anode can be expressed as follows:

$$\dot{N}_{H_2O_{an}} = \dot{N}_{H_2O_{an,in}} - \dot{N}_{H_2O_{an,cons}} - \dot{N}_{H_2O_{mem}} - \dot{N}_{H_2O_{an,out}} \tag{4.4}$$

$$\dot{N}_{O_{2an}} = \dot{N}_{O_{2an,in}} + \dot{N}_{O_{2an,gen}} - \dot{N}_{O_{2an,out}} \tag{4.5}$$

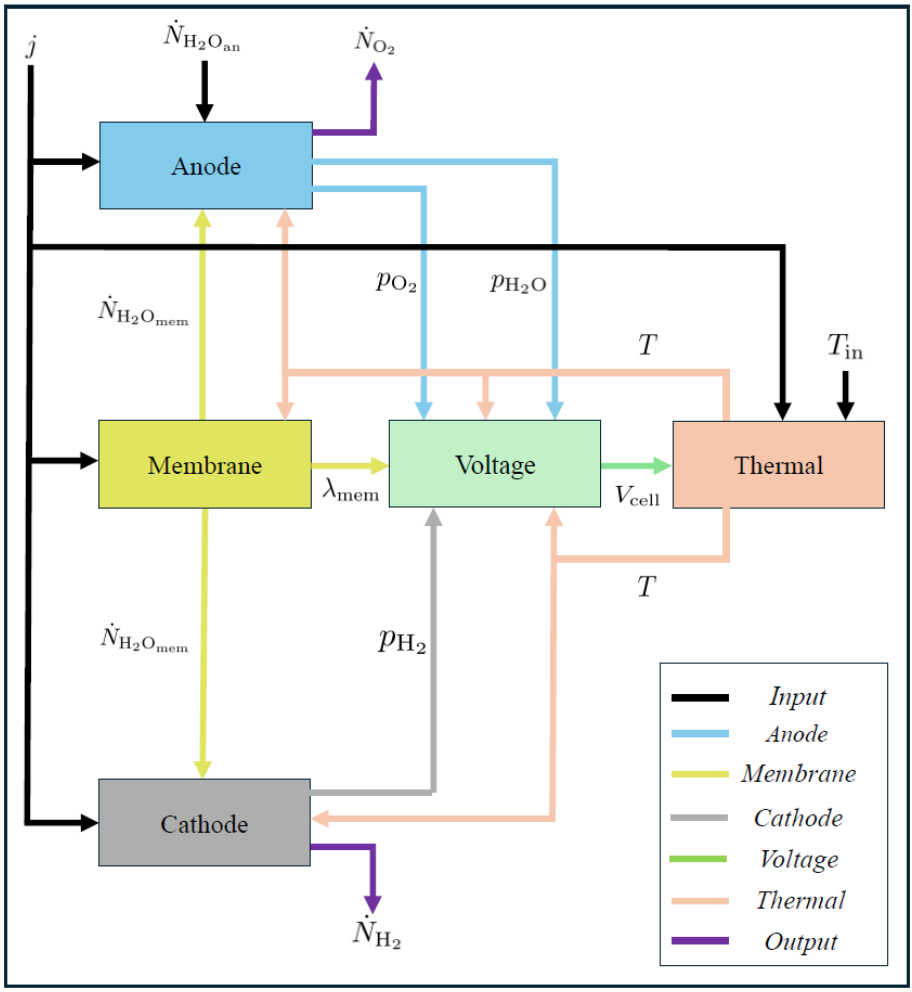

Figure 4.1: Overview of the developed model in Simulink

where $\dot{N}_{H_2O_{an,in}}$ and $\dot{N}_{H_2O_{an,out}}$ are the anode inlet and outlet molar flow rate of water, $\dot{N}_{O_{2an,in}}$ and $\dot{N}_{O_{2an,out}}$ denote the anode inlet and outlet molar flow rate of oxygen, $\dot{N}_{H_2O_{an,cons}}$ is the molar flow rate of the consumed water at the anode, $\dot{N}_{H_2O_{mem}}$ represents the molar flow rate of water migrated from anode to the cathode through the membrane, and $\dot{N}_{O_{2an,gen}}$ stands for the molar flow rate of the generated oxygen at the anode.

As mentioned earlier, the fluctuations of the input water, if any, can be incorporated into the model using (4.4). It is essential to note that in this model, the anode inlet molar flow rate of oxygen is assumed to be zero, and its inclusion is merely for the sake of having a complete molar balance equation.

According to (4.1), (4.2) and Faraday's first law of electrolysis, the molar

flow rate of the consumed water and generated oxygen at the anode of the PEM electrolyser are given as follows:

$$\dot{N}_{H_2O_{an,cons}} = \frac{nI}{2F} \tag{4.6}$$

$$\dot{N}_{O_{2an,gen}} = \frac{nI}{4F} \tag{4.7}$$

where n is the number of cells, I is the applied current and F is the Faraday constant.

By substituting (4.6) into (4.4), and (4.7) into (4.5), and solving the algebraic loops, the partial pressures of water and oxygen at the anode can be derived via the ideal gas law as follows:

$$p_{H_2O_{an}} = \frac{N_{H_2O_{an}} R_u T}{v_{an}} \tag{4.8}$$

$$p_{O_{2an}} = \frac{N_{O_{2an}} R_u T}{v_{an}} \tag{4.9}$$

where $N_{H_2O_{an}}$ and $N_{O_{2an}}$ are the number of moles of water and oxygen at the anode, respectively, R_u is the universal gas constant, T represents the operating temperature of the electrolyser, and v_{an} denotes the anode volume. It is worth noting that, given the typical operating conditions of the PEM electrolyser, the ideal gas law has been used, as the compressibility factor for both the relevant substances under these conditions is approximately equal to one [15].

The pressure at the anode is equal to the total partial pressures of water and oxygen, described as:

$$P_{an} = p_{H_2O_{an}} + p_{O_{2an}} \tag{4.10}$$

Then, the molar fraction of each substance at the anode can be calculated as follows:

$$X_{H_2O_{an}} = \frac{p_{H_2O_{an}}}{P_{an}} \tag{4.11}$$

$$X_{O_{2an}} = \frac{p_{O_{2an}}}{P_{an}} \tag{4.12}$$

4.3.2 Cathode Module

In the cathode compartment, where hydrogen is evolved, a similar approach to the anode module is followed, with hydrogen replacing oxygen. Thus, the molar flow rates of water and hydrogen at the cathode are represented as follows:

$$\dot{N}_{H_2O_{ca}} = \dot{N}_{H_2O_{ca,in}} + \dot{N}_{H_2O_{mem}} - \dot{N}_{H_2O_{ca,out}} \tag{4.13}$$

$$\dot{N}_{\mathrm{H_{2ca}}} = \dot{N}_{\mathrm{H_{2ca,in}}} + \dot{N}_{\mathrm{H_{2ca,gen}}} - \dot{N}_{\mathrm{H_{2ca,out}}} \tag{4.14}$$

In (4.13) and (4.14), $\dot{N}_{\mathrm{H_2O_{ca,in}}}$ and $\dot{N}_{\mathrm{H_2O_{ca,out}}}$ stand for the cathode inlet and outlet molar flow rate of water, subsequently, $\dot{N}_{\mathrm{H_{2ca,in}}}$ and $\dot{N}_{\mathrm{H_{2ca,out}}}$ are the inlet and outlet molar flow rate of hydrogen at the cathode, respectively, and $\dot{N}_{\mathrm{H_{2ca,gen}}}$ represents the molar rate of the generated hydrogen at the cathode.

In this model, both the inlet hydrogen and water flow rates to the cathode are set to zero.

Considering the intermediate reactions taking place in the electrolyser and Faraday's first law of electrolysis, the molar flow rate of the generated hydrogen at the cathode is described as follows:

$$\dot{N}_{\mathrm{H_{2ca,gen}}} = \frac{nI}{2F} \tag{4.15}$$

By substituting (4.15) into (4.14), the partial pressures of water and hydrogen at the cathode can be obtained using the ideal gas law, expressed as:

$$p_{\mathrm{H_2O_{ca}}} = \frac{N_{\mathrm{H_2O_{ca}}} R_u T}{v_{\mathrm{ca}}} \tag{4.16}$$

$$p_{\mathrm{H_{2ca}}} = \frac{N_{\mathrm{H_{2ca}}} R_u T}{v_{\mathrm{ca}}} \tag{4.17}$$

where $N_{\mathrm{H_2O_{ca}}}$ and $N_{\mathrm{H_{2ca}}}$ are the number of moles of water and hydrogen at the cathode, subsequently and v_{ca} is the cathode volume.

The pressure at the cathode is equal to the total partial pressures of water and hydrogen, given as:

$$P_{\mathrm{ca}} = p_{\mathrm{H_2O_{ca}}} + p_{\mathrm{H_{2ca}}} \tag{4.18}$$

Using the partial pressures of the associated substances and the total pressure of the cathode, the molar fractions of water and hydrogen at the cathode can be given as:

$$X_{\mathrm{H_2O_{ca}}} = \frac{p_{\mathrm{H_2O_{ca}}}}{P_{\mathrm{ca}}} \tag{4.19}$$

$$X_{\mathrm{H_{2ca}}} = \frac{p_{\mathrm{H_{2ca}}}}{P_{\mathrm{ca}}} \tag{4.20}$$

4.3.3 Membrane Module

When the water is introduced into the anode of the PEM electrolyser, a substantial portion of it undergoes the oxygen evolution reaction, leading to the generation of protons and oxygen. However, a part of the water passes through the membrane, which influences the performance of the electrolyser. Generally, three mechanisms cause the passage of water through the membrane, namely electro-osmotic drag, diffusion and hydraulic pressure effect. While the first two mechanisms result in the water flow from the anode to the cathode, the hydraulic pressure effect yields water passage in the opposite direction. As a result, the net molar flow rate of water through the membrane is given as follows:

$$\dot{N}_{\mathrm{H_2O_{mem}}} = \dot{N}_{\mathrm{H_2O_{mem,eod}}} + \dot{N}_{\mathrm{H_2O_{mem,diff}}} - \dot{N}_{\mathrm{H_2O_{mem,hp}}} \tag{4.21}$$

where $\dot{N}_{\mathrm{H_2O_{mem,eod}}}$, $\dot{N}_{\mathrm{H_2O_{mem,diff}}}$ and $\dot{N}_{\mathrm{H_2O_{mem,hp}}}$ denote the water passage through the membrane due to the electro-osmotic drag, diffusion and hydraulic pressure effect, respectively.

In [9], it is shown that the electro-osmotic drag is the dominant mechanism in the water transport through the membrane. Commonly, electro-osmotic drag and diffusion are taken into account in the models, given that the influence of hydraulic pressure effect is negligible compared to them [3, 7].

As protons traverse the proton-conducting membrane, they drag water molecules with them, a phenomenon known as electro-osmotic drag. This process is quantified using the dimensionless electro-osmotic drag coefficient, denoted as n_{d}, which represents the number of water molecules per proton travelling from the anode to the cathode (mol[H_2O]/mol[H^+]). The molar flow rate of water through the membrane due to the electro-osmotic drag can be described as follows [6]:

$$\dot{N}_{\mathrm{H_2O_{mem,eod}}} = \frac{n_{\mathrm{d}} j A}{F} \tag{4.22}$$

where j is the current density and A represents the active area of the MEA.

There are several methods in the literature to deal with the electro-osmotic drag coefficient. Despite being influenced by factors such as water input pressure, cathode pressure, current density, and temperature, there seems to be no satisfactory definitive quantitative equation for determining this coefficient in the literature. For instance, n_{d} has been considered as a constant parameter, as in [16], a fitting parameter, as illustrated in [5, 6] or derived via empirical equations, as seen in [3, 7]. In this thesis, the empirical equation as a function of temperature, which is obtained in [17], has been utilised, where the authors propose a linear fit of n_{d} as a function of temperature, expressed in K, based on measured electro-osmotic drag for a solid polymer electrolyte, given as:

$$n_{\mathrm{d}} = -2.89556 + 0.016T \tag{4.23}$$

Stemming from the concentration gradient between the anode and cathode sides of the membrane, the flow rate of water through the membrane via diffusion can be derived by integrating Fick's law of diffusion between the anode and cathode sides of the membrane interfaces as follows:

$$\dot{N}_{\mathrm{H_2O_{mem,diff}}} = \frac{AD_{\mathrm{w}}}{\delta_{\mathrm{mem}}}(C_{\mathrm{H_2O_{mem,cat}}} - C_{\mathrm{H_2O_{mem,an}}}) \tag{4.24}$$

where D_{w} denotes the diffusion coefficient, δ_{mem} is the membrane thickness and $C_{\mathrm{H_2O_{mem,cat}}}$ and $C_{\mathrm{H_2O_{mem,an}}}$ are the water concentration at the cathode and anode side of the membrane, respectively. The diffusion coefficient can be expressed as follows [7]:

$$D_{\mathrm{w}} = D'_{\mathrm{w}} \exp\left[2416\left(\frac{1}{303} - \frac{1}{T}\right)\right] \tag{4.25}$$

$$D'_{\mathrm{w}} = \begin{cases} 10^{-10}\lambda_{\mathrm{mem}} & \lambda_{\mathrm{mem}} < 2 \\ 10^{-10}[1 + 2(\lambda_{\mathrm{mem}} - 2)] & 2 \leq \lambda_{\mathrm{mem}} < 3 \\ 10^{-10}[3 - 1.67(\lambda_{\mathrm{mem}} - 3)] & 3 \leq \lambda_{\mathrm{mem}} < 4.5 \\ 1.25 \times 10^{-10} & \lambda_{\mathrm{mem}} \geq 4.5 \end{cases} \tag{4.26}$$

where D'_{w} is the diffusion coefficient at the reference temperature and λ_{mem} represents the water content of the membrane. In this model, λ_{mem} is computed in the membrane module using the following temperature-dependent expression [18]:

$$\lambda_{\mathrm{mem}} = 0.08533\,T - 6.77632 \tag{4.27}$$

It is noteworthy that diffusion through a porous medium, as in the membrane of the PEM electrolyser, is principally a function of two mechanisms: molecular diffusion and Knudsen diffusion. When the mean free path of molecules is shorter than the pore size of the membrane, the molecules tend to collide more with each other rather than with the pore walls, leading to molecular diffusion being more prominent than Knudsen diffusion. Conversely, if the pore size is much smaller with respect to the mean free path of the species, the probability of molecules colliding with the walls of the pores is higher than with each other. In this case, Knudsen diffusion becomes the dominant term over molecular diffusion [6]. In this study, both mechanisms are taken into consideration.

The water concentration at the anode and cathode sides of the membrane can be expressed as a function of water concentration in the electrode channels, represented as:

$$C_{\mathrm{H_2O_{mem,an}}} = C_{\mathrm{H_2O_{ch,an}}} - \frac{\delta_{\mathrm{an}}\dot{n}_{\mathrm{H_2O,an}}}{D_{\mathrm{eff,an}}} \tag{4.28}$$

$$C_{H_2O_{mem,ca}} = C_{H_2O_{ch,ca}} - \frac{\delta_{ca}\dot{n}_{H_2O,ca}}{D_{eff,ca}} \tag{4.29}$$

where $C_{H_2O_{ch,an}}$ and $C_{H_2O_{ch,ca}}$ are the water concentrations in the anode and cathode channels, δ_{an} and δ_{ca} represent the anode and cathode electrode thicknesses, $\dot{n}_{H_2O,an}$ and $\dot{n}_{H_2O,ca}$ are the molar fluxes of water through the anode and cathode, and $D_{eff,an}$ and $D_{eff,ca}$ stand for the effective binary diffusion coefficient at the anode (O_2-H_2O) and cathode (H_2-H_2O), consecutively. The water concentrations in the anode and cathode channels can be expressed as follows:

$$C_{H_2O_{ch,an}} = C_{H_2O_{ch,ca}} = \frac{\rho_{H_2O_T}}{M_{H_2O}} \tag{4.30}$$

where ρ_{H_2O} is water density at temperature T and M_{H_2O} is molar mass of water.

Considering the second terms in (4.28) and (4.29), water molar fluxes at the anode and cathode can be written as follows:

$$\dot{n}_{H_2O,an} = \frac{\dot{N}_{H_2O_{mem}} + \dot{N}_{H_2O_{an,cons}}}{A} \tag{4.31}$$

$$\dot{n}_{H_2O,ca} = \frac{\dot{N}_{H_2O_{ca}}}{A} \tag{4.32}$$

The effective binary diffusion coefficients, i.e, $D_{eff,an}$ and $D_{eff,ca}$ as described in (4.28) and (4.29), respectively, are represented as follows:

$$\frac{1}{D_{eff,an}} = \frac{\epsilon}{\xi}\left(\frac{1}{D_{eff,O_2-H_2O}} + \frac{1}{D_{eff,H_2O-k}}\right) \tag{4.33}$$

$$\frac{1}{D_{eff,ca}} = \frac{\epsilon}{\xi}\left(\frac{1}{D_{eff,H_2-H_2O}} + \frac{1}{D_{eff,H_2O-k}}\right) \tag{4.34}$$

In (4.33) and (4.34), the terms D_{eff,O_2-H_2O} and D_{eff,H_2-H_2O}, referred to as the effective molecular diffusion coefficient for the O_2-H_2O and H_2-H_2O binary systems, reflect the molecular diffusion mechanism. On the other hand, D_{eff,H_2O-k}, known as the effective Knudsen diffusion coefficient for water, accounts for the Knudsen diffusion effect on the rate of water flow through the membrane. Additionally, ϵ is electrode porosity and ξ denotes tortuosity.

Regarding the effective Knudsen diffusion coefficient for water, introduced in (4.33) and (4.34), as the molecules collide with the walls of the pores frequently, the movement of molecules can be modelled using kinetic theory, described as:

$$D_{eff,H_2O-k} = \frac{4}{3} r \sqrt{\frac{8R_u T}{\pi M_{H_2O}}} \tag{4.35}$$

where r is the mean pore radius. On the other hand, to calculate D_{eff,O_2-H_2O} and D_{eff,H_2-H_2O}, Chapman-Enskog theory of the ideal gas has been utilised, giving:

$$D_{\text{eff},O_2-H_2O} = 0.00133 \frac{T^{3/2}}{P_{\text{an}} \Theta^2_{O_2-H_2O} \Omega_D} \sqrt{\frac{1}{M_{O_2}} + \frac{1}{M_{H_2O}}} \tag{4.36}$$

$$D_{\text{eff},H_2-H_2O} = 0.00133 \frac{T^{3/2}}{P_{\text{ca}} \Theta^2_{H_2-H_2O} \Omega_D} \sqrt{\frac{1}{M_{H_2}} + \frac{1}{M_{H_2O}}} \tag{4.37}$$

where $\Theta_{O_2-H_2O}$ and $\Theta_{H_2-H_2O}$ stand for the mean molecular radii of the associated substances, Ω is the dimensionless diffusion collision integral and M_{O_2} and M_{H_2} denote the molar weight of oxygen and hydrogen, respectively.

By calculating the remaining parameters, namely $\Theta_{O_2-H_2O}$, $\Theta_{H_2-H_2O}$ and Ω_D, the flow rate due to diffusion can be calculated. To start with, $\Theta_{O_2-H_2O}$ and $\Theta_{H_2-H_2O}$ can be written as:

$$\Theta_{O_2-H_2O} = \frac{\Theta_{O_2} + \Theta_{H_2O}}{2} \tag{4.38}$$

$$\Theta_{H_2-H_2O} = \frac{\Theta_{H_2} + \Theta_{H_2O}}{2} \tag{4.39}$$

On the other hand, Ω_D can be expressed analytically as follows:

$$\Omega_D = \frac{1.06}{\tau^{0.156}} + \frac{0.193}{\exp(0.76\tau)} + \frac{1.036}{\exp(1.53\tau)} + \frac{1.765}{3.894\tau} \tag{4.40}$$

where the dimensionless temperature τ can be represented as follows:

$$\tau_{O_2-H2O} = \frac{kT}{\varepsilon_{O_2-H_2O}} \tag{4.41}$$

$$\tau_{H_2-H2O} = \frac{kT}{\varepsilon_{H_2-H_2O}} \tag{4.42}$$

where $\varepsilon_{O_2-H_2O}$ and $\varepsilon_{H_2-H_2O}$, referred to as Lennard-Jones energies, are given as:

$$\varepsilon_{O_2-H_2O} = \sqrt{\varepsilon_{O_2} \varepsilon_{H_2O}} \tag{4.43}$$

$$\varepsilon_{H_2-H_2O} = \sqrt{\varepsilon_{H_2} \varepsilon_{H_2O}} \tag{4.44}$$

In summary, the process involves substituting (4.41)–(4.44) into (4.40) to derive diffusion collision integral. Thereafter, by inserting (4.38)–(4.40) into (4.36) and (4.37) the effective molecular diffusion coefficient for the O_2-H_2O and H_2-H_2O binary systems is computed. Next, (4.35)–(4.37) are substituted into (4.33) and (4.34) to obtain the effective binary diffusion coefficient at the anode and cathode, facilitating the determination of water concentration at both sides of the membrane expressed in (4.28) and (4.29). Finally, by substituting (4.23) into (4.22), as well as (4.28) and (4.29) into (4.24), the net molar flow rate of water through the membrane due to the molecular diffusion and Knudsen diffusion can be expressed as follows:

$$\dot{N}_{\mathrm{H_2O_{mem}}} = \frac{AD_{\mathrm{w}}}{\delta_{\mathrm{mem}}}\left[\left(\frac{\rho_{\mathrm{H_2O_T}}}{M_{\mathrm{H_2O}}} + \frac{\delta_{\mathrm{ca}}\dot{n}_{\mathrm{H_2O,ca}}}{D_{\mathrm{eff,ca}}}\right) - \left(\frac{\rho_{\mathrm{H_2O_T}}}{M_{\mathrm{H_2O}}} - \frac{\delta_{\mathrm{an}}\dot{n}_{\mathrm{H_2O,an}}}{D_{\mathrm{eff,an}}}\right)\right] + \frac{n_{\mathrm{d}}jA}{F} \tag{4.45}$$

4.3.4 Voltage Module

Ideally, a minimum voltage, which depends on the operating conditions of the electrolyser, such as pressure and temperature, is necessary to initiate the electrolysis process. This minimum voltage is referred to as the reversible or open-circuit voltage. However, in practice, a higher voltage than the reversible voltage must be applied to the electrolyser due to the several voltage drops occurring within the cell. Thus, the total cell voltage comprises the reversible voltage as well as the additional overvoltages, as shown below:

$$V_{\mathrm{cell}} = V_{\mathrm{rev}} + V_{\mathrm{act}} + V_{\mathrm{ohm}} + V_{\mathrm{con}} \tag{4.46}$$

where V_{rev} is the reversible cell voltage, V_{act} denotes the activation overvoltage, V_{ohm} stands for the ohmic overvoltage and V_{con} indicate the concentration or diffusion overvoltage. The concentration overvoltage happens in the case of the accumulation of oxygen and hydrogen in the catalyst layer of the anode and cathode. Nonetheless, it is insignificant if the flow field is suitable for gas removal [7]. Furthermore, for current densities less than 3 $\mathrm{A/cm^2}$, which is the case in this thesis, the activation and ohmic overvoltage are notably higher than concentration overvoltage [7, 19]. Thus, the latter is neglected in this model.

Reversible voltage

Using the Nernst equation, the reversible voltage can be expressed as follows [7]:

$$V_{\mathrm{rev}} = E_0 + \frac{R_u T}{2F}\ln\left(\frac{p_{\mathrm{H2}}\sqrt{p_{\mathrm{O2}}}}{p_{\mathrm{H_2O}}}\right) \tag{4.47}$$

where E_0 is the cell reversible voltage in standard conditions. It is worth mentioning that in (4.47), the second term expresses the deviation of the reversible voltage from its standard value at various operating conditions. The standard reversible voltage can be empirically described as follows [6]:

$$E_0 = 1.229 - 0.9 \times 10^{-3}(T - 298) \tag{4.48}$$

Activation overvoltage

As the name suggests, the activation overvoltage describes the required voltage to activate the electrochemical reactions taking place at the anode and cathode sides within the electrolyser. In other words, it accounts for the energy losses arising from the charge transfer kinetics in the electrolysis process. Thus, the activation overvoltage is composed of two terms, each representing the activation overvoltage at the anode and cathode. Commonly, the Butler-Volmer equation is used to express the activation overvoltages, given as [20]:

$$V_{\text{act}} = V_{\text{act,an}} + V_{\text{act,ca}} \tag{4.49}$$

$$V_{\text{act,an}} = \frac{R_u T}{\alpha_{\text{an}} F} \text{arcsinh}\left(\frac{j}{2j_{0,\text{an}}}\right) \tag{4.50}$$

$$V_{\text{act,ca}} = \frac{R_u T}{\alpha_{\text{ca}} F} \text{arcsinh}\left(\frac{j}{2j_{0,\text{ca}}}\right) \tag{4.51}$$

where α_{an} and α_{ca} are charge transfer coefficients, and $j_{0,\text{an}}$ and $j_{0,\text{ca}}$ stand for the exchange current density of the anode and cathode, consecutively. In the literature, a wide range of values is reported for the exchange current densities, and to a lesser extent, for the charge transfer coefficients. Hence, in this model, these four parameters are considered as fitting parameters. Apart from that, the exchange current density values are temperature-dependent which can be expressed as follows:

$$j_{0,\text{an}} = j_{0,\text{an-ref}} \exp\left[-\frac{E_{\text{act}}}{R_u}\left(\frac{1}{T} - \frac{1}{T_{\text{ref}}}\right)\right] \tag{4.52}$$

$$j_{0,\text{ca}} = j_{0,\text{ca-ref}} \exp\left[-\frac{E_{\text{act}}}{R_u}\left(\frac{1}{T} - \frac{1}{T_{\text{ref}}}\right)\right] \tag{4.53}$$

While E_{act} is the activation energy of the electrodes, $j_{0,\text{an-ref}}$ and $j_{0,\text{ca-ref}}$ indicate the reference exchange current densities of the anode and cathode, at the reference temperature T_{ref}, respectively.

Ohmic overvoltage

In the PEM electrolyser, there are several sources contributing to the ohmic overvoltage of the cell, which can be divided into two types: ionic overvoltage, arising from the membrane resistance, and electronic overvoltage, attributed to electronic components such as bipolar plates, electrodes, etc. Nonetheless, the conductivity of the membrane is significantly lower compared to that of electronic parts. Therefore, the ionic overvoltage dominates the ohmic overvoltage. In this model, similar to many other models, the electronic ohmic overvoltage is neglected to avoid unnecessary complexity [5, 21, 22].

Since the ionic conduction path in the PEM electrolyser is rather short and uniform, the ionic resistance can be simply modelled by assuming constant resistivity, given as [23]:

$$R_{\text{ohm},i} = \frac{\delta_{\text{mem}}}{\sigma_{\text{mem}}} \tag{4.54}$$

where σ_{mem} is the membrane conductivity in S.m^{-1}, which can be described as follows [24]:

$$\sigma_{\text{mem}} = \left(0.514\lambda_{\text{mem}} - 0.326\right) \cdot \exp\left[1268\left(\frac{1}{303} - \frac{1}{T}\right)\right] \tag{4.55}$$

Finally, the ohmic overvoltage can be derived using Ohm's law:

$$V_{\text{ohm}} = R_{\text{ohm,i}} \cdot j \tag{4.56}$$

4.3.5 Thermal Module

By implementing the equations that have been mentioned so far, the static response of the PEM electrolyser can be simulated. Although the response of the PEM electrolyser is fast, it is not instantaneous and exhibits a certain degree of dynamics. Hence, considering the dynamic behaviour of the PEM electrolyser is essential to enhance the accuracy of the model. To achieve this, the model incorporates a thermal module to account for the temperature variations of the PEM electrolyser during its operation. This enables the model to simulate the thermal inertia of the system, meaning how fast the electrolyser heats up or cools down in response to the changes in the operating condition. In the thermal module, the cell/stack temperature is considered to be homogeneous and is treated as a lumped thermal capacity, given as:

$$C_{l,\text{stack}} = \sum_{k} c_{p,k} \cdot v_k \cdot \rho_k \tag{4.57}$$

where $C_{l,\text{stack}}$ is the lumped thermal capacitance of the stack, $c_{p,k}$ represents the specific heat, v_k stands for volume and ρ_k indicates the density of the species

$k = \{H_2O, O_2, H_2\}$. Taking into account the inlet and outlet enthalpy flows in the electrolyser, the stack enthalpy balance equation can be written as [21]:

$$C_{l,\text{stack}}\frac{dT}{dt} = Q_{\text{gen}} + \sum_k \dot{M}_{\text{in},k} c_{p,k} T_{\text{in}} - Q_{\text{loss}} - Q_{\text{cool}} - \sum_k \dot{M}_{\text{out},k} c_{p,k} T_{\text{out}} \tag{4.58}$$

where Q_{gen} indicates the generated heat due to the electrical work done in the electrolyser, $\dot{M}_{\text{in},k}$ and $\dot{M}_{\text{out},k}$ are the inlet and outlet flow rate of the substance k, Q_{loss} is the heat exchanged between the electrolyser and environment, Q_{cool} stands for the heat extracted by the coolant, and T_{in} and T_{out} represent the inlet and outlet temperatures, successively. Despite T_{in} being a known parameter, specifically the temperature of the inlet water, T_{out} can be determined by solving (4.58). Furthermore, in this model, the operational temperature of the electrolyser is considered to be the average of the inlet and outlet temperatures.

The overall heat generated within the cell must be extracted to ensure proper operation. It is essential to maintain the cell/stack temperature below a specific threshold, typically 80–90 °C, which is primarily determined by the thermal stability of the perfluoro-sulfonic acid (PFSA) materials used as polymer electrolytes in the electrolyser. In addition, avoiding temperature gradients within the cell is crucial, as such gradients not only accelerate ageing and degradation but also lead to non-homogeneous cell loading, thereby affecting the overall performance of the electrolyser [25].

Among the cooling methods utilised for the electrolyser, using an excess flow of water for cooling purposes is selected in this model. This choice is made due to the several advantages offered by water as a coolant, such as the efficient heat transfer between the flowing water and the electrolyser. To effectively determine the required amount of water needed for the cooling, the inlet and outlet temperature difference of the electrolyser, denoted as ΔT, is considered. The aim is to keep ΔT less than 10 °C to avoid large temperature gradients within the cell due to the mentioned undesired effects. To this end, by introducing the parameter Λ_{H_2O}, which is the ratio of the actual water flow through the electrolyser for every mole of water used for the electrolysis process, the required amount of water can be related to the temperature difference in the cell.

The inlet flows in (4.58) can be expressed as [26]:

$$\dot{M}_{\text{in},H_2O,\text{an}} = (1 + \Lambda_{H_2O}) M_{H_2O} \frac{I}{2F} \tag{4.59}$$

$$\dot{M}_{\text{in},H_2O,\text{ca}} = \Lambda_{H_2O} M_{H_2O} \frac{I}{2F} \tag{4.60}$$

Similarly, the outlet flows can be represented as follows:

$$\dot{M}_{\mathrm{out,H_2O,an}} = \dot{M}_{\mathrm{out,H_2O,ca}} = \Lambda_{\mathrm{H_2O}} M_{\mathrm{H_2O}} \frac{I}{2F} \tag{4.61}$$

$$\dot{M}_{\mathrm{out,O_2,an}} = M_{\mathrm{O_2}} \frac{I}{4F} \tag{4.62}$$

$$\dot{M}_{\mathrm{out,H_2,ca}} = M_{\mathrm{H_2}} \frac{I}{2F} \tag{4.63}$$

The heat produced due to the work done in the electrolyser can be expressed as follows:

$$Q_{\mathrm{gen}} = \left(V_{\mathrm{cell}} - \frac{\Delta H}{2F}\right) I \tag{4.64}$$

where ΔH is the total reaction enthalpy, which can be described as follows for the electrolysis process [27]:

$$\Delta H(T, p) = \Delta H_{\mathrm{H_2}} + \frac{1}{2}\Delta H_{\mathrm{O_2}} - \Delta H_{\mathrm{H_2O}} \tag{4.65}$$

In (4.65), the enthalpy of each substance can be calculated as follows:

$$\widehat{\Delta H_k} = \widehat{\Delta H_k^0} + c'_{\mathrm{p}}(T - T_0) \tag{4.66}$$

where c'_{p} is the specific heat capacity and $\widehat{\Delta H_k^0}$ is the standard enthalpy of the substance k at the pressure and temperature of P_0 and T_0, respectively.

The heat transfer between the electrolyser and the environment, in the absence of any insulation, can be expressed as follows:

$$Q_{\mathrm{loss}} = hA_{\mathrm{st}}(T - T_{\mathrm{amb}}) \tag{4.67}$$

where h is the heat transfer coefficient, A_{st} represents the outside surface area of the stack and T_{amb} indicates the ambient temperature.

In general, compared to the term Q_{loss}, the other three terms on the right-hand side of (4.58) have a more pronounced impact on the cell temperature. Additionally, as water is chosen to be the coolant of the electrolyser, and is present in a significantly higher quantity compared to oxygen and hydrogen in the outlet flows, its impact on the cooling of the electrolyser is substantially greater. Thus, neglecting the mentioned terms and modifying (4.58), $\Lambda_{\mathrm{H_2O}}$ can be expressed in terms of the operating cell voltage and desired ΔT as follows:

$$\Lambda_{\mathrm{H_2O}} = \frac{F}{M_{\mathrm{H_2O}} \cdot c_{p,\mathrm{H_2O}} \cdot \Delta T}\left(V_{\mathrm{cell}} - \frac{\Delta H}{2F}\right) \tag{4.68}$$

For various operating cell voltages, the required number of moles of water for each mole of the electrolysed water can be depicted, shown in Fig. 4.2. As

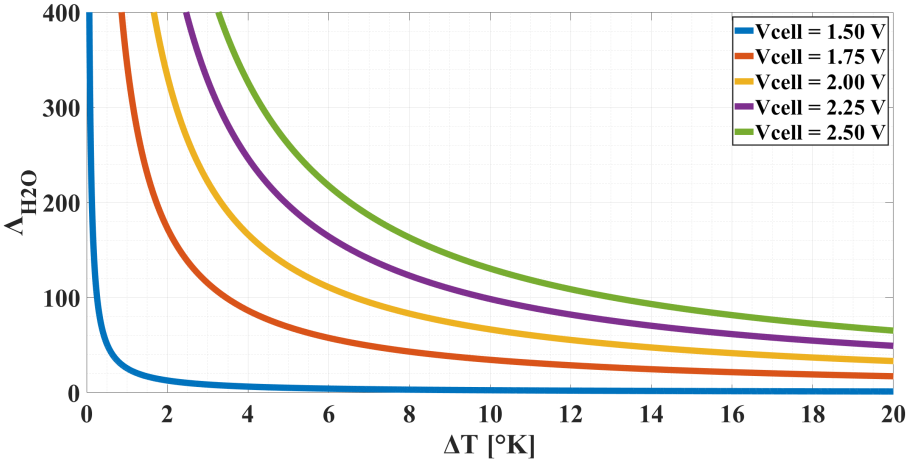

Figure 4.2: The required number of water moles for various operating cell voltages as a function of ΔT

can be seen, the curves illustrate that at very low ΔT values, the electrolyser requires a substantially larger amount of water for cooling. This introduces a clear design trade-off. As stated earlier, the design aim is to keep ΔT below 10 °C and choosing very low values of ΔT results in a significantly higher cooling-water demand. The choice of ΔT therefore represents a balance between cooling-water requirements and electrolyser performance.

4.4 Results

In this section, the developed model is validated using the set of experimental data reported in [28] and [2]. The choice of these references for validation is based on the availability of the experimental data under a range of operating conditions. Initially, the static response of the model is validated at various constant temperatures, without considering the thermal module. The validation is carried out employing the static polarisation curves from [28]. Subsequently, the dynamic response of the model, taking into account the variations in the cell temperature, is validated using the results reported in [2].

4.4.1 Static Model Validation

The specifications of the PEM electrolyser utilised for the validation, along with the parameters used for the simulation, are presented in Table 4.2.

Apart from the fixed model parameters summarised in Table 4.2, the aforementioned fitting parameters were allowed to vary within their feasible region to ensure that the model aligns with the experimental results as closely as

Table 4.2: Specifications of the PEM electrolyser used for the static validation [28]

Parameter	Value	Unit
Anode material	Pt-Ir	-
Cathode material	Pt	-
Membrane	Nafion 1110	-
A	100	cm^2
F	96485.33	A.s/mol
M_{H_2}	0.002	kg/mol
M_{H_2O}	0.018	kg/mol
M_{O_2}	0.032	kg/mol
n	1	-
P_{an-ca}	1	bar
R_u	8.31	J/K.mol
T_{in}	80	°C
δ_{an-ca}	0.08	mm
δ_{mem}	0.254	mm
ϵ	0.3	-
ε_{H_2}/k	59.7	K
ε_{H_2O}/k	809.1	K
ε_{O_2}/k	106.7	K
Θ_{H_2}	2.827	Å
Θ_{H_2O}	2.641	Å
Θ_{O_2}	3.467	Å
ξ	4	-

possible. Based on the literature, $j_{0,an-ref}$, $j_{0,ca-ref}$, α_{an} and α_{ca} were varied in the ranges of 10^{-11}–10^{-4}A/cm^2, 10^{-6}–10^{-1} A/cm^2, 0.4–2.5, and 0.2–1, respectively. Moreover, the combinations in which either $j_{0,an-ref} > j_{0,ca-ref}$ or $\alpha_{an} < \alpha_{ca}$ were excluded from the search space since typical values for the fitting parameters adhere to these criteria. This arises from the fact that the anode contribution to the activation overvoltage is higher than the cathode. In Table 4.3, the fitted parameters along with their conventional feasible ranges are shown.

To illustrate the deviation of the results of the model from the experimental dataset, the relative error parameter is used. The general expression for the relative error in percentage can be written as follows:

$$e = \frac{100}{Z_{exp}} \sum_{z=1}^{Z_{exp}} \frac{V_{sim,z} - V_{exp,z}}{V_{exp,z}} \tag{4.69}$$

Table 4.3: Fitted parameters for static validation

Parameter	Considered range	Fitted value	Unit
$j_{0,\mathrm{an-ref}}$	10^{-11}–10^{-4}	2.00×10^{-8}	$\mathrm{A/cm^2}$
$j_{0,\mathrm{ca-ref}}$	10^{-6}–10^{-1}	1.91×10^{-2}	$\mathrm{A/cm^2}$
α_{an}	0.4–2.5	2.47	-
α_{ca}	0.1–1	0.93	-

where Z_{exp} is the number of experiments, and $V_{\mathrm{sim},z}$ and $V_{\mathrm{exp},z}$ indicate the results obtained from the z^{th} simulation and experiment, respectively.

The relative error obtained from different combinations of fitting parameters, irrespective of their sequence of iterations, is depicted in Fig. 4.3. As 80 °C is a typical operating temperature for the PEM electrolyser, the curve fitting was implemented at this temperature, and the polarisation curve with the least average relative error was chosen. As can be seen in Table 4.3 and Fig. 4.3, $j_{0,\mathrm{an-ref}} = 2.00 \times 10^{-8}$ $\mathrm{A/cm^2}$, $j_{0,\mathrm{ca-ref}} = 1.91 \times 10^{-2}$ $\mathrm{A/cm^2}$, $\alpha_{\mathrm{an}} = 2.47$ and $\alpha_{\mathrm{ca}} = 0.93$ were derived, resulting in the relative error of 0.55 %. Given the materials in use for the electrodes, i.e., Pt-Ir for the anode and Pt for the cathode, the obtained values hold validity [20, 29]. It should be noted that although temperature variation has been selected as the parameter to confirm the applicability of the model, the effect of operating-pressure variations on the performance of the PEM electrolyser can also be investigated using the developed model. However, the influence of pressure variation is less significant than that of temperature, since water electrolysis is a liquid-to-gas reaction and increasing the gas-phase pressure affects the reaction's Gibbs free energy only logarithmically.

It is essential to emphasise that the sets of combinations that exhibited high errors, such as those exceeding 100%, are specific to the particular electrolyser employed for obtaining the experimental data. For a different electrolyser with distinct specifications, these combinations might yield lower errors compared to what they demonstrated in this case. In this thesis, by exploring within the ranges specified in Table 4.3, it is ensured that the obtained best point, shown with a green star in Fig.3, is indeed the most optimal point.

In Fig. 4.4, the polarisation curves obtained from the experiment and model are compared at different temperatures. Evidently, the static behaviour of the model corresponds closely with the experimental results of the PEM electrolyser. The slight discrepancy between the simulation and experimental curves can be attributed to the neglected factors in the model, like concentration overvoltage and electronic resistance. However, the resulting relative error, depicted in Fig. 4.5, is entirely insignificant, especially when considering the simulation time of the mathematical model.

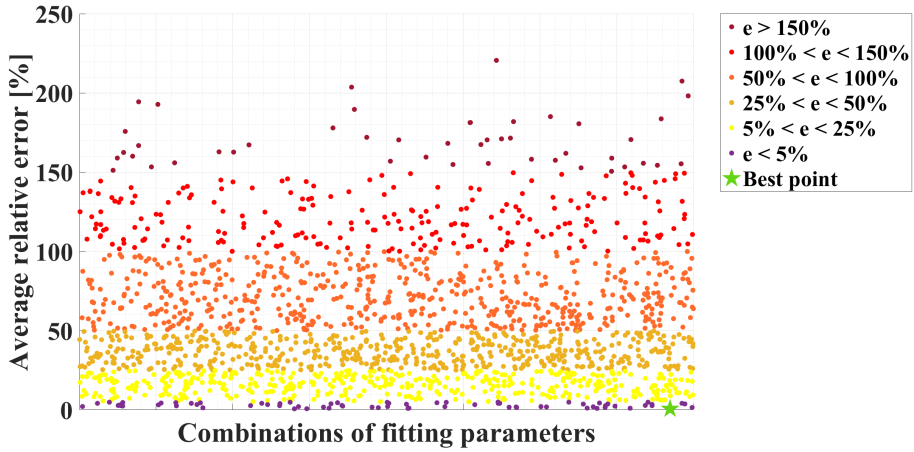

Figure 4.3: The average relative error derived from various combinations of the fitting parameters for static validation

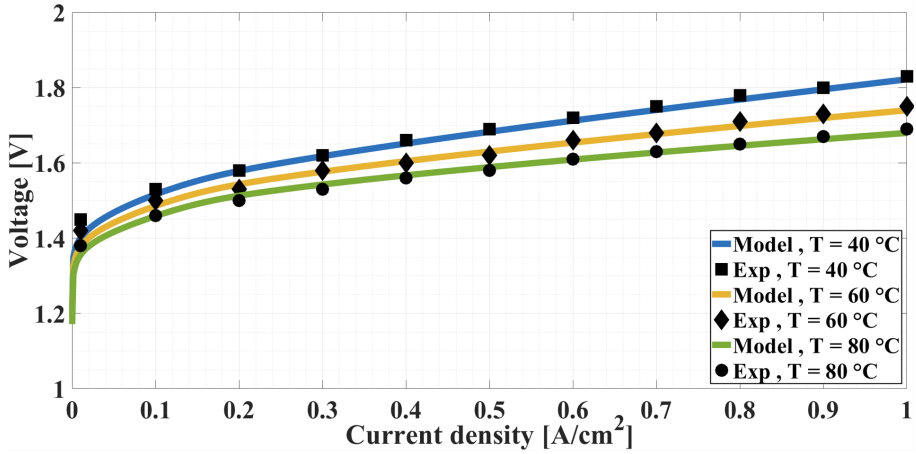

Figure 4.4: Comparison of the polarisation curves obtained from the best point of the model and experiment at various temperatures and atmospheric pressure

The average relative error between the model and experiment at 40 °C, 60 °C, and 80 °C are 0.68%, 0.75%, and 0.55%, consecutively. The higher relative error observed at 40 °C and 60 °C is believed to arise from the fact that the fitting parameters were fine-tuned at 80 °C to match the experimental data. Subsequently, these parameters were maintained unchanged for other temperatures. Thus, the adjusted fitting parameters of the model are not optimal for other operating temperatures. Additionally, considering Fig. 4.5, the most substantial relative error is attributed to the current densities lower than 0.1 A/cm^2.

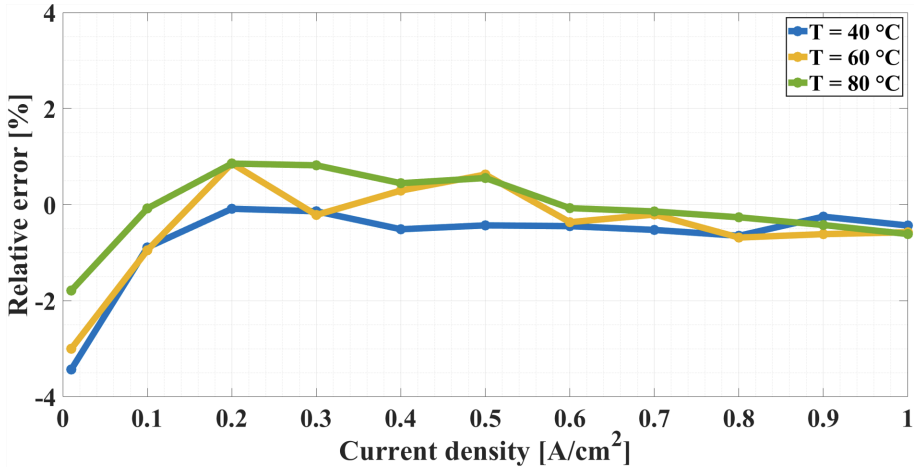

Figure 4.5: The relative error between the polarisation curves obtained from the best point of the model and experiments at various temperatures and atmospheric pressure

This stems from the dependency of reversible voltage on the partial pressures of water, hydrogen and oxygen. During the initial steps of the simulation, the partial pressures take several steps to stabilise, resulting in the highest relative error observed at the outset of the simulation. Nevertheless, taking 80 °C as an example, the reversible voltage eventually converges to 1.29 V after multiple iterations in the simulation. Considering the enthalpy of water vapour at 80 °C, approximately 239.5 kJ/mol, which corresponds to 1.24 V, the ability of the model to replicate the reversible voltage after several iterations is deemed to be acceptable [30].

4.4.2 Dynamic Model Validation

In this section, the model is validated against the experimental data reported in [2]. Since the dynamic response of the PEM electrolyser is examined, the thermal module, hence the temperature variations, are included in the simulation. The specifications of the PEM electrolyser employed for the dynamic verification as well as the values of the parameters utilised for the simulation are summarised in Table 4.4.

In order to highlight the importance of dynamic simulations for the PEM electrolyser, a comparison between the static and dynamic responses is performed prior to obtaining the fitting parameters for the dynamic operation mode. This comparison is carried out over a 30-second timeframe, based on the specifications listed in Table 4.4. While Fig. 4.6(a) shows the static and dynamic responses of the PEM electrolyser to a 10 A step current, Fig. 4.6(b)

Table 4.4: Specifications of the PEM electrolyser used for the dynamic validation [2]

Parameter	Value	Unit
A	50	cm^2
c_{p,H_2}	14337	J/kg.K
c_{p,H_2O}	4179	J/kg.K
c_{p,O_2}	920.5	J/kg.K
F	96485.33	A.s/mol
M_{H_2}	0.002	kg/mol
M_{H_2O}	0.018	kg/mol
M_{O_2}	0.032	kg/mol
n	3	-
P_{an}	1	bar
P_{ca}	10.5	bar
R_u	8.31	J/K.mol
T_{in}	20	°C
$\widehat{\Delta H^0_{H_2}}$	0	J/mol
$\widehat{\Delta H^0_{H_2O}}$	-285830	J/mol
$\widehat{\Delta H^0_{O_2}}$	0	J/mol
δ_{an-ca}	0.08	mm
δ_{mem}	0.30	mm
ϵ	0.3	-
ε_{H_2}/k	59.7	K
ε_{H_2O}/k	809.1	K
ε_{O_2}/k	106.7	K
Θ_{H_2}	2.827	Å
Θ_{H_2O}	2.641	Å
Θ_{O_2}	3.467	Å
ξ	4	-

illustrates the corresponding responses to a 6 A step current. As can be seen in Fig. 4.6, the static response follows an ideal step-shaped waveform, whereas the dynamic response gradually rises after a step increase in the current.

To quantify the error between the static and dynamic responses, the area under the power curves in Fig. 4.6, which represents the consumed energy, is compared. The resulting error between the static and dynamic responses in Fig. 4.6(a) is 1.94%, while the error in Fig. 4.6(b) is 3.17%. The higher error observed at lower current densities is due to the fact that, at higher current densities, the ohmic overvoltage, which according to (4.56) has a linear

Table 4.5: Fitted parameters for dynamic validation

Parameter	Considered range	Fitted value	Unit
$j_{0,\mathrm{an-ref}}$	10^{-11}–10^{-4}	3.90×10^{-6}	$\mathrm{A/cm^2}$
$j_{0,\mathrm{ca-ref}}$	10^{-6}–10^{-1}	2.52×10^{-2}	$\mathrm{A/cm^2}$
α_{an}	0.4–2.5	0.49	-
α_{ca}	0.1–1	0.12	-

relation with the current, becomes the dominant term in the total overvoltage, giving the power curve a more step-like behaviour. In contrast, at lower current densities, the activation overvoltage becomes the dominant component, leading to a slower rise in the power curve as governed by (4.50) and (4.51).

It is worth noting that temperature is not the sole factor governing the start-up time of the electrolyser. Start-up is constrained by several safety and operational requirements, particularly gas-purity specifications. For example, the oxygen concentration in the hydrogen outlet must fall below safe limits, typically below 2%, before hydrogen production can proceed, and achieving this purity level generally requires several seconds to minutes. In addition, purge cycles are required at each start-up to remove nitrogen, residual air, or residual contaminants from the previous shutdown [12]. Beyond gas purity, pressure build-up in the system also contributes to the start-up duration, as the inlet pump must ramp up the water-feed pressure to the operating level of the PEM stack. These combined processes extend the overall start-up time. A detailed investigation of these start-up-influencing factors falls beyond the scope of this thesis.

Not unlike the section dedicated to the static validation, the fitting parameters were varied so that the results closely aligned with the experimental data. Also, the same range of variations were considered for the parameters. The fitted parameters alongside their evaluated feasible range are tabulated in Table 4.5.

In Fig. 4.7, the relative error resulting from various combinations of fitting parameters, regardless of their order of iteration, is illustrated. Following the determination of the fitting parameters, they were held constant for other scenarios.

The dynamic responses of the model to three distinct step current waveforms characterised by amplitudes of 3, 6, and 10 A, along with the experimental results, are depicted in Fig. 4.8. In the dynamic validation of the model, the case with the applied current of 6 A was chosen for the curve fitting.

The relative error of the obtained results from the simulation is shown in Fig. 4.9. Considering Table 4.5 and Fig. 4.9, $j_{0,\mathrm{an-ref}} = 3.90 \times 10^{-6}$, $j_{0,\mathrm{ca-ref}} = 2.52 \times 10^{-2}$, $\alpha_{\mathrm{an}} = 0.49$ and $\alpha_{\mathrm{ca}} = 0.12$ were obtained, leading

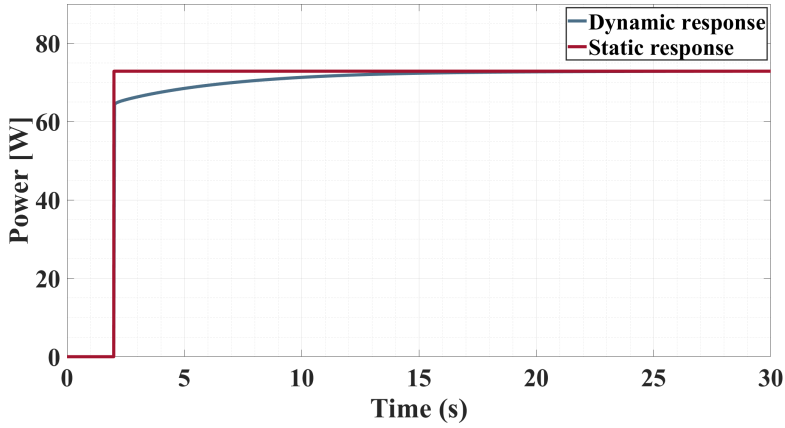

(a) Static and dynamic responses to a 10 A step current

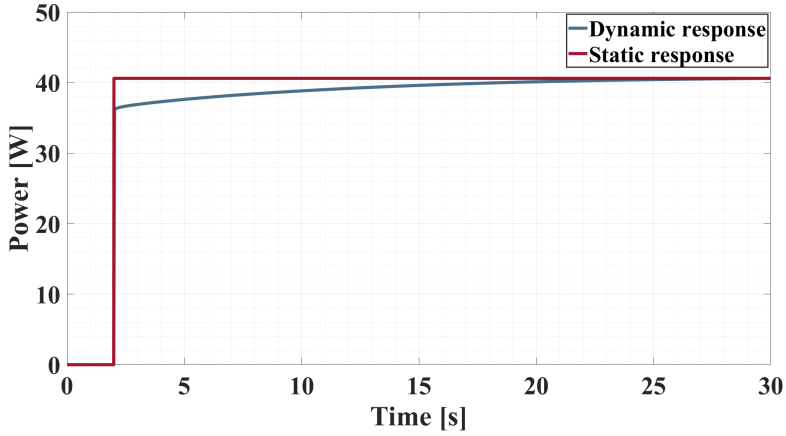

(b) Static and dynamic responses to a 6 A step current

Figure 4.6: Comparison between the dynamic and static consumed power curves of the PEM electrolyser

to an average relative error of 2.03%. Moreover, the average error for the applied step currents with amplitudes of 3 and 10 A are 5.21% and 4.55%, respectively.

As the exact operating temperature of the electrolyser in the experimental setup is unspecified, in all simulations the inlet temperature is assumed to be 20 °C. Additionally, the inlet and outlet temperature difference of the electrolyser, ΔT, is set to 10. It is noteworthy to emphasise that these parameters exert a considerable influence on the performance of the electrolyser, thereby

the results of the model. The effects of ΔT variations under a consistent inlet temperature of 20 °C, along with the impact of inlet temperature changes at a constant ΔT of 10 on the performance of the electrolyser, while applying the step current of 6 A, are represented in Fig. 4.10 and Fig. 4.11, respectively.

In Fig. 4.10, when maintaining a constant inlet temperature, an increase in ΔT results in a subsequent elevation in the operating temperature of the electrolyser, defined as the average of the inlet and outlet temperatures in this model. This, in turn, leads to a reduction in stack voltage. Conversely, a decrease in ΔT lowers the operating temperature, which in turn causes an elevation in stack voltage.

Alternatively, in Fig. 4.11, by holding ΔT unchanged, when the inlet temperature is raised, the operating temperature of the electrolyser increases, since the operating temperature is the average of the inlet and outlet temperatures. This results in a decrease in stack voltage. On the contrary, lowering the inlet temperature while ΔT remains constant, causes the operating temperature to decrease, leading to a reduction in stack voltage.

This clearly demonstrates the impact of thermal parameters on the behaviour of the electrolyser in dynamic operation mode. As a result, the discrepancy between the results of the model and experiments is primarily attributed to the unspecified thermal parameters. In [2], different reversible stack voltages observed in the experiments highlight the dissimilarity of thermal parameters for the explored scenarios.

It is worth noting that, in practical scenarios, the transient behaviour of the electrolyser changes under different operating conditions. This variation is clearly reflected in Fig. 4.10 and Fig. 4.11 where, for instance, the regression

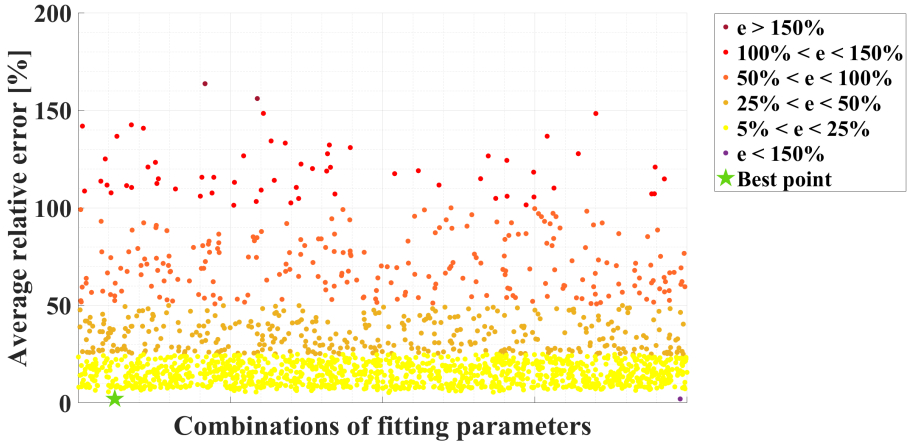

Figure 4.7: The average relative error derived from various combinations of the fitting parameters for dynamic validation

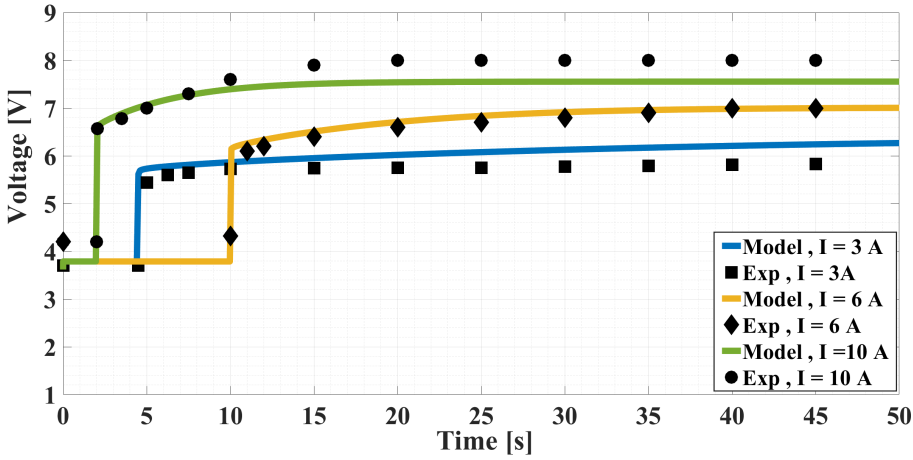

Figure 4.8: Comparison of the stack voltage between the best point obtained from the model and experiment with the applied currents of 3, 6 and 10 A

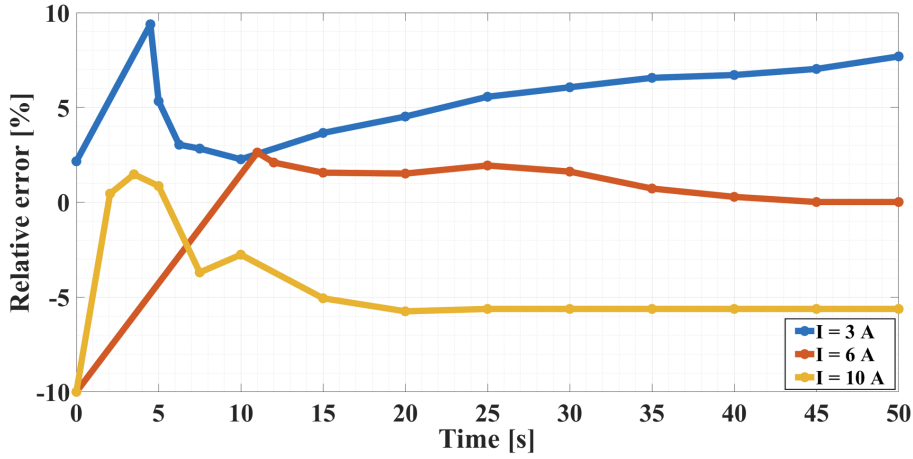

Figure 4.9: The relative error between the best point obtained from the model and experiments with the applied currents of 3, 6 and 10 A

of temperature vs. time varies across different operating conditions, as shown in Fig. 4.10(b) and Fig. 4.11(b).

Apart from the mentioned reasons, the higher relative error for other cases than the reference one arises from the fitting parameters not being optimal for them. Furthermore, given the impact of the thermal parameters on the performance of the electrolyser, aligning temperature with its actual value can lead to a reduction in error. Nevertheless, the model still shows decent accuracy

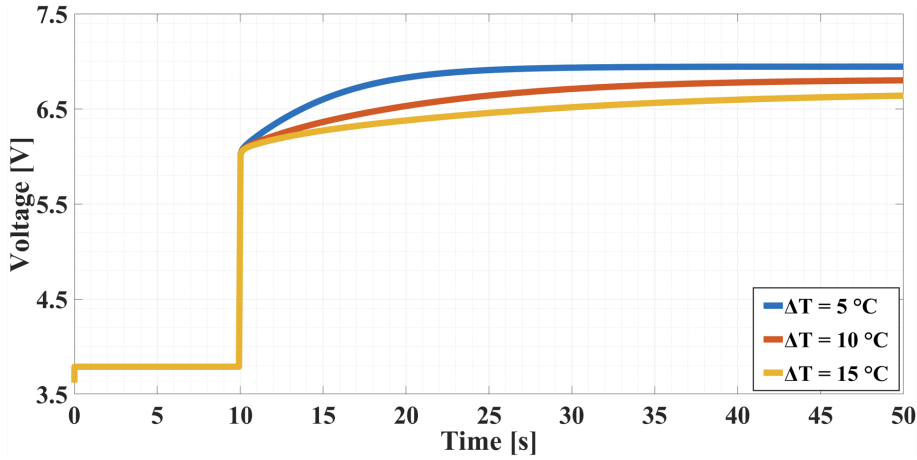

(a) Effect of ΔT variations on the stack voltage

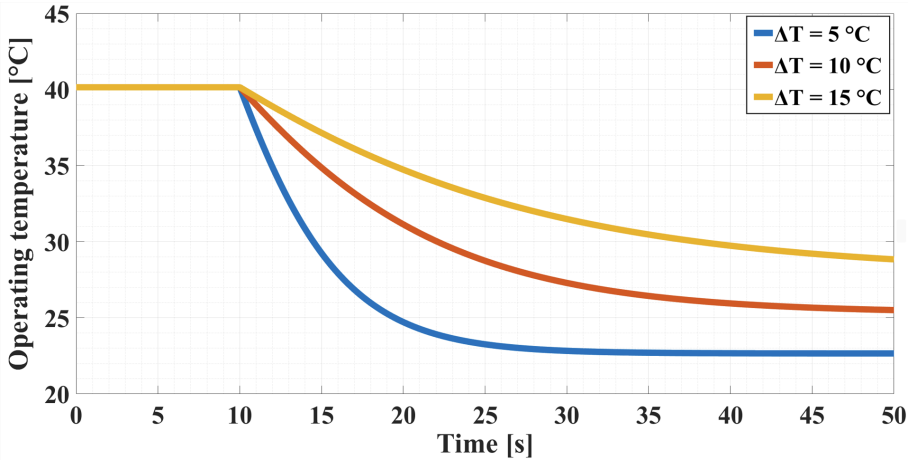

(b) Effect of ΔT variations on the operating temperature

Figure 4.10: The impact of varying ΔT on the stack voltage and operating temperature with the applied current of 6 A

at different operating conditions.

4.5 Conclusions

This chapter presented a simplified yet accurate static-dynamic model of the PEM electrolyser, enabling its straightforward integration into large-scale simulations of the power system. For instance, it can effectively contribute to modelling the ancillary service provision of the PEM electrolyser alongside

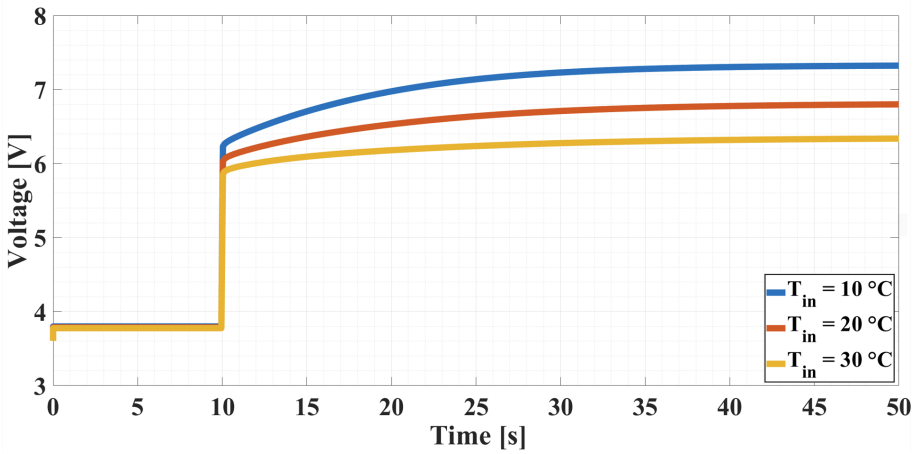

(a) Effect of inlet temperature variations on the stack voltage

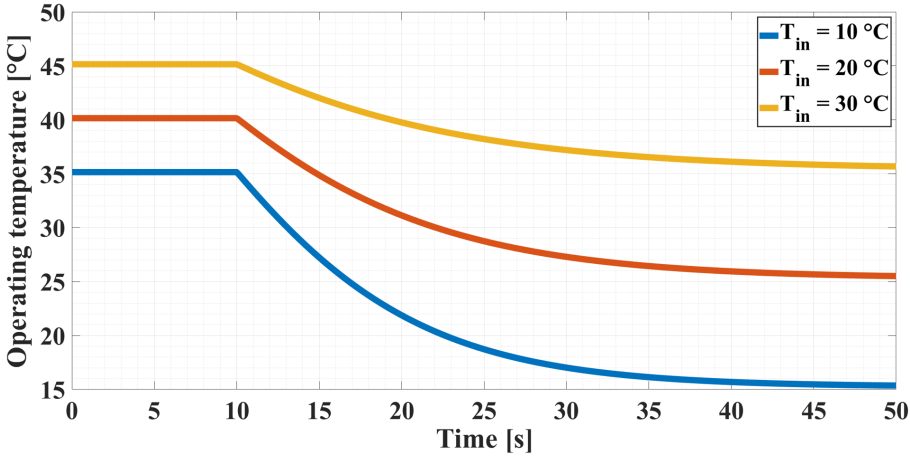

(b) Effect of inlet temperature variations on the operating temperature

Figure 4.11: The impact of varying inlet temperature on the stack voltage and operating temperature

other units or examining the flexible operation of the PEM electrolyser in the presence of intermittent RESs, without introducing excessive complexity. Upon deriving the fitting parameters for the model, it can be integrated into more complex simulations, such as those involving a large-scale power system.

The model comprised five distinct modules, including the anode, cathode, membrane, voltage and thermal, each utilising physical/empirical relations to replicate the behaviour of the PEM electrolyser. Furthermore, water-based cooling for the electrolyser was taken into account, mirroring the practical

operation of electrolysers. As anticipated, given the temperature-dependent nature of several mechanisms taking place in the electrolyser, the thermal characteristic of the electrolyser demonstrated a notable influence on the average operating temperature, thereby the performance of the electrolyser.

The model, implemented in MATLAB/Simulink, underwent validation against experimental data in both static and dynamic operation modes. Regarding the former case, the experimental data of a single cell with 100 cm^2 active area operating at temperatures of 40, 60, and 80 °C was employed and the model exhibited an average relative error of 0.68%, 0.75%, and 0.55%, successively. Thus, across the investigated operating conditions, an overall average relative error of 0.66% was obtained. Concerning the dynamic response of the PEM electrolyser, the experimental data from a 3-cell stack featuring an active area of 50 cm^2 was utilised. Under applied currents of 3, 6, and 10 A, the developed model showed an average relative error of 5.21%, 2.03%, and 4.55%, consecutively. This results in an overall average relative error of 3.93% among the examined cases. Consequently, it can be concluded that the omission of factors such as concentration overvoltage, electronic resistance, and water passage through the membrane due to the hydraulic pressure effect did not significantly impact the accuracy of the model in either static or dynamic operations. Yet, it did lead to enhanced computational efficiency.

Nonetheless, the model can still be improved through the incorporation of more physics-based relationships instead of the empirical ones, for example, for the calculation of the electro-osmotic drag coefficient. For future studies, it would be interesting to integrate the model into more intricate systems, exploring how the dynamic characteristics of the BoP components, like water desalination systems, shape the dynamic response of the PEM electrolyser. Moreover, in scenarios where the synthesis of other green molecules is considered, the impact of the dynamic behaviour of the PEM electrolyser on the subsequent systems, such as the methanol production unit, holds substantial interest.

In the following chapter, the focus will be placed on water provision for the electrolyser, which is another key component of offshore electrolysis. As previously mentioned, since this thesis addresses hydrogen production at sea, the use of seawater is a viable option. Therefore, based on a literature review, one of the two main approaches, either direct seawater electrolysis or seawater electrolysis with upfront water treatment, is selected, and the corresponding model is developed. Subsequently, this model is integrated with the PEM electrolyser model to facilitate further studies.

Bibliography

[1] D. Guilbert and G. Vitale, "Experimental validation of an equivalent dynamic electrical model for a proton exchange membrane electrolyzer," in *2018 IEEE International Conference on Environment and Electrical Engineering and 2018 IEEE Industrial and Commercial Power Systems Europe (EEEIC/I&CPS Europe)*, 2018.

[2] Á. Hernández-Gómez, V. Ramirez, D. Guilbert, and B. Saldivar, "Development of an adaptive static-dynamic electrical model based on input electrical energy for PEM water electrolysis," *International Journal of Hydrogen Energy*, vol. 45, no. 38, pp. 18817–18830, 2020.

[3] H. Görgün, "Dynamic modelling of a proton exchange membrane (PEM) electrolyzer," *International Journal of Hydrogen Energy*, vol. 31, no. 1, pp. 29–38, 2006.

[4] B. Lee, K. Park, and H.-M. Kim, "Dynamic simulation of PEM water electrolysis and comparison with experiments," *International Journal of Electrochemical Science*, vol. 8, no. 1, pp. 235–248, 2013.

[5] A. Awasthi, K. Scott, and S. Basu, "Dynamic modeling and simulation of a proton exchange membrane electrolyzer for hydrogen production," *International Journal of Hydrogen Energy*, vol. 36, no. 22, pp. 14779–14786, 2011.

[6] Z. Abdin, C. Webb, and E. M. Gray, "Modelling and simulation of a proton exchange membrane (PEM) electrolyser cell," *International Journal of Hydrogen Energy*, vol. 40, no. 39, pp. 13243–13257, 2015.

[7] T. Yigit and O. F. Selamet, "Mathematical modeling and dynamic simulink simulation of high-pressure PEM electrolyzer system," *International Journal of Hydrogen Energy*, vol. 41, no. 32, pp. 13901–13914, 2016.

[8] R. García-Valverde, N. Espinosa, and A. Urbina, "Simple PEM water electrolyser model and experimental validation," *International Journal of Hydrogen Energy*, vol. 37, no. 2, pp. 1927–1938, 2012.

[9] H. Kim, M. Park, and K. S. Lee, "One-dimensional dynamic modeling of a high-pressure water electrolysis system for hydrogen production," *International Journal of Hydrogen Energy*, vol. 38, no. 6, pp. 2596–2609, 2013.

[10] M. Lebbal and S. Lecœuche, "Identification and monitoring of a PEM electrolyser based on dynamical modelling," *International Journal of Hydrogen Energy*, vol. 34, no. 14, pp. 5992–5999, 2009.

[11] F. Z. Aouali, M. Becherif, H. S. Ramadan, M. Emziane, A. Khellaf, and K. Mohammedi, "Analytical modelling and experimental validation of proton exchange membrane electrolyser for hydrogen production," *International Journal of Hydrogen Energy*, vol. 42, no. 2, pp. 1366–1374, 2017.

[12] A. E. Samani, A. D'Amicis, J. D. M. De Kooning, D. Bozalakov, P. Silva, and L. Vandevelde, "Grid balancing with a large-scale electrolyser providing primary reserve," *IET Renewable Power Generation*, vol. 14, no. 16, pp. 3070–3078, 2020.

[13] A. Alex, R. Petrone, B. Tala-Ighil, D. Bozalakov, L. Vandevelde, and H. Gualous, "Optimal techno-enviro-economic analysis of a hybrid grid connected tidal-wind-hydrogen energy system," *International Journal of Hydrogen Energy*, vol. 47, no. 86, pp. 36448–36464, 2022.

[14] A. Dadkhah, D. Bozalakov, J. D. M. De Kooning, and L. Vandevelde, "Techno-economic analysis and optimal operation of a hydrogen refueling station providing frequency ancillary services," *IEEE Transactions on Industry Applications*, vol. 58, no. 4, pp. 5171–5183, 2022.

[15] L. M. Valle-Falcones, C. Grima-Olmedo, L. F. Mazadiego-Martínez, A. Hurtado-Bezos, S. Eguilior-Díaz, and R. Rodríguez-Pons, "Green hydrogen storage in an underground cavern: a case study in salt diapir of spain," *Applied Sciences*, vol. 12, no. 12, p. 6081, 2022.

[16] F. Marangio, M. Santarelli, and M. Calì, "Theoretical model and experimental analysis of a high pressure PEM water electrolyser for hydrogen production," *International Journal of Hydrogen Energy*, vol. 34, no. 3, pp. 1143–1158, 2009.

[17] X. Li, S. Qu, H. Yu, M. Hou, Z. Shao, and B. Yi, "Membrane water-flow rate in electrolyzer cells with a solid polymer electrolyte (SPE)," *Journal of Power Sources*, vol. 190, no. 2, pp. 534–537, 2009.

[18] Á. Hernández-Gómez, V. Ramirez, and D. Guilbert, "Investigation of PEM electrolyzer modeling: Electrical domain, efficiency, and specific energy consumption," *International Journal of Hydrogen Energy*, vol. 45, no. 29, pp. 14625–14639, 2020.

[19] A. Majumdar, M. Haas, I. Elliot, and S. Nazari, "Control and control-oriented modeling of PEM water electrolyzers: A review," *International Journal of Hydrogen Energy*, 2023.

[20] D. Falcão and A. Pinto, "A review on PEM electrolyzer modelling: Guidelines for beginners," *Journal of Cleaner Production*, vol. 261, p. 121184, 2020.

[21] P. Olivier, C. Bourasseau, and P. B. Bouamama, "Low-temperature electrolysis system modelling: A review," *Renewable and Sustainable Energy Reviews*, vol. 78, pp. 280–300, 2017.

[22] M. Espinosa-López, C. Darras, P. Poggi, R. Glises, P. Baucour, A. Rakotondrainibe, S. Besse, and P. Serre-Combe, "Modelling and experimental validation of a 46 kW PEM high pressure water electrolyzer," *Renewable Energy*, vol. 119, pp. 160–173, 2018.

[23] L. Järvinen, P. Puranen, A. Kosonen, V. Ruuskanen, J. Ahola, P. Kauranen, and M. Hehemann, "Automized parametrization of PEM and alkaline water electrolyzer polarisation curves," *International Journal of Hydrogen Energy*, vol. 47, no. 75, pp. 31985–32003, 2022.

[24] T. E. Springer, T. Zawodzinski, and S. Gottesfeld, "Polymer electrolyte fuel cell model," *Journal of the Electrochemical Society*, vol. 138, no. 8, p. 2334, 1991.

[25] A. Villagra and P. Millet, "An analysis of PEM water electrolysis cells operating at elevated current densities," *International Journal of Hydrogen Energy*, vol. 44, no. 20, pp. 9708–9717, 2019.

[26] J. Palathingal, "Mathematical modelling and dynamic simulation of a PEM electrolyser, Master thesis, University of Lorraine," 2017.

[27] K. Agbli, M. Péra, D. Hissel, O. Rallières, C. Turpin, and I. Doumbia, "Multiphysics simulation of a PEM electrolyser: Energetic macroscopic representation approach," *International Journal of Hydrogen Energy*, vol. 36, no. 2, pp. 1382–1398, 2011.

[28] Ö. F. Selamet, M. C. Acar, M. D. Mat, and Y. Kaplan, "Effects of operating parameters on the performance of a high-pressure proton exchange membrane electrolyzer," *International Journal of Energy Research*, vol. 37, no. 5, pp. 457–467, 2013.

[29] M. Koundi, H. El Fadil, Z. EL Idrissi, A. Lassioui, A. Intidam, T. Bouanou, S. Nady, and A. Rachid, "Investigation of hydrogen production system-

based PEM EL: PEM EL modeling, DC/DC power converter, and controller design approaches," *Clean Technologies*, vol. 5, no. 2, pp. 531–568, 2023.

[30] R. O'hayre, S.-W. Cha, W. Colella, and F. B. Prinz, *Fuel cell fundamentals*. John Wiley & Sons, 2016.

Chapter 5

Modelling the RO System for Seawater Desalination

This chapter presents the modelling steps of the offshore seawater reverse osmosis (SWRO) system, which is the chosen feedwater approach for the proton exchange membrane (PEM) electrolyser in this thesis. The model is then validated against experimental data. Subsequently, the integrated SWRO and PEM electrolyser models are validated and upscaled to reflect a realistic scenario, in which the sizing of these devices corresponds to real-life applications. Finally, a straightforward control strategy for the SWRO unit, based on the operation of the electrolyser, is proposed.

5.1 Introduction

Freshwater scarcity and its uneven global distribution pose challenges for electrolysis-based green hydrogen production [1, 2], leading to interest in alternative sources such as groundwater, brackish water, and seawater [3, 4]. As stated in Chapter 3, offshore wind energy has emerged as a strong renewable energy source (RES) for powering electrolysers, particularly in coastal regions [5, 6], enabling offshore deployment that allows seawater use, supports land-constrained regions, and facilitates integration with other marine RESs such as wave and tidal energy [7], in line with the energy island concept [8]. Nonetheless, offshore electrolysis introduces higher operation and maintenance costs [9, 10], while seawater impurities, mainly sodium and chloride, reduce efficiency and durability [11, 12]. There are two main approaches for seawater electrolysis: direct seawater electrolysis (DSWE), which requires redesign and new electrocatalysts for both alkaline electrolysers (AE) and PEM electrolysers, and seawater electrolysis with upfront treatment, which adds complexity and cost but mitigates impurity-related issues [13]. These two methods will

be investigated more in detail, and the preferred method for offshore hydrogen production will be selected in this chapter.

The rest of the chapter is structured as follows: In Section 5.2, offshore hydrogen production is examined based on the literature, including a comparison between DSWE and seawater electrolysis with upfront water treatment. Section 5.3 presents the selection of the configuration for the offshore hydrogen production system, based on the conducted literature review of the previous section. Afterwards, Section 5.4 provides a detailed modelling approach for the reverse osmosis (RO) system, and its validation against experimental data is presented in Section 5.5. Thereafter, in Section 5.6, the validated models of the SWRO and PEM electrolyser are first upscaled and then coupled. A computationally efficient control method is introduced to adjust the settings of the RO unit based on the energy consumption of the PEM electrolyser. The results of this section are presented in Section 5.7. Finally, Section 5.8 discusses the conclusions and highlights potential areas for future research, and defines the scope of the subsequent chapter.

5.2 Literature Review

In this section, a thorough literature review is conducted to identify the most effective current topologies and pathways for offshore hydrogen production. Based on this review, the configuration considered in this study will be chosen, and key areas requiring further investigation will be highlighted.

In the literature, offshore hydrogen production has been explored from various perspectives, including comparisons between DSWE and electrolysers coupled with desalination systems. These studies have also investigated the most suitable type of electrolyser and desalination system for offshore hydrogen production, deciding where to place the electrolyser onshore or offshore, and if offshore, determining the optimal location, such as integrated with a wind turbine, on a stationary platform, on a moving vessel, etc. Additionally, there are studies that have examined methods for transporting the produced hydrogen to shore and how all these factors influence the levelised cost of hydrogen (LCOH).

When comparing DSWE and seawater electrolysis with upfront treatment in terms of energy consumption, the electrolysis process is far more energy-intensive than water desalination. Current commercial RO systems require around 2-3 kWh to produce 1 m^3 of ultrapure water suitable for electrolysis, whereas over 5000 kWh of energy is needed to split that same 1 m^3 of water into hydrogen and oxygen [13–15].

As discussed in Chapter 3, the authors in [13] have provided a detailed breakdown of the energy requirement, capital costs, operating costs and LCOH

for an SWRO system coupled with a PEM electrolyser plant with a production capacity of 50 tons hydrogen per day. The study showed that SWRO consumes only 0.1% of the total energy required for the entire system. Additionally, the capital costs of SWRO, including its installation, make up around 3% of the total capital expenditure (CapEx), while the capital costs for the electrolyser, including its installation and balance of plant (BoP) equipment, account for the remaining 97%. In terms of operational expenditure (OpEx), SWRO represents around 0.2% of the costs. Concerning the levelised cost of hydrogen, it rises marginally from 3.81 $\$/kg_{H_2}$ to 3.83 $\$/kg_{H_2}$ when SWRO is included. The authors suggested that the integration of SWRO and the PEM electrolyser is the most viable option to be utilised in the near-term applications, considering that it is a more practical immediate method than investing in developing catalysts and systems for DSWE. It is concluded that, in the SWRO-PEM system, the required energy for the electrolysis phase remains dominant compared to the SWRO process, making the capital and operating costs of the SWRO system negligible in comparison.

The authors in [16] have compared the production of 1 kg of purified water from seawater via the SWRO system and the electrolysis of that 1 kg of water from the perspectives of energy, economic and footprint. In terms of thermodynamic energy requirements, it has been shown that electrolysis requires around 3000 times more energy than desalination of seawater. Generally, electrolysis involves breaking strong covalent O-H bonds, whereas the energy for desalination is required for the reversal of entropy, overcoming the osmotic pressure which is resisting the separation of water from salt, and breaking the ion-dipole interactions between dissolved salts and water molecules. All of these energy requirements in desalination are significantly lower than breaking O-H bonds during electrolysis. Therefore, seawater desalination increases thermodynamic energy requirements by only 0.03%. About energy consumption, with a higher heating value of 1.48 V, the voltage efficiency for acidic and alkaline electrolysers has been estimated to be 62-82%, yielding 19.38-25.63 MJ/kg_{water}. In contrast, based on the assumption of 2.5-4 kWh/m^3_{water} needed energy for seawater desalination, the energy consumption of desalination reduces to 9-14.4 kJ/kg_{water}. Consequently, electrolysis requires roughly 1350-2850 times more energy than desalination. The authors have also compared the space required by a desalination system and an electrolyser. They have estimated that desalination can produce 1000 kg of water per day per 1 m^2 of the membrane. Conversely, an electrolyser operating at 1 A/m^2 demands around 8 kg of water per day per 1 m^2 of electrochemical cell, including a gas separator, either membrane or diaphragm, and two electrodes, meaning an electrolyser needs roughly 125 times more surface area than an RO system.

As for the choice of the desalination type, membrane-based seawater desalination is recognised as one of the most practical solutions [17]. Within

this category, RO and forward osmosis (FO) are the most prominent technologies. RO is a pressure-driven process that relies on the difference between the applied hydraulic pressure and the osmotic pressure, the former opposing the osmotic pressure gradient. In contrast, FO employs osmotic pressure difference across the membrane as its driving force, eliminating the need for hydraulic pressure [18]. This makes RO more energy-intensive compared to FO. However, RO offers several advantages such as high reliability and high salt rejection [14]. Additionally, thanks to the development of membranes with higher efficiency, materials with lower friction and variable-frequency drives, the energy consumption of RO has decreased significantly, from 20 kWh/m^3_{water} in the 1970s to 2-3 kWh/m^3_{water} today [14]. That is why most of the current commercial desalination plants work based on the RO process, while FO has not yet been implemented on a large full-scale for seawater desalination.

Considering the type of electrolyser suitable for offshore use, the authors in [19] have explored seawater electrolysis technologies for offshore hydrogen production. In this study, it is shown that the differences between AE and PEM electrolysers are indeed trivial. Seeking the best current electrolysis technology to produce hydrogen at sea using marine energy, this study compared AE, PEM electrolyser, solid oxide (SO) electrolyser and DSWE based on economic, environmental and social criteria. Subsequently, five different decision-making methods are utilised to compare the mentioned hydrogen production technologies. Overall, this study concluded that both AE and PEM electrolysers are likely to play major roles in the sector of hydrogen production at sea, with PEM currently presenting the best prospects for applicability. Furthermore, the authors suggested that if AE advances to become less risky for offshore applications, it could become a more promising technology. This arises from the fact that not only AE is cheaper than PEM electrolyser but also has the longest lifespan at sea in comparison with other seawater electrolysis technologies, as it does not suffer from irreversible damage due to impurities in feed water.

The authors in [20] have conducted a techno-economic analysis of hydrogen production from an offshore wind farm, comparing both offshore and onshore production methods. Furthermore, in terms of offshore hydrogen production, they have assessed hydrogen offloading pathways to export it from an offshore facility to shore. Besides onshore hydrogen production, four pathways for offshore hydrogen production have been investigated: transporting compressed hydrogen gas to shore via pipeline, transporting liquified hydrogen to shore via vessel, converting hydrogen to ammonia (NH_3) and then transporting it to shore by either pipeline or vessel, and loading hydrogen into liquid organic hydrogen carriers (LOHC) and then transporting to shore by pipeline or vessels. Among the explored cases, producing hydrogen offshore and transporting it to shore via pipeline led to the lowest LCOH at 5.35 $€/kg_{H_2}$, with the potential to drop as low as 2.17 $€/kg_{H_2}$. Regarding onshore hydrogen production, the

study suggested that onshore production is suitable if the wind farm is relatively close to land, yielding an LCOH of 5.39 €/kg_{H_2} for onshore production, with the potential to be as low as 2.61 €/kg_{H_2}.

The authors in [21] have investigated both onshore and offshore hydrogen production powered by large-scale wind turbines. In this study, three various topologies were defined as follows: placing the electrolyser onshore in remote areas and powering it using floating offshore wind turbines via submarine electric cables, locating the electrolyser on the turbine platform to avoid power transmission loss and costs, and transporting hydrogen to shore via pipelines, and finally, placing the electrolyser on a floating vessel offshore and transporting hydrogen to shore via pipelines. For each proposed topology, a comparison regarding the choice of electrolyser, floating offshore wind platform and energy transmission vector (electric power or offshore hydrogen pipelines) is made. About the first topology, the authors concluded that AE powered by a spar floating offshore wind platform is the most suitable option, with energy transmission via submarine high voltage direct current (HVDC) cables. It is important to note that in the conducted study by the authors, HVDC was investigated due to the relatively long distance between the wind farm and the electrolysers. Regarding the second topology, either the AE or PEM electrolyser is suggested with either the spar or semi-submersible offshore wind turbine, with the spar being preferred for sites with high depths, and hydrogen pipelines for transport. In terms of the third topology, they recommended the PEM electrolyser combined with semi-submersible floating offshore wind turbines and hydrogen pipelines for transport.

In [22], motivated by the construction of the artificial energy island in Denmark, the authors have assessed how to minimise the cost of green hydrogen production. In this study, the electrolyser is powered by offshore wind energy, where three different electrolyser placements are taken into account: in-turbine, offshore and onshore. Additionally, the authors have evaluated three types of electrolysers, namely, AE, PEM and SO electrolysers, and two different operation modes, hydrogen-driven (prioritising hydrogen production) and electricity-driven (utilising only excess electricity for electrolysis). The study concluded that although all three mentioned types of electrolysers are competitive, AE achieves slightly lower costs. For electrolyser location, offshore placement yields the lowest cost of hydrogen, with the minimum LCOH in hydrogen-driven mode calculated at 2.4 €/kg_{H_2}. Finally, in electricity-driven mode, they concluded that the levelised cost of electricity (LCOE) can be reduced by up to 13% when the electrolyser is installed compared to when it is not.

On the other hand, the authors in [23] have examined offshore hydrogen production via AE, PEM and SO electrolysers powered by offshore wind power, based on the Chinese power system data. They have concluded that the PEM

electrolyser is currently the most suitable electrolyser for hydrogen production. Furthermore, the study has concluded that integrating the PEM electrolyser into the wind turbine is a better solution, as it eliminates the need for submarine cables along with several power conversion and conditioning units.

To determine the most economical approach to connecting offshore wind power to electrolysers, the authors in [7] have conducted a techno-economic analysis on three various configurations, including distributed hydrogen production, centralised hydrogen production and onshore hydrogen production. In the first scenario, each wind turbine is equipped with an electrolyser, producing hydrogen on floating structures. In the centralised generation case, the electrolyser is placed on an offshore platform near the wind farm. Lastly, in the onshore production configuration, the electrolyser is located onshore. The LCOH using a PEM electrolyser coupled with a 160 MW offshore wind farm was found to be 13.81, 13.84 and 14.58 $\$/kg_{H_2}$ for distributed, centralised, and onshore production, respectively. Additionally, a sensitivity analysis revealed that the capacity factor of the wind farm and the tax rate are the two most influential parameters in determining LCOH, followed by wind turbine costs, the electrolysis unit cost for distributed production, and floating configuration for the other two scenarios.

5.3 Topology Selection

In summary, due to the fluctuations of RESs, new emerging concepts such as energy islands, and limited onshore areas, investigating offshore hydrogen from seawater is crucial.

Based on the conducted studies in [13] and [16], in this thesis, offshore hydrogen production in the presence of a desalination system is going to be explored. This is due to the negligible complexity and costs that the desalination unit adds to the topology of the system, whereas DSWE requires significant redesigns of currently available electrolysers.

For the choice of the destination system, based on the literature, the main drawback of RO compared to FO is its higher energy consumption, while it offers several advantages [14]. Most importantly, when integrated with an electrolyser, the higher energy consumption of RO compared to FO becomes significantly less relevant, as the specific energy consumption of RO is negligible compared to that of the electrolyser, according to [13] and [16]. Additionally, the global installed capacity for RO was around 65.5 Mm^3/day in 2019, accounting for approximately 70% of the total desalination capacity at the time. This capacity has since grown to about 100 Mm^3/day. Conversely, FO capacity has remained below 0.95 Mm^3/day, primarily limited to pilot scales operations [24, 25]. Given its maturity, the RO system is chosen for

desalinating seawater to provide the feed water for the electrolyser.

Considering the conducted studies in [19], [21], [22], [23] and [7], AE and PEM electrolysers are currently further along in development and more feasible solutions for near-term offshore hydrogen production. Therefore, the focus for selecting the type of electrolyser is limited to these two types.

Although AE is a more mature technology compared to its PEM counterpart, the PEM electrolyser offers several advantages over AE, particularly when it comes to integration with RESs. As discussed in Chapter 4, the PEM electrolyser has the capability to operate at higher current densities of more than 2 A/cm^2 [26], reducing the footprint compared to AE of the same capacity. This, in turn, makes PEM electrolyser suitable for applications with limited space, such as offshore hydrogen production on an energy island. Additionally, the solid electrolyte of the PEM electrolyser allows for faster response times compared to AE, where a liquid electrolyte is utilised, resulting in higher inertia, and thus, more sluggish ion transportation [27]. This rapid response is crucial when connected to an intermittent RES, as the electrolyser needs to operate under fast dynamics. Consequently, due to its maturity, AE is mainly employed in fixed-power applications. Conversely, the PEM electrolyser is preferred for integration with renewables since it can start up in several minutes and ramp up from idle mode to rated power in just a few seconds [27]. Moreover, the PEM electrolyser not only has higher efficiency compared to AE but also is capable of operating under a wider range of current densities, making it a more suitable choice for providing ancillary services for the electricity grid when coupled with RESs [28, 29].

Thus, in this thesis, the PEM electrolyser is selected for offshore hydrogen production coupled with the RO desalination system.

Although numerous studies have indicated that coupling RO with either AE or PEM electrolyser has the highest potential for near-future offshore hydrogen production, there are few studies in the literature that examine the integrated operation of these units. Since the costs and energy consumption of water treatment are lower compared to the overall hydrogen production system, it is often overlooked, despite being an essential component of the system. Therefore, a coupled model of the PEM electrolyser and RO system, as the two most promising technologies for offshore hydrogen production from seawater, is necessary for further studies.

While it is certainly valid that the consumed energy, added costs and footprint of the RO system are negligible compared to the electrolyser, hydrogen production with upfront water treatment is only deemed acceptable and competitive to DSWE if only it is ensured that the feed water for the electrolyser meets the minimum requirement in terms of quantity and quality [13].

In the context of the SWRO-PEM topology, in [30], the authors have explored an off-grid offshore PEM electrolyser and RO system powered by

wave energy. The model also includes battery storage systems and compression units for hydrogen storage. Furthermore, a simple energy management strategy is proposed to operate the components based on the available energy, battery state of charge and water availability. Although wave energy is less fluctuating compared to offshore wind, the dynamic behaviour of the PEM electrolyser is not accounted for, which impacts the accuracy of results. Consequently, the consumed power by the electrolyser, and thus the amount of hydrogen produced, is miscalculated. Additionally, the behaviour of the RO system, and hence the quality and quantity of feed water for the electrolyser, is not explored. This omission hinders the proper sizing of the RO system, which is of paramount importance when electrolysis with upfront treatment is considered.

The authors in [31] have compared the water demands and operating costs for a solar-powered electrolyser supplied with desalinated seawater, which is produced through either RO or low-temperature multi-effect distillation. They found that the costs associated with the latter are up to 85% lower than those for RO, and that the electrolyser coupled with low-temperature multi-effect distillation exhibited lower water demands. These advantages are attributed to the elimination of the need to install and operate cooling towers in low-temperature multi-effect distillation. Nevertheless, the study has primarily focused on waste heat management, and an integrated model of the electrolyser with either RO or distillation has not been in the scope of their research. Furthermore, although the desalination process costs affect the levelised cost of water (LCOW), they have a negligible influence on the LCOH when considered as a single system.

Hence, in this chapter, an SWRO-PEM model is developed and integrated into a single system-level simulation, which constitutes the main novelty of this work. The SWRO model itself is constructed based on established formulations in the literature, while the system-level coupling of SWRO and PEM electrolysis enables several new opportunities for further studies in offshore hydrogen production from non-freshwater sources. This integrated framework can also be extended for data-driven analyses and for investigating subsequent system components, for example, the synthesis of other green molecules such as methane and methanol.

5.4 Reverse Osmosis Model

In this thesis, the dynamics of the RO system are excluded, and a static model is developed. This assumption is based on two considerations. First, RO systems typically respond to input changes within a timescale of a few seconds, which is considered relatively fast [32, 33]. Second, as mentioned in Section 5.2, while seawater desalination requires approximately 2–3 kWh of electricity to produce

1 m^3 of purified water, nearly 5000 kWh is required to convert the same volume of water into hydrogen and oxygen through electrolysis. As such, the energy demand of the desalination process is negligible in comparison to that of the PEM electrolyser. Consequently, the dynamic behaviour of the SWRO system is not modelled, as it does not significantly influence the overall accuracy of the seawater electrolysis process.

5.4.1 RO Model Description

In the osmosis process, a semi-permeable membrane separates a diluted solution from a concentrated one, allowing water to naturally flow from the diluted to the concentrated side. Conversely, reverse osmosis involves applying an external pressure that exceeds the osmotic pressure, which forces water to migrate from the concentrated side to the dilute side. In this process, saline water is fed into the RO system at high pressure, where a portion of this water passes through the membrane, resulting in a low-concentration output known as permeate, while the remaining water, typically at a higher concentration than the feed, exits the RO unit, referred to as brine. In this study, each element of the RO system is divided into several increments, and the associated equations are solved sequentially for each increment. Hence, the brine flow from one increment ($Q_{b,x}$) serves as the feed flow for the next increment ($Q_{fb,(x+1)}$), while the permeate from each element ($Q_{p,x}$) is stored to form part of the final permeate. A schematic of a single element with a differential increment is shown in Fig. 5.1.

Among the various approaches for modelling RO membranes, this study utilises the solution-diffusion method. According to this method, the movement of polymer chains governs the permeation process, followed by diffusion

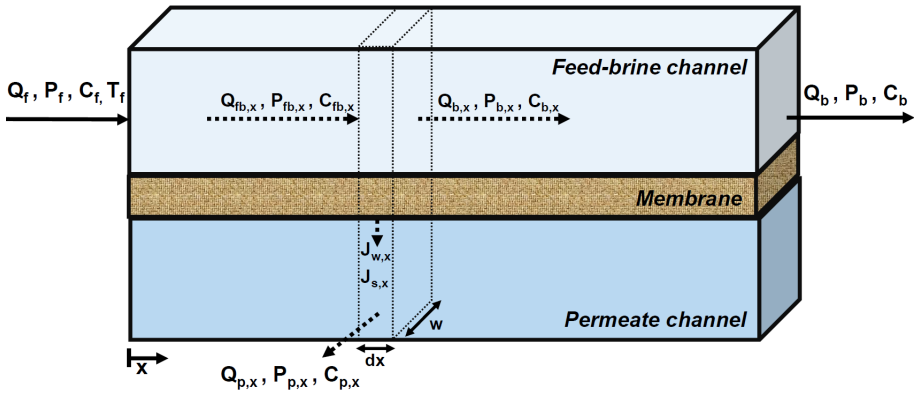

Figure 5.1: Schematic of an RO element divided into increments

through the membrane toward the permeate side [34].

Each of the three existing sub-entities in the RO system (feed, brine, and permeate) is characterised by its flow rate (Q_f for feed, Q_b for brine, and Q_p for permeate), concentration (C_f for feed, C_b for brine, and C_p for permeate), temperature (T_f for feed, T_b for brine, and T_p for permeate), and pressure (P_f for feed, P_b for brine, and P_p for permeate). In steady-state, the governing equations for flow balance and mass balance are shown in (5.1) and (5.2) [35].

$$Q_f = Q_b + Q_p \tag{5.1}$$

$$Q_f C_f = Q_b C_b + Q_p C_p \tag{5.2}$$

In the RO system, the water flux at increment x, indicated as $J_{w,x}$, is proportional to the driving force in the reverse osmosis process, denoted as the net driving pressure (NDP) in this study, as described in (5.3), where k_w is the water permeability. The NDP is the difference between ΔP_x, the applied pressure differential at increment x, and $\Delta\pi_{m,x}$, the transmembrane osmotic pressure differential at the corresponding increment.

$$J_{w,x} = k_w(\Delta P_x - \Delta\pi_x) \tag{5.3}$$

The pressure differential ΔP_x can be calculated using (5.4), with $P_{fb,ave}$ being the pressure in the feed-brine channel, which is calculated using (5.5).

$$\Delta P_x = P_{fb,ave} - P_p \tag{5.4}$$

$$P_{fb,ave} = \frac{(P_f + P_b)}{2} \tag{5.5}$$

The transmembrane osmotic pressure differential is given by (5.6), where $\pi_{m,x}$ is the osmotic pressure at the membrane surface of the feed-brine channel in increment x, and $\pi_{p,x}$ represents the osmotic pressure of the permeate in increment x.

$$\Delta\pi_x = \pi_{m,x} - \pi_p \tag{5.6}$$

The osmotic pressure of the sub-entities can be expressed by (5.7), where i_p is the number of ions produced during solute dissociation, ϕ is the osmotic coefficient, and C is the concentration of the respective flow.

$$\pi = \frac{i_p \phi C R_u T}{M} \tag{5.7}$$

On the other hand, the solute flux at increment x is proportional to the difference between the solute concentration near the membrane on the feed

side, $C_{m,x}$, and the permeate side of the corresponding increment, C_p, as shown in (5.8), where k_s is the solute permeability. The definition of $C_{m,x}$ accounts for the fact that both water and solute flux are affected by the concentration polarisation factor, β_x.

$$J_{s,x} = k_s(C_{m,x} - C_p) \times 10^{-6} \tag{5.8}$$

This occurs because impurities are retained by the membrane. Simultaneously, there is a lateral flow, known as cross-flow, which removes these accumulated solutes from the membrane surface. The concentration polarisation factor accounts for the balance between these forces, which varies for each solute due to differing diffusion constants. Thus, the feed concentration at the membrane interface can be described using (5.9).

$$C_{m,x} = \beta_x C_{fb,x} \tag{5.9}$$

The concentration polarisation factor is determined by (5.10), where S_r is salt rejection and k_m represents the mass transfer coefficient.

$$\beta_x = (e^{-J_{w,x}/(k_m \times 3.6 \times 10^6)})S_r + (1 - S_r) \tag{5.10}$$

The mass transfer coefficient is defined via (5.11), where Sh is the dimensionless Sherwood number, D_f represents the diffusivity of the solute, and d_h stands for the hydraulic diameter of the spacer-filled channel.

$$k_m = \frac{Sh \cdot D_f}{d_h} \tag{5.11}$$

For a spiral wound topology, the Sherwood number is calculated using (5.12), where Re is the Reynolds number and Sc is the Schmidt number of the solute.

$$Sh = 0.065 \cdot Re^{0.875} \cdot Sc^{0.25} \tag{5.12}$$

The Reynolds and Schmidt numbers are determined employing (5.13) and (5.14), respectively, where ρ_{sw} is the seawater density, $v_{c,x}$ indicates the cross-flow velocity in the feed-brine channel for increment x, and μ_{sw} is the dynamic viscosity of seawater.

$$Re = \frac{\rho_{sw} \cdot v_{c,x} \cdot d_h}{\mu_{sw}} \tag{5.13}$$

$$Sc = \frac{\mu_{sw}}{\rho_{sw} \cdot D_f} \tag{5.14}$$

The empirical equation employed for seawater density is as follows [35]:

$$\rho_{sw} = 10^3 (A_1 F_1 + A_2 F_2 + A_3 F_3 + A_4 F_4) \tag{5.15}$$

where

$$B = \frac{0.002C - 150}{150} \tag{5.16}$$

$$G_1 = 0.5 \tag{5.17}$$

$$G_2 = B \tag{5.18}$$

$$G_3 = 2B^2 - 1 \tag{5.19}$$

$$A_1 = 4.032219\, G_1 + 0.115313\, G_2 + 3.26 \times 10^{-4}\, G_3 \tag{5.20}$$

$$A_2 = -0.108199\, G_1 + 1.571 \times 10^{-3}\, G_2 - 4.23 \times 10^{-4}\, G_3 \tag{5.21}$$

$$A_3 = -0.012247\, G_1 + 1.74 \times 10^{-3}\, G_2 - 9 \times 10^{-6}\, G_3 \tag{5.22}$$

$$A_4 = 6.29 \times 10^{-4}\, G_1 - 8.7 \times 10^{-5}\, G_2 - 5.3 \times 10^{-5}\, G_3 \tag{5.23}$$

$$A = \frac{2T - 200}{160} \tag{5.24}$$

$$F_1 = 0.5 \tag{5.25}$$

$$F_2 = A \tag{5.26}$$

$$F_3 = 2A^2 - 1 \tag{5.27}$$

$$F_4 = 4A^3 - 3A \tag{5.28}$$

In the above equations, T is expressed in °C. Using these equations, the variation in seawater density as a function of feed temperature and total dissolved solids (TDS), expressed in ppm, is presented in Fig. 5.2 and Table 5.1.

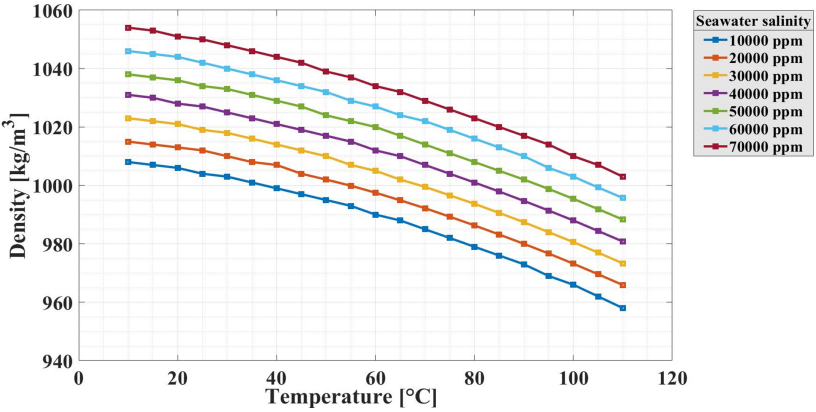

Figure 5.2: Variations in the seawater density as a function of temperature and concentration

Table 5.1: Variations in the seawater density as a function of temperature and TDS

T [°C]	10000	20000	30000	40000	50000	60000	70000
10	1008	1015	1023	1031	1038	1046	1054
15	1007	1014	1022	1030	1037	1045	1053
20	1006	1013	1021	1028	1036	1044	1051
25	1004	1012	1019	1027	1034	1042	1050
30	1003	1010	1018	1025	1033	1040	1048
35	1001	1008	1016	1023	1031	1038	1046
40	999	1007	1014	1021	1029	1036	1044
45	997	1004	1012	1019	1027	1034	1042
50	995	1002	1010	1017	1024	1032	1039
55	993	999.9	1007	1015	1022	1029	1037
60	990	997.5	1005	1012	1020	1027	1034
65	988	994.9	1002	1010	1017	1024	1032
70	985	992.2	999.5	1007	1014	1022	1029
75	982	989.3	996.6	1004	1011	1019	1026
80	979	986.3	993.7	1001	1008	1016	1023
85	976	983.2	990.6	997.9	1005	1013	1020
90	973	980	987.4	994.7	1002	1010	1017
95	969	976.7	984.1	991.4	998.8	1006	1014
100	966	973.2	980.6	988	995.4	1003	1010
105	962	969.6	977	984.4	991.9	999.3	1007
110	958	965.9	973.3	980.8	988.3	995.7	1003

As for the seawater dynamic viscosity, the empirical equation suggested in [35] is used, given as:

$$\mu_{sw} = \mu_w \cdot \mu_r \cdot 10^{-3} \tag{5.29}$$

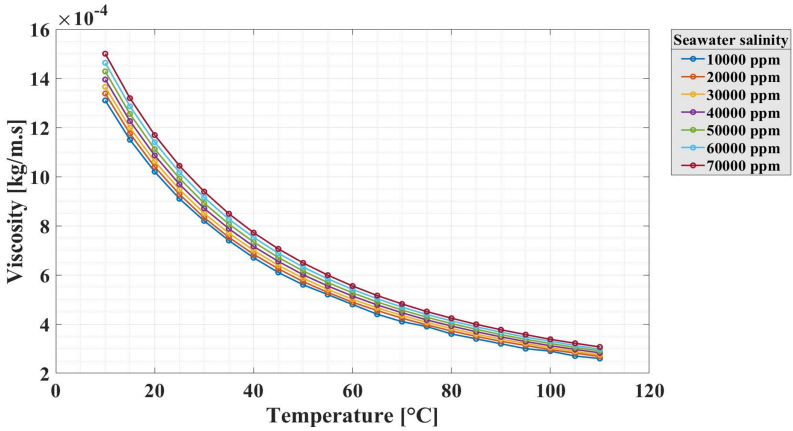

Figure 5.3: Variations in the seawater density as a function of temperature and concentration

where

$$ln(\mu_{sw}) = -3.79418 + \frac{604.129}{139.18 + T} \tag{5.30}$$

$$\mu_r = 1 + \left(V_1 \cdot \frac{C}{1000}\right) + \left(V_2 \cdot \frac{C}{1000}\right) \tag{5.31}$$

$$V_1 = 1.474 \times 10^{-3} + 1.5 \times 10^{-5} \cdot T - 3.927 \times 10^{-8} \cdot T^2 \tag{5.32}$$

$$V_2 = 1.0734 \times 10^{-5} - 8.5 \times 10^{-8} \cdot T + 2.23 \times 10^{-10} \cdot T^2 \tag{5.33}$$

It should be noted that in these equations, T is expressed in °C. By applying the above equations, the variations in seawater dynamic viscosity as a function of feed temperature and concentration are illustrated in Fig. 5.3 and Table 5.2.

The cross-flow velocity can be derived using (5.34), where h_c is the channel height and w represents the channel width [36].

$$v_{c,x} = \frac{Q_{fb,x}}{h_c \cdot w} \tag{5.34}$$

The hydraulic diameter is calculated using (5.35) [37].

$$d_h = \frac{h_c \cdot w}{(2h_c + 2w)} \tag{5.35}$$

Table 5.2: Variation in seawater viscosity as a function of temperature and TDS

T [°C]	10000	20000	30000	40000	50000	60000	70000
10	1.31	1.338	1.365	1.395	1.428	1.463	1.5
15	1.15	1.175	1.199	1.226	1.255	1.286	1.319
20	1.02	1.04	1.062	1.086	1.112	1.14	1.169
25	0.91	0.928	0.948	0.969	0.993	1.018	1.044
30	0.82	0.833	0.851	0.871	0.892	0.915	0.939
35	0.74	0.753	0.77	0.788	0.807	0.827	0.849
40	0.67	0.684	0.7	0.716	0.734	0.753	0.772
45	0.61	0.625	0.639	0.655	0.671	0.688	0.706
50	0.56	0.573	0.587	0.601	0.616	0.632	0.649
55	0.52	0.529	0.541	0.555	0.569	0.584	0.599
60	0.48	0.489	0.501	0.514	0.527	0.541	0.555
65	0.44	0.455	0.466	0.478	0.49	0.503	0.516
70	0.41	0.424	0.435	0.446	0.457	0.469	0.482
75	0.39	0.397	0.407	0.417	0.428	0.439	0.451
80	0.36	0.372	0.382	0.392	0.402	0.413	0.424
85	0.34	0.35	0.359	0.369	0.379	0.389	0.399
90	0.32	0.33	0.339	0.348	0.357	0.367	0.377
95	0.3	0.313	0.321	0.329	0.338	0.347	0.357
100	0.29	0.296	0.304	0.312	0.321	0.33	0.338
105	0.27	0.282	0.289	0.297	0.305	0.313	0.322
110	0.26	0.268	0.275	0.283	0.291	0.298	0.307

Diffusivity is calculated using (5.36), where $D_{\mathrm{f},25}$ represents the diffusivity of seawater at 25 °C, and μ_{25} is the viscosity of seawater at 25 °C [37]. This equation also accounts for the temperature dependency of diffusivity.

$$D_{\mathrm{f}} = D_{\mathrm{f},25} \frac{T_{\mathrm{f}} + 273.15}{25 + 273.15} \frac{\mu_{25}}{\mu} \tag{5.36}$$

Given the significant effect of temperature on the fluxes in the RO system, a correction factor is introduced to modify water and solute permeability, ensuring more precise calculations of water and solute fluxes. The empirical relationships expressed in (5.37) and (5.38) are used to modify the values of $k_{\mathrm{w},25}$ and $k_{\mathrm{s},25}$, respectively, at different feed water temperatures [37].

$$k_{\mathrm{w}} = k_{\mathrm{w},25} \times \exp\left(\mathrm{k_{wt}}\left(\frac{1}{\mathrm{T_f} + 273.15} - \frac{1}{25 + 273.15}\right)\right) \tag{5.37}$$

$$k_{\mathrm{s}} = k_{\mathrm{s},25} \times \exp\left(\mathrm{k_{st}}\left(\frac{1}{\mathrm{T_f} + 273.15} - \frac{1}{25 + 273.15}\right)\right) \tag{5.38}$$

In (5.37) and (5.38), k_{wt} and k_{st} are temperature coefficients for water and solute transport, successively. These coefficients are derived through regression analysis of water permeability data obtained across various temperatures.

Because of head loss through the channel, the pressure in the feed-brine channel also drops. The head loss over an incremental length of the membrane, which is a function of feed velocity, can be determined using (5.39), where δ_{hl} is the head loss coefficient [36].

$$h_{l,x} = \delta_{\mathrm{hl}} v_{\mathrm{c,x}}^2 dx \tag{5.39}$$

The permeate flow rate and the mass of solute passing through the membrane are calculated as the product of water flux and solute flux, respectively, and the area of an increment, as described in (5.40) and (5.41) [36].

$$Q_{p,x} = J_{w,x} w dx \tag{5.40}$$

$$M_{s,x} = \frac{1}{3600} J_{s,x} w dx \tag{5.41}$$

Once (5.1)–(5.41) are solved for all increments, the overall performance of the RO system can be evaluated. The total permeate production of an RO element is obtained by summing the permeate produced in each increment, as shown in (5.42) [36].

$$Q_p = \sum_{x=1}^{\mathrm{num}} Q_{p,x} \tag{5.42}$$

Likewise, the salt transfer through the membrane in one element is the sum of salt that migrates through the membrane in each increment, as expressed in (5.43) [36].

$$M_s = \sum_{x=1}^{\mathrm{num}} M_{s,x} \tag{5.43}$$

Based on these parameters, the permeate concentration can then be calculated using (5.44) [36].

$$C_p = \frac{J_s}{J_w \times 1000} \tag{5.44}$$

Finally, the performance of the RO system is mainly evaluated using two key factors, namely, the recovery, R_{r} and salt rejection, S_{r}, as quantified in (5.45) and (5.46), respectively [36].

$$R_{\mathrm{r}} = \frac{Q_{\mathrm{p}}}{Q_{\mathrm{f}}} \tag{5.45}$$

$$S_{\mathrm{r}} = 1 - \left(\frac{C_{\mathrm{p}}}{C_{\mathrm{m}}} \right) \tag{5.46}$$

5.5 RO Model Validation

In this section, the RO model, developed using the discussed equations in the previous section and simulated in MATLAB/Simulink, is validated against experimental data as well as the results obtained from WAVE commercial software (formerly known as ROSA), as reported in [38] and [39]. The reference [38] is selected due to the availability of both experimental and WAVE results across a broad range of operating conditions. Although WAVE is a software based on the mathematical modelling of RO systems, it is widely recognised as one of the most reliable tools in the water treatment field [38, 40]. Nevertheless, the operating points examined in [38] involve water with lower TDS values, more comparable to brackish water than seawater, resulting in lower feed pressure compared to seawater desalination. To ensure the model is valid for higher TDS levels, such as those in seawater, the reference [39] is also included, as it provides experimental results of high-pressure seawater desalination.

Regarding reference [38], the results from the developed model in this study are compared with those from experimental data and WAVE at two different feed pressures, 7 bar and 11 bar, each at feed concentrations of 2000, 3000, 4000, and 5000 ppm. The range of conditions is chosen to ensure that the model is valid under various operating scenarios. To this end, the recovery, indicating

Table 5.3: Specifications of the RO unit used for the validation based on reference [38]

Parameter	Value	Unit
A_{mem}	37.2	m^2
C_{f}	2000–5000	ppm
$D_{\mathrm{f},25}$	1.611×10^{-9}	m^2/s
h_{c}	0.125	mm
h_{l}	0.1	bar
i_{p}	2	-
$k_{\mathrm{s},25}$	2×10^{-5}	m/h
k_{st}	-3281	K
$k_{\mathrm{w},25}$	2.85	$\mathrm{L}/(\mathrm{m}^2.\mathrm{h.bar})$
k_{wt}	-2849	K
l	1.02	m
num	10	-
P_{f}	7–11	bar
Q_{f}	26–45	$\mathrm{m}^3/\mathrm{day}$
T_{f}	15	°C
Φ	1	-

the quantity of treated water produced by the RO system, is used as one of the verification parameters. Moreover, to ensure the model accurately estimates water quality, the salt rejection of the RO model is compared with the experimental data and WAVE software results. These two factors are selected for comparison because, in a coupled model of an RO system and electrolyser, accurately estimating the recovery rate and salt rejection is essential, as it ensures that the electrolyser consistently receives water of the necessary quantity and quality. The employed parameters for RO validation, based on reference [38], are listed in Table 5.3.

In Fig. 5.4, the model is compared with experimental data and WAVE at an experimental pressure of 7 bar. Fig. 5.4(a) presents the recovery obtained from the model alongside the experimental and WAVE results, while Fig. 5.4(b) illustrates the comparison of salt rejection and permeate concentration between the developed model, experimental data and WAVE.

Fig. 5.5 shows the results derived from the model in addition to the experimental and WAVE results at the experimental pressure of 11 bar. The comparison between the recovery values obtained from the model, experiment and WAVE is depicted in Fig. 5.5(a), and Fig. 5.5(b) shows the comparison of salt rejections as well as permeate concentrations.

In Fig. 5.4(a) and Fig. 5.5(a), as feed concentration increases at a constant feed pressure, the recovery decreases. This occurs because, according to (5.3), (5.6), and (5.7), at constant feed pressure, a rise in feed concentration increases the osmotic pressure, which in turn reduces the driving force, resulting in a lower permeate flow rate and thus a lower recovery rate.

As for water quality in Fig. 5.4(b) and Fig. 5.5(b), at a constant feed pressure, increasing the feed concentration leads to a decrease in permeate flow rate. Additionally, considering (5.8) and (5.9), the salt passage through the membrane increases. Consequently, based on (5.44), the permeate concentration also rises, leading to a reduction in salt rejection as described in (5.46).

Regarding the accuracy of the model, the average relative error between the model, the experiment and WAVE is calculated using the same approach as in (4.69). Fig. 5.6 displays the average relative error for the specified feed concentrations at feed pressures of 7 bar and 11 bar, as well as the overall average relative error across all investigated cases for both feed pressures.

In Fig. 5.6, the average relative error for the recovery between the model and both the experiment and WAVE at feed pressures of 7 bar and 11 bar is 5.16% and 2.13%, respectively, resulting in an overall average relative error of 3.64% across all investigated cases with different feed concentrations and pressures. Besides, the average relative error for salt rejection between the model and the experiment, as well as between the model and WAVE, is 1.28% and 1.55% at 7 bar, successively. At 11 bar, the average relative error for salt rejection between the model and experiment is 1.69%, and between the model

and WAVE, it is 0.32%. This yields an overall average relative error of 1.48% between the model and experiment, and 0.93% between the model and WAVE for salt rejection across all the explored cases.

The discrepancy between the model and experimental results, as well as the obtained results from WAVE, primarily arises from the fact that the developed model employs parameters for seawater, such as viscosity and density, which

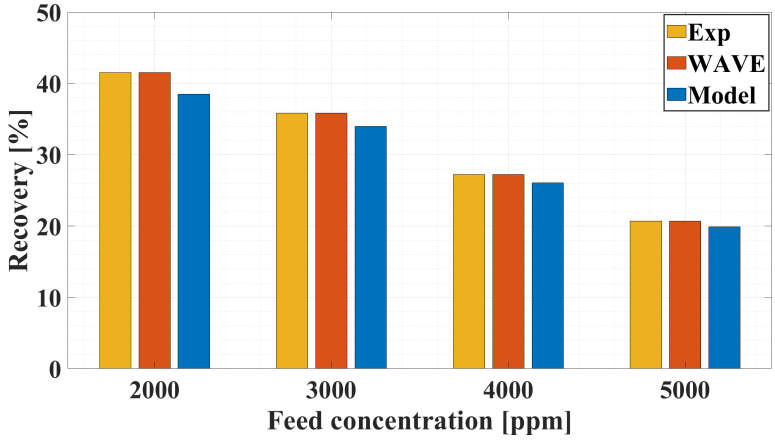

(a) Comparison of the recovery rate between the developed model, experimental data, and WAVE at 7 bar

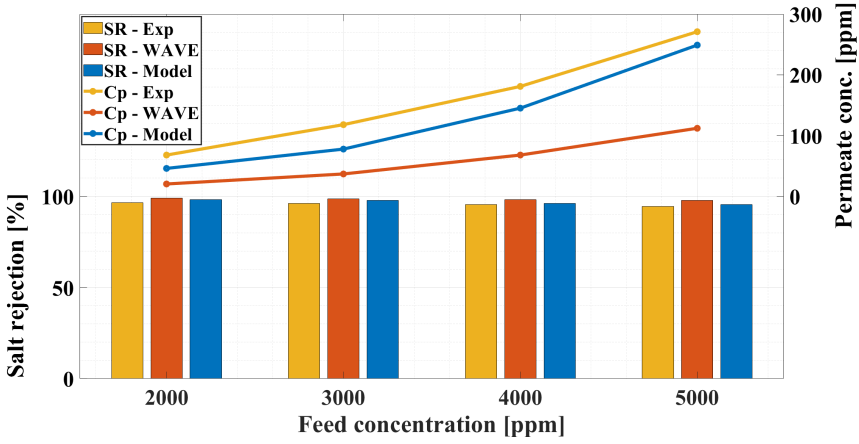

(b) Comparison of salt rejection and permeate concentration between the developed model, experimental data, and WAVE at 7 bar

Figure 5.4: Comparison of the developed model, experimental data, and WAVE at the experimental pressure of 7 bar

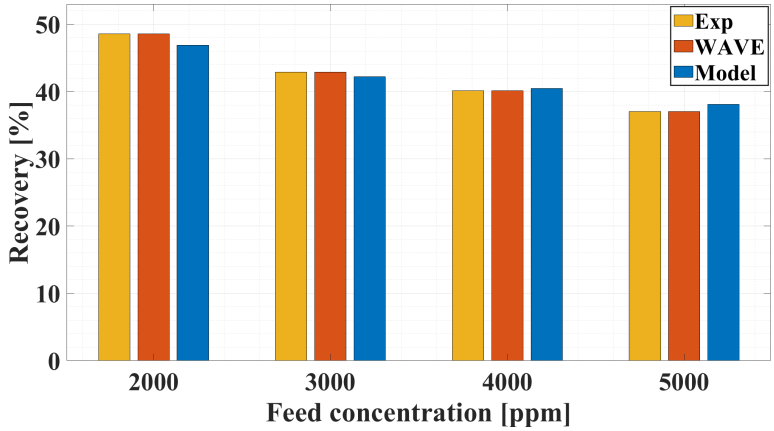

(a) Comparison of the recovery rate between the developed model, experimental data, and WAVE at 11 bar

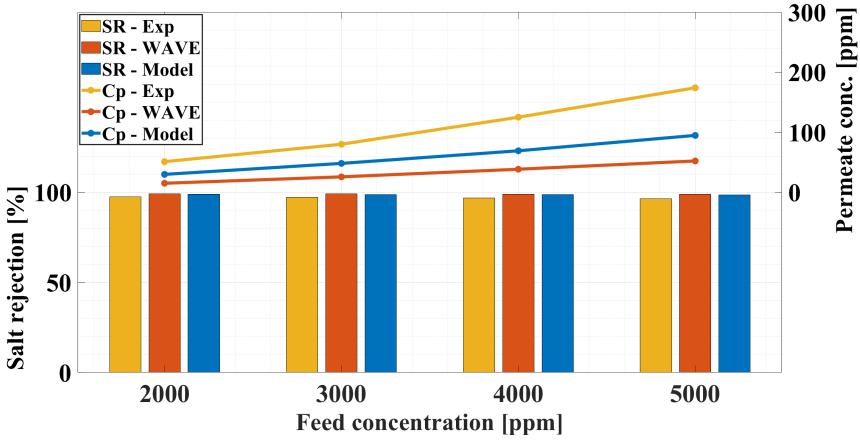

(b) Comparison of salt rejection and permeate concentration between the developed model, experimental data, and WAVE at 11 bar

Figure 5.5: Comparison of the developed model, experimental data, and WAVE at the experimental pressure of 11 bar

contains a concentration of roughly 35000 ppm. However, the low concentration of water utilised in the experiment is close to that of brackish water. Moreover, the WAVE software employs experimental equations for the associated membrane, whereas this model relies on mathematical equations to govern the RO process. Regarding the higher error observed at lower concentrations, as can be seen in Table 5.1 and Table 5.2, it can be attributed to the fact that the accurate data for seawater is only available starting from 10000 ppm, resulting

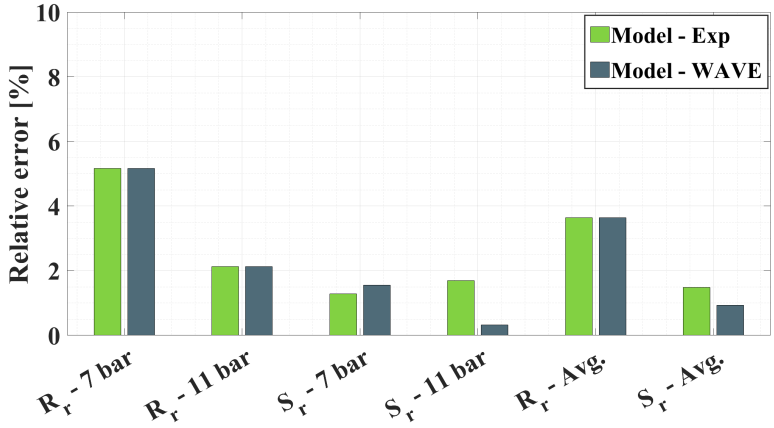

Figure 5.6: Average relative error between the developed RO model, experiment, and WAVE

in higher error when extrapolating to lower concentrations.

To confirm the applicability of the developed model at higher TDS values, similar to those of seawater, the obtained results from the developed model are compared with the experimental data, detailed in [39]. The same parameters as the previous case, i.e., the recovery and salt rejection, are chosen as the comparison criteria. The utilised parameters for RO validation based on the reference [39] are summarised in Table 5.4.

Fig. 5.7 shows the results obtained from the model alongside experimental results for six various cases. The feed pressure is 50 bar for cases 1 and 4, 55 bar for cases 2 and 5, and 60 bar for cases 3 and 6. Additionally, the feed concentration for the first three cases is 25000 ppm, while for the last three cases it is 35000 ppm.

Fig. 5.7(a) compares the recovery rates derived from the model and experiment, while Fig. 5.7(b) presents a comparison of salt rejections and permeate concentrations obtained from both the model and the experimental results.

In Fig. 5.7(a), it is evident that, at a constant feed concentration, the recovery increases as feed pressure rises from case 1 to 3 and from case 4 to 6. This is due to the increase in the NDP, which enhances water passage through the membrane, as described by (5.3). Moreover, at a constant feed pressure, such as in cases 1 and 4, an increase in feed concentration raises the osmotic pressure, which reduces the NDP and, in turn, decreases the water passage through the membrane according to (5.3).

About the accuracy of the model, using (4.69), the relative error between the model and experimental results is derived, as shown in Fig. 5.8. The average relative errors for recovery and salt rejection across all explored cases are 2.74%

Table 5.4: Specifications of the RO unit used for the validation based on reference [39]

Parameter	Value	Unit
A_{mem}	1.14	m^2
C_{f}	25000–40000	ppm
$D_{\text{f,25}}$	1.611×10^{-9}	m^2/s
h_{c}	0.043	cm
h_{l}	0.1	bar
i_{p}	2	-
$k_{\text{s,25}}$	2×10^{-4}	m/h
k_{st}	-3281	K
$k_{\text{w,25}}$	2.20	L/(m^2.h.bar)
k_{wt}	-2849	K
l	0.94	m
num	10	-
P_{f}	50-80	bar
Q_{f}	14.50–15.30	m^3/day
T_{f}	20	°C
Φ	1	-

and 0.13%, respectively, which validate the accuracy of the developed model.

5.6 SWRO-PEM Electrolyser Coupled Model

After ensuring that the developed models are sufficiently accurate, in this section, the PEM electrolyser and RO models are upscaled to create a more realistic scenario. Afterwards, the models are coupled, and the performance of the integrated system is assessed.

5.6.1 PEM Electrolyser Upscaling

In this thesis, a 2 MW PEM electrolyser is considered, which is a typical capacity for commercial PEM electrolysers for integrating with RESs [41]. For this purpose, the validated cells from Chapter 4 are used as the basis for upscaling. Also, the currently feasible ratings and sizes for PEM electrolysers reported by IRENA have been utilised to ensure the scenario is as realistic as possible [41]. Although the parameter tuning in Chapter 4 relies on experimental data from small lab-scale setups, the governing electrochemical and thermodynamic principles remain the same across scales. The main model parameters, such as activation losses, depend primarily on cell-level physics rather than

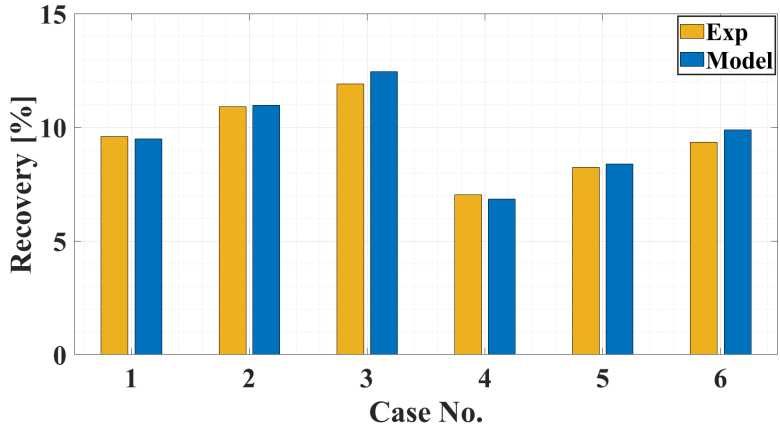

(a) Comparison of recovery rate between the developed model and experimental results

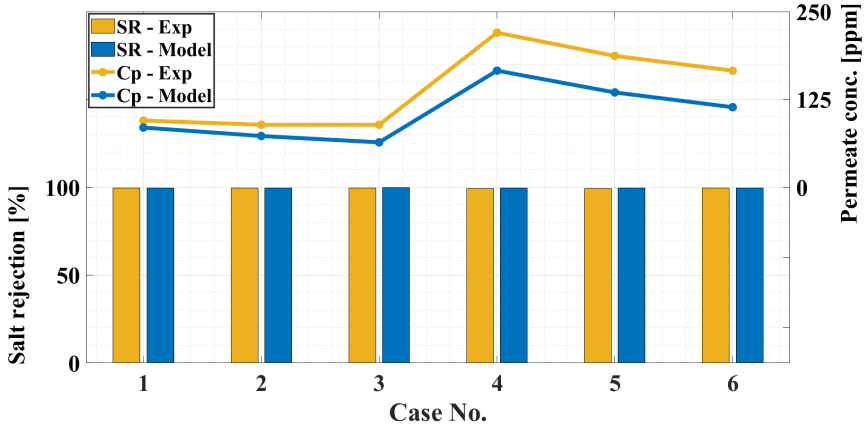

(b) Comparison of salt rejection and permeate concentration between the developed model and experimental results

Figure 5.7: Comparison between the developed model and experimental results for seawater

stack or plant size. Therefore, due to the limited availability of industrial-scale electrolyser data, which are mostly confidential, the potential loss of accuracy when scaling up is considered negligible in this study.

It is notable that exploring RESs type and power input variations to the electrolyser, which affect its sizing, is beyond the scope of this study. However, the approach presented in this thesis allows for modelling various sizing scenarios based on specific applications. Further details on scaling the electrolyser

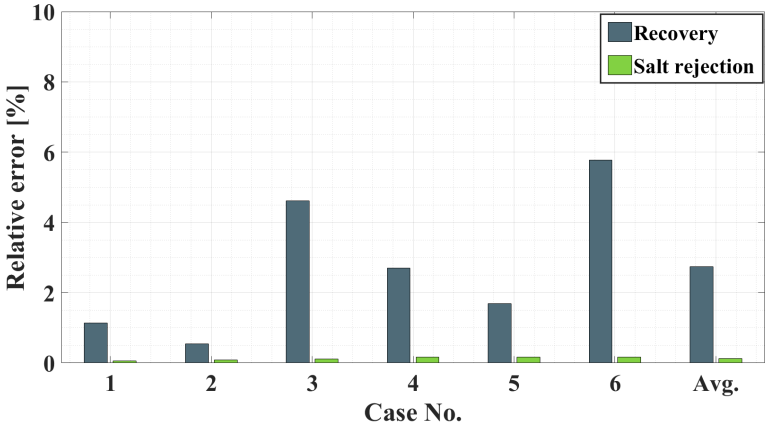

Figure 5.8: Average relative error between the developed RO model and experimental results for seawater

capacity based on RESs type and power input capacity can be found in [42] and [43].

To start with, the PEM stack voltages around 0.9–1 kV are deemed acceptable, with 1 kV assumed in this study. Given the assumed capacity of the electrolyser, this yields a rated current of 2 kA flowing in the stack. To maintain a reasonable current density of 2 A/cm^2 at rated capacity, the active area of the cell validated in Chapter 4 is enlarged to 0.1 m^2. To attain the aforementioned voltage using the enlargened cells, 420 cells need to be stacked. This results in approximately 2.4 V per cell, which is within the accepted range of 1.4-2.5 V [41]. Additionally, the partial load operation of the PEM electrolyser is taken into account. To eliminate the start-up and shut-down time for nitrogen purging, a minimum operation capacity of 10% is maintained for the electrolyser [44]. Thus the electrolyser operates between 10% and 100% load, resulting in a current density ranging from 0.2 to 2 A/cm^2, and thus a current varying from 0.2 to 2 kA. The main parameters of the PEM stack are detailed in Table 5.5.

5.6.2 SWRO Upscaling

Theoretically, based on (4.6) and (4.15), to produce $nI/2F$ moles of hydrogen per second via electrolysis, $nI/2F$ moles of water per second is required. Considering the molar weights of water and hydrogen, this translates to 9 kg of water, or roughly 9 L, for the generation of 1 kg of hydrogen. Nonetheless, more water is injected into the commercial electrolyser, for example, 10 L for Siemens-Silyzer-300, 11.1 L for Hydrogenics-HyLZER and CHE hydrogen

Table 5.5: Specifications of the upscaled PEM electrolyser

Parameter	Value	Unit
A	0.1	m^2
j	0.2–2	A/cm^2
n	420	-
P_{an}	1	bar
P_{ca}	30	bar
Power	2	MW
V_{stack}	1	kV

generation plant, and 15.5 L for Hydrogenics' PEM electrolyser [45].

This additional water is injected for several reasons. It cools the electrolyser and removes excess heat, maintains membrane hydration to preserve high conductivity, and compensates for evaporation losses caused by system inefficiencies. Moreover, part of the water bypasses electrolysis and migrates through the membrane, as discussed in Section 4.3.3. Thus, a safety margin is typically included for this extra water. Based on the aforementioned amount of water needed for commercial electrolysers, this study applies a safety factor of 1.25 for the additional required water. Given the known number of cells in the upscaled PEM electrolyser and the operating current, using the considered safety factor, the needed amount of water can be calculated. For the rated operation of the electrolyser, around 8.5 m^3/day of pure water is needed, decreasing to approximately 4.25, 2.12, and 0.85 m^3/day for 50%, 25% and 10% operation of the PEM electrolyser, as the required water changes linearly with respect to the current.

In terms of water quality, conventional PEM electrolysers are typically supplied with water having a purity of around less than 10 ppm TDS [16]. Using water with a higher TDS accelerates the ageing rate and adversely affects the performance of the electrolyser. Thus, in this study, the PEM electrolyser is fed with water having a TDS of less than 5 ppm to provide an extra level of precaution.

In RO systems, the brine from one stage can be fed into a subsequent stage to enhance the recovery rate, a process known as a multistage or brine-staged system. Alternatively, the permeate from one stage can be passed to a second stage to improve solute removal, referred to as a two-pass or permeate-staged system. Since the water source in this study is seawater with a high TDS of around 35000 ppm, reaching a TDS of less than 5 ppm is challenging. Nevertheless, it has been demonstrated that passing the permeate from the first stage of SWRO through a second stage can reduce the TDS to below 5 ppm [16]. Hence, this thesis considers a two-pass SWRO system to achieve a TDS of less

Table 5.6: Specifications of the upscaled SWRO unit

Parameter	Value	Unit
$C_{\mathrm{f,1st}}$	35000	ppm
$k_{\mathrm{s,25,1st}}$	2×10^{-5}	m/h
$k_{\mathrm{s,25,2nd}}$	5×10^{-5}	m/h
$k_{\mathrm{w,25,1st}}$	2.85	L/(m^2.h.bar)
$k_{\mathrm{w,25,2nd}}$	3.6	L/(m^2.h.bar)
$Q_{\mathrm{f,1st}}$	20	m^3/day
$Q_{\mathrm{p,rated}}$	8.5	m^3/day
$R_{\mathrm{r,rated,1st}}$	50	%
$R_{\mathrm{r,rated,2nd}}$	85	%
Stages	2	-
T_{f}	10	°C

than 5 ppm.

As for the recovery, the parameters are adjusted to achieve a recovery of 50% for the first pass and 85% for the second pass under rated conditions, which are standard values for high-pressure and low-pressure RO systems, respectively [36].

The main characteristics of the SWRO unit are presented in Table 5.6.

5.6.3 Coupling the Upscaled Systems

There are two procedures for controlling the permeate flow rate in an RO system, i.e. changing the feed flow rate, and altering the feed pressure. However, the feed pressure is the primary variable that governs the permeate flow rate, as the driving force of the process can be directly regulated by adjusting the feed pressure, while changes in the feed flow rate have a less direct impact on the feed flow rate, as shown in Fig. 5.9. Consequently, in this study, the permeate flow rate is controlled by adjusting the feed pressure. It is also worth noting that Fig. 5.9 is generated based on the RO element described in Section 5.4 at the feed concentration of 5000 ppm.

Additionally, the P_{f}-Q_{p} curve in Fig. 5.9 exhibits an almost linear relationship between the permeate flow rate and the feed pressure, as also verified in [46] for various feed concentrations. This linearity offers the advantage of using a lookup table to control the RO system when coupled with the electrolyser during single-system simulations. Given that the integrated model is primarily designed for large-scale simulations, which include multiple complex power system elements, such as generators and transformers, this approach significantly enhances computational efficiency. In this method, the feed pressure of each RO pass is regulated through a control signal that dynamically responds

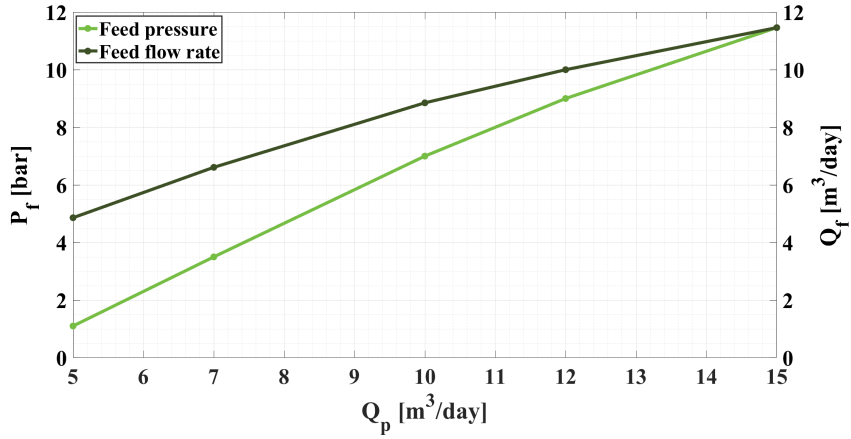

Figure 5.9: Variation of permeate flow rate as a function of feed pressure and feed flow rate

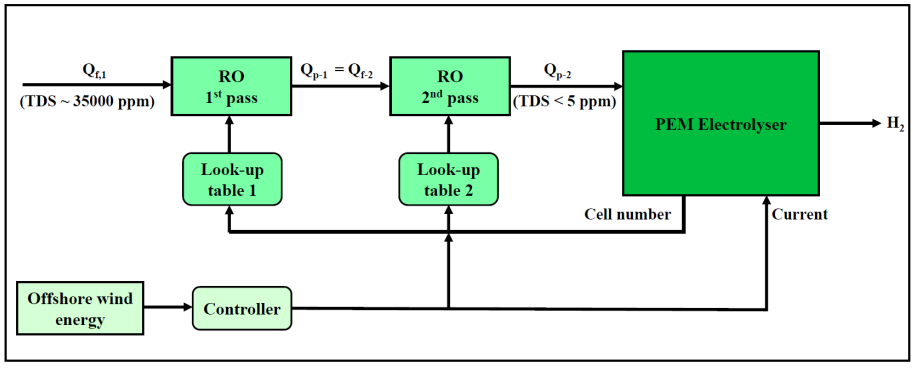

Figure 5.10: Process scheme of the SWRO-PEM electrolyser model

to variations in the electrolyser current to meet its water demand.

To establish this control strategy, prior to coupling the PEM electrolyser and SWRO models, the operation of both the first and second passes was examined across a range from 10% to 100% capacity, with a resolution of 5%, to be consistent with the upscaled PEM electrolyser. The process scheme of the SWRO unit and an overview of the integrated SWRO-PEM model are shown in Fig. 5.10 and Fig. 5.11, respectively.

In summary, the operation of the two-pass SWRO system is first evaluated across its operating range, from 10% to full capacity. The integrated SWRO-PEM system is then implemented, as depicted in Fig. 5.10. Due to the fluctuating nature of offshore wind energy, the power output from the offshore

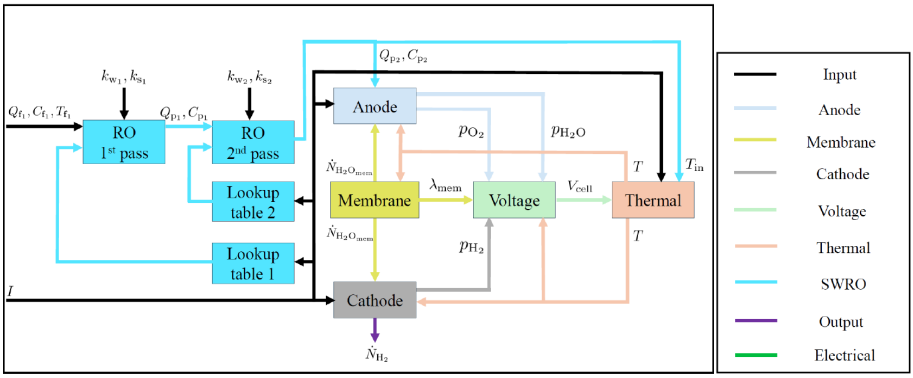

Figure 5.11: An overview of the coupled SWRO-PEM electrolyser model

wind turbines block, shown in Fig. 5.10, varies accordingly, which in turn affects the output of the current controller in the following block of the same figure. This current, combined with the number of cells in the electrolyser stack, determines the required water flow from the SWRO system, as described by (4.6). The current values are subsequently mapped, using lookup tables 1 and 2, to the feed pressures of the first and second RO passes, respectively. As shown in Fig. 5.9, this approach effectively regulates the permeate flow rates of both passes.

It should be noted that this study does not consider the current controller presented in Fig. 5.10; instead, the current waveform is directly generated and applied to the electrolyser. A controller scheme for translating power to current based on grid frequency variations for providing frequency ancillary services has been proposed in [44].

5.7 Results

The step response of the electrolyser, starting from no load and then shifting to full load, 50% of full load, 25% of full load, 10% of full load, and subsequently ramping back up to 25%, 50%, and 100% of full load, is shown in Fig. 5.12. While Fig. 5.12(a) shows the applied step current waveform, Fig. 5.12(b) and Fig. 5.12(c) depict the voltage on the 2 MW PEM stack, and the power consumed by the electrolyser, respectively.

It is important to note that the response time of the electrolyser is slower at lower current densities. This can be explained by the fact that, at lower current densities, activation overvoltage is the dominant term in the total stack voltage, whereas, at higher current densities, ohmic overvoltage becomes the

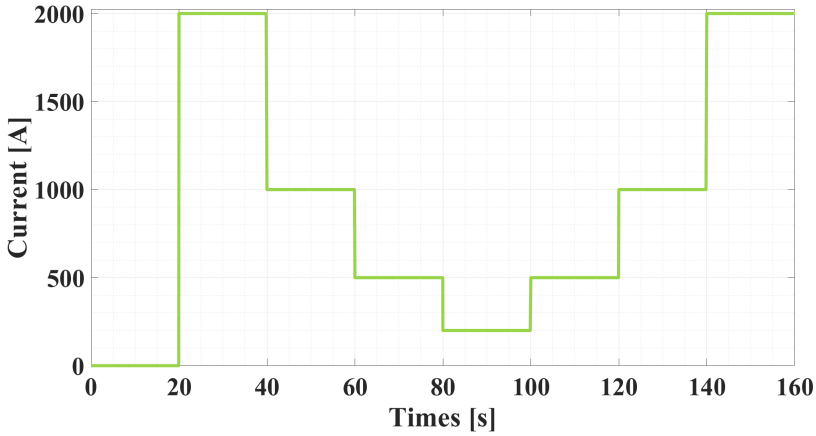

(a) Applied step current waveform

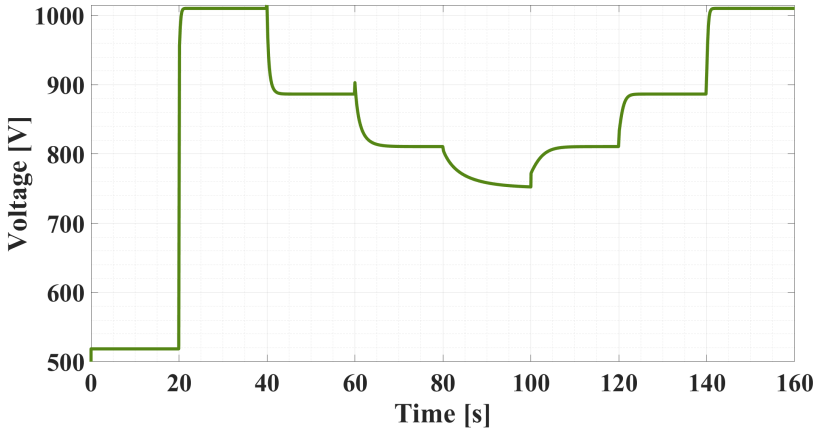

(b) Dynamic voltage waveform

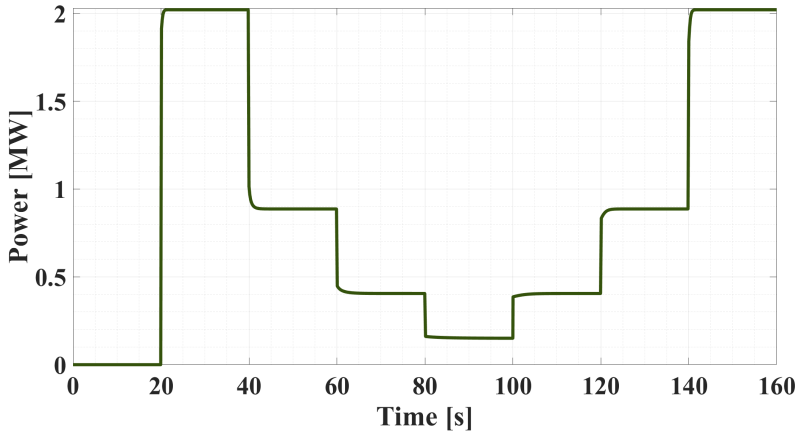

(c) Dynamic power waveform

Figure 5.12: Dynamic step response of the 2 MW PEM electrolyser

main contributor to the stack voltage. Since activation overvoltage follows an exponential curve, at lower loads, changes in the current cause the stack voltage to behave more like the activation overvoltage pattern, leading to a more gradual response. On the other hand, at higher loads, when current density changes, the response is faster because ohmic overvoltage, which is directly proportional to the current, has a more immediate impact on the stack voltage.

The behaviour of the upscaled SWRO system suitable for the 2 MW PEM electrolyser is presented in Fig. 5.13. While Fig. 5.13(a) shows the recovery ratios of the first and second passes of the SWRO system, Fig. 5.13(b) and Fig. 5.13(c) depict the salt rejection and permeate concentration of the two passes. This figure corresponds to the changes depicted in Fig. 5.12.

It is worth mentioning that, although the first pass is able to produce fresh water with a TDS of around 150 ppm at its highest, this level is still insufficient for the PEM electrolyser, which requires a TDS of less than 5 ppm. Regardless, as shown in Fig. 5.13(c), the permeate concentration after the second pass is below 5 ppm even at its worst.

As mentioned earlier, adjusting the feed pressure regulates the NDP, and hence the required amount of water. When the feed pressure is decreased at a constant feed flow rate, the permeate flow rate is reduced, leading to a lower recovery ratio at lower loads, as shown in Fig. 5.13(a). Additionally, considering Fig. 5.13(b), decreasing feed pressure reduces salt rejection, yielding a higher permeate concentration in both passes. This occurs because, when the feed pressure is decreased, the permeate from each pass becomes more saline, leading to an increased level TDS level.

Furthermore, it can be seen that the first pass exhibits a lower recovery ratio but higher salt rejection compared to the second pass. This is expected since the membrane utilised in the first pass typically has smaller pores, resulting in a higher salt rejection and reduced water passage, thereby a lower recovery rate. The choice of the membrane with smaller pores is because the first feed is more saline. As shown in Fig. 5.13(c), the first pass reduces the feed concentration from 35000 ppm to a permeate concentration of around 150 ppm at its worst. In contrast, the second pass commonly handles feed water with a lower concentration, similar to brackish water. Therefore, to increase the recovery rate, the pores of the membrane are larger. In the modelling stage, this membrane behaviour is simulated by combining a lower value of k_s (indicating higher salt rejection) with a lower value of k_w for the first pass compared to the second one, and vice versa for the second pass, as shown in Table 5.6. It is important to note that the lower recovery in the first pass, compared to the second, can also be explained by the high salt concentration of seawater, which increases the osmotic pressure.

To verify the accuracy of the control method in estimating the required amount of water, the theoretical water demand of the electrolyser is compared

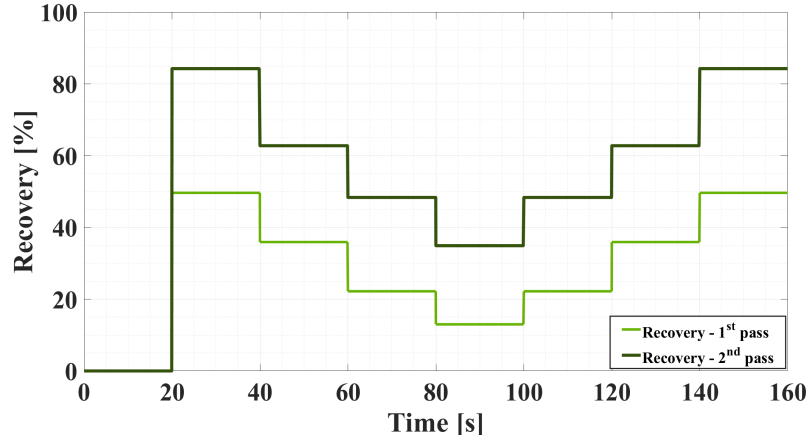

(a) Recovery rate of the first and second passes

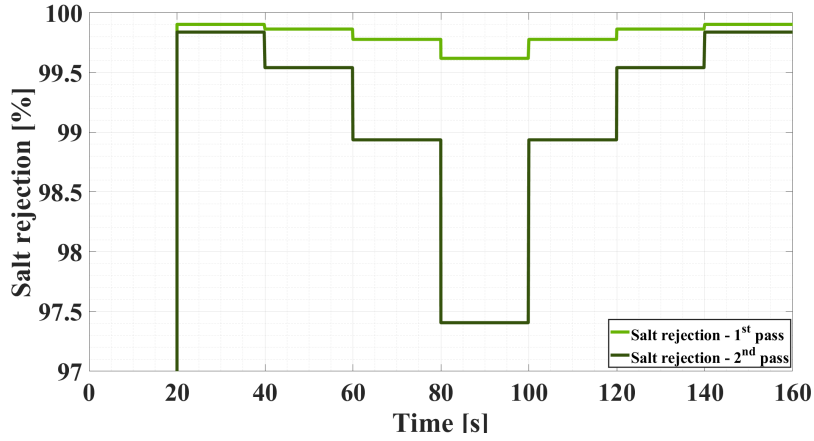

(b) Salt rejection of the first and second passes

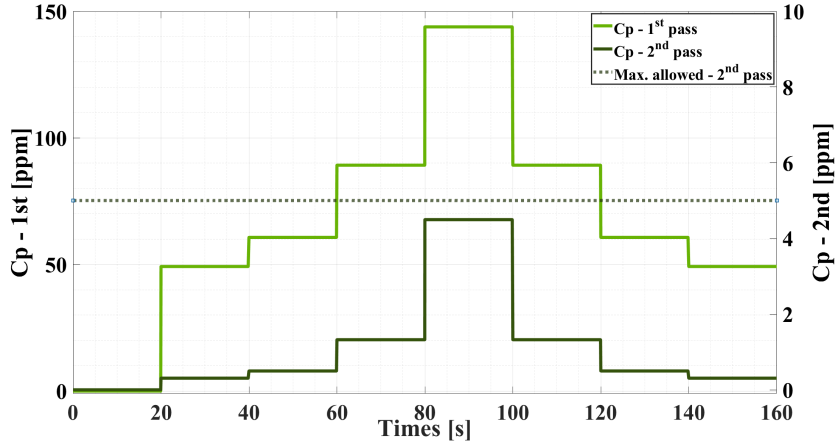

(c) Permeate concentration of the first and second passes

Figure 5.13: Behaviour of the two-pass SWRO system

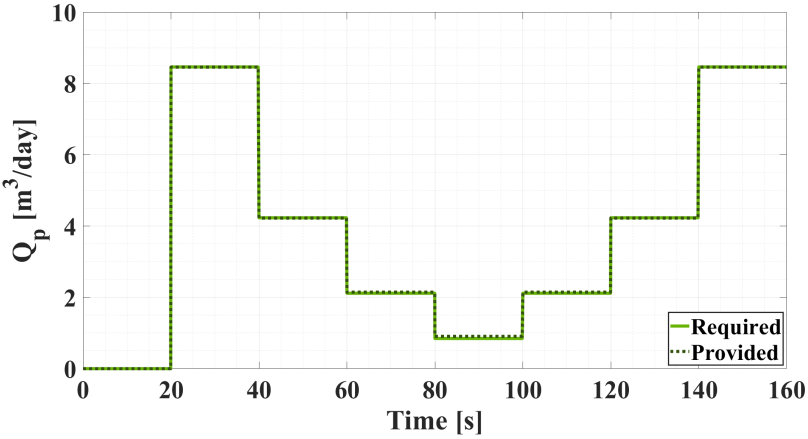

(a) Water demand of the PEM electrolyser and amount provided by the SWRO unit

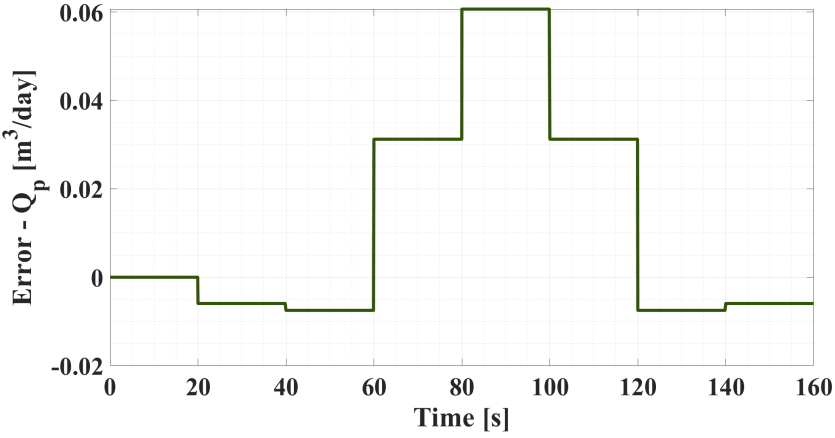

(b) Discrepancy between the water demand of the PEM electrolyser and the amount provided by the SWRO unit

Figure 5.14: Comparison between the required water for the PEM electrolyser and the amount provided by the SWRO system

with the actual amount provided by the control method, as depicted in Fig. 5.14. While Fig. 5.14(a) shows the comparison of the actual water demand, derived using (4.6) with a safety factor of 1.25, and the estimated amount of water, Fig. 5.14(b) illustrates the discrepancy between these two values, yielding an average relative error of 1.20% over the evaluated timeframe. The results indicate that the control method can effectively estimate the actual water required.

5.8 Conclusions

In this chapter, a coupled model of an SWRO system and a PEM electrolyser was developed in MATLAB/Simulink, which facilitates further studies on seawater electrolysis with upfront water treatment. Moreover, the model can be integrated into large-scale power system simulations without introducing excessive complexity.

By following the steps described in this chapter, the offshore hydrogen production system can be examined under different operating conditions upon sizing the electrolyser based on factors such as available input power, available offshore area, and hydrogen demand. This integrated model is essential for advancing offshore hydrogen, offering important insights into green hydrogen production using seawater as the feedwater.

Using the solution-diffusion method, a model for the SWRO system was developed. Thereafter, validation against the experimental data at low TDS values exhibited an average relative error of 3.64% for recovery and 1.48% for salt rejection. When compared with WAVE software, the model demonstrated an average relative error of 3.64% for recovery and 0.96% for salt rejection. At seawater TDS levels, the model showed an average relative error of 2.74% and 0.13% for recovery and salt rejection, respectively, compared to experimental results.

Following validation, the PEM electrolyser and SWRO models were upscaled to simulate a realistic scenario: a 2 MW electrolyser containing 420 cells coupled with a two-pass SWRO system, with rated recovery rates of 50% and 85% for the first and second pass, respectively, and a production capacity of 8.5 m^3/day. To efficiently couple the validated models and enhance computational efficiency, an uncomplicated control method based on lookup tables, generated before coupling the models, was proposed, taking advantage of the nearly linear relationship between feed pressure and permeate flow rate. The water injected into the electrolyser was delivered at a maximum of 4.5 ppm TDS, and the control method estimates the required water quantity with a 1.20% error.

Notably, the integrated model allows for adjustments to various parameters, such as feed flow rate, feed concentration, feed temperature, etc, as well as electrolyser parameters like inlet temperature, current density, etc.

Nevertheless, the coupled model can be further improved by incorporating more physics-based equations instead of empirical ones, such as those for the PEM electrolyser discussed in Chapter 4, or for the mass transfer coefficient in the SWRO model. Furthermore, other BoP components could be integrated into the model, allowing for the evaluation of their impact on hydrogen production. Finally, future studies could also consider social, environmental and legal aspects of the coupled SWRO-PEM electrolyser.

In the following chapter, the integrated SWRO-PEM system is utilised to determine the optimal operating mode that maximises revenue. To achieve this, the Belgian power system is employed as the reference case, with electricity prices derived from historical data in Belgium.

Bibliography

[1] Y. Zhang, Y. Zhang, Z. Li, E. Yu, H. Ye, Z. Li, X. Guo, D. Zhou, C. Wang, Q. Sha, *et al.*, "A review of hydrogen production via seawater electrolysis: Current status and challenges," *Catalysts*, vol. 14, no. 10, p. 691, 2024.

[2] S. Jiang, H. Suo, T. Zhang, C. Liao, Y. Wang, Q. Zhao, and W. Lai, "Recent advances in seawater electrolysis," *Catalysts*, vol. 12, no. 2, p. 123, 2022.

[3] J. Mohammed-Ibrahim and H. Moussab, "Recent advances on hydrogen production through seawater electrolysis," *Materials Science for Energy Technologies*, vol. 3, pp. 780–807, 2020.

[4] R. A. Tufa, E. Curcio, W. van Baak, J. Veerman, S. Grasman, E. Fontananova, and G. Di Profio, "Potential of brackish water and brine for energy generation by salinity gradient power-reverse electrodialysis," *RSC Advances*, vol. 4, no. 80, pp. 42617–42623, 2014.

[5] J. Li, G. Wang, Z. Li, S. Yang, W. T. Chong, and X. Xiang, "A review on development of offshore wind energy conversion system," *International Journal of Energy Research*, vol. 44, no. 12, pp. 9283–9297, 2020.

[6] S. Santhakumar, H. Meerman, A. Faaij, R. M. Gordon, and L. F. Gusatu, "The future role of offshore renewable energy technologies in the North Sea energy system," *Energy Conversion and Management*, vol. 315, p. 118775, 2024.

[7] D. Jang, K. Kim, K.-H. Kim, and S. Kang, "Techno-economic analysis and Monte Carlo simulation for green hydrogen production using offshore wind power plant," *Energy Conversion and Management*, vol. 263, p. 115695, 2022.

[8] "Denmark's energy islands." https://ens.dk/en/our-responsibilities/offshore-wind-power/denmarks-energy-islands. Accessed: December 8, 2025.

[9] T. R. Lucas, A. F. Ferreira, R. S. Pereira, and M. Alves, "Hydrogen production from the WindFloat Atlantic offshore wind farm: A techno-economic analysis," *Applied Energy*, vol. 310, p. 118481, 2022.

[10] M. Rezaei, A. Akimov, and E. M. A. Gray, "Techno-economics of offshore wind-based dynamic hydrogen production," *Applied Energy*, vol. 374, p. 124030, 2024.

[11] H. Becker, J. Murawski, D. V. Shinde, I. E. Stephens, G. Hinds, and G. Smith, "Impact of impurities on water electrolysis: a review," *Sustainable Energy & Fuels*, vol. 7, pp. 1565–1603, 2023.

[12] Z. Liu, B. Han, Z. Lu, W. Guan, Y. Li, C. Song, L. Chen, and S. C. Singhal, "Efficiency and stability of hydrogen production from seawater using solid oxide electrolysis cells," *Applied Energy*, vol. 300, p. 117439, 2021.

[13] M. Khan, T. Al-Attas, S. Roy, M. M. Rahman, N. Ghaffour, V. Thangadurai, S. Larter, J. Hu, P. M. Ajayan, and M. G. Kibria, "Seawater electrolysis for hydrogen production: a solution looking for a problem?," *Energy & Environmental Science*, vol. 14, no. 9, pp. 4831–4839, 2021.

[14] B. Peñate and L. García-Rodríguez, "Current trends and future prospects in the design of seawater reverse osmosis desalination technology," *Desalination*, vol. 284, pp. 1–8, 2012.

[15] J. Kim, K. Park, D. R. Yang, and S. Hong, "A comprehensive review of energy consumption of seawater reverse osmosis desalination plants," *Applied Energy*, vol. 254, 2019.

[16] J. N. Hausmann, R. Schlögl, P. W. Menezes, and M. Driess, "Is direct seawater splitting economically meaningful?," *Energy & Environmental Science*, vol. 14, no. 7, pp. 3679–3685, 2021.

[17] A. Altaee, G. Zaragoza, and H. R. van Tonningen, "Comparison between forward osmosis-reverse osmosis and reverse osmosis processes for seawater desalination," *Desalination*, vol. 336, pp. 50–57, 2014.

[18] N. Rastogi, A. Cassano, and A. Basile, "Water treatment by reverse and forward osmosis," in *Advances in Membrane Technologies for Water Treatment*, pp. 129–154, Elsevier, 2015.

[19] R. d'Amore Domenech, O. Santiago, and T. J. Leo, "Multicriteria analysis of seawater electrolysis technologies for green hydrogen production at sea," *Renewable and Sustainable Energy Reviews*, vol. 133, 2020.

[20] B. A. Franco, P. Baptista, R. C. Neto, and S. Ganilha, "Assessment of offloading pathways for wind-powered offshore hydrogen production: Energy and economic analysis," *Applied Energy*, vol. 286, 2021.

[21] O. S. Ibrahim, A. Singlitico, R. Proskovics, S. McDonagh, C. Desmond, and J. D. Murphy, "Dedicated large-scale floating offshore wind to hydrogen: Assessing design variables in proposed typologies," *Renewable and Sustainable Energy Reviews*, vol. 160, 2022.

[22] A. Singlitico, J. Østergaard, and S. Chatzivasileiadis, "Onshore, offshore or in-turbine electrolysis? Techno-economic overview of alternative integration designs for green hydrogen production into offshore wind power hubs," *Renewable and Sustainable Energy Transition*, vol. 1, 2021.

[23] Z. Luo, X. Wang, H. Wen, and A. Pei, "Hydrogen production from offshore wind power in South China," *International Journal of Hydrogen Energy*, vol. 47, no. 58, pp. 24558–24568, 2022.

[24] H. T. Do Thi, T. Pasztor, D. Fozer, F. Manenti, and A. J. Toth, "Comparison of desalination technologies using renewable energy sources with life cycle, PESTLE, and multi-criteria decision analyses," *Water*, vol. 13, no. 21, 2021.

[25] "Desalination in the context of global water security." https://thirdworldcentre.org/2024/03/. Accessed: December 8, 2025.

[26] T. Lickert, M. L. Kiermaier, K. Bromberger, J. Ghinaiya, S. Metz, A. Fallisch, and T. Smolinka, "On the influence of the anodic porous transport layer on PEM electrolysis performance at high current densities," *International Journal of Hydrogen Energy*, vol. 45, no. 11, pp. 6047–6058, 2020.

[27] Z. Abdin, C. Webb, and E. M. Gray, "Modelling and simulation of a proton exchange membrane (PEM) electrolyser cell," *International Journal of Hydrogen Energy*, vol. 40, no. 39, pp. 13243–13257, 2015.

[28] R. Bhandari, C. A. Trudewind, and P. Zapp, "Life cycle assessment of hydrogen production via electrolysis–a review," *Journal of Cleaner Production*, vol. 85, pp. 151–163, 2014.

[29] M. Nasser and H. Hassan, "Techno-enviro-economic analysis of hydrogen production via low and high temperature electrolyzers powered by PV/wind turbines/waste heat," *Energy Conversion and Management*, vol. 278, 2023.

[30] Á. Serna and F. Tadeo, "Offshore hydrogen production from wave energy," *International Journal of Hydrogen Energy*, vol. 39, no. 3, pp. 1549–1557, 2014.

[31] P. Ellersdorfer, A. Omar, R. A. Taylor, R. Daiyan, and G. Leslie, "Multi-effect distillation: a sustainable option to large-scale green hydrogen production using solar energy," *International Journal of Hydrogen Energy*, vol. 48, no. 81, pp. 31491–31505, 2023.

[32] J. S. Kim, J. Chen, and H. E. Garcia, "Modeling, control, and dynamic performance analysis of a reverse osmosis desalination plant integrated within hybrid energy systems," *Energy*, vol. 112, pp. 52–66, 2016.

[33] A. Joseph and V. Damodaran, "Dynamic simulation of the reverse osmosis process for seawater using labview and an analysis of the process performance," *Computers & Chemical Engineering*, vol. 121, pp. 294–305, 2019.

[34] H. Lonsdale, U. Merten, and R. Riley, "Transport properties of cellulose acetate osmotic membranes," *Journal of Applied Polymer Science*, vol. 9, no. 4, pp. 1341–1362, 1965.

[35] H. T. El-Dessouky and H. M. Ettouney, *Fundamentals of salt water desalination*. Elsevier, 2002.

[36] J. C. Crittenden, R. R. Trussell, D. W. Hand, K. J. Howe, and G. Tchobanoglous, *MWH's water treatment: principles and design*. John Wiley & Sons, 2012.

[37] X. Jin, A. Jawor, S. Kim, and E. M. Hoek, "Effects of feed water temperature on separation performance and organic fouling of brackish water RO membranes," *Desalination*, vol. 239, no. 1-3, pp. 346–359, 2009.

[38] Z. Hadadian, S. Zahmatkesh, M. Ansari, A. Haghighi, and E. Moghimipour, "Mathematical and experimental modeling of reverse osmosis (RO) process," *Korean Journal of Chemical Engineering*, vol. 38, pp. 366–379, 2021.

[39] S. Avlonitis, W. Hanbury, and M. B. Boudinar, "Spiral wound modules performance an analytical solution: Part II," *Desalination*, vol. 89, no. 3, pp. 227–246, 1993.

[40] K. P. Chee, K. P. Wai, C. H. Koo, and W. C. Chong, "Performance evaluation of reverse osmosis desalination pilot plants using ROSA simulation software," in *E3S Web of Conferences*, vol. 65, p. 05022, EDP Sciences, 2018.

[41] IRENA, "Green hydrogen cost reduction: Scaling up electrolysers to meet the 1.5 °C climate goal," *Report*, 2020.

[42] IEA, "Global hydrogen review 2024," *Report*, 2024.

[43] R. A. Abdelsalam, M. Mohamed, H. E. Farag, and E. F. El-Saadany, "Green hydrogen production plants: A techno-economic review," *Energy Conversion and Management*, vol. 319, 2024.

[44] A. E. Samani, A. D'Amicis, J. D. M. De Kooning, D. Bozalakov, P. Silva, and L. Vandevelde, "Grid balancing with a large-scale electrolyser providing primary reserve," *IET Renewable Power Generation*, vol. 14, no. 16, pp. 3070–3078, 2020.

[45] R. Saulnier, K. Minnich, and P. Sturgess, "Water for the hydrogen economy," *WaterSMART Solutions Ltd*, p. 13, 2020. Available online: https://watersmartsolutions.ca/wp-content.

[46] M. Ansari, M. A. Al-Obaidi, Z. Hadadian, M. Moradi, A. Haghighi, and I. M. Mujtaba, "Performance evaluation of a brackish water reverse osmosis pilot-plant desalination process under different operating conditions: Experimental study," *Cleaner Engineering and Technology*, vol. 4, p. 100134, 2021.

Chapter 6

Techno-economic Comparison of PEM Electrolyser Operation Modes

6.1 Introduction

As stated in the previous chapters, proton exchange membrane (PEM) electrolysers are promising technologies for electrolysis due to their fast dynamic response to electricity fluctuations and their lower spatial footprint compared to alternative options. However, the high costs associated with green hydrogen production remain a key challenge for the large-scale deployment of PEM electrolysers within the energy system. This chapter, therefore, compares three operational modes of PEM electrolysers: continuous operation at full capacity, price-responsive operation, and combined price- and frequency-responsive operation providing ancillary services. Accordingly, future hourly electricity prices in Belgium, which represent the case study of this thesis, are estimated based on three potential evolutions of the Belgian energy system and are subsequently applied to the defined scenarios. Furthermore, a sensitivity analysis is conducted to identify the most influential parameters affecting the hydrogen break-even price. This chapter provides a globally applicable framework for determining suitable electrolyser operation strategies across a range of power system configurations.

6.2 Literature Review

In line with the European Union's (EU) target of achieving net-zero carbon emissions by 2050, European countries are rapidly transitioning to renewable

energy sources (RESs). However, as discussed in Chapter 2, the intermittency of RESs poses challenges for power system operators in maintaining grid stability. As the share of RESs in the power system increases, grid frequency becomes more unstable. Therefore, the transmission system operator (TSO) is responsible for ensuring the availability of a set of services from voluntary producers and consumers that can generate or consume energy in real time to correct any imbalances in the grid.

In Chapter 3, it was discussed how electrolysers can support power system operators (PSOs) when electricity supply exceeds demand by converting surplus electricity into green molecules such as hydrogen (H_2). Conversely, when supply does not meet demand, they can reduce their power consumption to assist the PSO. In addition, electrolysers can enhance grid flexibility by providing ancillary services, particularly frequency containment reserve (FCR), to address frequency instability caused by the integration of RESs. They can also deliver further flexibility by assisting balance responsible parties (BRPs) in managing their portfolios and capitalising on imbalance market opportunities. The authors in [1] explored the potential of large-scale PEM electrolysers as providers of flexibility services. Their findings indicated that, owing to the rapid response of PEM electrolysers, along with their efficient and safe part-load operation, they can effectively support grid services and compensate for wind power forecast errors.

The authors in [2] also examined the balance of plant (BoP) components for a PEM electrolyser during partial-load operation. The study primarily aimed to enhance the performance of BoP components under partial-load conditions to reduce the average net specific consumption. The authors concluded that this objective can be achieved by controlling water flow to the stack and managing the regeneration of the hydrogen dryer.

When it comes to providing flexibility via electrolysers, several characteristics become critical, including their response time, the ability to frequently ramp power up and down without significantly affecting their lifetime, and their capability to operate efficiently across a wide partial-load range. In Chapter 4, it was shown that PEM electrolysers can satisfy these conditions. Furthermore, a review study in [3] confirmed that both alkaline electrolyser (AE) and PEM electrolysers can provide grid flexibility by adjusting their load range within their rated temperature in timescales from less than a second to a few seconds, making them suitable for grid balancing services. Additionally, the study highlighted that both electrolyser types can dynamically regulate stack power to achieve a sub-second response, thereby minimising the duration of frequency disturbances in the grid.

The authors in [4] examined the integration of an AE with a capacity of 3.4 Nm^3/h alongside two 6 kW wind turbines and two 2.5 kW solar panels in an Energy Park in Norway. The study aimed to investigate the load-following

capability of the electrolyser when coupled with RESs. The findings confirmed that the AE effectively captures variations in wind power input within an operational range of 10–100%.

These studies collectively demonstrate that electrolysers can assist PSOs, as well as other parties such as BRPs and flexibility service providers (FSPs), in balancing the grid, with their BoP components demonstrating robust performance.

In Chapter 5, offshore hydrogen generation was presented as a strategy for countries with access to the sea, offering the potential to use seawater for electrolysis and to benefit from the concept of energy islands [5–8].

With respect to energy islands, the authors in [9] presented a comprehensive framework from a distinctive perspective. By exploring various definitions of the term energy island, they identified key challenges, assessed the vulnerabilities of existing systems, and proposed both physical and institutional solutions. Regarding artificial energy islands, they emphasised liberalisation and decentralisation, as well as research and development in emerging technologies for generation, storage, transmission, regulation, and community building, as key institutional solutions.

The authors in [10] examined the risks, benefits, and potential opportunities associated with the development of energy islands. They concluded that, in the absence of well-established economic frameworks, a definitive assessment of the benefits remains unfeasible. Based on past experience, they argued that the viability of offshore projects is primarily driven by economic considerations.

Inspired by the concept of energy islands, this chapter aims to address the economic gap in hydrogen production via PEM electrolysers, due to their aforementioned advantages. Although green hydrogen offers environmental benefits and strong potential for decarbonisation across sectors, it remains more expensive than hydrogen produced from fossil fuels, such as via steam methane reforming. This mainly stems from the high cost of electricity. According to [11], 73% of the total cost associated with green hydrogen production is attributed to electricity consumption. This clearly indicates that the electricity consumption strategy of electrolysers has a significant impact on the cost of the produced hydrogen. Consequently, this chapter examines multiple electrolyser operating modes to determine the most effective strategy for reducing the hydrogen break-even price across a range of predicted electricity price trajectories.

This study differentiates itself from prior researches in the literature in several key aspects.

First, regarding the electrolyser model, unlike some earlier studies, this research employs a dynamic, rather than static, PEM electrolyser model that was dicussed in detail in Chapter 4. As stated, although PEM electrolysers are known for their fast response, their operation is not instantaneous and involves

inherent dynamic behaviour. Accounting for this behaviour is particularly important in flexibility studies where the electrolyser is integrated with RESs. Neglecting the capacitive effects of the PEM electrolyser, and consequently its dynamic response, can lead to inaccurate estimations of both electricity consumption and hydrogen production, with the extent of this discrepancy depending on the operating conditions and the characteristics of the electrolyser, as shown in [12] and [13]. Given the cost difference between electricity input and hydrogen output, such misestimations may result in significant errors in techno-economic analyses, especially over the 20-year operational lifetime of the PEM electrolyser.

Second, in contrast to circuit-based models built using electrical components, the model employed in this study is formulated through mathematical equations that capture the electrochemical interactions among the anode, cathode, membrane, voltage, and thermal modules. A key drawback of circuit-based models is their limited applicability, as the derived parameters are only valid under specific operating conditions, as confirmed by [13]. This limitation can lead to significant inaccuracies in flexibility studies, where frequent changes in operating conditions, such as power consumption, are required.

Moreover, this study incorporates the ageing rate of the PEM electrolyser, which affects its power consumption. Accounting for this factor enables a more accurate estimation of the generated hydrogen price.

Finally, unlike the previous researches in the literature, this study examines the operation of the electrolyser over its entire 20-year lifetime, based on hourly estimated electricity prices specific to the test case considered, Belgium. The design parameters are based on the technical characteristics of the Belgian artificial energy island currently being developed by the national transmission system operator (TSO), Elia. In addition, this study takes into account European regulations related to green hydrogen production.

Exploring the performance of the SWRO system is highly relevant to offshore hydrogen production, and the detailed modelling steps as well as the integration of the SWRO system with the PEM electrolyser were thoroughly examined in Chapter 5. Nevertheless, the SWRO unit is excluded from this chapter in the context of determining the most suitable operating mode of the PEM electrolyser, as its power consumption is considerably lower than that of the electrolyser and therefore has a negligible effect on the hydrogen price.

This study provides insights into the techno-economic analysis of green hydrogen production on energy islands and offers guidance for other countries with access to the sea. Although the Belgian power system was used as the reference case, the developed models and methodologies for green hydrogen generation are broadly applicable to other power systems. Thus, Belgium serves only as a representative test case for this research.

The rest of this chapter is organised as follows: Section 6.3 is dedicated to

a comprehensive discussion of the methodology and characteristics considered in this study. This is followed by a brief description of the PEM electrolyser model, with its technical and economic specifications based on the Belgian developing energy island. This section also summarises the relevant EU legislation for green hydrogen, as well as the definition of the PEM electrolyser operation modes employed in this work. Furthermore, the method used to derive the predicted hourly electricity prices, based on three different energy system configurations in Belgium, is described. Section 6.4 is devoted to the obtained results based on the defined scenarios and parameters, including the derived hydrogen break-even prices, the electrolysis cost breakdown for each scenario, and a sensitivity analysis. This section also provides a comparison of the scenarios. Finally, in Section 6.5, the results are discussed and conclusions are drawn.

6.3 Methodology

This section provides a detailed discussion of the methods and data used for assessing hydrogen production in this study.

6.3.1 PEM Electrolyser Model

The dynamic PEM electrolyser model employed in this study, as noted previously, incorporates five interconnected modules: anode, cathode, membrane, voltage, and thermal, each examined in depth in Chapter 4.

The anode and cathode modules are formulated based on the molar balances of the relevant species, water and oxygen in the anode, and water and hydrogen in the cathode. In the membrane module, the mechanisms governing water transport through the membrane are represented, including electro-osmotic drag and diffusion. The voltage module includes calculations of the reversible voltage, as well as the ohmic overvoltage of the membrane and the activation overvoltages of both the anode and cathode. Finally, the thermal module accounts for heat sources and sinks, along with the water injected into the electrolyser for cooling purposes.

Subsequently, the sizing of the PEM electrolyser plant was carried out based on the Belgian energy island. The island will be located at the centre of the Princess Elizabeth Zone, Belgium's second offshore wind farm zone, which is expected to host new wind farms with a total capacity of up to 3.5 GW [14]. In this study, it is assumed that 10% of this capacity, equivalent to 35 MW and comprising seven 5 MW electrolysers, is allocated to offshore hydrogen production. This 35 MW figure is motivated by the Belgian Federal Government's goal of developing 150 MW of electrolysis capacity as part of its broader

energy transition strategy [15]. As such, the chosen capacity represents approximately 25% of the national target, a reasonable share given the limited offshore space and the higher maturity of onshore hydrogen production. Additionally, renewable electricity in Belgium is also required to support the electrification of broader power sectors, which further justifies the limited share allocated to electrolysis.

The choice of 5 MW per electrolyser unit is based on Belgian TSO regulations, which specify that FCR must be provided in positive or negative increments of at least 1 MW. Therefore, a 5 MW capacity is chosen as it offers sufficient flexibility to accommodate FCR provision within the operational range of the electrolyser, as the investigation of FCR provision represents one of the case studies in this chapter. The inclusion of FCR as a scenario is further justified by the growing penetration of RESs, which increases the demand for fast frequency containment services that electrolysers are particularly well-suited to provide while simultaneously producing hydrogen. Nonetheless, FCR is not the only type of ancillary service that electrolysers can deliver, and it merely represents a fast and unpredictable service chosen in this study to demonstrate their potential. The 5 MW capacity further corresponds to commercially available designs, with manufacturers such as Cummins already having developed units of this size [16]. Nonetheless, although 35 MW is used as the baseline capacity for offshore electrolysis in this study, a sensitivity analysis is also conducted to evaluate the impact of varying this parameter.

6.3.2 EU Legislation

In this chapter, given the focus on green hydrogen production within the Belgian energy system, the defined scenarios take into account both the characteristics of the Belgian power grid and, importantly, the EU's legislation on renewable hydrogen.

As specified in the revised Renewable Energy Directive (RED II) of the EU, electricity is classified as renewable if the renewable power plant and the electrolyser are either co-located within the same installation or directly connected, without relying on electricity from the grid for electrolysis [17].

Nevertheless, the European Commission recently adopted delegated regulations establishing the rules for renewable hydrogen production and defining the additionality criteria for renewable electricity. Under these regulations, electricity sourced from the grid may be considered fully renewable if it meets the conditions of additionality, geographical correlation, and temporal correlation, as outlined below [17]:

Additionality: Hydrogen producers are required to ensure that the electricity utilised for hydrogen production is matched by renewable electricity production.

This can be achieved either by generating renewable electricity within the same installation, demonstrating that the amount produced corresponds to the hydrogen classified as renewable, or by obtaining renewable electricity through a power purchase agreement (PPA) with renewable energy suppliers.

Geographical correlation: Entities involved in hydrogen production are obliged to ensure that additional renewable energy sources are placed within the region where hydrogen production occurs. To meet this requirement, at least one of the following spatial conditions must be met regarding the placement of the renewable electricity generator relative to the electrolyser: (i) the renewable electricity generator is positioned within the same bidding zone as the electrolyser, (ii) it is located in a connected bidding zone where day-ahead electricity market prices are equal to or higher than those in the electrolyser's zone, or (iii) it operates within an offshore zone that is directly connected to the bidding zone of the electrolyser.

Temporal correlation: Hydrogen producers must ensure that renewable electricity generation is temporally aligned with hydrogen production. Until the end of 2029, hydrogen production must achieve a net-zero balance within the same calendar month, and from the beginning of 2030, within the same one-hour period, while Member States have the option to implement the latter rule earlier.

These delegated regulations enable the production of green hydrogen at potentially competitive prices compared to hydrogen generated from other sources, such as fossil fuels.

6.3.3 Defined Scenarios

Based on EU legislation for renewable hydrogen and the requirements of the Belgian power system, three main scenarios for electrolyser operation are defined and described in this section.

In this study, the annual net present value (NPV) for each scenario under various electricity price pathways is calculated, and based on these values, the hydrogen break-even price is determined. The NPV is expressed as:

$$\mathrm{NPV} = \sum_{y=1}^{20} \frac{\mathrm{CF}(y)}{(1+i)^y} \tag{6.1}$$

where $\mathrm{CF}(y)$ represents the cash flow in year y, and i is the discount rate.

The three main operational strategies for electrolysers are as follows:

Full-capacity operation: The first scenario, referred to as full-capacity operation (FCO), reflects the well-established operating mode in which electrolysers continuously operate at their full rated capacity. Based on the additionality criterion from EU legislation, when the electrolyser plant is owned by the same entity, a variable electricity price is applied. However, since in this scenario the electrolysers always operate at their rated capacity, a variable electricity price effectively corresponds to purchasing electricity under a PPA with the same average price as the variable prices over the lifetime of the electrolysers.

The annual cash flow for the FCO scenario is given by:

$$\mathrm{CF}(y) = \sum_{t=1}^{8760} [(H_{2(\mathrm{be})} \cdot H^t_{2(\mathrm{gen})}) - (C^t_{\mathrm{e}} \cdot P_{\mathrm{el}})] \cdot 1\mathrm{h} \tag{6.2}$$

where t denotes the respective hour in year y, $H_{2,\mathrm{be}}$ is the hydrogen break-even price, $H^t_{2,\mathrm{gen}}$ is the hourly hydrogen production, C^t_{e} corresponds to the variable hourly electricity price, and P_{el} is the operating power of the electrolysers. In the FCO scenario, P_{el} is always equal to the rated power of the electrolyser, P_{rated}, described as:

$$P_{\mathrm{el}} = P_{\mathrm{rated}} \tag{6.3}$$

An overview of the operation of the electrolysers in this scenario is presented in Fig. 6.1(a), where the electrolysers operate continuously at their rated capacity.

Price-adaptive operation: The second scenario, defined as price-adaptive operation (PAO), assumes that the operation of the electrolysers is adjusted dynamically based on the variable electricity price per hour. Specifically, when the electricity price increases, the electrolysers reduce their power consumption, and vice versa. Furthermore, beyond a certain threshold, when the electricity price rises, the electrolysers operate at their minimum load, while below a specific point, when the electricity price falls, they operate at their rated power. This scenario is directly motivated by the additionality criterion in the RED II legislation, which allows electrolysers to consume grid electricity, while the resulting hydrogen is still considered green, if the entity can demonstrate renewable generation capacity within the installation equivalent to the hydrogen produced. Therefore, operating electrolysers as a function of electricity prices represents a highly relevant case for green hydrogen production.

In this scenario, since the operation of the electrolysers depends on variations in the electricity price, a fixed electricity price is not applicable, and C^t_{e} represents the variable hourly electricity price.

While the cash flow equation for this scenario is the same as in the FCO

(a) FCO scenario

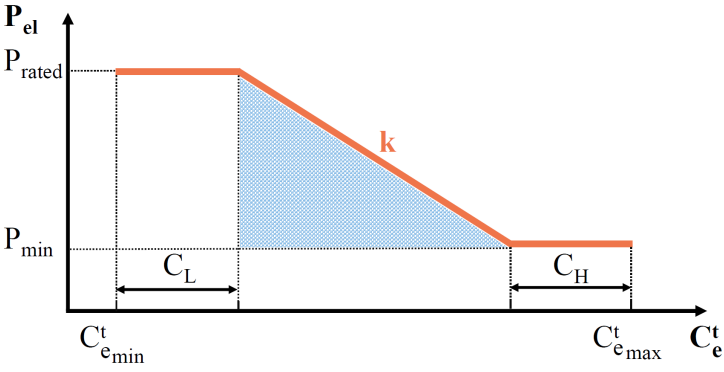

(b) PAO scenario

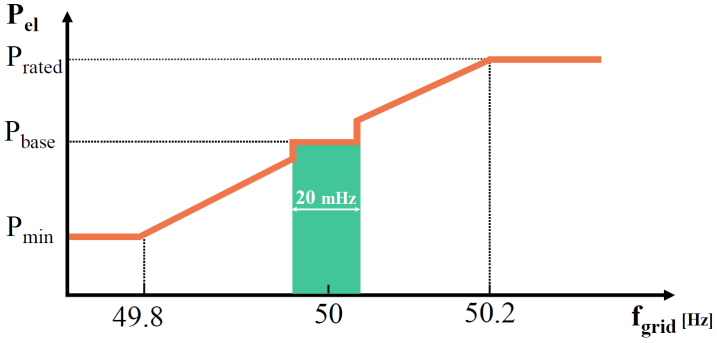

(c) FCR scenario

Figure 6.1: Overview of operational scenarios for the electrolysers

scenario, presented in (6.2), the governing equation for the power consumption of the electrolysers is expressed as:

$$P_{\text{el}} = \begin{cases} P_{\text{rated}} & C_{\text{e}}^{t} < C_{\text{L}} \\ P_{\text{rated}} - kC_{\text{e}}^{t} & C_{\text{L}} < C_{\text{e}}^{t} < C_{\text{H}} \\ P_{\text{min}} & C_{\text{e}}^{t} > C_{\text{H}} \end{cases} \tag{6.4}$$

where C_{L} denotes the lower percentile threshold of the electricity price distribution within which the electrolysers are assumed to operate continuously at full load. In contrast, C_{H} is the upper percentile threshold within which the electrolysers operate at their minimum load. In this chapter, a minimum operational capacity of 10% is maintained for the electrolysers in the PAO scenario to avoid start-up and shut-down delays associated with nitrogen purging [18]. The parameter k, expressed in MW^2.h/€, determines the sensitivity of the response of the electrolysers to electricity price variations between these two thresholds. In this scenario, three parameters are optimised: C_{L}, C_{H}, and k.

In the PAO scenario, the predicted hourly electricity price values, C_{e}^{t}, are scaled to the range 0.5–5, corresponding to the minimum and rated power of each electrolyser over its lifetime, based on the maximum predicted price of each electricity price pathway. This formulation allows the parameter k to vary between 0 and 1, since values of k below 0 or above 1 would yield power outputs exceeding the rated capacity or falling below the minimum capacity of the electrolysers, respectively, as defined in (6.4). The percentile thresholds C_{L} and C_{H} are adjusted in 5% increments, while k is incremented in steps of 0.2, resulting in a total of 855 cases analysed over the 20-year lifetime of the electrolysers for the PAO scenario under each electricity price estimation pathway. The selected step sizes provide an effective trade off between computational efficiency and adequate resolution for optimisation.

An overview of the electrolyser operation in this scenario is shown in Fig. 6.1(b).

Frequency containment reserve: As a complement to the PAO scenario, the last scenario considers electrolyser participation in the ancillary services market by providing FCR, hereafter referred to as the FCR scenario. In this case, the optimal values of C_{L}, C_{H}, and k derived from the PAO scenario are kept constant, while in the shaded segment shown in Fig. 6.1(b), hereafter in this chapter referred to as the linear decreasing region, the electrolysers provide FCR whenever the required minimum free capacity is available. This scenario is motivated by the operational requirements of the power grid, which necessitate maintaining a continuous balance between the mechanical driving generation and the net electrical consumption. As this study focuses on Bel-

gium, given that since July 2020 the symmetric FCR 200 mHz product has been the sole FCR product supplied by Elia, only this type is analysed in this thesis. For this product, a deadband of ± 10 mHz around 50 Hz, within which no primary control action is permitted by the electrolysers, is authorised. Furthermore, when the frequency deviation remains within ± 200 mHz of 50 Hz, the electrolysers adjust their power consumption to help restore the nominal frequency. Similar to the PAO scenario, a minimum operational capacity of 10% is maintained for the electrolysers in this scenario.

The annual cash flow, $\mathrm{CF}(y)$, as shown in (6.1), is calculated as:

$$\mathrm{CF}(y) = \sum_{t=1}^{8760} [(H_{2(\mathrm{be})} \cdot H^t_{2(\mathrm{gen})}) + (C^t_{\mathrm{FCR}} \cdot P^t_{\mathrm{res}}) - (C^t_{\mathrm{e}} \cdot P_{\mathrm{el}})] \cdot 1\mathrm{h} \tag{6.5}$$

where C^t_{FCR} is the hourly FCR price, and P^t_{res} is the hourly reserved electrolyser capacity dedicated to grid support via FCR provision. The reserved electrolyser capacity, P^t_{res}, can be expressed as a share of the rated capacity of the electrolysers, P_{rated}, as follows:

$$P^t_{\mathrm{res}} = \alpha_{\mathrm{el}} \cdot P_{\mathrm{rated}} \tag{6.6}$$

where α_{el} is a dimensionless constant between 0 and 1. The governing equation for the power of the electrolysers in this scenario is given as:

$$P_{\mathrm{el}} = \begin{cases} P_{\mathrm{min}}, & \Delta f < -200 \text{ mHz}, \\ \gamma_{\mathrm{el}} \cdot P_{\mathrm{rated}}, & -10 \text{ mHz} \leq \Delta f \leq 10 \text{ mHz}, \\ \gamma_{\mathrm{el}} \cdot P_{\mathrm{rated}} + P^t_{\mathrm{FCR}}, & \begin{array}{l} -200 \text{ mHz} \leq \Delta f < -10 \text{ mHz}, \\ 10 \text{ mHz} < \Delta f \leq 200 \text{ mHz}, \end{array} \\ P_{\mathrm{rated}}, & \Delta f > 200 \text{ mHz}. \end{cases} \tag{6.7}$$

where γ determines the baseload at which the electrolysers operate, Δf is the deviation of the frequency from its nominal value of 50 Hz, and P^t_{FCR} is the power adjusted by the electrolysers to contain frequency deviations, which can be expressed as:

$$P^t_{\mathrm{FCR}} = P^t_{\mathrm{res}} \times \frac{\Delta f}{200 \text{ mHz}} \tag{6.8}$$

Moreover, the relationship between γ_{el} and α_{el} can be expressed as:

$$\alpha_{\mathrm{el}} < \gamma_{\mathrm{el}} < 1 - \alpha_{\mathrm{el}} \tag{6.9}$$

The activation mechanism, which includes the correlation between P_{FCR} and P_{res} as well as the 10 mHz frequency deadband, is illustrated in Fig. 6.2.

While in the PAO scenario the electrolysers operate solely as a function of the electricity price, adjusting their power consumption on an hourly basis, in

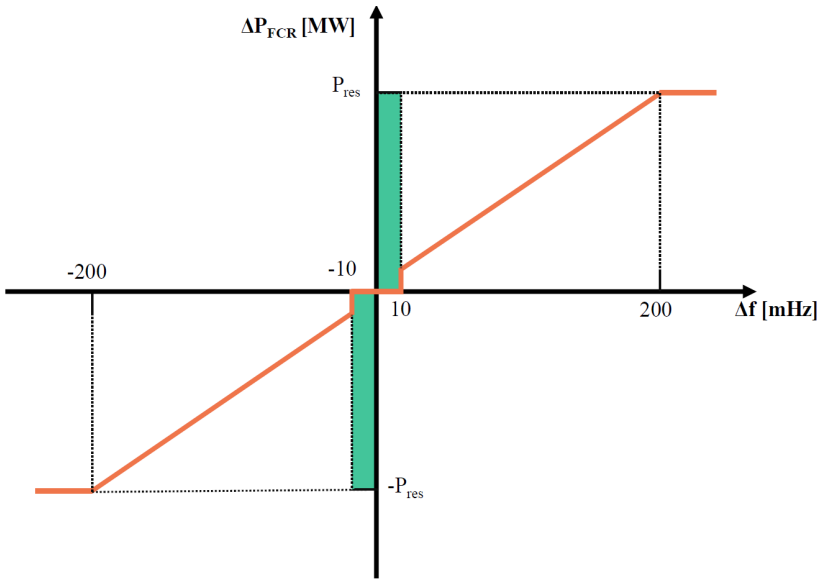

Figure 6.2: Activation principle of the 200 mHz symmetric FCR product

Table 6.1: Technical and operational specifications of the PEM electrolysers

Parameter	Value	Unit
Electrolyser type	PEM	-
P_{rated}	5	MW
Efficiency	65	%
Number of electrolysers	7	-
P_{min}	0.5	MW
Operating temperature	80	°C
Operating temperature	30	bar
Cell active area	0.25	m^2
Number of cells	510	-

the FCR scenario, they operate in the linearly decreasing region as a function of both electricity price and grid frequency, adjusting their power consumption every 10 seconds according to the measured frequency.

An overview of the operation of the electrolysers in the FCR scenario is depicted in Fig. 6.1(c).

In addition to the specific characteristics of each scenario, the following assumptions are applied to all scenarios:

Table 6.2: Economic and performance parameters of the PEM electrolysers

Parameter	Value	Unit	Ref.
Capital expenditure (CapEx)	1300	€/kW	[19]
Operational expenditure (OpEx)	2% of CapEx	€/kW	[19]
Degradation	1% per year	-	[20]
End of lifetime	10% voltage loss	-	[21]
Stack replacement cost	50% of CapEx	-	[18]
Discount rate	3%	-	[22]
Connection costs to power grid	500,000	€	[18]
Connection costs to gas grid	2,250,000	€	[18]
Availability	98%	-	[18]
Oxygen price	24.5	€/ton	[18]

- Given that the Belgian energy island is expected to become operational in 2030, this study assumes that the electrolysers will become operational in that year and continue for 20 years, consistent with the typical lifetime of current electrolyser plants [14].
- It is assumed that the electrolyser plant is owned by an entity with sufficient renewable capacity in its portfolio to match the amount of hydrogen produced. Thus, in all scenarios, a variable electricity price based on the day-ahead market clearing price is assumed, rather than a fixed electricity price as under a PPA.
- Considering the temporal correlation requirement, which mandates a net-zero balance within the same hour starting from 2030, it is assumed that the electrolysers are directly supplied with electricity generated by the associated entities. Consequently, no electrical storage systems, such as batteries, are considered in the system configuration.
- The end of life of the electrolysers is defined as the point at which the stack voltage has degraded by 10% relative to the beginning of life, measured at the same current density.
- As it is assumed that the electrolysers are located on the Belgian energy island, this arrangement fulfils the geographical correlation requirement, which mandates that the renewable electricity generator and the electrolysers operate within the same bidding zone.

A summary of the technical parameters and the economic parameters applied to the electrolysers is provided in Table 6.1 and Table 6.2, respectively.

Table 6.3: Comparison between the electricity price pathways in Belgium [23]

Parameter	Central	Clean molecules	Electrification
2050 climate goal	Achieves net-zero emissions through a mix of efficiency enhancement measures, including building renovation, more efficient vehicles, and carbon capture	Achieves net-zero emissions with greater reliance on imported synthetic molecules from locations outside the EU	Achieves net-zero emissions primarily through investments in large-scale electrification with offshore wind power and nuclear power technologies
New nuclear power technologies	Not considered	Not considered	Investments in small modular reactors, operational from 2045
Additional offshore wind power	Not considered	Not considered	Investments in access to 16 GW offshore wind outside of the Belgian territorial waters
Carbon capture and storage	Unlimited cross-border access to CO_2 storage in the North Sea and Norway	Limited cross-border access of 5 Mt/year to CO_2 storage, mainly in the Netherlands and Norway	Unlimited cross-border access to CO_2 storage in the North Sea and Norway

6.3.4 Electricity Price in Belgium

As described in the scenario definitions, variable electricity prices are applied across all three scenarios. Since the Belgian energy island is expected to become operational in 2030, this study uses estimated hourly electricity prices from 2030 onwards, covering a 20-year period until 2050, corresponding to the assumed lifetime of the electrolysers. Given that the electrolyser model employed in this study is dynamic, the model is able to capture the transient behaviour of the electrolyser while operating under continuously changing loads. Moreover, the use of a mathematical model ensures accuracy across the full operating range of the electrolysers, particularly when power consumption fluctuates as in the PAO and FCR scenarios.

In this study, the hourly day-ahead market prices for the Belgian system are estimated based on the historical annual, monthly, daily, and hourly price correlations observed in the Belgian grid, as published by Elia [24]. To account for electricity price uncertainty, three distinct pathways for Belgium's energy transition towards 2050, as proposed by EnergyVille and ENGIE, are considered [23]. The three projected electricity price trajectories, namely the central pathway, the clean molecules pathway, and the electrification pathway, each reflect a different evolution of the Belgian energy system.

Under the central pathway, in order to reach carbon neutrality, the involved sectors can invest in energy efficiency measures such as building renovation, more efficient vehicles, and efficiency gains in space heating systems, without additional investments in new offshore wind or nuclear plants. In this pathway, the option of carbon capture and storage (CCS) is not limited. Although Belgium does not have its own storage facilities for carbon dioxide (CO_2), it is assumed that the country will have unlimited access to the commercial phase of cross-border carbon storage in the North Sea and Norway. By contrast, in the clean molecules pathway, the main assumption is the large-scale import of synthetic molecules. As in the central pathway, no new nuclear or offshore wind projects are considered, but access to cross-border CO_2 storage is limited to 5 Mt/year, mainly in the Netherlands and Norway. Finally, the electrification pathway assumes investment in a high voltage direct current (HVDC) connection to unlock an additional 16 GW of offshore wind potential in other parts of the North Sea, outside Belgian territorial waters. Furthermore, new investments in nuclear technologies, primarily small modular reactors, are assumed, with operation starting from 2045. In this pathway, no restrictions on CCS are considered. A comparison of the three pathways is presented in Table 6.3.

In summary, the central pathway represents a balanced approach through a mix of decarbonisation options, with electricity costs mainly driven by CO_2 pricing. This pathway leads to the highest predicted electricity prices compared to the clean molecules and electrification pathways. In the clean molecules path-

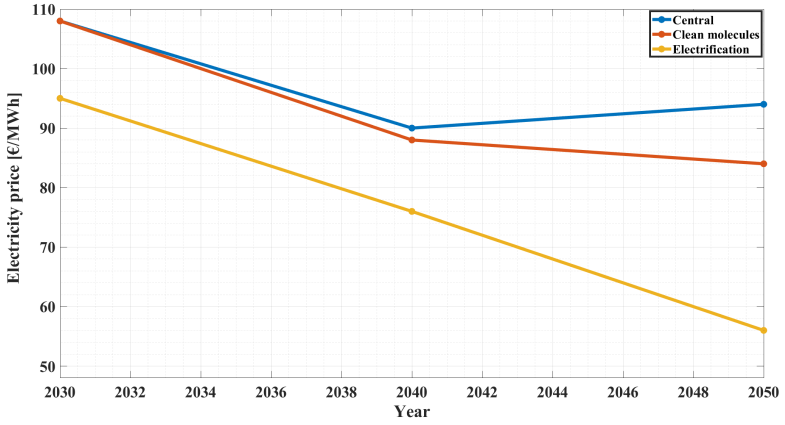

Figure 6.3: Comparison of the predicted electricity prices in Belgium under the central, clean molecules, and electrification pathways

way, lower imported synthetic fuel costs reduce dependency on high electricity prices, but at the expense of greater import reliance, resulting in prices lower than those in the central pathway but higher than in the electrification pathway. Lastly, the electrification pathway appears most suitable for long-term energy independence through wind and nuclear energy, leading to the lowest projected electricity prices compared to the central and clean molecules pathways. In Fig. 6.3, a comparison of the estimated annual electricity prices for the three pathways over the period 2030–2050 is shown [23].

To translate the average annual prices shown in Fig. 6.3 into hourly electricity prices, essential for this study for the reasons stated earlier, historical hourly electricity prices in Belgium from 2016 to 2023, published by Elia, were collected and analysed [24]. The years 2016–2023 are selected for the analysis due to the availability of data at the time this research was carried out.

Subsequently, the correlations between annual, monthly, daily, and hourly prices in Belgium over the past years were determined. Using these correlations, the annual prices in each electricity price pathway, i.e., the central, clean molecules and electrification pathways, were mapped into hourly prices for each pathway over the period 2030 to 2050. This correlation-based method preserves realistic intra-year variability by allowing hourly fluctuations around the fixed annual average, ensuring that not every hour has the same value.

The three-dimensional and averaged two-dimensional monthly-to-annual ratios for the years 2016 to 2023 are shown in Fig. 6.4(a) and Fig. 6.4(b), respectively. Likewise, the three-dimensional hourly-to-monthly and averaged two-dimensional hourly-to-monthly ratios for the same years are presented in

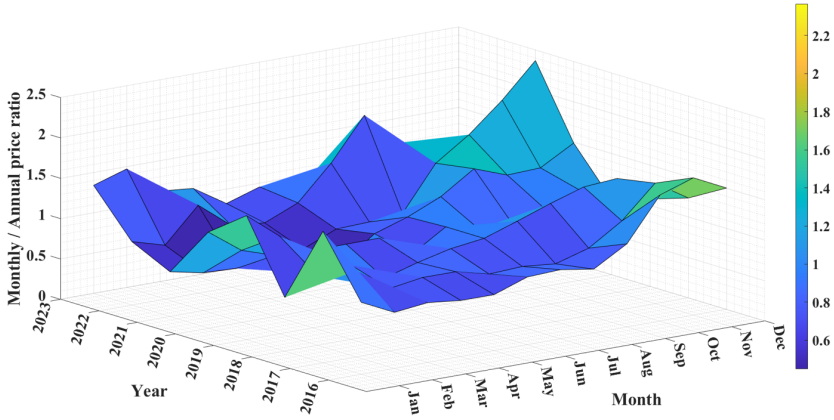

(a) 3-D Monthly to annual ratio

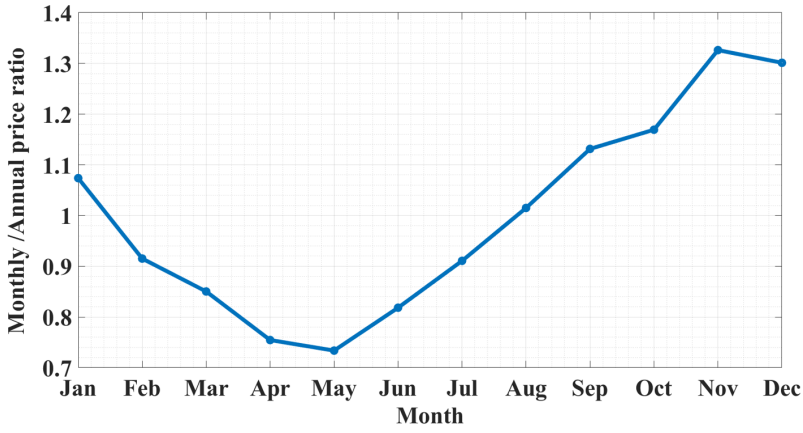

(b) 2-D Monthly to annual ratio

Figure 6.4: Correlation between monthly and annual electricity prices in Belgium from 2016 to 2023

Fig. 6.5(a) and Fig. 6.5(b), respectively.

As shown in Fig. 6.4, in Belgium from 2016 to 2023, November had the greatest influence on the annual electricity price, while May had the least impact. The same trend observed in Fig. 6.4(b) was applied to the annual prices presented in Fig. 6.3 to convert the yearly prices into monthly prices for the period 2030 to 2050. Fig. 6.5(a) and Fig. 6.5(b) illustrate the expected daily pattern, characterised by two peaks: one in the morning and another in the evening. The morning peak shifts earlier during months with longer daylight, while the evening peak moves closer to midnight in those same months. This pattern clearly indicates that electricity prices are largely driven by demand, as

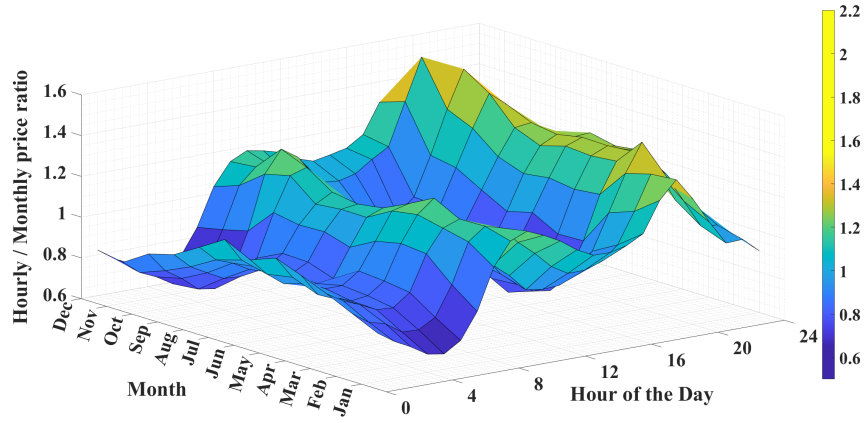

(a) 3-D Hourly to monthly ratio

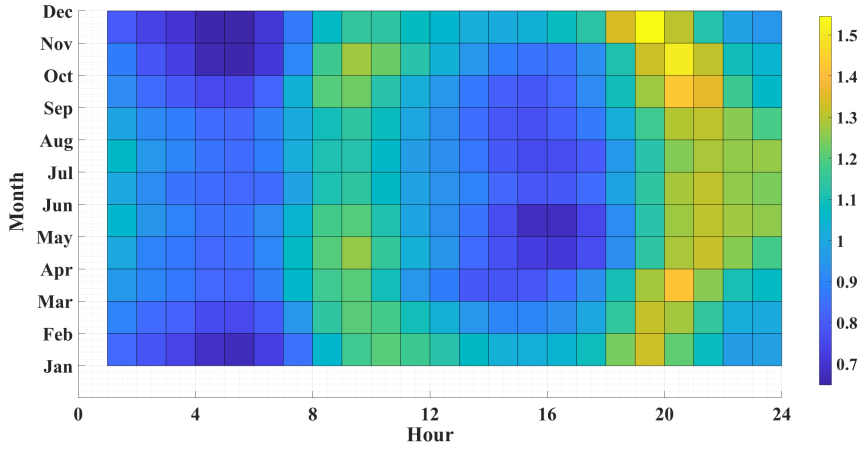

(b) 2-D Hourly to monthly ratio

Figure 6.5: Correlation between monthly and hourly electricity prices in Belgium from 2016 to 2023

the temporal distribution of prices aligns closely with typical demand profiles. It is worth noting that no specific justification exists for the daily-to-monthly ratios, which primarily serve as a randomiser to distribute the calculated monthly price across the corresponding month. Therefore, these ratios are not depicted.

6.4 Results

This section analyses the operation of the electrolysers, taking into account the defined scenarios in Section 6.3.3 and the estimated hourly electricity prices

from Section 6.3.4.

6.4.1 FCO Scenario

In the FCO scenario, the hydrogen break-even price is calculated over the 20-year lifetime of the electrolysers using (6.1)–(6.3). For the 35 MW electrolyser plant, the hydrogen break-even prices were calculated at 5.57 €/kg_{H_2}, 5.41 €/kg_{H_2}, and 4.65 €/kg_{H_2} under the central, clean molecules, and electrification pathways, respectively. These results align with expectations, as the average electricity price is lowest under the electrification pathway, followed by the clean molecules pathway, and highest under the central pathway. The contribution of each factor to the total cost over the 20-year lifetime of the electrolyser plant is illustrated in Fig. 6.6.

As shown in Fig. 6.6, electricity costs remain the dominant expense driver in all three scenarios, accounting for 86.73%, 86.28%, and 83.93% of total costs in the central, clean molecules, and electrification pathways, respectively, followed by the CapEx. This outcome supports the definition of the PAO scenario, in which electrolysers adjust operation to electricity prices and reduce consumption during high-price periods.

Thereafter, a sensitivity analysis is conducted to identify the most influential parameters affecting the hydrogen break-even price in the FCO scenario. To this end, each parameter, namely electrolyser plant capacity, efficiency, oxygen value, CapEx (including connection costs to the power and gas grids), OpEx, stack replacement, discount rate, and degradation rate, was varied by ±50% relative to their chosen ranges specified in Table 6.1 and Table 6.2. It must be noted that the end-of-life of the electrolyser, specified in Section 6.3.3,

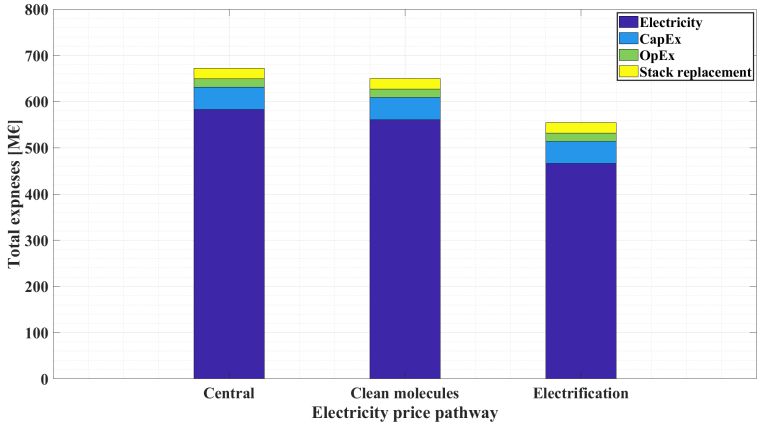

Figure 6.6: Cost breakdown of the FCO scenario

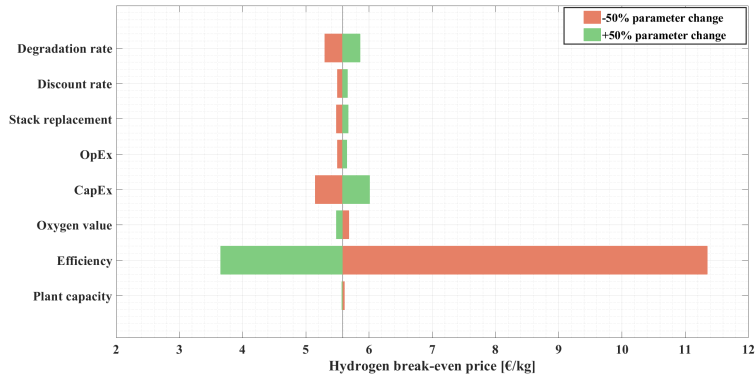

(a) Central electricity price pathway

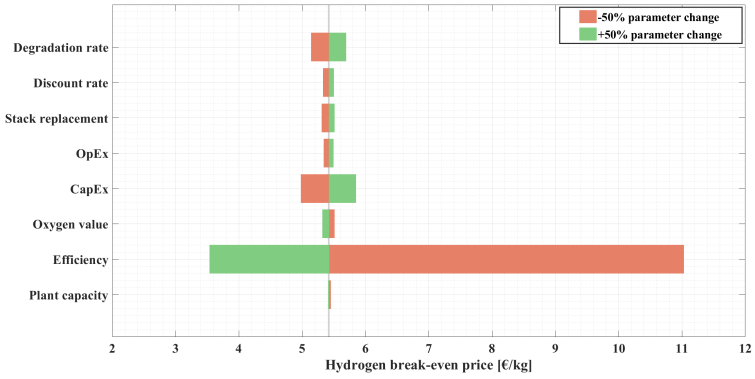

(b) Clean molecules electricity price pathway

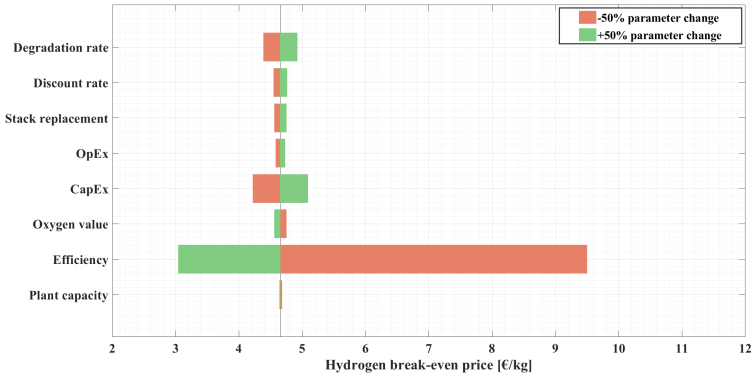

(c) Electrification electricity price pathway

Figure 6.7: Effect of ±50% parameter variations on the hydrogen break-even price in the FCO scenario

was kept constant when varying the degradation rate. Thus, the effect of this parameter on the number of stack replacements has also been considered. Also, although the upper bound of some parameters, such as efficiency, exceeds current technological limits, it is included for sensitivity analysis purposes.

Fig. 6.7 illustrates the effect of variations of the aforementioned parameters on the derived hydrogen break-even prices in the FCO scenario, based on the central, clean molecules, and electrification pathways.

Across all three electricity pathways, efficiency is the most influential parameter, as it determines the amount of electricity required for a given hydrogen output, which accounts for the largest share in the electrolysis cost breakdown, as shown in Fig. 6.6. This was followed by CapEx and degradation rate. In contrast, plant capacity, OpEx, and the discount rate were found to have the least influence on the derived hydrogen break-even price.

6.4.2 PAO Scenario

Regarding the scenario in which the electrolysers adjust their power consumption based on electricity market prices, the three parameters introduced in Section 6.3.3, namely C_{L}, C_{H}, and k, were varied within their respective ranges, resulting in 2565 investigated cases across the three electricity price pathways. For each parameter combination, the dynamic power consumption and hydrogen production of the electrolysers were calculated. Fig. 6.8, Fig. 6.9, and Fig. 6.10 present the results for the central, clean molecules, and electrification pathways, respectively. As shown, the lowest hydrogen break-even price in the PAO scenario is obtained with the parameter set C_{L} = 35, C_{H}=40, and k=1 at 4.84 €/$\mathrm{kg_{H_2}}$ for the central pathway, C_{L}=35, C_{H}=40, and k=1 at 4.71 €/$\mathrm{kg_{H_2}}$ for the clean molecules pathway, and C_{L}=45, C_{H}=30, and k=1 at 4.12 €/$\mathrm{kg_{H_2}}$ for the electrification pathway.

Compared to the FCO scenario, the hydrogen break-even price is reduced in the PAO scenario by 13.10%, 12.93%, and 11.39% for the central, clean molecules, and electrification pathways, respectively. This indicates that the PAO scenario is effective in lowering hydrogen production costs. The effect is most significant in the central pathway, where higher electricity prices allow the algorithm to achieve greater cost reductions. Furthermore, obtaining the lowest price at $k = 1$ in all three pathways shows that the algorithm tends to allocate the maximum number of hours to the C_{L} and C_{H} regions, while in the linearly decreasing region with slope k, illustrated in Fig. 6.1(b), the algorithm forces the electrolysers to respond strongly to electricity prices, thereby achieving the lowest hydrogen break-even price.

The differences in the optimal thresholds C_{L} and C_{H} across the three electricity price pathways are directly attributable to the shape of the respective price distributions, depicted in Fig. 6.11, which presents the electricity price

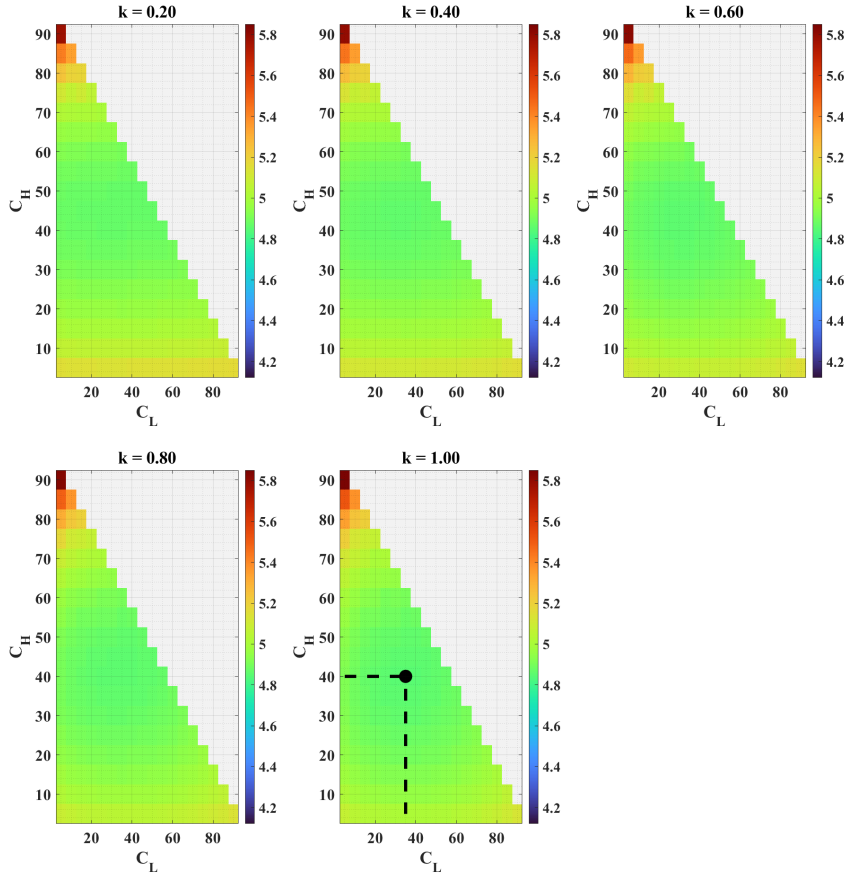

Figure 6.8: Central electricity price pathway

distribution curves for each pathway from 2030 to 2050.

The shape of the price distribution curve, depicted in Fig. 6.11, reflects the trend of the predicted electricity prices for the three pathways, as shown in Fig. 6.3. While the projected prices for the central pathway increase from 2040 onwards, those for the electrification pathway decrease consistently and sharply from 2030 to 2050. A similar downward trend is observed in the clean molecules pathway, although its average prices remain higher than those in the electrification pathway. As a result, the electrification trajectory exhibits a higher concentration of hours at lower prices compared to both the central and clean molecules pathways.

In Fig. 6.11, for the central scenario, the curve is right-shifted and exhibits a fatter tail compared to the other two scenarios, indicating a greater number of hours with higher electricity prices. The PAO algorithm therefore enables maximum power utilisation in the lowest 35% of price hours (C_L=35%,) and limits

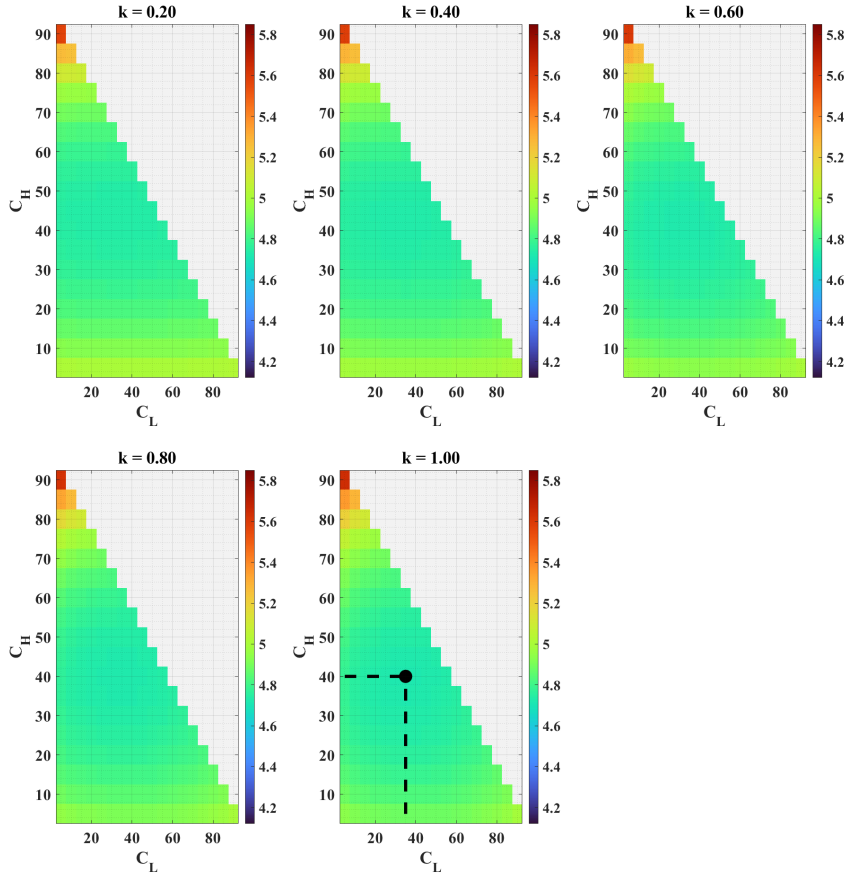

Figure 6.9: Clean molecules electricity price pathway

electrolyser power consumption in the highest 40% of price hours (C_H=40%), resulting in a hydrogen break-even price of 4.84 €/kg_{H_2}.

In the clean molecules pathway, the price distribution shifts moderately downward and to the left relative to the central pathway, with fewer hours at high prices. Given the similarity in the shapes of the price distribution curves for the central and clean molecules pathways, the algorithm converges to the same thresholds, with C_L=35%, C_H=40% and k=1, yielding a hydrogen break-even price of 4.71 €/kg_{H_2}. It should be noted, however, that although C_L and C_H are equal in both the central and clean molecules pathways, the higher concentration of hours within the C_L range and the lower concentration within the C_H range in the clean molecules pathway enable the electrolyser to operate for a greater number of hours, resulting in a higher capacity factor than in the central pathway.

Regarding the electrification pathway, the distribution curve is more

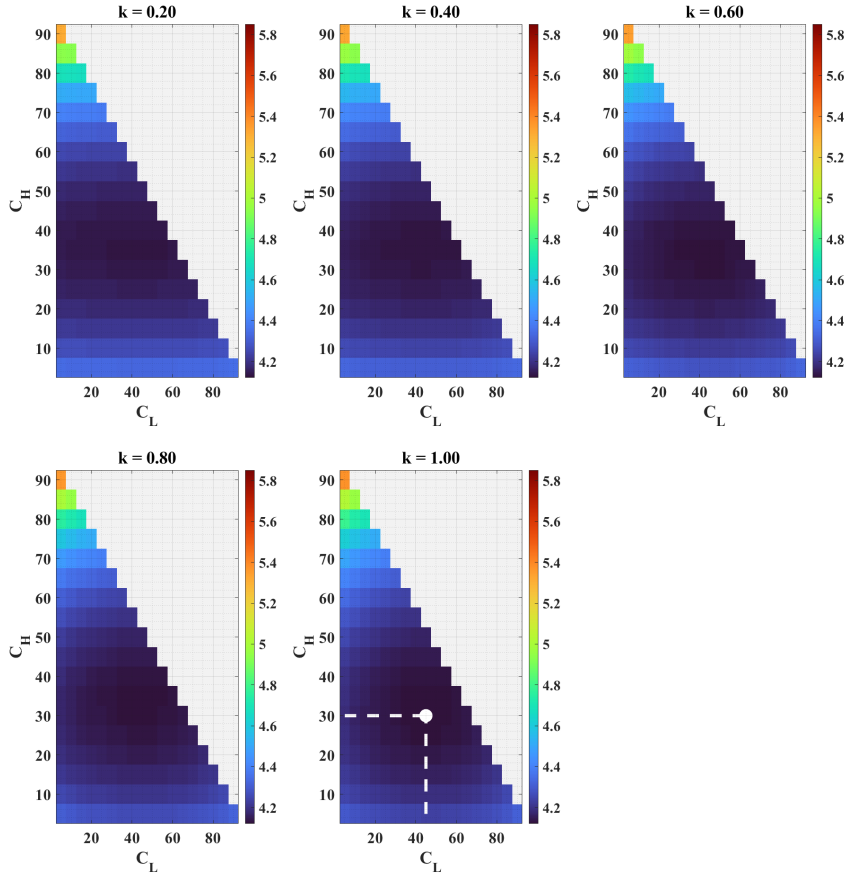

Figure 6.10: Electrification electricity price pathway

strongly left-shifted than in the central and clean molecules pathways, with a substantial concentration of hours at relatively low prices and fewer hours in the expensive tail. Hence, the algorithm extends the maximum operation region to C_{L}=45%, and sets the minimum power operation region at C_{H}=30%. This larger share of low-price hours allows for greater utilisation at reduced electricity costs, leading to a hydrogen break-even price of 4.12 €/$\mathrm{kg_{H_2}}$.

The contribution of each parameter to the overall cost of hydrogen production at the optimised points for the central, clean molecules, and electrification pathways is shown in Fig. 6.12. As in the FCO scenario, electricity remains the dominant contributor to overall costs, followed by CapEx. However, comparing Fig. 6.6 and Fig. 6.12, it can be observed that the PAO algorithm reduces the share of electricity costs to 73.42%, 73.06%, and 71.90%, corresponding to decreases of 15.34%, 15.32%, and 14.33% relative to the FCO scenario for the central, clean molecules, and electrification pathways, respectively.

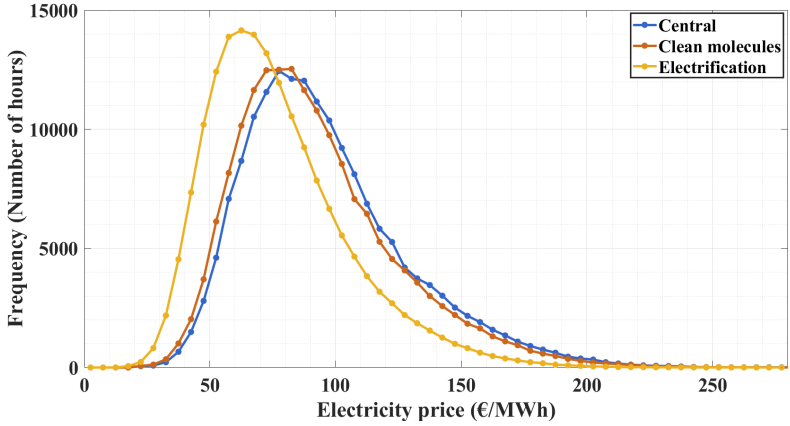

Figure 6.11: Price distribution curves for the central, clean molecule and electrification electricity pathways

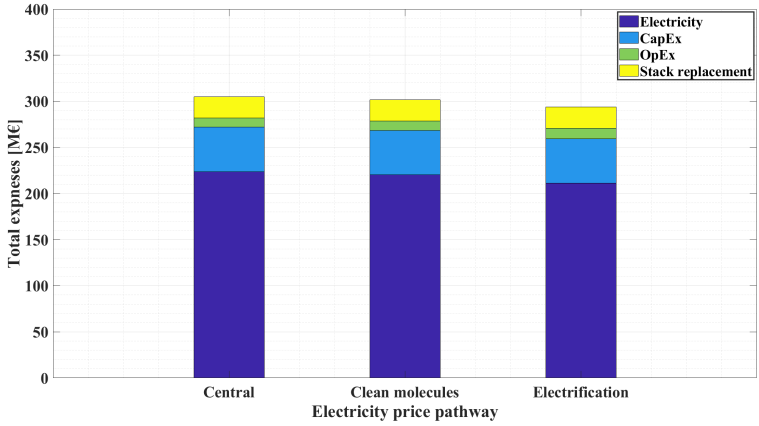

Figure 6.12: Cost breakdown of the PAO scenario

Finally, a sensitivity analysis was conducted for the optimal cases of the central, clean molecules, and electrification pathways by varying the electrolyser plant rated capacity, efficiency, oxygen value, CapEx (including the connection costs to the gas and power grids), OpEx, stack replacement cost, discount rate, and degradation rate. Each of these parameters was varied by ±50% relative to the values specified in Table 6.1 and Table 6.2, and the results are shown in Fig. 6.13. When compared with the FCO scenario sensitivity analysis in Fig. 6.7, efficiency remains the most influential parameter. However, the effects of CapEx and degradation rate become more pronounced due to their higher shares in hydrogen production costs in the PAO scenario. Plant capacity, OpEx,

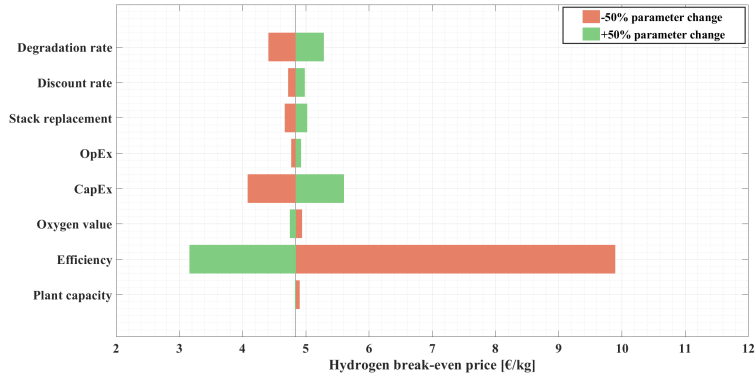

(a) Central electricity price pathway

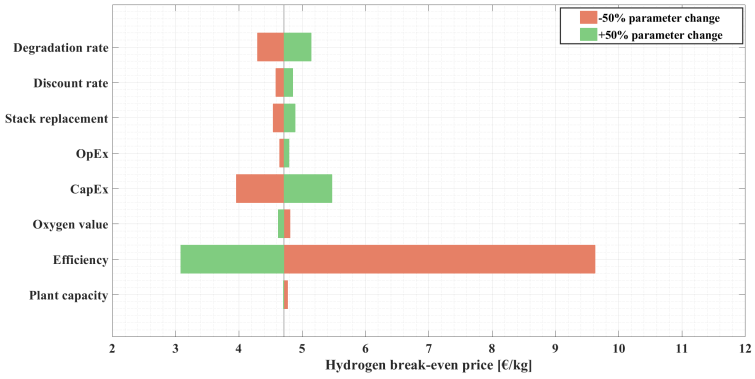

(b) Clean molecules electricity price pathway

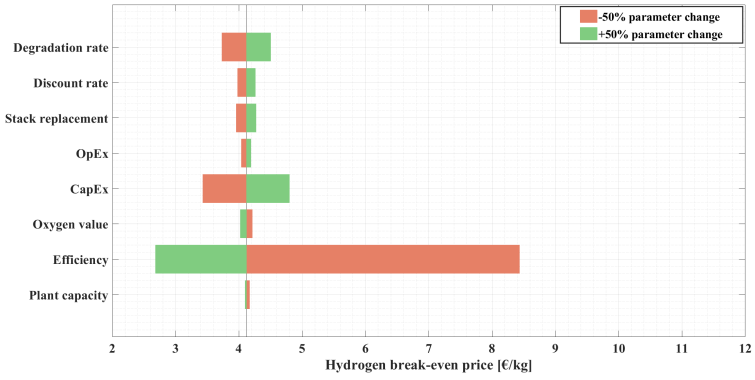

(c) Electrification electricity price pathway

Figure 6.13: Effect of ±50% parameter variations on the hydrogen break-even price in the PAO scenario

and the discount rate remain the least influential parameters.

6.4.3 FCR Scenario

In the FCR scenario, as described in Section 6.3.3, the electrolysers provide the symmetric 200 mHz FCR product within the shaded area shown in Fig. 6.1(b), responding linearly to frequency deviations within ±200 mHz, except for the ±10 mHz deadband around 50 Hz. Therefore, generating frequency time-series data is required for this scenario. In well-structured power systems, the annual frequency distribution typically exhibits a bell-shaped profile, since the frequency remains close to 50 Hz for most of the time, with deviations becoming increasingly rare as they move further from 50 Hz. As a result, strong power systems are characterised by a centred bell-shaped distribution with low probabilities in the tails, whereas weaker power systems may exhibit right- or left-shifted distributions [25]. In Belgium, the interconnection of its power system with neighbouring countries such as the Netherlands, Germany, and France provides strong system support. Accordingly, the historical frequency data published by Elia confirms the presence of a bell-shaped distribution [26].

Since only the symmetric ±200 mHz FCR product is available in Belgium, random frequency values between 49.80 and 50.20 Hz are generated in this study, with the average values following a centred bell-shaped distribution. Frequency deviations beyond ±200 mHz are assumed to be rare events and are thus disregarded in this study. The generated frequency distribution curve used for the FCR scenario is presented in Fig. 6.14. This bell-shaped curve provides a balanced and realistic basis for comparison with the FCO and PAO scenarios. In addition, consistent with real-world applications, frequency signals are sampled every 10 seconds over the 20-year lifetime of the electrolysers. It is worth noting that, to ensure a fair comparison among the three electricity price pathways, the same frequency time series is applied for the central, clean molecules, and electrification trajectories.

In this scenario, priority is given to the PAO algorithm. First, the price-adaptive algorithm is applied in the linear decreasing region. Then, based on the operating power determined for the electrolysers, while accounting for the minimum allowed power of 0.5 MW, the rated power of 5 MW, and minimum FCR increments of 1 MW, the available power is calculated, and the corresponding FCR bid is submitted to the TSO. Using these values, any operating power derived from the PAO algorithm in the linear decreasing region between 1.5 MW and 4 MW can serve as the baseload of the electrolyser for FCR provision. After determining the baseload and P^t_{res}, the electrolysers adjust their power consumption based on the measured instantaneous frequency to restore frequency deviations.

It is worth noting that the remuneration of FCR covers only the reservation

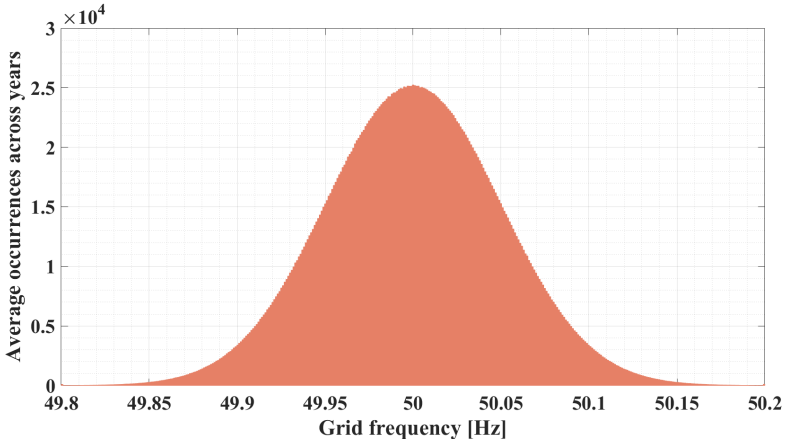

Figure 6.14: Frequency distribution curve from 2030 to 2050 utilised in the FCR scenario

of the capacity dedicated to FCR (P^t_{res}), with no remuneration foreseen for the energy supplied, either upward or downward (P^t_{FCR}) [27].

To avoid complexity, an average price is considered for FCR provision over the lifetime of the electrolysers. For the same year range as considered in Section 6.3.4, the average FCR price in Belgium was found to be 20.5 €/MWh. Nevertheless, this parameter is also included in the sensitivity analysis. Lastly, for simplicity in the modelling framework, electrolysers are assumed to be granted priority in FCR provision as an incentive.

By applying the abovementioned constraints, hydrogen break-even prices of 4.49 €/kg_{H_2}, 4.38 €/kg_{H_2}, and 3.81 €/kg_{H_2} are obtained, corresponding to reductions of 19.38%, 19.03%, and 18.06% compared to the FCO scenario in the central, clean molecules, and electrification electricity price pathways, respectively. These results demonstrate that combining FCR provision with price-adaptive operation of electrolysers can not only reduce hydrogen production costs compared to the FCO scenario but also contribute to grid stability and facilitate the integration of additional RESs into the power system.

The cost breakdown of the FCR scenario is presented in Fig. 6.15. Similar to the FCO and PAO scenarios, electricity remains the largest contributor to overall costs, followed by CapEx, across all electricity price pathways. In the FCR scenario, the electricity shares are 73.49%, 73.13%, and 71.98% for the central, clean molecules, and electrification pathways, respectively. These correspond to reductions of 15.26%, 15.24%, and 13.77% relative to the FCO scenario for the central, clean molecules, and electrification pathways. Although the reduction in the share of electricity cost is smaller than in the PAO scenario, the additional revenue from FCR provision enables the electrolysers

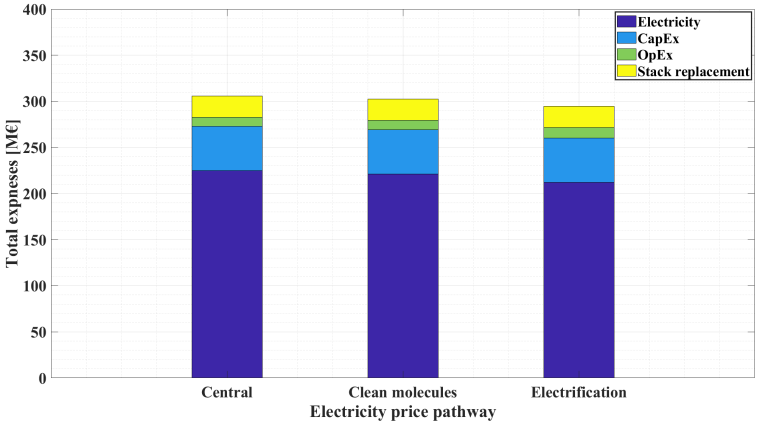

Figure 6.15: Cost breakdown of the FCR scenario

to achieve a lower hydrogen break-even price compared to that scenario.

A sensitivity analysis was also conducted in which the parameters plant capacity, efficiency, oxygen value, CapEx (including the connection costs to the gas and power grids), OpEx, stack replacement costs, discount rate, and degradation rate, in addition to the FCR price, were varied by ±50% relative to their corresponding ranges in Table 6.1 and Table 6.2. The results of the sensitivity analysis for the FCR scenario are shown in Fig. 6.16. Similar to the FCO and PAO scenarios, the electricity price has the greatest impact on the hydrogen break-even price. By contrast, the FCR price has only a minor effect on the hydrogen break-even price for two reasons. First, given the C_{L} and C_{H} values in the three electricity price pathways, the linear decreasing region in which the electrolysers can provide FCR is relatively small. Second, considering the rated capacity, minimum capacity, and minimum FCR step dictated by the TSO, not all operating points within this region are eligible for FCR provision, particularly since priority is given to the PAO scenario.

6.4.4 Comparison of Scenarios

Based on the analysis of the 35 MW PEM electrolyser plant under the FCO, PAO, and FCR scenarios, the lowest break-even hydrogen price is obtained at 3.81 €/$\mathrm{kg_{H_2}}$ in the FCR scenario for the electrification price pathway, derived from historical and projected Belgian power system data. This indicates that operating the electrolysers at their rated load may not be the optimal strategy when the objective is maximising plant revenue. However, in both the PAO and FCR scenarios, the electrolysers do not produce hydrogen at their maximum potential output, despite achieving lower break-even prices. For the most

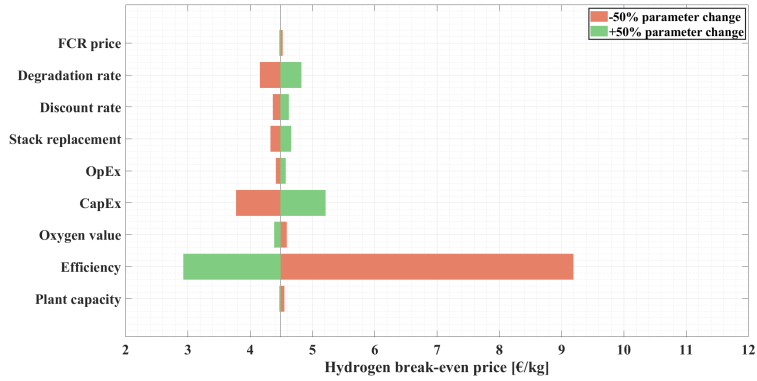

(a) Central electricity price pathway

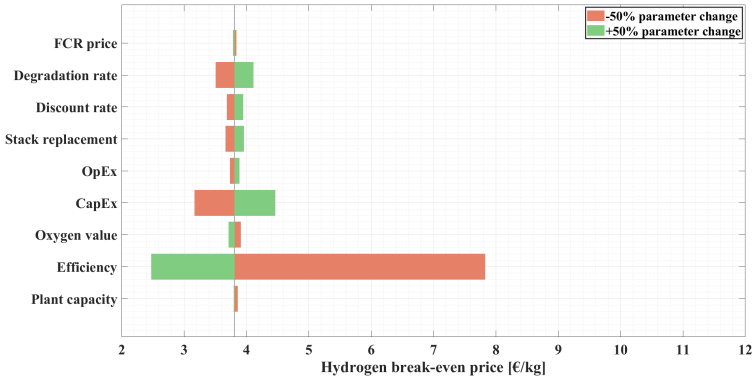

(b) Clean molecules electricity price pathway

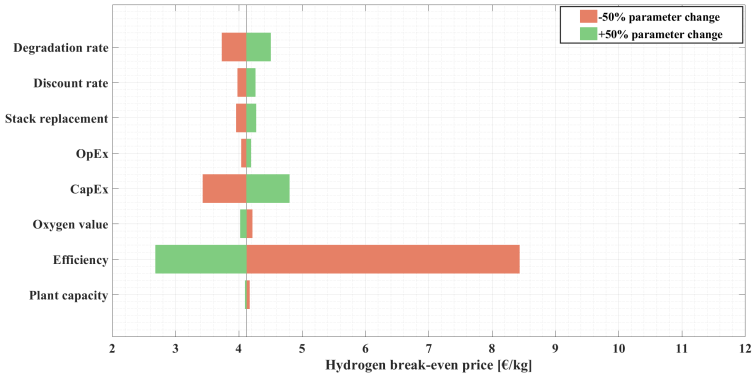

(c) Electrification electricity price pathway

Figure 6.16: Effect of ±50% parameter variations on the hydrogen break-even price in the FCR scenario

optimal cases across the three scenarios, the share of produced hydrogen relative to the full production capacity, along with the corresponding break-even prices, is shown in Fig. 6.17. As illustrated, in the PAO scenario the algorithm reduces the capacity factor to as low as 55% in the central pathway, owing to higher electricity prices compared to the other pathways. In the FCR scenario, because the linearly decreasing region is small and not all operating points are eligible for FCR provision, and since the symmetric product can either increase or decrease the power consumption of the electrolyser, nearly the same capacity factors as in the PAO scenario are obtained across the three pathways. Consequently, in applications where maximising hydrogen output is the priority, the PAO and FCR scenarios may be less relevant, and the FCO scenario becomes the preferred option.

Conversely, the PAO scenario has the potential to make the price of green hydrogen competitive with hydrogen produced from fossil fuels, particularly under higher electricity price conditions such as those in the central pathway. The comparison of cost breakdowns in Fig. 6.6 and Fig. 6.12 clearly demonstrates that the PAO algorithm nearly equalises the costs in the central pathway with those in the clean molecules and electrification pathways. As noted, this effect is achieved by decreasing the capacity factor from 63.4% in the electrification pathway to 55.0% in the central pathway. Consequently, when the objective is to produce green hydrogen at a competitive price with other technologies, the PAO scenario represents the most favourable option.

On the other hand, in the FCR scenario, besides lowering the hydrogen break-even price compared to the FCO and PAO scenarios, electrolysers also support the power system operator in integrating more intermittent RESs. This is achieved by contributing to grid frequency balancing on short time scales through the provision of ancillary services. Such an operation mode is particularly valuable in low-inertia power systems where conventional generators are increasingly being replaced by RESs. However, the control systems of the electrolyser become more complex, which may subsequently lead to higher costs for the associated systems.

As shown in the sensitivity analyses of all three scenarios, efficiency is the most influential parameter. This implies that, for instance, compared with the effect of stack replacement, developing materials that enhance electrolyser efficiency, such as more conductive membranes, rather than durability, results in a lower hydrogen production cost per kilogram. This is directly driven by electricity prices, and in regions with higher electricity costs, such as those represented by the central pathway, improvements in electrolyser efficiency have an even more significant impact.

Finally, compared to hydrogen produced from natural gas, the obtained prices remain relatively high, especially considering that they represent hydrogen break-even prices with no profit margin included. Reported selling prices

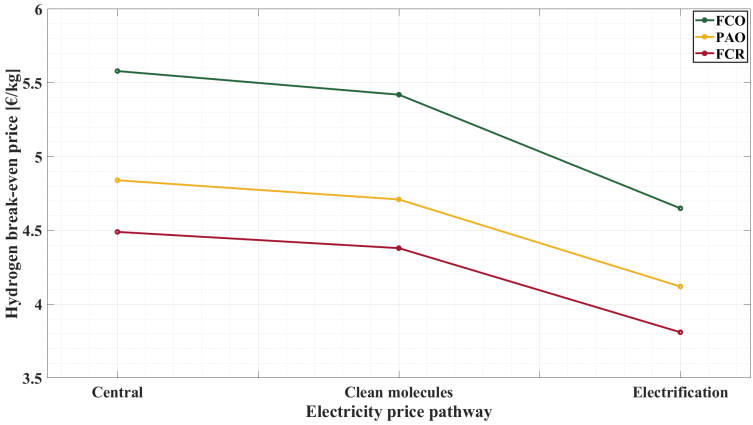

(a) Hydrogen break-even price

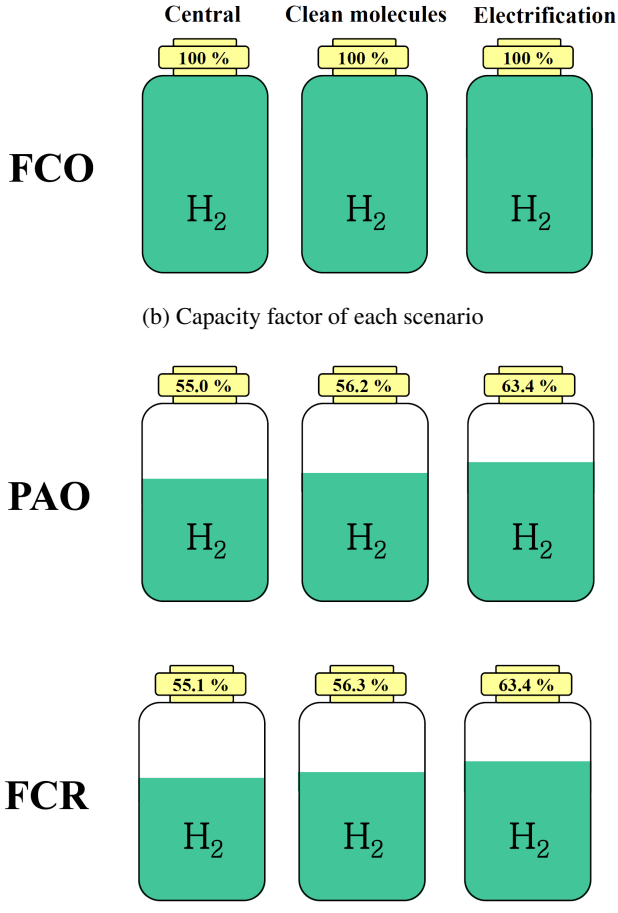

(b) Capacity factor of each scenario

Figure 6.17: Derived hydrogen break-even prices and capacity factors across the three scenarios

for hydrogen produced from natural gas typically range, on average, from 1 to 3 €/kg_{H_2} [28, 29]. In regions with abundant, low-cost domestic natural gas, such as the Middle East and parts of the United States, grey hydrogen prices are lower than in regions that depend on expensive imports, such as Europe and parts of Asia. However, fluctuations in natural gas prices and potential increases in carbon taxes can raise the cost of grey hydrogen, making green hydrogen a more competitive alternative, particularly as advances in materials and system design continue to improve electrolyser efficiency.

6.5 Conclusions

In this chapter, three operational modes of PEM electrolysers are investigated: continuous operation at full capacity, operation based on day-ahead market electricity prices, and operation based on both day-ahead market electricity prices and grid frequency to provide ancillary services. Furthermore, considering the characteristics of the Belgian power system, three future electricity price pathways were analysed to address uncertainties in electricity price trends, namely the central, clean molecules, and electrification pathways. The analysis also accounted for degradation effects, including the increased power consumption of electrolysers over their lifetime. In addition, EU legislation for green hydrogen production was considered, which allows electrolyser operation based on variable grid electricity prices, provided that the responsible entity could demonstrate sufficient renewable capacity in its portfolio. Finally, a sensitivity analysis was conducted for each scenario to identify the most influential parameters and to decouple the results from uncertainties associated with parameter selection.

In the FCO scenario, hydrogen break-even prices of 5.57 €/kg_{H_2}, 5.41 €/kg_{H_2}, and 4.65 €/kg_{H_2} were calculated for the central, clean molecules, and electrification electricity price pathways, respectively, with the electrolyser plant operating at a 100% capacity factor throughout its lifetime.

In the PAO scenario, the algorithm effectively reduced the hydrogen break-even price to 4.84 €/kg_{H_2}, 4.71 €/kg_{H_2}, and 4.12 €/kg_{H_2} for the central, clean molecules, and electrification pathways, respectively. This reduction was achieved by lowering the share of electricity in the total costs by 15.34%, 15.32%, and 14.33% compared to the FCO scenario for the respective electricity price trajectories. However, this optimisation was achieved by lowering the capacity factor of the electrolysers over the 20-year plant lifetime to 55.0%, 56.2%, and 63.4% for the three electricity price pathways, respectively.

In the FCR scenario, hydrogen break-even prices of 4.49 €/kg_{H_2}, 4.38 €/kg_{H_2}, and 3.81 €/kg_{H_2} were calculated for the central, clean molecules, and electrification pathways, respectively. In this case, electrol-

ysers supported the grid by providing symmetric 200 mHz FCR, enabling system operators to facilitate the integration of variable RESs generation. The corresponding capacity factors of 55.1%, 56.3%, and 63.4% were observed across the respective electricity price pathways, which are similar to those obtained in the PAO scenario. The results demonstrated that, thanks to their fast dynamic response, PEM electrolysers were capable of delivering FCR while simultaneously increasing revenues and thereby reducing the hydrogen break-even price.

Based on the obtained results, it can be concluded that the selected operational strategy of the electrolysers strongly depends on both the accurate prediction of future electricity prices and the intended application. Although the PAO and FCR scenarios reduced the hydrogen break-even price across all three electricity price pathways, this reduction was achieved at the expense of a lower capacity factor and, consequently, a lower hydrogen output. Both the reduction in break-even price and the reduction in capacity factor, relative to the FCO scenario, were more pronounced under higher electricity prices, as in the central pathway, where price reductions of 13.10% (PAO scenario) and 19.38% (FCR scenario) were accompanied by a capacity factor of approximately 55.0% for both scenarios. In contrast, under lower electricity prices, as in the electrification pathway, the reductions were less substantial, with price decreases of 11.39% (PAO scenario) and 18.06% (FCR scenario), and a capacity factor of around 63.4% for both scenarios, since the algorithm restricted electrolyser operation less frequently than in the central pathway.

Additionally, based on the sensitivity analysis conducted for the three scenarios, it can be deduced that investing in materials that enhance electrolyser efficiency would have a more pronounced impact on the hydrogen production cost, given the high sensitivity of the results to efficiency compared to durability-related parameters such as degradation rate and stack replacement costs.

For future work, modelling the ageing behaviour of PEM electrolysers more accurately and integrating it with the approach presented in this study could improve the reliability of the results. This is important because, for instance, in the FCO scenario, the electrolysers always operate at full load, which may exhaust critical components more quickly and increase the degradation rate compared to the PAO and FCR scenarios, where the units are not continuously at full load. On the other hand, frequent ramping up and down in the PAO and FCR scenarios may accelerate ageing relative to the FCO scenario. In addition, by mimicking the inertial response of PEM electrolysers, the extent to which they can enhance grid flexibility could be assessed, helping to determine whether the reduction in hydrogen break-even price compared to the FCO and PAO scenarios justifies the associated decrease in electrolyser capacity factor and the increased complexity of the control systems.

Bibliography

[1] D. Gusain, M. Cvetković, R. Bentvelsen, and P. Palensky, "Technical assessment of large scale PEM electrolyzers as flexibility service providers," in *2020 IEEE 29th International Symposium on Industrial Electronics (ISIE)*, pp. 1074–1078, IEEE, 2020.

[2] E. Crespi, G. Guandalini, L. Mastropasqua, S. Campanari, and J. Brouwer, "Experimental and theoretical evaluation of a 60 kW PEM electrolysis system for flexible dynamic operation," *Energy Conversion and Management*, vol. 277, 2023.

[3] A. Buttler and H. Spliethoff, "Current status of water electrolysis for energy storage, grid balancing and sector coupling via power-to-gas and power-to-liquids: A review," *Renewable and Sustainable Energy Reviews*, vol. 82, pp. 2440–2454, 2018.

[4] H. J. Fell, P. Chladek, O. Wallevik, and S. T. Briskeby, "Flexible production of hydrogen from sun and wind: challenges and experiences," in *Proc. 18th World Hydrogen Energy Conf.(WHEC 2010)*, pp. 112–118, 2010.

[5] J. Mohammed-Ibrahim and H. Moussab, "Recent advances on hydrogen production through seawater electrolysis," *Materials Science for Energy Technologies*, vol. 3, pp. 780–807, 2020.

[6] R. A. Tufa, E. Curcio, W. van Baak, J. Veerman, S. Grasman, E. Fontananova, and G. Di Profio, "Potential of brackish water and brine for energy generation by salinity gradient power-reverse electrodialysis," *RSC Advances*, vol. 4, no. 80, pp. 42617–42623, 2014.

[7] L. Wan, T. Moan, Z. Gao, and W. Shi, "A review on the technical development of combined wind and wave energy conversion systems," *Energy*, 2024.

[8] T. Egeland-Eriksen and S. Sartori, "Techno-economic analysis of the effect of a novel price-based control system on the hydrogen production for an offshore 1.5 GW wind-hydrogen system," *Energy Reports*, vol. 11, pp. 2633–2655, 2024.

[9] E. Rettig, I. Fischhendler, and F. Schlecht, "The meaning of energy islands: Towards a theoretical framework," *Renewable and Sustainable Energy Reviews*, vol. 187, 2023.

[10] A. Lüth and D. Keles, "Risks, strategies, and benefits of offshore energy hubs: A literature-based survey," *Renewable and Sustainable Energy Reviews*, vol. 203, 2024.

[11] A. Patonia and R. Poudineh, *Cost-competitive green hydrogen: how to lower the cost of electrolysers?* No. 47, The Oxford Institute for Energy Studies, 2022.

[12] S. Asiaban, D. Bozalakov, and L. Vandevelde, "Development of a dynamic mathematical model of PEM electrolyser for integration into large-scale power systems," *Energy Conversion and Management: X*, vol. 23, p. 100610, 2024.

[13] Á. Hernández-Gómez, V. Ramirez, D. Guilbert, and B. Saldivar, "Development of an adaptive static-dynamic electrical model based on input electrical energy for PEM water electrolysis," *International journal of hydrogen energy*, vol. 45, no. 38, pp. 18817–18830, 2020.

[14] "The Princess Elisabeth Island." https://www.elia.be/en/infrastructure-and-projects/infrastructure-projects/princess-elisabeth-island. Accessed: December 8, 2025.

[15] "Vision and strategy, hydrogen - Belgian Federal Government." https://economie.fgov.be, 2022. Accessed: March 8, 2023.

[16] "Cummins using hydrogen technology to enable renewable energy for public utilities in Washington with the largest PEM electrolyzer in the United States." https://www.cummins.com/news/releases. Accessed: December 8, 2025.

[17] G. Erbach and S. Svensson, "EU rules for renewable hydrogen delegated regulations on a methodology for renewable fuels of non-biological origin," 2023.

[18] A. E. Samani, A. D'Amicis, J. D. M. De Kooning, D. Bozalakov, P. Silva, and L. Vandevelde, "Grid balancing with a large-scale electrolyser providing primary reserve," *IET Renewable Power Generation*, vol. 14, no. 16, pp. 3070–3078, 2020.

[19] P. Hesel, S. Braun, F. Zimmermann, and W. Fichtner, "Integrated modelling of European electricity and hydrogen markets," *Applied Energy*, vol. 328, 2022.

[20] "EPRI, Water electrolyzer stack degradation. (2022)." https://www.epri.com/research/products/. Accessed: December 8, 2025.

[21] "Technical targets for proton exchange membrane electrolysis - U.S. Department of Energy." https://www.energy.gov/eere/fuelcells/technical-targets-proton-exchange-membrane-electrolysis. Accessed: December 8, 2025.

[22] E. Lenaerts, W. Nijs, and P. Valkering, "Scenario towards a climate neutral Belgium by 2050 (2024)," *EnergyVille - VITO*. Available online: https://climat.be/doc/climate-neutral-belgium-by-2050-report.

[23] J. C. Laguna, A. Moglianesi, P. Vingerhoets, and P. Lodewijks, "Description of the EnergyVille TIMES BE model," *EnergyVille (2022)*, 2022. Available online: https://energyville.be/en/blog/samen-modelleren-we-beter-epoc-paths-2050-en-de-belgische-energietoekomst/.

[24] "Elia - Belgian bidding zone day-ahead reference price." https://www.elia.be/en/grid-data/transmission/day-ahead-reference-price. Accessed: December 8, 2025.

[25] Y. Zhang, W. Yao, S. You, W. Yu, L. Wu, Y. Cui, and Y. Liu, "Impacts of power grid frequency deviation on time error of synchronous electric clock and worldwide power system practices on time error correction," *Energies*, vol. 10, no. 9, 2017.

[26] "Elia, Frequency and FCR demand per 10 seconds." https://opendata.elia.be/explore/dataset/ods057/information/. Accessed: December 8, 2025.

[27] "Elia, FCR design note (2019)." https://www.elia.be/en/electricity-market-and-system/system-services/keeping-the-balance/fcr. Accessed: December 8, 2025.

[28] Stargate Hydrogen, "Grey hydrogen: The most widely used form of hydrogen – and why we need to move towards green hydrogen." https://stargatehydrogen.com/blog/grey-hydrogen/, 2025. Accessed: December 8, 2025.

[29] Montel, "Hydrogen production cost trends 2025." https://montel.energy/resources/blog/hydrogen-production-cost-trends-2025current-state-of-hydrogen-production-costs/, 2025. Accessed: December 8, 2025.

Chapter 7

Life Cycle Assessment of Green Hydrogen Production

In this chapter, a life cycle assessment (LCA) is presented to evaluate the environmental impacts of green hydrogen production. To this end, a cradle-to-gate LCA study is conducted, where the system boundaries include offshore wind turbines, seawater reverse osmosis (SWRO) systems, proton exchange membrane (PEM) electrolysers, and hydrogen compression and storage units (foreground processes), along with the corresponding upstream and downstream processes (background processes). Environmental impacts are evaluated based on the Environmental Footprint (EF) v3.0 method, developed by the European Commission.

7.1 Introduction

LCA is a widely recognised methodology to quantify the environmental impacts associated with the entire life cycle of a product or a process. The two primary applications of LCA include [1]:

- analysing the contribution of each life cycle stage to the overall environmental load, which aids in identifying product footprints and prioritising improvements in specific stages of products or processes;
- comparing different production pathways for a given product, or evaluating alternative products, to select the option with the least environmental impact.

The methodology for conducting an LCA has been revised and standardised multiple times over time [2]. This study follows the standard established by

the International Organisation for Standardisation (ISO) 14040 and ISO 14044, which consists of four key stages [1, 3, 4]:

Stage 1: Goal and Scope Definition

This stage determines which phases of the product life cycle will be included in the assessment and defines the overall purpose of the study. It also involves the definition of system boundaries, which determines the extent of processes and subsystems to be analysed. Thereafter, based on these boundaries, a strategy for data collection is developed. The functional unit is then defined, which is the quantified reference basis for all subsequent calculations. Finally, decisions regarding the selection of environmental impact categories and assessment methods are made.

Stage 2: Life Cycle Inventory (LCI)

In this phase, data on all relevant inputs (e.g., raw materials, energy) and outputs (e.g., emissions, waste) are collected in accordance with the system boundaries and functional unit defined in Stage 1. The inventory quantifies the environmental loads resulting from resource consumption, material production, emissions to air, water, and soil, and waste generation for each subsystem involved in the life cycle.

Stage 3: Life Cycle Impact Assessment (LCIA)

In this stage, the environmental impacts resulting from the inputs and outputs quantified in the LCI are evaluated. According to the ISO standards for life cycle impact assessment, the process begins by linking the inventory data to appropriate impact categories, such as climate change, toxicity, acidification, and so on. These categories are selected based on the goals and scope of the study. The contribution of each inventory flow to the selected impact categories is then quantified. Subsequently, these impact values are normalised using reference values specific to each category, enabling a better understanding of their relative significance. Eventually, based on the chosen impact assessment method, weighting factors are applied to each category to assess and compare their relative significance in contributing to the overall environmental load.

Stage 4: Interpretation of Results

The final phase involves deriving and interpreting the results obtained from the previous three stages. This includes identifying the most environmentally impactful processes or subsystems, recognising data limitations, assessing the

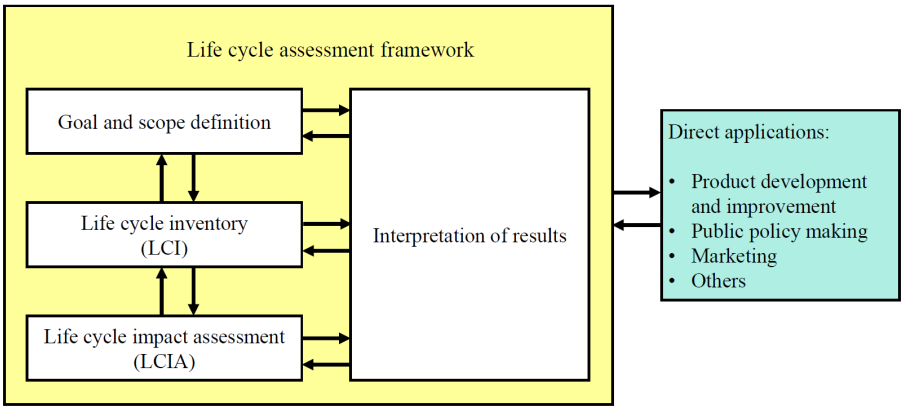

Figure 7.1: Working procedure of an LCA based on ISO 14040 guidelines [1]

reliability and robustness of the results, and drawing conclusions regarding the environmental performance of the system.

An overview of the LCA stages, in accordance with ISO 14040 guidelines, is illustrated in Fig. 7.1 [1].

Generally, three main system boundary approaches can be adopted in an LCA study. The cradle-to-grave method covers the entire life cycle of a product, from raw material extraction and manufacturing, through the use phase, to final disposal. The cradle-to-gate approach, by contrast, considers only a partial life cycle, from raw material extraction and manufacturing up to the product leaving the production facility, excluding transportation, use, and disposal stages. Lastly, the cradle-to-cradle method extends the cradle-to-grave framework by including the recycling or reuse of the product at end-of-life. This process can result in either the same product being regenerated (e.g., aluminium cans made from used cans) or a different product being generated from the recovered materials (e.g., glass wool insulation made from recycled glass bottles).

The LCA approach applied to a given product is chosen based on the goal of the study, product type, the system boundaries, and other influencing factors such as data availability and the relative importance of different life cycle stages.

7.2 Literature Review

In the existing literature, LCA of green hydrogen production have been conducted using various system boundaries and from different perspectives.

The authors in [5] performed a cradle-to-grave LCA for a 5 MW PEM electrolysis plant, where three scenarios were considered: (i) a state-of-the-art

(SoA) plant powered by the German electricity grid mix, (ii) a SoA plant operating within a fully decarbonised energy system, and (iii) a future electrolysis plant developed with reduced energy and material requirements, also operating in a completely decarbonised energy system. The global warming potential (GWP) in the first scenario was reported at 34 kg CO_2-eq/kg_{H_2}, while the second and third scenarios achieved reductions of 89% and an additional 9%, respectively. Thus, due to the significant benefits of operating electrolysers within a fully decarbonised energy system, the authors suggested operating electrolysis systems in regions with high offshore wind availability.

In [6], the authors conducted an LCA of four types of electrolyser technologies: alkaline electrolyser (AE), PEM electrolyser, solid oxide (SO) electrolyser and anion exchange membrane (AEM) electrolyser. The study focused on identifying material-related environmental hotspots during electrolyser operation, where four impact categories were considered: climate change, human health, ecosystem quality, and abiotic resource depletion. It was found that steel in AE and AEM electrolysers, platinum in PEM electrolysers, and nickel in both SO and AE electrolysers were the most impactful materials.

The authors in [7] carried out an LCA of green hydrogen production, focusing on the influence of electricity sources. The study concluded that using wind energy instead of the German electricity grid mix could substantially reduce the GWP of hydrogen production. For AE and PEM electrolysers, the GWP can be reduced up to 93%, while SO electrolysers showed a reduction potential up to 81%. Furthermore, by 2045, operating electrolysers with wind power can lower the climate change impacts to as low as 1.33 kg CO_2-eq/kg_{H_2}. The authors also recommended replacing environmentally harmful substances such as per- and polyfluoroalkyl substances (PFAS) with alternatives like PTFE-based gaskets to further mitigate environmental impacts.

To quantify the greenhouse gas (GHG) emissions associated with wind-based hydrogen production using an alkaline electrolyser, a cradle-to-gate LCA study was performed in [8]. The total GHG emissions of the wind-powered hydrogen production plant were estimated at approximately 0.68 kg CO_2-eq/kg_{H_2}. The breakdown of emissions showed that 65% was attributed to the construction of the wind power infrastructure, 22% to hydrogen compression, 7% to the electrolyser system, and 6% to hydrogen transportation. In contrast to natural gas-based hydrogen production, where the majority of emissions occur during the plant operational phase, wind-based hydrogen production via alkaline electrolysis results in approximately 94% lower GHG emissions compared to steam methane reforming (SMR).

In another study, the authors in [2] conducted an LCA comparing hydrogen production via PEM electrolysers with the SMR process. Their findings indicated that when PEM electrolysers are powered by renewable electricity, CO_2 emissions can be reduced by up to 75% compared to SMR. The authors also

concluded that the composition of the electricity mix is the dominant factor influencing global warming potential, while reducing material consumption contributes only marginally to emissions reduction. Under the German electricity mix in 2017, the GWP of hydrogen production via the PEM electrolyser was calculated at 29.5 kg CO_2-eq/kg_{H_2}. By operating the electrolyser only with 3000 hours per year of excess electricity from renewable energy sources (RESs), emissions could be reduced to as low as 3.3 kg CO_2-eq/kg_{H_2}.

In [9], a cradle-to-gate LCA was carried out to evaluate green hydrogen production using AE and PEM electrolysers. The study also included a comparative analysis of three hydrogen production routes: green hydrogen (produced from RESs), grey hydrogen (produced from fossil fuels), and blue hydrogen (produced from fossil fuels equipped with carbon capture and storage). The authors found only marginal differences in the environmental impacts between AE and PEM electrolysers, with PEM performing slightly better, primarily due to its higher efficiency and possibly because alkaline electrolysers rely more on grid electricity to meet their minimum load requirements. The results further indicated that emerging green hydrogen technologies outperform both grey and blue hydrogen production technologies across all impact categories, except for mineral and metal resource use, due to the presence of rare earth elements in electrolyser stacks. Blue hydrogen, in comparison to grey hydrogen, showed improved performance only in the climate change category. Based on this, the authors concluded that direct transition from grey to green hydrogen is a more effective and sustainable strategy than investing in blue hydrogen pathways.

The study in [9] also identified that the electricity source and then, electrolyser stacks are the primary contributors to overall environmental impacts, while balance of plant (BoP) and power electronics components have a minimal effect. Also, technological improvements in AE and PEM electrolyser designs, particularly those aimed at increasing current density, were shown to reduce environmental impacts across most categories. Finally, in addition to enhancing current density, improving minimum load requirements of electrolysers, advancing sustainable mining methods, and lowering the carbon intensity of steel production could further reduce the environmental impacts associated with green hydrogen production.

The authors in [10] compared the climate change impacts of hydrogen production through four different pathways: grey hydrogen (produced via SMR), blue hydrogen (produced via SMR with CCS), turquoise hydrogen (produced through methane pyrolysis), and green hydrogen (produced via PEM electrolysers). For the three fossil fuel-based routes, the analysis considered two natural gas supply chains: one using pipeline transport and the other using liquefied natural gas (LNG). The LCA results showed that grey hydrogen has the highest emissions in terms of climate change, with 13.9 kg CO_2-eq/kg_{H_2} for LNG route and 12.3 kg CO_2-eq/kg_{H_2} for the pipeline route, while blue hy-

drogen showed moderate improvements, with 9.3 and 7.6 kg CO_2-eq/kg_{H_2} for the LNG and pipeline routes, respectively. Turquoise hydrogen demonstrated lower emissions than grey and blue, with 8.3 kg CO_2-eq/kg_{H_2} for LNG and 6.1 kg CO_2-eq/kg_{H_2} for the pipeline route. Among all options, green hydrogen exhibited the lowest climate impact, with emissions of 0.6 kg CO_2-eq/kg_{H_2} when powered by wind energy and 2.5 kg CO_2-eq/kg_{H_2} when powered by solar energy.

In [11], the authors performed an LCA to compare three solar-driven green hydrogen pathways using PEM electrolysers. The study examined the environmental performance of coupling the electrolyser with: photothermal (PHT) power generation, photovoltaic (PV) power generation, and thermochemical water splitting via sulphur-iodine cycle integrated with solar photothermal technology (S-I/PHT). The study focused on four impact categories, namely, global warming potential, acidification potential, ozone depletion potential, and nutrient enrichment potential. Among the three configurations, the S-I/PHT approach showed the best environmental performance across all categories. It exhibited the lowest global warming potential at 1.02 kg CO_2-eq/kg_{H_2}, followed by PHT at 8.67 and PV at 9.37 kg CO_2-eq/kg_{H_2}. For acidification potential, S-I/PHT again showed the best performance at 6.56×10^{-3} kg SO_2-eq/kg_{H_2}, followed by PV at 0.0295 and PHT at 0.0339 kg SO_2-eq/kg_{H_2}. Nutrient enrichment potential was also lowest for S-I/PHT at 4.78×10^{-4} kg Phosphate-eq/kg_{H_2}, followed by PV with 2.91×10^{-3} and PT with 2.98×10^{-3}. Regarding ozone depletion potential, S-I/PHT resulted in the lowest emissions at 8.72×10^{-14} kg R11-eq/kg_{H_2}, while PHT and PV recorded 7.82×10^{-13} and 3.19×10^{-11} kg R11-eq/kg_{H_2}, successively. The study also concluded that increasing the system lifetime is an effective strategy to further reduce the environmental impact of solar-based green hydrogen production.

7.3 Life Cycle Assessment of Green Hydrogen Production

This section presents an LCA of green hydrogen production, following the framework established by ISO 14040 and ISO 14044 standards. The four main phases of the LCA methodology are addressed in the subsequent subsections.

7.3.1 Goal and Scope Definition

In this section, the objective of the study is described, along with the defined functional unit and the system boundaries considered in the assessment.

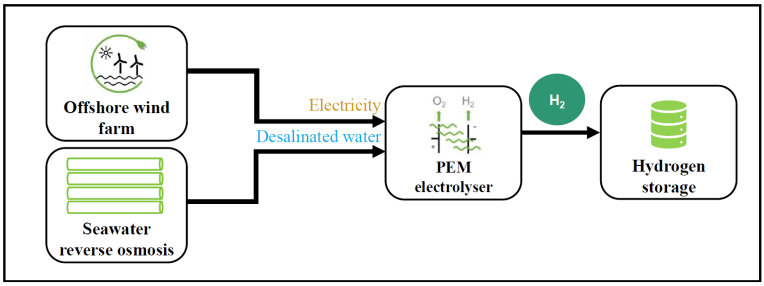

Figure 7.2: Production of hydrogen from offshore wind farm

Goal of the study

The purpose of this study is to evaluate the environmental impacts associated with the production of green hydrogen using seawater and offshore wind energy. Accordingly, with reference to the LCA applications discussed in Section 7.1, this study aims to determine the contribution of each process required for hydrogen production, form electricity generation using wind energy to seawater treatment, electrolysis and hydrogen storage, to the overall environmental footprint of the system. To this end, a cradle-to-gate LCA approach is performed, wherein electricity generated by offshore wind turbines is utilised to power both an SWRO system and a PEM electrolyser. An overview of the system configuration evaluated in this study is depicted in Fig. 7.2.

Scope of the study

Regarding the system boundaries, the supply of raw materials required for the manufacturing of wind turbines, the SWRO unit, the PEM electrolyser and the compression/storage system is included. It is assumed that both the SWRO and PEM systems are exclusively powered by renewable electricity generated from wind turbines. Moreover, essential BoP components needed for each system, such as electrical infrastructure for the wind farm, water storage tanks for the SWRO system, and foundation structures for the PEM electrolyser, are also considered within the system boundary. The overall material and energy flows, as well as the associated emissions related to hydrogen production under the defined system boundaries, are shown in Fig. 7.3.

The analysis is conducted using a functional unit of 1 kg of green hydrogen, which provides a standardised reference point that enables scalability to real-life scenarios and potential extension to alternative hydrogen-derived pathways, such as the production of methane or methanol.

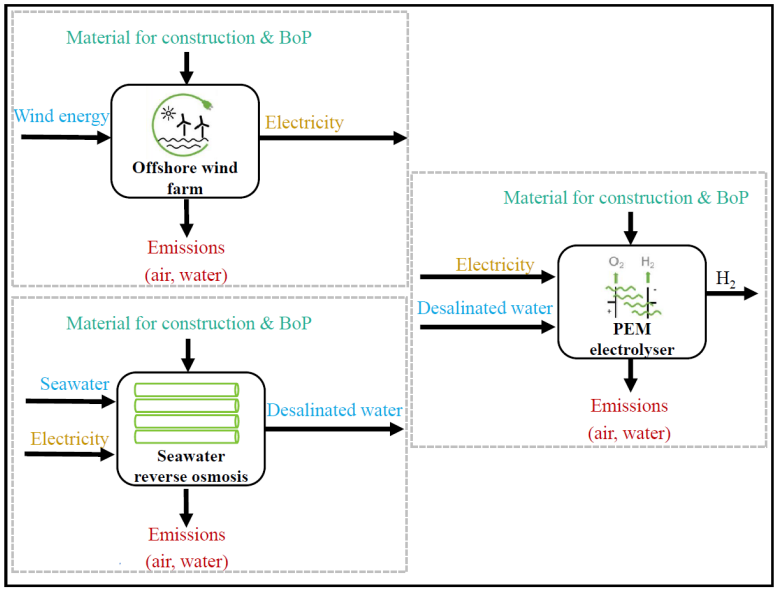

Figure 7.3: System boundaries for the production of hydrogen from an offshore wind farm

7.3.2 Life Cycle Inventory

This section describes the materials requirements for each subsystem included within the system boundaries, along with the materials associated with their respective BoP components. All reported material quantities in this section are expressed relative to the functional unit of 1 kg of hydrogen production, as defined in Section 7.3.1.

The material inventory for the wind turbine, including BoP elements such as foundations, electrical cables, and transformers, is provided in Table 7.1 [8].

Regarding the desalination system, the materials required for constructing

Table 7.1: Material breakdown of the wind turbine and its BoP components for 1 kg of hydrogen production [8]

Material [kg]	Turbine	Foundations	Cables	Transformers
Steel and iron	5.82×10^{-2}	1.41×10^{-2}	0	1.68×10^{-4}
Aluminium/Aluminium alloys	4.94×10^{-4}	0	1.80×10^{-3}	12.25×10^{-4}
Copper	7.30×10^{-4}	0	8.99×10^{-4}	5.62×10^{-5}
Polymer materials	2.25×10^{-3}	5.62×10^{-5}	1.40×10^{-3}	0
Process polymers	3.37×10^{-4}	0	0	0
Ceramic/glass	2.92×10^{-3}	0	0	0
Concrete	0	2.55×10^{-1}	0	0
Electronics	5.06×10^{-4}	0	0	0
Lubricants	2.25×10^{-4}	0	0	1.68×10^{-4}

Table 7.2: Material breakdown of the SWRO system for 1 kg of hydrogen production [12]

Material	Required amount	Unit
Seawater	3.87×10^{-2}	m^3
Antiscalant	4.14×10^{-8}	m^3
Anti-foam agent	1.92×10^{-8}	m^3
Hydrochloric acid	5.94×10^{-4}	kg
Sodium hydroxide	3.72×10^{-4}	kg
Chlorine	3.57×10^{-3}	kg
Poly-aluminum chloride	6.30×10^{-7}	kg
Ferric chloride	3.53×10^{-6}	kg
Lubricants	4.10×10^{-6}	kg
Grease	5.96×10^{-9}	kg

Table 7.3: Material breakdown of the PEM electrolyser for 1 kg of hydrogen production [8, 11–13].

Material	Required amount	Unit
Activated carbon	9.94×10^{-6}	kg
Aluminium	2.98×10^{-5}	kg
Copper	4.97×10^{-6}	kg
Electricity	60.00	kWh
Iridium	8.30×10^{-8}	kg
Platinum	8.00×10^{-8}	kg
Stainless steel	1.11×10^{-4}	kg
Titanium	5.83×10^{-4}	kg
Water	9.00	kg
Nafion	1.76×10^{-5}	kg

the SWRO unit are considered, along with those needed for the water storage tank that holds seawater prior to treatment. The complete material breakdown for the SWRO system and its BoP components is provided in Table 7.2 [12].

The material composition for the PEM electrolyser is summarised in Table 7.3, while that of its associated BoP components is listed in Table 7.4 [8, 11–13].

Finally, the materials involved in the hydrogen compression and storage system are detailed in Table 7.5.

7.3.3 Impact Assessment Method

In the LCIA, first, total emissions were first quantified based on the material requirements for the construction of each subsystem and their respective BoP components, as shown in Tables 7.1–7.5. These were then combined with

Table 7.4: Material breakdown of the BoP of the PEM electrolyser for 1 kg of hydrogen production [8, 11–13].

Material	Required amount	Unit
Concrete	6.19×10^{-3}	kg
Aluminium	1.11×10^{-4}	kg
Copper	3.31×10^{-4}	kg
Polycarbonate compound	1.11×10^{-4}	kg
Steel	7.40×10^{-3}	kg

Table 7.5: Material breakdown of hydrogen storage/compression system for the PEM electrolyser for 1 kg of hydrogen production [12]

Material	Required amount	Unit
Chromium steel	1.34×10^{-3}	kg
Cast iron	4.23×10^{-4}	kg
Ethylene glycol	4.94×10^{-6}	kg
Lubricants	1.27×10^{-5}	kg
Aluminium	4.23×10^{-5}	kg
Tube insulation	1.06×10^{-5}	kg
Copper	3.17×10^{-5}	kg
Electricity	7.05×10^{-4}	kWh

emissions generated during both the construction and operational phases. The aggregated emission breakdown is presented in Table 7.6 [12, 14].

It is assumed that the operation of the wind farm does not result in any direct emissions to air or water. For the PEM electrolyser, Nickel or Platinum (commonly coated with Nickel) is employed as the anode catalyst. During operation of the electrolyser, the Nickel at the anode can oxidise to form Nickel cation (Ni^{2+}), which is released into the water. Therefore, Ni^{2+} is considered as an emission to water in this study [12].

As previously stated, the environmental impacts in this study are assessed using the EF v3.0 method established by the European Commission. This method includes 16 midpoint impact categories, as described in [15]. Based on the collected data shown in Table 7.6, 10 impact categories are chosen for this study: climate change, ecotoxicity (freshwater), human toxicity (non-cancer), human toxicity (cancer), photochemical ozone formation, acidification, particulate matter, eutrophication (marine), eutrophication (terrestrial), and water use.

Following the selection of the relevant midpoint impact categories, the emissions listed in Table 7.6 are matched with the corresponding characterisation factors provided in EF v3.0. These factors are then applied to quantify

Table 7.6: Emissions for the production of 1 kg of hydrogen [12, 14]

Emissions to air [kg]	Wind turbine	SWRO	PEM electrolyser	Storage
Carbon dioxide	7.42×10^{-1}	3.77×10^{-3}	4.18×10^{-2}	1.66×10^{-1}
Carbon monoxide	7.23×10^{-4}	0	3.15×10^{-5}	1.46×10^{-4}
Methane	2.77×10^{-4}	1.65×10^{-5}	8.40×10^{-6}	1.44×10^{-5}
Nitrogen oxide	2.16×10^{-3}	0	2.21×10^{-3}	3.29×10^{-4}
Nitrous oxide	3.36×10^{-5}	0	2.80×10^{-6}	1.37×10^{-5}
Non-methane hydrocarbons	2.75×10^{-3}	0	3.08×10^{-4}	1.32×10^{-3}
Particulates	2.70×10^{-2}	0	2.01×10^{-4}	1.44×10^{-3}
Sulfur oxides	3.77×10^{-3}	0	1.59×10^{-3}	7.38×10^{-4}
Sulfur dioxide	2.51×10^{-3}	0	1.01×10^{-3}	5.56×10^{-4}
Emissions to water [kg]	Wind turbine	SWRO	PEM electrolyser	Storage
Phosphate	0	8.64×10^{-7}	0	0
Chloride	0	2.68×10^{-1}	0	0
Ammonium	0	4.23×10^{-4}	0	0
Nitrate	0	3.38×10^{-5}	0	0
Calcium	0	3.67×10^{-3}	0	0
Magnesium	0	1.10×10^{-2}	0	0
Lithium	0	1.56×10^{-6}	0	0
Boron	0	2.12×10^{-8}	0	0
Phosphorus	0	7.19×10^{-6}	0	0
Titanium	0	7.65×10^{-9}	0	0
Arsenic	0	8.45×10^{-9}	0	0
Strontium	0	5.41×10^{-5}	0	0
Molybdenum	0	5.76×10^{-8}	0	0
Silver	0	3.21×10^{-8}	0	0
Antimony	0	1.84×10^{-8}	0	0
Barium	0	2.28×10^{-8}	0	0
Tungsten	0	3.44×10^{-8}	0	0
Thallium	0	2.40×10^{-8}	0	0
Nickel	0	0	2.37×10^{-7}	0

the environmental impacts across the selected categories. The relevant impact categories associated with emissions to air for each system are summarised in Table 7.7, whereas those related to emissions to water are presented in Table 7.8.

Table 7.7: EF v3.0 LCI method characterisation of air emissions per kg of substance

Impact	Impact category	Value	Unit
Carbon dioxide	Climate change	1.00	kg CO_2-eq
Carbon monoxide	Climate change	1.57	kg CO_2-eq
Carbon monoxide	Ecotoxicity, freshwater	2.28×10^{-2}	CTUe
Carbon monoxide	Human toxicity, non-cancer	1.08×10^{-6}	CTUh
Carbon monoxide	Photochemical ozone formation	4.56×10^{-2}	kg NMVOC-eq
Methane	Climate change	3.68×10^{1}	kg CO_2-eq
Methane	Ecotoxicity, freshwater	3.20×10^{-1}	CTUe
Methane	Human toxicity, non-cancer	3.26×10^{-7}	CTUh
Methane	Photochemical ozone formation	1.01×10^{-2}	kg NMVOC-eq
Nitrogen oxides	Acidification	8.37×10^{-1}	mol H^+ eq
Nitrogen oxides	Particulate matter	1.60×10^{-6}	Disease incidence
Nitrogen oxides	Eutrophication marine	3.89×10^{-1}	kg N-eq
Nitrogen oxides	Eutrophication, terrestrial	2.72	mol N-eq
Nitrogen oxides	Photochemical ozone formation	1.00	kg NMVOC-eq
Nitrous oxide	Climate change	2.98×10^{2}	kg CO_2-eq
Nitrous oxide	Human toxicity, non-cancer	1.60×10^{-8}	CTUh
Non-methane hydrocarbons	Ecotoxicity, freshwater	2.98×10^{-2}	CTUh
Non-methane hydrocarbons	Human toxicity, non-cancer	4.16×10^{-10}	CTUh
Particles	Particulate matter	1.89×10^{-5}	Disease incidence
Sulfur oxides	Acidification	1.58	mol H^+ eq
Sulfur oxides	Particulate matter	8.00×10^{-6}	Disease incidence
Sulfur oxides	Photochemical ozone formation	8.11×10^{-2}	kg NMVOC-eq
Sulfur dioxide	Acidification	1.58	mol H^+ eq
Sulfur dioxide	Particulate matter	8.00×10^{-6}	Disease incidence
Sulfur dioxide	Photochemical ozone formation	8.11×10^{-2}	kg NMVOC-eq

As discussed in Section 7.1, the normalisation factors in EF v3.0 are applied to bring the different impact categories onto a comparable scale [15]. Furthermore, to reflect the relative importance of each category, weighting factors are subsequently applied to the normalised values. The normalisation and weighting factors corresponding to each selected midpoint category in EF v3.0 are summarised in Table 7.9.

7.3.4 Interpretation of Results

This section presents the LCA of hydrogen production via the PEM electrolyser, utilising seawater and powered by wind energy, using the collected data in the previous sections.

To this end, the corresponding impact values for each of the ten selected midpoint categories are computed for all subsystems, and the relative contribution of each subsystem to the overall environmental load is determined.

The absolute subsystem-level contributions to the selected impact categories – acidification, climate change, ecotoxicity (freshwater), eutrophication (freshwater), eutrophication (marine), eutrophication (terrestrial), Human toxicity (cancer), Human toxicity (non-cancer), Particulate matter, Photochemical

Table 7.8: EF v3.0 LCI method characterisation of water emissions per kg of substance

Impact	Impact category	Value	Unit
Phosphate	Eutrophication, freshwater	0	kg P-eq
Chloride	Ecotoxicity, freshwater	2.15×10^{-9}	CTUe
Chloride	Human toxicity, non-cancer	2.90×10^{-11}	CTUh
Ammonium	Ecotoxicity, freshwater	6.67×10^{-2}	CTUe
Ammonium	Eutrophication marine	7.78×10^{-1}	kg N-eq
Ammonium	Human toxicity, non-cancer	1.55×10^{-12}	CTUh
Nitrate	Eutrophication marine	2.26×10^{-1}	kg N-eq
Calcium	Ecotoxicity, freshwater	7.01×10^{-45}	CTUe
Magnesium	Ecotoxicity, freshwater	8.29×10^{-7}	CTUe
Magnesium	Human toxicity, non-cancer	6.24×10^{-14}	CTUh
Lithium	Ecotoxicity, freshwater	4.71×10^{-17}	CTUe
Lithium	Human toxicity, non-cancer	6.80×10^{-12}	CTUh
Boron	Ecotoxicity, freshwater	1.91×10^{-4}	CTUe
Phosphorus	Ecotoxicity, freshwater	4.01×10^{-3}	CTUe
Phosphorus	Eutrophication, freshwater	0	CTUe
Phosphorus	Human toxicity, non-cancer	2.36×10^{-10}	CTUh
Titanium	Ecotoxicity, freshwater	2.75×10^{-12}	CTUe
Titanium	Human toxicity, non-cancer	8.31×10^{-15}	CTUh
Arsenic	Ecotoxicity, freshwater	8.57×10^{-18}	CTUe
Arsenic	Human toxicity, cancer	3.02×10^{-6}	CTUh
Arsenic	Human toxicity, non-cancer	2.24×10^{-4}	CTUh
Strontium	Ecotoxicity, freshwater	3.39×10^{-16}	CTUe
Molybdenum	Ecotoxicity, freshwater	6.59×10^{-21}	CTUe
Molybdenum	Human toxicity, non-cancer	2.96×10^{-8}	CTUh
Silver	Ecotoxicity, freshwater	2.09×10^{-17}	CTUe
Silver	Human toxicity, non-cancer	8.79×10^{-6}	CTUh
Antimony	Ecotoxicity, freshwater	8.22×10^{-19}	CTUe
Antimony	Human toxicity, cancer	0	CTUh
Antimony	Human toxicity, non-cancer	1.67×10^{-6}	CTUh
Barium	Ecotoxicity, freshwater	9.34×10^{-16}	CTUe
Barium	Human toxicity, cancer	0	CTUh
Barium	Human toxicity, non-cancer	2.77×10^{-6}	CTUh
Tungsten	Ecotoxicity, freshwater	2.17×10^{-20}	CTUe
Thallium	Ecotoxicity, freshwater	9.50×10^{-18}	CTUe
Thallium	Human toxicity, non-cancer	1.05×10^{-5}	CTUh
Nickel	Ecotoxicity, freshwater	4.91×10^{-16}	CTUe
Nickel	Human toxicity, cancer	6.12×10^{-7}	CTUh
Nickel	Human toxicity, non-cancer	3.44×10^{-8}	CTUh

ozone formation, and water use – as well as the share of each subsystem contributing to the impact categories, are depicted in Fig. 7.4 to Fig. 7.13,

Table 7.9: Impact factors and normalisation factors of each impact category based on EF v3.0 per person

Impact category	Normalisation factors	Unit	Weighting factors [%]
Acidification	5.56×10^{1}	mol H^+ eq	6.20
Climate change	8.10×10^{3}	kg CO_2-eq	21.06
Ecotoxicity, freshwater	4.27×10^{4}	CTUe	1.92
Eutrophication, marine	1.95×10^{1}	kg N-eq	2.96
Eutrophication, terrestrial	1.77×10^{2}	mol N-eq	3.71
Human toxicity, cancer	1.69×10^{-5}	CTUh	2.13
Human toxicity, non-cancer	2.30×10^{-4}	CTUh	1.84
Particulate matter	5.95×10^{-4}	disease incidences	8.96
Photochemical ozone formation	4.06×10^{1}	kg NMVOC-eq	4.78
Water use	1.15×10^{4}	m^3 water-eq of deprived water	8.51

respectively.

As shown in Fig.7.4, the SWRO-PEM system yields a total of 0.02 mol H^+ eq/kg_{H_2}, with the wind turbine being the dominant contributor to acidification among the subsystems, followed by the PEM electrolyser. This stems from the higher levels of sulfur oxide and sulfur dioxide emissions associated with the manufacturing processes of these components. The wind turbine shows the highest contribution due to its steel-intensive construction, which is known to generate considerable SO_x emissions. In case of the PEM electrolyser, the acidification impact arises from the manufacturing of catalyst and membrane materials such as platinum, iridium and Nafion. Specifically, the wind turbine accounts for 61.82% of sulfur oxide and 61.58% of sulfur dioxide emissions, whereas the PEM electrolyser contributes 26.07% and 24.78%, respectively.

Regarding the climate change in Fig. 7.5, the SWRO-PEM system results in 0.98 kg CO_2-eq/kg_{H_2}, with the wind turbine remaining the largest contributor among the four subsystems. This is primarily due to the substantial steel and concrete requirements, which lead to higher emissions during the construction phase of the wind turbine compared to the other subsystems. Consequently, the wind turbine is responsible for 77.81% of the total carbon monoxide emissions, 80.29% of carbon monoxide, 94.38% of methane, and 67.07% of nitrous oxide emissions per kilogram of hydrogen produced. Additionally, as reported by [16], the average energy demand for wind-powered electrolysis, including hydrogen storage, is approximately 9.1 MJ per kilogram of hydrogen, based on the lower heating value (LHV). The majority of this energy, about 72.6%, is consumed for manufacturing the materials for wind turbines.

When it comes to freshwater ecotoxicity, the SWRO-PEM system yields a total of 2.80×10^{-4} CTUe/kg_{H_2}, as illustrated in Fig. 7.6, with the impact primarily driven by methane emissions among those considered in this study. Consequently, the wind turbine, which is responsible for 87.58% of total methane emissions, exhibits the highest contribution to this impact category. In contrast, the PEM electrolyser, with a methane emission share of only 2.66%, has the

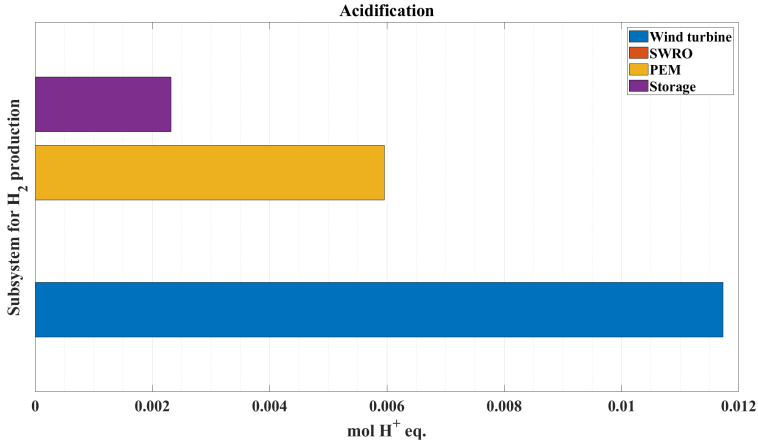

(a) Contribution of each subsystem to acidification

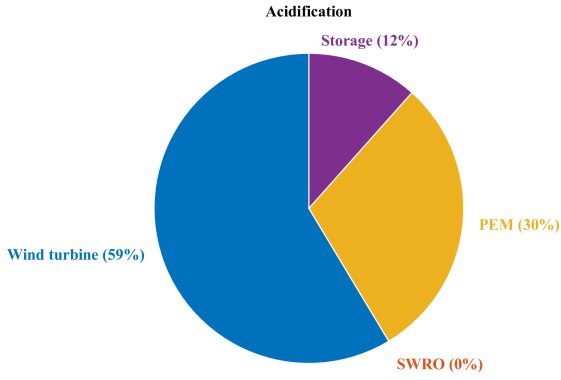

(b) Share of each subsystem in acidification

Figure 7.4: Acidification impact category

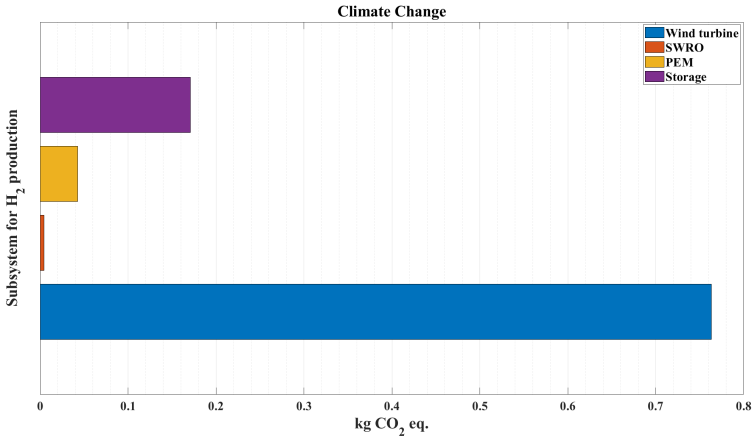

(a) Contribution of each subsystem to climate change

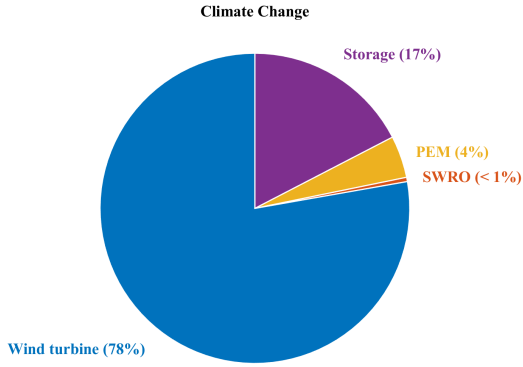

(b) Share of each subsystem in climate change

Figure 7.5: Climate change impact category

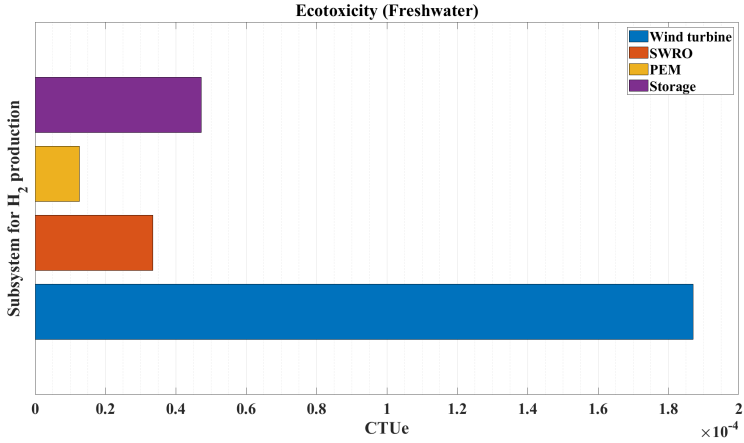

(a) Contribution of each subsystem to Ecotoxicity (freshwater)

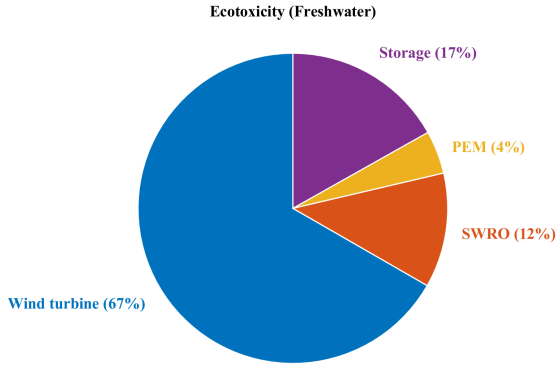

(b) Share of each subsystem in Ecotoxicity (freshwater)

Figure 7.6: Ecotoxicity (freshwater) impact category

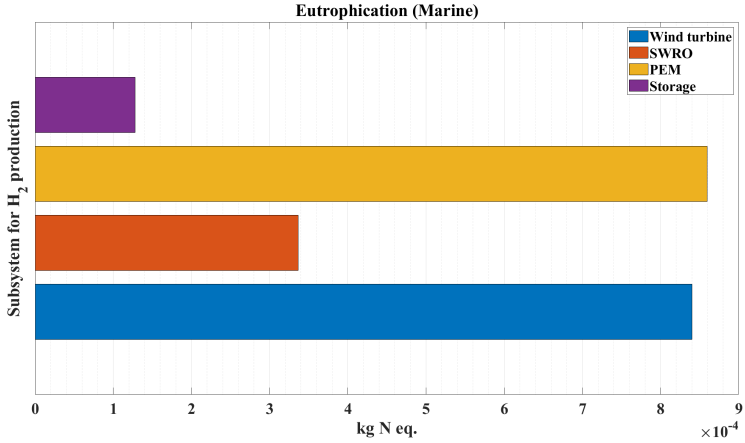

(a) Contribution of each subsystem to Eutrophication (marine)

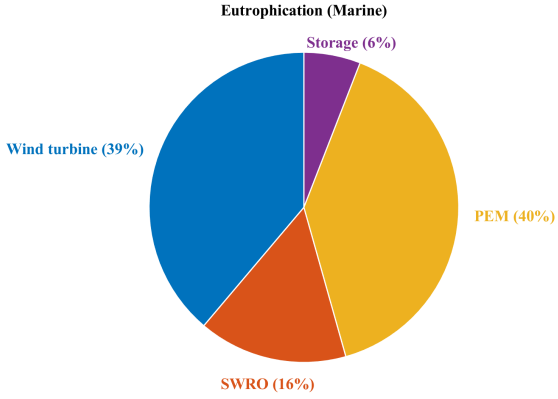

(b) Share of each subsystem in Eutrophication (marine)

Figure 7.7: Eutrophication (marine) impact category

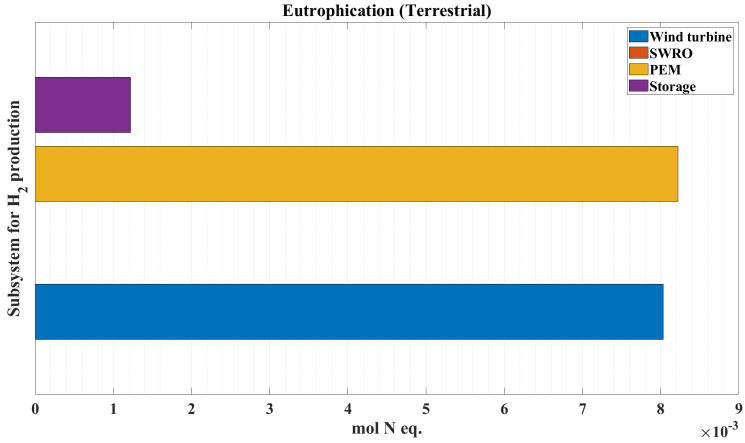

(a) Contribution of each Share of each subsystem in Eutrophication (terrestrial)

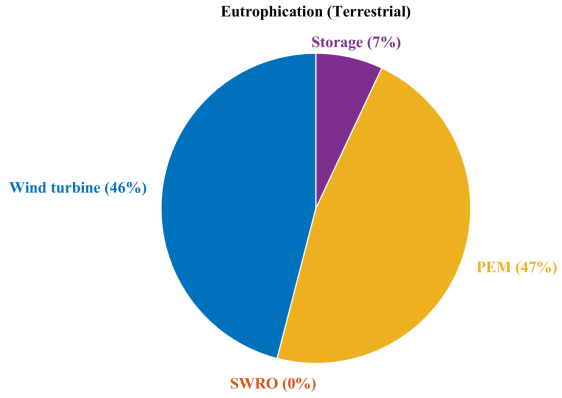

(b) Share of each subsystem in Eutrophication (terrestrial)

Figure 7.8: Eutrophication (terrestrial) impact category

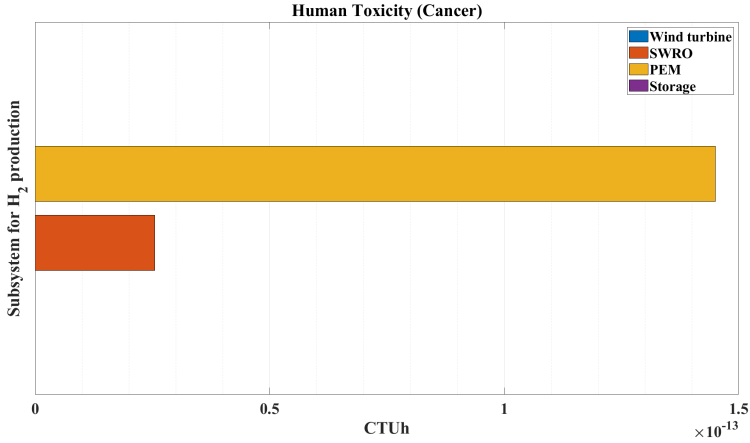

(a) Contribution of each subsystem to Human toxicity (cancer)

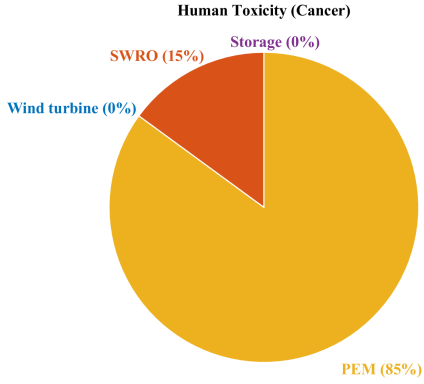

(b) Share of each subsystem in Human toxicity (cancer)

Figure 7.9: Human toxicity (cancer) impact category

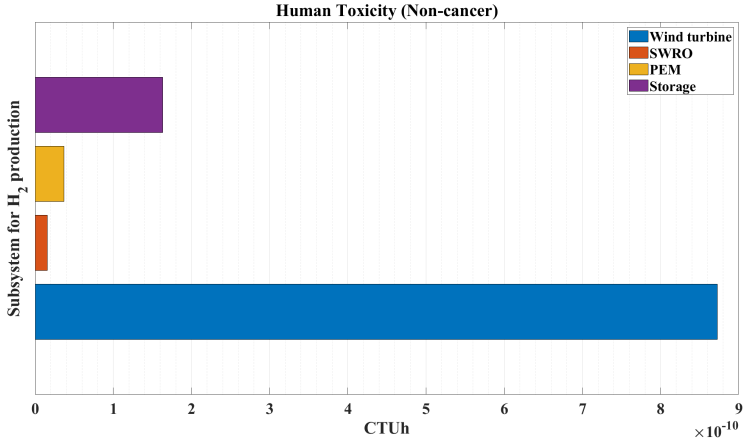

(a) Contribution of each subsystem to Human toxicity (non-cancer)

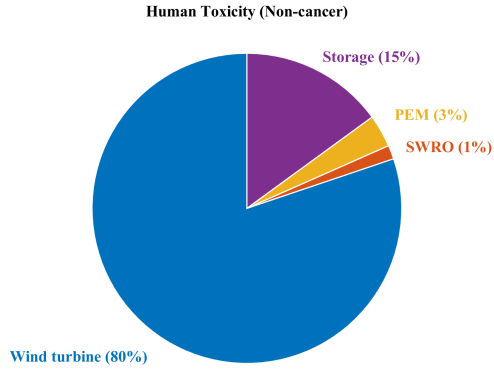

(b) Share of each subsystem in Human toxicity (non-cancer)

Figure 7.10: Human toxicity (non-cancer) impact category

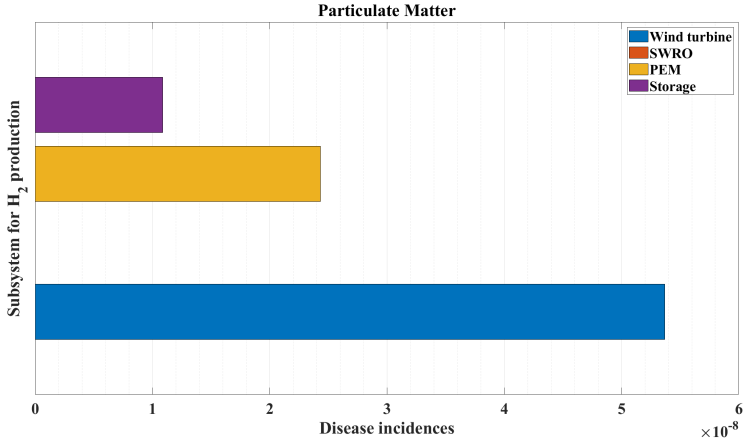

(a) Contribution of each subsystem to Particulate matter

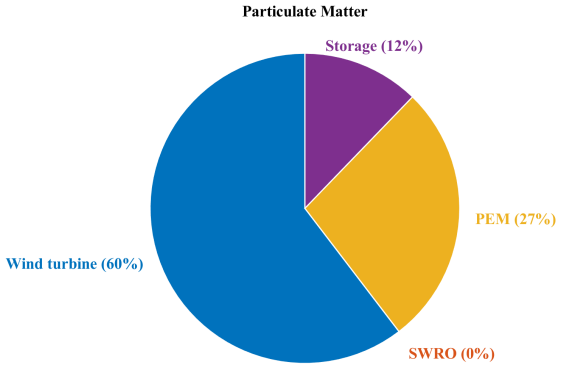

(b) Share of each subsystem in Particulate matter

Figure 7.11: Particulate matter impact category

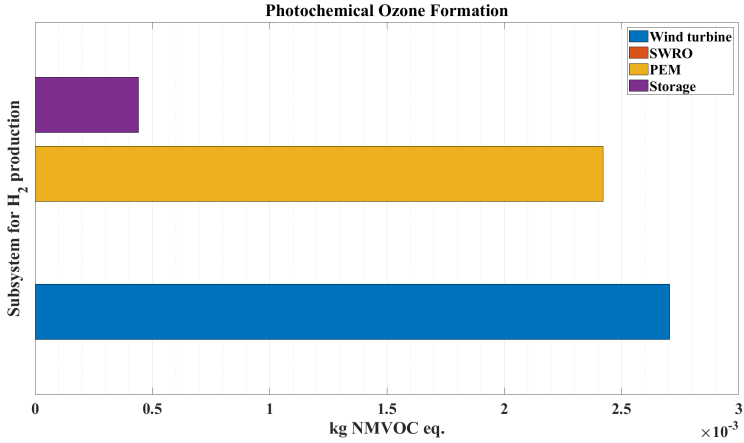

(a) Share of each subsystem in Photochemical ozone formation

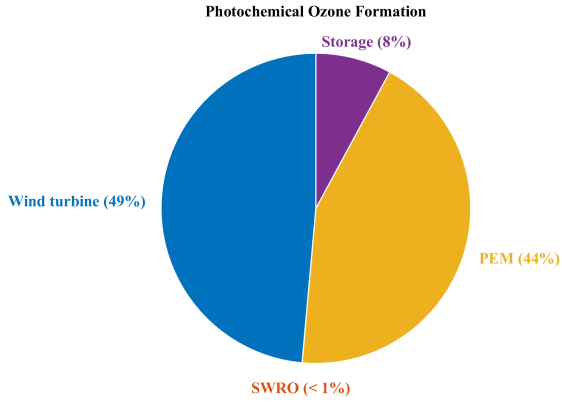

(b) Contribution of the system to Photochemical ozone formation

Figure 7.12: Photochemical ozone formation impact category

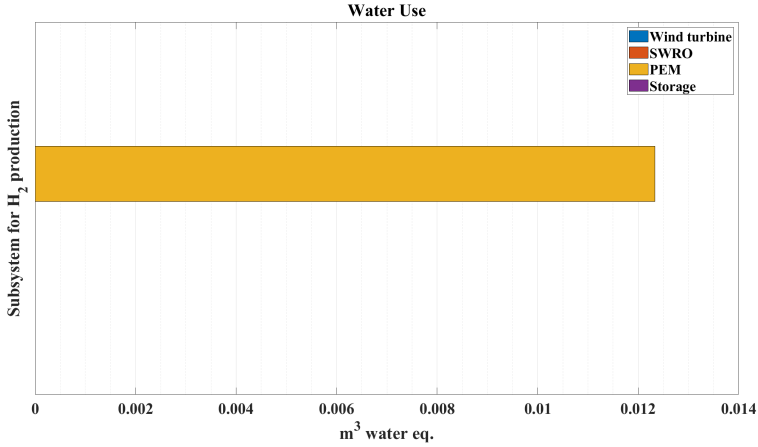

(a) Contribution of each subsystem to water use

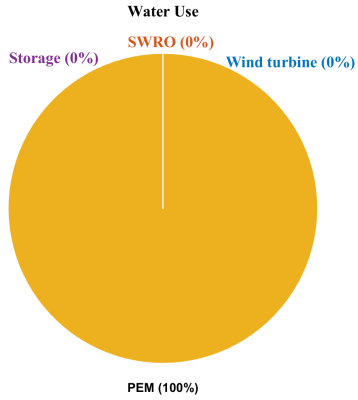

(b) Share of each subsystem in water use

Figure 7.13: water use impact category

lowest contribution among all subsystems.

Marine eutrophication, amounting to a total of 2.20×10^{-3} kg N-eq/kg_{H_2} for the SWRO-PEM system, as depicted in Fig. 7.7, is mainly driven by nitrogen oxides production, with the PEM electrolyser contributing the largest share at 47.03%, followed by the wind turbine at 45.97%. This is mainly attributed to the high-temperature industrial processes involved in the production of high-purity materials such as platinum for the PEM electrolyser, and the production of steel and concrete in the case of the wind turbine. A similar trend is observed for the terrestrial eutrophication, indicating a total of of 1.75×10^{-2} mol N-eq/kg_{H_2}, as shown in Fig. 7.8, which is also mostly driven by by nitrogen oxide emissions.

For human toxicity (cancer), the SWRO-PEM system yields a total of 1.70×10^{-13} CTUh/kg_{H_2}, as presented in Fig. 7.9, with the PEM electrolyser and the SWRO system are the principal contributors. This is mainly attributed to nickel emissions associated with the PEM electrolyser and arsenic emissions linked to the SWRO system. Other materials included in this study do not significantly affect this impact category.

In the case of human toxicity (non-cancer), the SWRO-PEM system resulted in 1.08×10^{-9} CTUh/kg_{H_2}, as illustrated in Fig. 7.10. The wind turbine is the most significant contributor, accounting for 80% of the total impact, followed by the storage system with 15%. This impact category is primarily driven by carbon monoxide emissions, for which the wind turbine and storage system contribute 80.29% and 16.21%, respectively.

Particulate matter, as depicted in Fig. 7.11, results in 8.89×10^{-8} disease incidences per kg of hydrogen, with the wind turbine being the largest contributor (60% of the total impact), followed by the PEM electrolyser and the storage system. This impact is largely influenced by emissions of sulfur oxides and sulfur dioxide, for which the wind turbine and the PEM electrolyser have the highest contribution, as previously discussed.

Regarding photochemical ozone formation, the SWRO-PEM system yields 5.60×10^{-3} kg NMVOC-eq/kg_{H_2}, as illustrated in Fig. 7.12, with the wind turbine and the PEM electrolyser are the major contributors, with shares of 49% and 44%, respectively. This impact category is mainly driven by emissions of nitrogen oxides, sulfur oxide and sulfur dioxide. Specifically, the wind turbine accounts for 45.97% of nitrogen oxide, 61.82% of sulfur oxide, and 61.58% of sulfur dioxide, respectively, while the PEM electrolyser contributes 47.03%, 26.07%, and 24.78% of these emissions, respectively

Lastly, for water use, the SWRO-PEM system leads to 1.23 $\times 10^{-2}$ m^3 water-eq of deprived water per kg of hydrogen, as shown in Fig. 7.13. Although the desalination system utilises seawater, it does not contribute to this impact category since seawater is not assigned a characterisation factor in the EF v3.0 method. Thus, the PEM electrolyser is the only subsystem contributing to water use in this study.

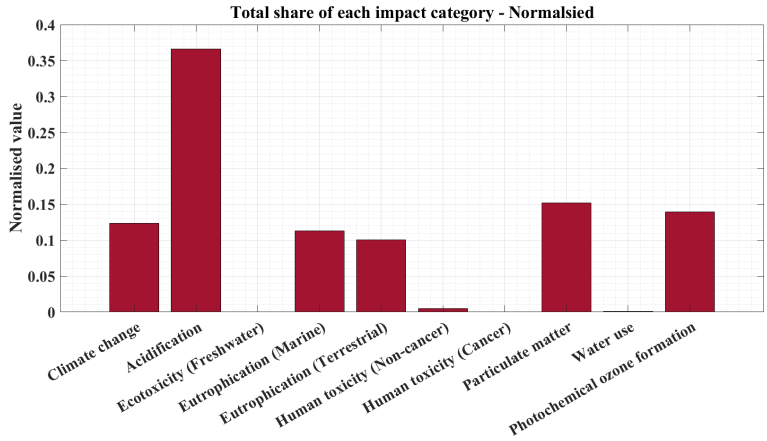

Figure 7.14: Share of each impact category after normalisation

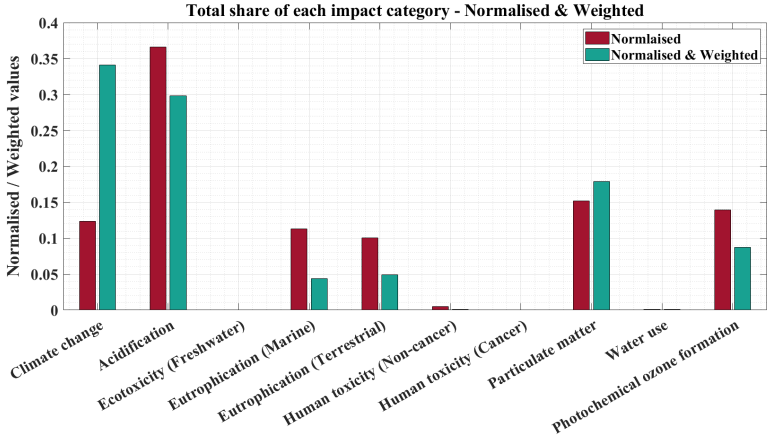

Figure 7.15: Share of each impact category after normalisation and weighting

The investigated impact categories are then normalised, and their relative contributions are compared, shown in Fig. 7.14.

Furthermore, as discussed in Section 7.1, each impact category is assigned a weighting factor based on its environmental significance and relative importance. By applying the weighting factor, provided in Table 7.9, to the normalised impact categories illustrated in Fig. 7.14, the weighted contributions of each category are determined, presented in Fig. 7.15.

As depicted in Fig. 7.15, the climate change category, for instance, gains greater significance after applying the weighting factors, due to its high assigned weighting factor of 21.0%, which reflects its environmental importance, despite

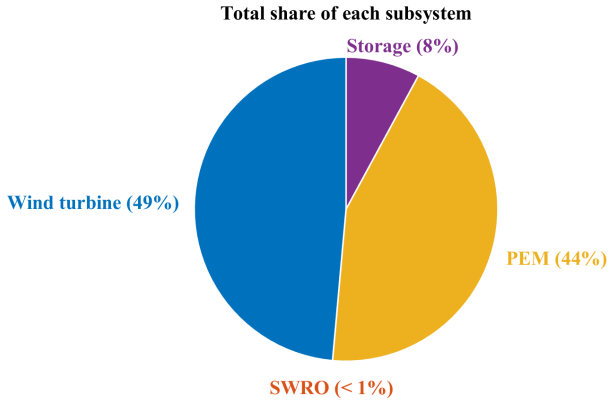

Figure 7.16: Share of each impact category after normalisation and weighting

having a lower normalised value compared to categories such as acidification and particulate matter.

Finally, to identify the overall impact of each subsystem, the aggregated sum of all weighted impact categories per subsystem is calculated, presented in Fig. 7.16.

As shown in Fig. 7.16, the wind turbine is the dominant contributor to the overall environmental impact, followed by the PEM electrolyser, the storage system, and the SWRO unit.

7.4 Conclusions

This chapter presented an LCA study of electrolytic hydrogen production, where a PEM electrolyser was integrated with a wind turbine, an SWRO unit, and a hydrogen compression and storage system. The main goal was to identify the dominant contributors to the environmental impacts across the system components.

To this end, using a functional unit of 1 kg of hydrogen, inventory data were collected for the aforementioned subsystems and their major BoP components. Thereafter, the associated emissions to air and water were translated into environmental impact categories, using the EF v3.0 method. These impact categories were subsequently normalised and weighted to assess and compare the relative contributions of each subsystem to the overall environmental footprint.

Among the four subsystems, the wind turbine was identified as the dominant contributor in majority of impact categories, including climate change (78%), acidification (59%), freshwater ecotoxicity (67%), non-cancer-related human

toxicity (80%), particulate matter (60%) and photochemical ozone formation (49%). This is primarily due to the material-intensive nature of wind turbine manufacturing, particularly the high demand for steel and concrete, which results in significant emissions of carbon dioxide, carbon monoxide, nitrogen oxide, nitrous oxide, sulfur oxide and sulfur dioxide. Overall, the wind turbine is responsible for approximately 49% of the total weighted environmental impact.

The SWRO unit, on the other hand, showed the lowest contribution, accounting for less than 1% of the total environmental impact. The main influence of the SWRO unit was observed in water-related categories, contributing 12% to freshwater ecotoxicity and 16% to marine eutrophication due to the discharge of brine. Moreover, the presence of arsenic emissions results in a 15% contribution to cancer-related human toxicity.

As for the PEM electrolyser, it was the leading contributor to marine eutrophication (40%), terrestrial eutrophication (47%), cancer-related human toxicity (85%), and water use (100%). It also ranked second in acidification (30%), particulate matter (27%), and photochemical ozone formation (44%). These impacts stem from the use of high-temperature industrial processes such as platinum, as well as the catalyst and membrane components, and emissions such as nickel associated with the operation of the electrolyser. In total, the PEM electrolyser contributed approximately 44% to the total weighted emissions, making it the second most impactful subsystem.

Finally, the hydrogen compression and storage unit had the second-highest contribution in impact categories such as climate change, freshwater ecotoxicity, and non-cancer human toxicity. It contributed around 8% to the overall weighted environmental impacts of the system.

Considering the investigated impact categories in this study, after applying the EF v3.0 weighting factors, climate change was found to be the most impactful category, accounting for 34.07% of the total, followed by acidification with 29.79%, particulate matter with 17.87%, photochemical ozone formation with 8.75%, terrestrial eutrophication with 4.89%, and marine eutrophication with 4.39%. The remaining categories, including non-cancer-related human toxicity with 0.48%, water use with 0.11%, cancer-related human toxicity with 1.26×10^{-3}%, and freshwater ecotoxicity with 6.68×10^{-4}% contribute marginally.

Future studies could explore alternative subsystems, such as other electrolyser technologies, including AE or SO electrolysers, to compare their environmental performance against PEM, under the same set of impact categories. Improving the efficiency of energy-intensive components, like the electrolyser, could potentially reduce the overall environmental impact of the system. This is because of the fact that the enhanced efficiency would not only reduce electricity consumption but also lower the material demand, both for the electrolyser itself and for the wind turbine per kilogram of hydrogen produced. In addition,

exploring the integration of alternative RESs, such as solar or hydropower, in comparison with wind energy, is essential for identifying optimal configurations for green hydrogen production. Nevertheless, other factors, especially in terms of grid stability and renewable resource intermittency, must be taken into account.

From an LCA perspective, the desalination system contributes less than 1% to the total environmental emissions of the entire system. This negligible impact further supports its competitiveness with direct seawater electrolysis in terms of environmental performance, in addition to other advantages discussed in Chapter 5.

Due to limitations in data availability, this study did not include an uncertainty analysis. Future research could incorporate methods such as Monte Carlo simulations to evaluate the robustness of the results.

Bibliography

[1] I. M. Krishna and V. Manickam, *Environmental management: science and engineering for industry*. Butterworth-Heinemann, 2017.

[2] K. Bareiß, C. de la Rua, M. Möckl, and T. Hamacher, "Life cycle assessment of hydrogen from proton exchange membrane water electrolysis in future energy systems," *Applied Energy*, vol. 237, pp. 862–872, 2019.

[3] M. Hauschild, M. Goedkoop, J. Guinee, R. Heijungs, M. Huijbregts, O. Jolliet, M. Margni, S. A. De, *et al.*, "Recommendations for life cycle impact assessment in the European context-based on existing environmental impact assessment models and factors (International Reference Life Cycle Data System-ILCD handbook)," 2011.

[4] I. Johansson and P. Somasundaran, *Handbook for cleaning/decontamination of surfaces*. Elsevier, 2007.

[5] J. Gerhardt-Mörsdorf, F. Peterssen, P. Burfeind, M. Benecke, B. Bensmann, R. Hanke-Rauschenbach, and C. Minke, "Life cycle assessment of a 5 MW polymer exchange membrane water electrolysis plant," *Advanced Energy and Sustainability Research*, vol. 5, no. 4, p. 2300135, 2024.

[6] X. Wei, S. Sharma, A. Waeber, D. Wen, S. N. Sampathkumar, M. Margni, F. Maréchal, *et al.*, "Comparative life cycle analysis of electrolyzer technologies for hydrogen production: Manufacturing and operations," *Joule*, vol. 8, no. 12, pp. 3347–3372, 2024.

[7] J. C. Koj, P. Zapp, C. Wieland, K. Görner, and W. Kuckshinrichs, "Life cycle environmental impacts and costs of water electrolysis technologies for green hydrogen production in the future," *Energy, Sustainability and Society*, vol. 14, no. 1, pp. 1–26, 2024.

[8] S. Ghandehariun and A. Kumar, "Life cycle assessment of wind-based hydrogen production in Western Canada," *International Journal of Hydrogen Energy*, vol. 41, no. 22, pp. 9696–9704, 2016.

[9] S. Krishnan, B. Corona, G. J. Kramer, M. Junginger, and V. Koning, "Prospective LCA of alkaline and PEM electrolyser systems," *International Journal of Hydrogen Energy*, vol. 55, pp. 26–41, 2024.

[10] G. H. Patel, J. Havukainen, M. Horttanainen, R. Soukka, and M. Tuomaala, "Climate change performance of hydrogen production based on life cycle assessment," *Green Chemistry*, vol. 26, no. 2, pp. 992–1006, 2024.

[11] J. Zhang, B. Ling, Y. He, Y. Zhu, and Z. Wang, "Life cycle assessment of three types of hydrogen production methods using solar energy," *International Journal of Hydrogen Energy*, vol. 47, no. 30, pp. 14158–14168, 2022.

[12] M. Hemmati, N. Bayati, and T. Ebel, "Life-cycle assessment of renewable-based hydrogen production via PEM electrolyzer in Indonesia," in *2024 12th International Conference on Smart Grid (icSmartGrid)*, pp. 112–117, IEEE, 2024.

[13] R. Bhandari, C. A. Trudewind, and P. Zapp, "Life cycle assessment of hydrogen production via electrolysis–a review," *Journal of Cleaner Production*, vol. 85, pp. 151–163, 2014.

[14] S. Fayyaz, S. K. Masjedi, A. Kazemi, E. Khaki, M. Moeinaddini, and S. I. Olsen, "Life cycle assessment of reverse osmosis for high-salinity seawater desalination process: Potable and industrial water production," *Journal of Cleaner Production*, vol. 382, 2023.

[15] S. Andreasi Bassi, F. Biganzoli, N. Ferrara, A. Amadei, A. Valente, S. Sala, and F. Ardente, "Updated characterisation and normalisation factors for the Environmental Footprint 3.1 method," *Publications Office of the European Union: Luxembourg*, 2023.

[16] M. Mann and P. Spath, "Life cycle assessment of renewable hydrogen production via wind/electrolysis: milestone completion report," tech. rep., National Renewable Energy Laboratory (NREL), Golden, CO (United States), 2004.

Chapter 8

Conclusions and Future Work

In this chapter, the results and findings of the previous chapters are summarised, and the key conclusions are highlighted. Furthermore, opportunities for future research are discussed.

8.1 Conclusions

Stemming from factors such as the limited availability of fossil fuels, their environmental pollution, and concerns over energy security, the global need to shift towards renewable energy sources (RESs) has been growing steadily. It is well known that the most efficient way to utilise RESs is through direct electrification. Nevertheless, while the advantages of RESs, such as the production of environmentally friendly energy and their abundance, are evident, their inherent intermittency poses several challenges for power system operators in the context of direct electrification. This topic was reviewed in detail in Chapter 2. It was shown that among the different types of RESs, solar and wind energy are the most widely recognised sources worldwide. Comparing these two renewable sources, it was demonstrated that solar irradiance exhibits more predictable variability than wind speed. In other words, the diurnal cycle of solar irradiance provides a more foreseeable pattern for the output power of solar systems. Moreover, the higher correlation between solar power generation and electricity demand facilitates the integration of solar energy into the power grid.

Regarding solar energy, it was shown that photovoltaic (PV) and concentrated solar power (CSP) are the dominant technologies for electricity generation. However, the latter is highly location-dependent and economically viable mainly in regions with direct normal irradiance (DNI) values exceeding 2000 $\mathrm{kWh/m^2}$ per year. Consequently, PV has gained greater popularity compared to CSP. In terms of wind energy, the resource can be harnessed either

onshore or offshore, with onshore systems being more mature, having undergone nearly a century of earlier development than offshore systems. On the other hand, offshore wind energy represents an attractive option for countries with access to the sea. This is why Belgium, which served as the case study in this thesis, is among the leading countries worldwide in terms of installed offshore wind capacity. Nonetheless, such large-scale integration requires careful consideration to ensure secure grid operation, since, as shown in Chapter 2, integrating RESs into the grid affects the power system over both the short and long term. Based on the above considerations, offshore wind energy in Belgium was selected for further investigation in this research.

Offshore wind energy is less affected by intermittency due to higher wind speeds and more consistent wind conditions offshore compared to other renewable sources, such as onshore wind and solar energy. Regardless, significant challenges arise when large-scale offshore wind farms are installed, and electricity must be transmitted to shore. When transmission limitations occur, the generated energy can alternatively be converted into molecules, such as hydrogen, and transported to shore through pipelines or shipping. This option becomes particularly attractive when the distance to shore is considerable, the offshore power generation capacity is large, or suitable infrastructure already exists. Consequently, the main objective of this research was to investigate the production of green hydrogen from offshore wind energy. This can be achieved through electrolysis, the most mature technologies for which are alkaline electrolysers (AEs) and proton exchange membrane (PEM) electrolysers.

In Chapter 3, it was shown that for offshore operation of electrolysers coupled with RESs, several factors must be considered. Although offshore wind is more consistent than onshore wind, it still exhibits a certain degree of intermittency. The main implication of this for electrolysers is the need for rapid ramping capability to accommodate variations in the input power. Compared to AEs, PEM electrolysers can adjust their power consumption more quickly. This is due to the solid electrolyte used in PEM electrolysers, in contrast to the liquid electrolyte in AEs, which results in lower inertia and faster ion transport and response. Furthermore, as discussed in Chapter 3, PEM electrolysers can operate at higher current densities than AEs, leading to a smaller spatial footprint and making them more suitable for offshore applications where space is limited. Therefore, in this thesis, a PEM electrolyser was selected for coupling with offshore wind energy.

However, although the PEM electrolyser benefits from a fast response to RES fluctuations, its operation is not instantaneous. Considering its dynamic behaviour is therefore crucial when PEM electrolysers are integrated with RESs, since these variations affect the consumed power and the amount of hydrogen produced, thereby influencing the outcomes of various studies, such as those investigating the flexibility provision of electrolysers. Consequently, in Chap-

ter 4, a PEM electrolyser model was developed in MATLAB/Simulink. To maintain accuracy while ensuring computational efficiency, negligible mechanisms were omitted to make the model faster and suitable for large-scale simulations. Moreover, the model was built upon mathematical equations rather than circuit elements, making it reliable across the entire operating range of the electrolyser. The model was validated against experimental data for both static and dynamic operation, showing average relative errors of 0.66% and 3.93%, respectively. It was concluded that omitting mechanisms such as concentration overvoltage, electronic resistance, or water permeation through the membrane due to hydraulic pressure has no substantial impact on the results, while significantly improving computational efficiency. Additionally, it was demonstrated that the thermal characteristics of the electrolyser, such as the operating temperature, influence its performance, particularly its dynamic behaviour, further highlighting the need for a dynamic PEM electrolyser model.

Thereafter, given the assumption that the PEM electrolyser is installed offshore in this study, using seawater as feedwater becomes a practical option. This approach helps address challenges such as freshwater scarcity and the uneven global distribution of freshwater resources associated with electrolyser operation. Nevertheless, due to the impurities present in seawater, directly feeding electrolysers with seawater requires a substantial redesign of conventional electrolyser types, including PEM electrolysers. Alternatively, seawater can be purified before entering the electrolyser, which is the approach investigated in this thesis. In Chapter 5, it was demonstrated that integrating a seawater desalination system, specifically a seawater reverse osmosis (SWRO) unit, with a PEM electrolyser has only a negligible effect on key factors compared to the electrolysis process itself, including the additional energy demand (~0.1%), capital expenditure (~3%), installation costs, and operational expenditure (~0.2%). Therefore, in this research, an SWRO system integrated with a PEM electrolyser was explored for offshore hydrogen production. To this end, a mathematical model of the SWRO system was developed based on the solution-diffusion mechanism. The model was validated against experimental data at low total dissolved solids (TDS) levels, showing an average relative error of 3.64% for recovery rate and 1.48% for salt rejection. At seawater-level TDS concentrations, the model exhibited errors of 2.74% and 0.13% for recovery and salt rejection, respectively, when compared to experimental results.

The model was then integrated with the developed PEM electrolyser model, demonstrating that the SWRO system can supply the electrolyser with purified water containing less than 5 ppm TDS, which represents a typical allowable level for PEM electrolyser operation.

Given that electricity accounts for the largest share of hydrogen production costs, various operation modes of the PEM electrolyser were investigated in Chapter 6. In this part of the study, the SWRO system was excluded since,

as previously stated, its contribution to offshore hydrogen production costs is negligible. Three operation modes of the PEM electrolyser were examined based on the predicted electricity prices in Belgium. In the first mode, the electrolyser operated continuously at full capacity. In the second mode, the electrolyser operated according to the day-ahead electricity market prices. In the third mode, the electrolyser operated based on day-ahead market prices while also providing frequency ancillary services when the grid requirements were met. The parameters for this analysis were defined according to the planned artificial energy island in Belgium to ensure a realistic representation of offshore hydrogen production. To account for uncertainties in future electricity prices, three different projections of the Belgian energy system were used, each resulting in distinct electricity price trajectories.

As shown in Chapter 6, operating the PEM electrolyser continuously at full capacity was not economically optimal, since hydrogen production during periods of high electricity prices was unfavourable. This mode resulted in hydrogen break-even prices ranging from 4.65–5.57 €/kg_{H_2} across the three electricity price trajectories but achieved the highest hydrogen yield with a 100% capacity factor, making it suitable when the objective is to maximise hydrogen output. In contrast, operating the electrolyser in response to day-ahead market prices reduced the hydrogen break-even price to a range of 4.12–4.84 €/kg_{H_2}, although this was achieved at the expense of lower capacity factors, ranging from 55.0% to 63.4%, depending on the electricity price trajectory. Finally, in the third mode, the provision of frequency containment reserve (FCR) by the electrolyser was investigated. Building upon the second scenario, the electrolyser provided symmetric ±200 mHz FCR while participating in the ancillary service market. This mode yielded the lowest hydrogen break-even prices, ranging from 3.81–4.49 €/kg_{H_2} for the considered electricity price pathways.

A sensitivity analysis was conducted in Chapter 6 to identify the most influential parameters affecting the hydrogen production cost. Based on the analysis performed for the three scenarios, it was concluded that investing in materials that enhance electrolyser efficiency would have a more pronounced impact on the hydrogen production cost, given the high sensitivity of the results to efficiency compared to durability-related parameters such as degradation rate and stack replacement costs

To evaluate the environmental impacts associated with hydrogen production using seawater, a cradle-to-gate life cycle assessment (LCA) was conducted in Chapter 7. The main objective was to identify the dominant contributors to the overall environmental impacts across the system components, including electricity generation from wind energy, water desalination using an SWRO system, hydrogen generation via the PEM electrolyser, and hydrogen storage. Using the Environmental Footprint (EF) v3.0 method, the emissions associated with seawater electrolysis were translated into environmental impact categories, which

were subsequently normalised and weighted to compare the relative contributions of each subsystem to the total environmental footprint. It was concluded that the wind turbine was the dominant contributor in most impact categories, particularly in climate change (78%), mainly attributed to the high material intensity of wind turbine construction, especially the extensive use of steel and concrete that results in notable emissions of carbon dioxide, carbon monoxide, nitrogen oxide, nitrous oxide, sulfur oxide and sulfur dioxide. Overall, the wind turbine accounted for approximately 49% of the total weighted environmental impact. The SWRO unit, on the other hand, showed the lowest contribution, accounting for less than 1% of the total environmental impact. From an LCA standpoint, this minimal contribution supports the competitiveness of the desalination-based hydrogen production pathway with direct seawater electrolysis, complementing the additional advantages discussed in Chapter 5.

8.2 Further Research Opportunities

This thesis focused on offshore hydrogen production using a PEM electrolyser integrated with an SWRO desalination system. During this research, several topics and ideas were identified, which can be further analysed in future.

In line with Chapter 4, the developed PEM electrolyser model, as described in that chapter, employs certain empirical equations, for example, those used to calculate the electro-osmotic drag coefficient. This reliance on empirical relations may introduce higher uncertainties compared to physics-based formulations, which form the foundation of the developed PEM electrolyser model. Replacing the remaining empirical equations with physics-based counterparts could therefore enhance the model's accuracy. Furthermore, the model could be extended by incorporating additional modules to improve its versatility, such as integrating the required components for balance of plant (BoP) operation or CO_2 capture. The captured CO_2 could originate either from the atmosphere or, in the context of this thesis, from seawater. By integrating such modules, the system could be expanded to investigate the production of other green molecules, such as methane and methanol. For instance, this would allow the assessment of how the dynamic response of the PEM electrolyser, when coupled with an intermittent renewable energy source such as offshore wind, influences the performance of subsequent units like the methanation system.

In addition, data-driven techniques could be incorporated into the model to improve parameter estimation or the prediction of operational behaviour under conditions that are not explicitly covered by the physics-based framework. Another possible direction relates to reduced-order modelling. Although the full dynamic model captures the governing electrochemical and thermodynamic mechanisms in detail, its behaviour can, under certain operating conditions,

be approximated by a reduced-order system. In such cases, the dominant dynamic modes typically originate from processes such as thermal inertia. The significance of non-linearity depends on the operating range, with the system exhibiting nearly linear behaviour around fixed operating points but stronger non-linearities during large power transients, such as in flexibility studies. Developing a reduced-order model that captures these dominant modes could further enhance computational efficiency while preserving the essential dynamic characteristics of the full model.

Following Chapter 5, a similar replacement of the empirical equations with physics-based formulations can be implemented, for instance, those used to calculate seawater density or dynamic viscosity. This modification would enhance the model's accuracy, albeit at the expense of greater complexity and reduced computational efficiency. Moreover, although this thesis assumed that the dynamic operation of the SWRO system does not influence the PEM electrolyser, this interaction could be incorporated into the SWRO model to investigate whether it alters the dynamic response of the PEM electrolyser. Such an approach would enable a more accurate representation of the offshore hydrogen production system.

Based on Chapter 6, incorporating a more detailed ageing model could improve the accuracy of the results and enhance the integration with the methodology presented in that chapter. This would be particularly relevant because, on one hand, operating electrolysers continuously at full capacity subjects their critical components to higher wear rates compared to the other two scenarios, where the capacity factors were lower. On the other hand, frequent ramping up and down of the electrolyser may also accelerate its ageing compared to operation at a constant load, such as full-capacity operation. Furthermore, in line with this chapter, simulating the inertial response of PEM electrolysers could help evaluate their potential contribution to grid flexibility and determine whether the reduction in hydrogen break-even price, relative to continuous and day-ahead price-based operation, justifies the associated decrease in electrolyser capacity factor and the increased control complexity. Finally, several other operational scenarios could be explored, such as cases where the electrolyser exclusively provides FCR without relying on day-ahead market prices or operates in response to other market signals, such as intraday imbalance prices.

Regarding Chapter 7, other electrolyser technologies, such as AE or solid oxide (SO) electrolysers, could be assessed using the same LCA methodology to compare the environmental footprint of electrolytic hydrogen production across different technologies. Considering that this chapter concluded wind energy to be the dominant contributor to the overall environmental impact of the system, this renewable source could also be compared with other renewable energy sources to assess the variations in impact categories among different RESs. Upon the availability of sufficient data, the proposed studies could further

incorporate an uncertainty analysis to evaluate the reliability and robustness of the obtained impact results. For instance, this could be achieved through Monte Carlo random sampling of inventory data probability distributions, using multiple iterations for LCA calculations.